# Precision phenomenology at the LHC and characterization of theoretical uncertainties

Emanuele Angelo Bagnaschi

Université Paris-Diderot (Paris 7)
Sorbonne Paris Cité

École Doctorale 560 STEP'UP
Laboratoire de Physique Théorique et Hautes Énergies (LPTHE)

LHCphenonet

**Doctorat**

Physique

**Emanuele Angelo Bagnaschi**

# Phénoménologie de Précision au LHC et caractérisation des incertitudes théoriques
# Precision phenomenology at the LHC and characterization of theoretical uncertainties

Soutenu le 19 Septembre 2014

Thèse dirigée par **Prof. Matteo Cacciari**

## Jury

| | |
|---|---|
| **PD. M. Grazzini** | Examinateur et Rapporteur |
| **Dr. JP. Guillet** | Examinateur et Rapporteur |
| **Prof. M. Cacciari** | Examinateur |
| **Dr. A. Djouadi** | Examinateur |
| **Dr. P. Slavich** | Examinateur |
| **Dr. R. Tanaka** | Examinateur |

*"Quotation is a serviceable substitute for wit."*

– Oscar Wilde

# CONTENTS

# ACRONYMS

**2HDM** The two Higgs-doublet model.

**CH** Cacciari-Houdeau Bayesian model.

**$\overline{\text{CH}}$** Modified Cacciari-Houdeau Bayesian model.

**DGLAP** Dokshitezer-Gribov-Lipatov-Altarelli-Parisi equations for the evolution for parton densities.

**DoB** Bayesian Degree of Belief.

**EW** Electro Weak.

**HQEFT** Heavy Quark Effective Field Theory – Effective field theory of the SM after the integration of the top quark degree of freedom.

**LHC** The Large Hadron Collider at CERN.

**LHEF** Les Houches Event File.

**LL** Leading Logarithmic.

**LO** Leading Order.

**MHO** Missing Higher Order.

**MHOU** Missing Higher Order Uncertainty due to uncomputed QCD corrections.

**MSSM** The Minimal Supersymmetric Standard Model.

**NLL** Next-to-Leading Logarithmic.

**NLO** Next-to-Leading Order.

**NNLL** Next-to-Next-to-Leading Logarithmic.

**NNLO** Next-to-Next-Leading Order.

**PDF** The Parton Distribution Function which describes the non-perturbative dynamic of the hadron.

**POWHEG** POsitive WEight Hardest Emission Generator.

**POWHEG-BOX** A Fortran77 implementation of the POWHEG method available at `http://powhegbox.mib.infn.it/`.

**PS** Parton Shower Monte Carlo software.

**QCD** Quantum Chromodynamics.

**RG** Renormalization Group.

**SM** The Standard Model of particle physics.

**SUSY** Super Symmetry.

**SVN** Subversion revision control system.

# OUTLINE

The Standard Model (SM) of the electroweak and strong interactions has been very successful in describing many different elementary particle processes at various energy scales, but suffers, on the other hand, from various severe problems.

For instance, if one considers the interplay between particle physics and cosmology, it is immediately clear that the observed matter/antimatter asymmetry in the universe can not be explained only in terms of the fundamental interactions described by the Standard Model, but requires in general an extension that includes a larger particle spectrum. The latter is also needed to explain the observed dark matter content of the universe. Moreover the SM does not include neutrino masses and mixing and, on the more theoretical side, it suffers from the "hierarchy problem" (i.e. the fact that quantum corrections to the Higgs boson mass have a quadratic dependence on the UV cutoff used in the computation) and from the fact that the gauge and Yukawa structure is not explained but assumed.

Aside from these issues, now that the Higgs boson has been discovered a quest has started to understand if its properties are compatible with the predictions of the Standard Model.

The Large Hadron Collider (LHC) has been designed to explore all these different questions, providing the necessary tools to search and understand the Higgs boson and allowing the production of new particles in the TeV mass range, if they exist. The very successful first run of the accelerator has been accompanied by an already large amount of high-quality data. From the first analysis of these data, it seems that there are no apparent important deviations from the Standard Model. This in turn makes the use of this huge amount of data to perform precision physics the next logic step. Such a class of studies requires not only a very high accuracy in experimental measures but also a control over the uncertainties in theoretical computations.

In light of this, during my graduate studies I have been involved in a series of projects whose aim was to improve either the accuracy of predictions, accounting for new effects, or the control over the uncertainties of theoretical calculations.

Among the theoretical uncertainties, a prominent role is occupied by the always-present problem, in precise calculations in quantum field theory, of how to estimate the contributions from missing higher orders in the perturbative expansion, the so-called Missing Higher Order Uncertainty (MHOU). Traditionally, these uncertainties have been estimated by varying the unphysical scales present in the result around their central values. Various prescriptions for this procedure are conventionally used by the community, however all are based on arbitrary choices and fail in giving a statistical meaning to the interval they produce. With M. Cacciari (LPTHE) and A. Guffanti and L. Jenniches, both at the N. Bohr Institute in Copenhagen, we studied the extension of the Cacciari-Houdeau (CH) Bayesian model to hadronic observables, with the specific aim of giving a more consistent estimate of the MHOU for LHC observables in general, and Higgs-boson production in particular [1]. The CH model tries to address the shortcomings of the standard prescription used to evaluate MHOU, the scale variation procedure. It is based on a totally different approach, where the behavior of the perturbative series is understood in the context of Bayesian probability. The advantage of this framework is its coherent theoretical formulation and the fact that it produces an uncertainty interval with an intrinsic statistical interpretation in terms

of Degree of Belief (DoB), which can be then consistently plugged in the machinery that experimental physicists use to analyze LHC data. As a byproduct of this study, we also revisited the application of the model to observables without initial state hadrons, its original field of definition and applicability, and we also studied statistically the performances of the scale variation procedure. The final outcome of this project is presented in Part I of the thesis.

Due to the importance of Higgs boson physics in the context of the LHC research program, it is of primary importance to have precise predictions of Higgs observables that are measured at the LHC and to have a deep understanding of the uncertainties that characterize them. My studies have been focused along two main lines. The first one is the study of the theoretical uncertainties of the total inclusive cross section for Higgs production in gluon fusion and bottom annihilation in the Minimal Supersymmetric Standard Model (MSSM). These include not only MHOU but also PDF+$\alpha_s$ uncertainty, renormalization scheme choices for the bottom Yukawa and the range of validity of the approximations used in the computation of supersymmetric corrections. This work was done in collaboration with R. Harlander (U. Wuppertal), S. Liebler (U. Hamburg), H. Mantler (CERN), P. Slavich (LPTHE) and A. Vicini (U. Milano) and it recently led to a publication in the Journal of High Energy Physics [2].

For a few years, with G. Degrassi (U. Roma 3), P. Slavich and A. Vicini I have been studying Higgs-boson production in gluon fusion process in the POWHEG-BOX framework, with specific attention to the problem of including the complete top and bottom amplitudes and of studying their effects on the calculation of the Higgs transverse-momentum distribution. The POWHEG method provides a systematic recipe to obtain the matching of a Next-to-Leading Order (NLO) calculation with a Parton Shower. These matched computations are extremely important to correctly and realistically simulate physical processes in a collider, with the possibility of imposing in a flexible way experimental acceptance cuts and to have, at the end, a sensible comparison between data and theoretical predictions. Our contribution was well appreciated by the experimental collaborations of ATLAS and CMS, which are now using our program and results in their analyses. Furthermore, it has created a rich debate in the community and it has led to several meetings between experimentalists and theorists on the issue. The work was originally done for the Standard Model and for the light Higgs of the MSSM and was published in [3]. It was then extended to the heavy and the pseudoscalar Higgs of the MSSM [4, 5] and to the Two Higgs-doublet model (2HDM). All code is freely available in the POWHEG-BOX Subversion (SVN) tree. More recently I have studied with Alessandro Vicini the issue of the uncertainties related to the matching procedure in the computation of this observable [6]. All these precision Higgs-phenomenology studies are presented in part II.

While it is not included in this thesis, during my graduate studies I have also participated in the computation of threshold corrections in split-Super Symmetry (SUSY) and high-scale SUSY models. The idea at the base of split-SUSY is that the mass scale $\tilde{m}$ of the scalar superpartners of the SM is much higher than the Electro Weak (EW) scale. The only remaining superpartners at the EW scale are higgsinos and gauginos. In high-scale SUSY also the latter are supposed to be at the high scale $\tilde{m}$. To properly study these theories and their predictions at the weak scale, it is necessary to define an effective theory where the heavy particles are integrated out. This and the use of Renormalization Group (RG) methods, allow to properly resum the large logarithms of the ratio of the $\tilde{m}$ over the weak scale that otherwise spoil the accuracy of the prediction. This technical computation is part of an ongoing study of the prediction of the Higgs mass in these models. The Higgs mass can indeed be used as a proxy to derive an estimate of the mass scale $\tilde{m}$ and hence to perform a phenomenological study of the two models. The work was

performed in collaboration with G. Giudice (CERN), P. Slavich (LPTHE) and A. Strumia (U. Pisa) [7]. As a complementary preparation I also served a three months internship at Wolfram Research in Champaign (Illinois, USA), during which I have written a top-level implementation of Mathieu functions in Mathematica.

All my work was supported by the Research Executive Agency (REA) of the European Commission under the Grant Agreements PITN-GA-2010-264564 (LHCPhenoNet).

# BIBLIOGRAPHY


[1] E. Bagnaschi, M. Cacciari, A. Guffanti, and L. Jenniches. "An extensive survey of theoretical uncertainty estimates in perturbative observables". *In preparation*.

[2] E. Bagnaschi, R.V. Harlander, S. Liebler, H. Mantler, P. Slavich, et al. Towards precise predictions for Higgs-boson production in the MSSM. *JHEP*, 06:167, 2014. doi: 10.1007/JHEP06(2014)167.

[3] E. Bagnaschi, G. Degrassi, P. Slavich, and A. Vicini. Higgs production via gluon fusion in the POWHEG approach in the SM and in the MSSM. *JHEP*, 1202:088, 2012. doi: 10.1007/JHEP02(2012)088.

[4] S. Dittmaier, S. Dittmaier, C. Mariotti, G. Passarino, R. Tanaka, et al. Handbook of LHC Higgs Cross Sections: 2. Differential Distributions. 2012. doi: 10.5170/CERN-2012-002.

[5] S Heinemeyer et al. Handbook of LHC Higgs Cross Sections: 3. Higgs Properties. 2013. doi: 10.5170/CERN-2013-004.

[6] E. Bagnaschi and A. Vicini. "Matching uncertainties in the computation of the resummed transverse momentum distribution of the Higgs boson in gluon fusion in the POWHEG framework". *In preparation*.

[7] Emanuele Bagnaschi, Gian F. Giudice, Pietro Slavich, and Alessandro Strumia. Higgs Mass and Unnatural Supersymmetry. *arXiv:1407.4081*, 2014.

Part I

# A BAYESIAN APPROACH TO MISSING HIGHER ORDER THEORETICAL UNCERTAINTIES IN QCD

We consider two approaches to estimate and characterize the theoretical uncertainties stemming from the missing higher orders in perturbative calculations in Quantum Chromodynamics (QCD), the traditional one based on renormalization and factorization scale variation, and the Bayesian framework proposed recently by Cacciari and Houdeau. We estimate uncertainties with these two methods for about thirty different observables in perturbative QCD and, when higher orders are known, we discuss their performance in estimating correctly the size of the missing terms. We find that scale variation with the conventional choice of varying scales within a factor of two of a central scale gives uncertainty intervals that tend to be somewhat too small to be interpretable as "68%-confidence-level-heuristic" ones. A slightly modified version of the Bayesian approach of Cacciari and Houdeau tends to perform well for non-hadronic observables and, after an empirical tuning of the relevant expansion parameter for the perturbative series, for hadronic ones too.

# 1 INTRODUCTION

Precision phenomenology of the kind aimed for by the Large Hadron Collider (LHC) physics program requires accuracy not only in experimental measurements but also in theoretical predictions. Once accuracy becomes high, and theoretical and experimental uncertainties are similar, it becomes important to be able to assess quantitatively the importance of missing higher order terms in perturbative calculations.

In QCD calculations, which we take as a model here given their importance in LHC physics, the theoretical uncertainty stemming from missing higher orders in the perturbative series is usually estimated by varying the unphysical renormalization and factorization scales that appear in the calculation. This approach has served well the QCD community for more than thirty years, and should still be regarded as the most effective way to quickly estimate the Missing Higher Order Uncertainties (MHOUs). It suffers, however, from some drawbacks. Chiefly among them the fact that the uncertainty intervals that it returns cannot be statistically characterized and therefore cannot be combined in a meaningful way with, e.g., likelihood profiles for other uncertainties, for instance of experimental origin.

M. Cacciari and N. Houdeau tried in [1] to overcome this limitation by proposing to estimate MHOUs in a Bayesian framework, so as to obtain a statistically meaningful probability density profile of the uncertainty interval. The Cacciari-Houdeau approach led to a model (henceforth CH) that relies on simple priors that, at their core, try to mimic assumptions that are anyway implicitly made when one employs the scale variation method.

The purpose of this study is twofold. On the one hand, we wish to revisit the CH model, and propose a slightly modified version (which we will denote $\overline{\text{CH}}$) that will trade some of the simplicity of the original CH model for a better adaptability to a broader class of observables, namely those related to hadron-initiated processes. On the other hand, we wish to study the results of both the scale variation and the $\overline{\text{CH}}$ model on a large number of perturbatively calculated observables, so as to be able to assess their performance in a (frequentist) statistically meaningful way. For the scale variation approach, this means that one can attempt to characterize its uncertainty intervals *a posteriori*, in terms of some confidence level, that they correctly describe the MHOU. For the Bayesian approach with the $\overline{\text{CH}}$ model, this study will allow one to either test that the 'Degree of Belief's (DoBs) that $\overline{\text{CH}}$ returns for the Missing Higher Order (MHO) uncertainty intervals are correct or, where needed, to estimate the appropriate expansion parameter that ensures that this will be the case.

The structure of the study is the following. In chapter 2 we introduce the basic concepts behind the Bayesian approach to probability and we illustrate the logic behind its use in the context of the estimation of the systematic uncertainties. Chapter 3 reviews the scale variation approach and the Bayesian method introduced in [1], and describes the modifications to the CH model that lead to the formulation of the $\overline{\text{CH}}$ model used in this study. Chapter 4 gives the methodology that we have followed in our study of the performances of the scale variation and the $\overline{\text{CH}}$ approaches, introduces the list of perturbative observables used in the survey, and presents its results. Chapter 5 compares the results of the scale variation and the $\overline{\text{CH}}$ method for the MHOUs of a small number of processes that we consider either particularly

relevant for LHC physics or simply quite iconic, namely $e^+e^- \to$ hadrons, Higgs decay to two gluons and to two photons, $W$ and $Z$ production in $pp$ collisions via Drell-Yan process, $pp \to t\bar{t}$ and Higgs production in proton-proton collisions. A concluding section follows, while a few appendices collect technical details and the numerical values of the perturbative coefficients of the observables used in the survey and the benchmarking.

# 2 A BRIEF INTRODUCTION TO BAYESIAN PROBABILITY

Before starting our study of MHOUs, we briefly recall the main concepts behind the Bayesian approach to probability since they will be important to understand properly the $\overline{\text{CH}}$ model, which is the cornerstone of our study. Moreover it will allow us to introduce the basic Bayesian lexicon which will be used in the subsequent chapters. For a complete introduction to probability theory see for example the book by E.T. Jaynes [2], while for a critical introduction to Bayesian reasoning see D' Agostini's book [3].

## 2.1 The concept of probability

**The frequentist definition** The standard frequentist approach to probability is built conceptually around the idea of a repeated experiment. Indeed, a textbook definition of probability could be:

> Probability is the ratio of the number of times the event under scrutiny occurs in a test series to the total number of trials in the series, in the limit of infinite number of trials.

A more careful analysis of the statement reveals that, by using this definition, the concept of probability is not carefully and precisely specified. Indeed, what this statement defines is not *probability* but the *relative frequency* with which an event occurred in the past. To use the relative frequency as a definition of probability we have to implicitly assume another hypothesis, that the event occurred in the past and it will occur in the future with the *same probability*. However this is an assumption that it is made and not accounted for in any explicit way. Moreover it also implies some degree of circularness in the definition itself.

We would like to stress that the scope of the frequentist framework, exactly because of its construction around the definition of probability given above, is limited to statements about the relative frequencies of experiments. Indeed probability distributions are defined only with respect to these. While it is common use to make frequentist statements about the true values that are approximately measured in the experimental repetitions, these are beyond the appropriate usage of the framework. Indeed, in a frequentist context the true values are fixed and not associated with any specific probability distribution.

**The Bayesian definition** At the core of the Bayesian approach to probability lies the notion of "subjective probability". It means that very same concept of probability is not something defined on the basis of a controlled experiment (like in the frequentist formulation), rather it is assumed as primitive and based on the beliefs of the subject performing the measurements. In other words, probability is a measure of the DoB of the subject that any well defined statement will turn out to be true.

To better elucidate this concept we use the notion, first introduced by De Finetti[4], of the "coherent bet". Suppose that the higher the degree of belief that an event will occur, the bigger the amount of money A that a rational bettor is willing to pay in order to receive a sum of money B if this event occurs.

The bet is required to be "coherent", i.e. it must be acceptable in both directions by the subjects taking it. This is translated into the condition $A \leqslant B$ and $A \geqslant 0$. The case $A = 0$ indicates that the event is considered to be always false/non-occurring, while $A = B$ means that event is considered to be true/always occurring. It follows that if a subject thinks that an event $E$ has a probability $p$, he will bet $A = pB$ to get $B$ if the event occurs, and it is willing to lose $pB$ if it does not. From this reasoning it follows that the condition of "coherence" implies that $0 \leqslant p \leqslant 1$.
Moreover it is demonstrated that this definition of probability respects all the standard axioms:

1. $0 \leqslant P(E) \leqslant 1$.

2. $P(\Omega) = 1$.

3. $P(E_1 \cup E_2) = P(E_1) + P(E_2)$, if $P(E_1 \cap E_2) = 0$.

In these formulae $E$, $E_1$ and $E_2$ indicate the events that are the objects of the probability statements and $\Omega$ is the "universe" set of all possible events.

## 2.2 Exemplification of the differences between the Bayesian and the frequentist approaches

Following [5], we now show with an example what are the implications of the different approach to probability in the Bayesian and the frequentist frameworks.

The frequentist approach Suppose that we are measuring a quantity $x$ whose probability distribution is a Gaussian with central value $\mu$ and standard deviation $\sigma$. We are now interested in trying to estimate from the repeated observations $\{x_1, x_2, x_3, \ldots, x_n\}$ the unobservable parameter $\mu$.

We first define an estimator[1] $\hat{\mu}$ for $\mu$. The simplest estimator is given by the arithmetic mean $\bar{x}$

$$\bar{x} \equiv \sum_{i=1}^{n} x_i/n\,. \tag{1}$$

Hence we define $\hat{\mu}(x_1, x_2, \ldots, x_n) = \bar{x}$. We observe that this estimator is unbiased: independently of the value of $\mu$ we have always that $\mathrm{Exp}\{\bar{x}(x)\} = \mu$, where with the notation $\mathrm{Exp}\{f(x)\} = \int f(x)g(x)dx$ we refer to the expectation value of $f(x)$ over the probability distribution $g(x)$, where in our case the $g(x)$ is a Gaussian distribution.

From the central limit theorem we have that, in the limit of a large number $n$ of repetitions of the averaging process, the distribution of the random variables $\bar{x}$ tends to a Gaussian with central value $\mu$ and standard deviation $\sigma/\sqrt{n}$. Hence it follows that

$$\mathrm{Exp}\{(\hat{\mu} - \mu)^2\} = \sigma^2/n\,. \tag{2}$$

1 By estimator we simply mean a rule to "estimate" the quantity we are interested in, starting from observed data.

However we are not only interested in giving a single value for our estimation of $\mu$, but a range of plausible values which are consistent with our data. From the properties of the Gaussian distribution we have that

$$\text{Prob}\{|\bar{x} - \mu| \leqslant 2\sigma/\sqrt{n}\} = 0.95\,. \tag{3}$$

This is equivalent to

$$\text{Prob}\{\mu - 2\sigma/\sqrt{n} \leqslant \bar{x} \leqslant \mu + 2\sigma/\sqrt{n}\} = 0.95\,. \tag{4}$$

The interval defined as $[\bar{x} - 2\sigma/\sqrt{n}, \bar{x} + 2\sigma/\sqrt{n}]$ is called, using the frequentist lexicon, "a 95% Confidence Level (CL) interval" for $\mu$. It is important to stress that, while usually it is assumed to be a result on the true value of $\mu$, it follows from eq. (4) that it is a statement on $\bar{x}$. Indeed the proper interpretation is that, in the long series of independent repetitions of the experiment (and therefore for many values of $\bar{x}$) the interval defined in eq. (4) covers the true value $\mu$ with a frequency of 95%. Moreover, also the other results such as eq. (2) and the definition of unbiased estimator are inherently frequentist in nature. Finally, it is here manifest the fundamental role of the hidden assumption that $\mu$ is fixed in the repetitions of the experiment, otherwise it would not have been feasible to relate the distribution of the $\bar{x}$ variables to the true value $\mu$.

The Bayesian approach As we have seen, in the frequentist approach the true value $\mu$ is considered to be an unknown but fixed value. We now suppose that $\mu$ itself is an uncertain[2] variable, known to be normally distributed with mean $m$ and standard deviation $s$, where the value of $m$ and $s$ are supposed to be *known* to the experimenter. The a priori knowledge of the subject performing the measurement is formalized, in a Bayesian context, in what is called the "prior" distribution. To understand in detail what this means we specialize our example.

Suppose that $\mu$ is the true I.Q. of a person randomly chosen from a population we are studying. We know, a priori (from previous studies for example), that $\mu$ is distributed according to a Gaussian with $m = 100$ and $s = 15$. This is indeed our prior for the measurement we are performing. The performance of the I.Q. test we are using, which represents our experimental apparatus, is known and can be quantified by defining the conditional probability[3] of observing the value $\bar{x}$ for a given value of $\mu$ (i.e. the experimental likelihood). We assume that $f(\bar{x}|\mu)$ is a Gaussian distribution $\mathcal{N}$:

$$f(\bar{x}|\mu) \equiv \mathcal{N}(\mu, \sigma/\sqrt{n})\,, \tag{5}$$

where $\mu$ is the true value, $\sigma$ is given and fixed by the test performance and $n$ the number of repetitions of the test.

We are now interested in computing our belief on the true value $\mu$. Bayes theorem is a mathematical construction that allows one to combine the a priori information of the subject, represent by the prior,

2 The variables that appear in frequentist probability distributions are called *random* variables since they assume different values in different repetitions of the experiment; here we call the Bayesian variable appearing in a credibility distribution *uncertain* variable to underline that in the Bayesian context the uncertainty is not linked to experiment realization but to the information available to the subject performing the measurement.

3 We recall that the conditional probability $f(E|F)$ is the probability that the event $E$ occurs *if* the event $F$ has occurred with certainty.

with our knowledge of the measurement process, represented by the experimental likelihood, to obtain a probabilistic statement on the true value $\mu$. In general terms we have the following derivation:

1. The conditional probability of $\mu$ given the data $\bar{x}$ is given by

$$f(\mu|\bar{x}) = \frac{f(\bar{x}, \mu)}{f(\bar{x})} = \frac{f(\bar{x}, \mu)}{\int f(\bar{x}, \mu) d\mu} , \tag{6}$$

   where $f(\bar{x}, \mu)$ is the joint probability distribution for $\bar{x}$ and $\mu$.

2. Usually the double distribution $f(\bar{x}, \mu)$ is not known, but we can compute it from $f(\bar{x}|\mu)$ and $f(\mu)$. We have then

$$f(\bar{x}, \mu) = f(\bar{x}|\mu) f(\mu) . \tag{7}$$

   Again we stress that $f(\bar{x}|\mu)$ quantifies our knowledge of the experimental apparatus, while $f(\mu)$ is our a priori knowledge of the true value $\mu$. If we know the experimental apparatus quite well, as is usually the case, the $f(\bar{x}|\mu)$ distribution will be narrow while the major source of uncertainty will be in $f(\mu)$.

3. Combining all the previous steps leads us to the explicit form of the Bayes theorem

$$f(\mu|\bar{x}) = \frac{f(\bar{x}|\mu) f(\mu)}{\int f(\bar{x}|\mu) f(\mu) d\mu} . \tag{8}$$

   It represents the best way to compute $f(\mu|\bar{x})$ given our knowledge, both a priori (as given by the prior) and a posteriori after the updates from the experiment. This is usually called the "posterior" of the model and it is the result of the process of Bayesian inference.

It is important to stress again that in the Bayesian context, at variance with the frequentist case, it is possible to define a probability distribution for $\mu$, since the latter was assumed from the start to be an uncertain variable as all the other quantities which appear in the measurement process. On the other hand, in the frequentist case, $\mu$ was supposed to be fixed to a value and therefore, while it is indeed unknown to experimenter, no probability distribution can be formally assigned to it. Hence, we can conclude that in the Bayesian case the averaging process is inversed with respect to the frequentist one, since data are held fixed and $\mu$ is the uncertain variable.

Applied to our case, Bayes theorem gives

$$f(\mu|\bar{x}) = \mathcal{N}\left(m + C(\bar{x} - m), \sqrt{D}\right) , \tag{9}$$

where the two factors C and D are given by

$$C = \frac{n/\sigma^2}{1/s^2 + n/\sigma^2} , \qquad D = \frac{1}{1/s^2 + n/\sigma^2} . \tag{10}$$

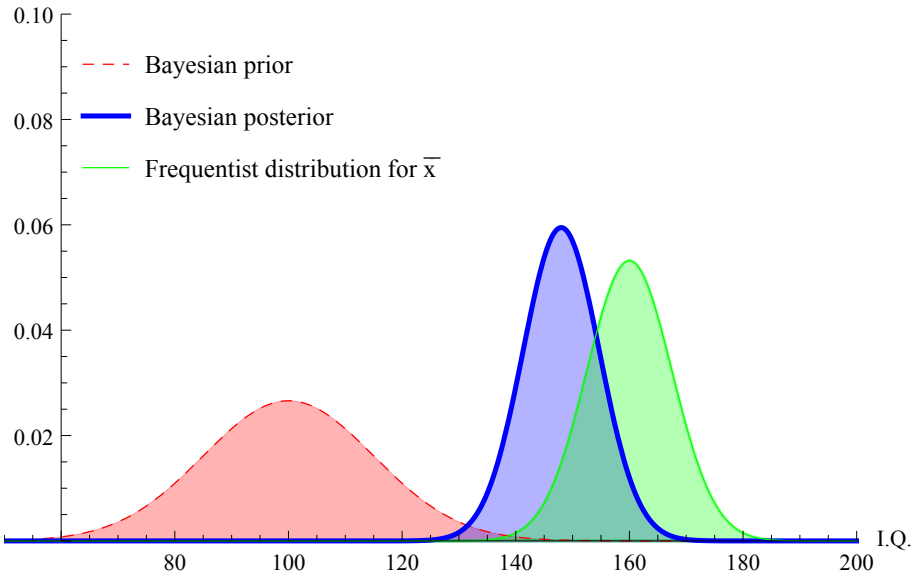


**Figure 1:** Graphical representation of the prior and the posterior distribution for the Bayesian analysis and of the frequentist distribution for $\bar{x}$.

We also define a Bayesian estimator for $\mu$. The most natural one is given by the mean of the posterior distribution $f(\mu|\bar{x})$

$$\mu^*(\bar{x}) = m + C(\bar{x} - m)\,. \tag{11}$$

We also define an analogous of the frequentist confidence interval, called the Credibility Interval (CI). In our Gaussian case we have:

$$\text{Prob}\{\mu^*(\bar{x}) - 2\sqrt{D} \leqslant \mu \leqslant \mu^*(\bar{x}) + 2\sqrt{D}|\bar{x}\} = 0.95\,. \tag{12}$$

This interval quantifies our DoB for the true value $\mu$.

We now perform a quantitative comparison between the Bayesian approach and the frequentist one in the case of our example. Suppose that $\bar{x} = 160$, $m = 100$, $s = 15$ and $\sigma/\sqrt{n} = 7.5$. We have then that 95% DoB C.I. interval is $\text{Prob}\{\mu^*(\bar{x}) - 2/\sqrt{D} \leqslant \mu \leqslant \mu^*(\bar{x}) + 2/\sqrt{D}|\bar{x}\} = 0.95$ and the best Bayesian estimate is $\mu^* = 148$. On the other hand using the frequentist estimator defined in the previous section, we have that the best estimate is given by $\hat{\mu} = \bar{x} = 160$. In the latter case, the only probability distribution defined is the one for $\bar{x}$ from which we have a 95% C.L. interval of $[145, 175]$. We see therefore that the inclusion of our prior knowledge on the quantity we are measuring changes our inference of the value of $\mu$ quite substantially. While the measured value of $\bar{x}$ is 160, the fact that in the Bayesian context we are using the information from our prior implies a much lower estimation of $\mu$. In figure 1 we show the prior distribution, the posterior distribution and the frequentist distribution for $\bar{x}$. We can see that the Bayesian posterior distribution is shifted to lower values of I.Q. with respect to the frequentist result which is peaked around the value of $\bar{x} = 160$, due to information coming from the prior.

We underline that in the Bayesian approach it is impossible to avoid the usage of priors. Their role is

to encode all the knowledge that the subject possesses and that it is not used in the traditional frequentist analysis. The fact that priors are subjective is often considered to be a weakness of the Bayesian approach, to be corrected with the use of some "objective prior" to be determined with the aid of an external and objective criterion. With respect to this issue, there are different schools of Bayesian thoughts.

One, labeled by the adjective "subjective", refuses this criticism and proposes to always asses the experimenter knowledge beforehand by using the concept of "coherent bet" that was introduced in section 2.1. This approach is very useful when the subject performing the experiment has already an opinion about the true value $\mu$ behind the measurement. A classic example that shows its power is the case of the "loaded dice". Suppose that we are playing dice with a person we know is prone to cheating and on fifteen rolls we get fifteen sixes. Should we not include our a priori knowledge on the possibility that the dice is loaded into the computation of the probability distribution for the dice rolls? It seems very reasonable to do so.

Other schools instead try to opt for a more objective approach to the definition of the priors. For example, in absence of a strong a priori knowledge, they propose to produce an uninformative, objective, prior which represents a completely neutral opinion with respect to $\mu$. In the case of the I.Q. estimation process, that prior would be in the form of a Gaussian $\mathcal{N}(0, \infty)$. It is interesting to observe that by using this prior the posterior distribution has the same form of the frequentist distribution for $\bar{x}$, namely $\mathcal{N}(\bar{x}, \sigma/\sqrt{n})$ and that moreover now the Bayes estimator is equal to the frequentist one, $\mu^* = \hat{\mu} = \bar{x}$.

Finally, we point out another feature of the the Bayesian approach. Since *all* quantities are associated to a probability density distribution, the Bayesian framework is particularly suited to the treatment of complex problems. For example, if we are interested in knowing the posterior distribution for a quantity $\mu_3$, which depends on other two quantities $\mu_1$, $\mu_2$, we can simply use the rules of probability to combine the distributions. Indeed, in the most general case we have

$$f(\mu_3) = \int f(\mu_1) f(\mu_2) \delta\left(\mu_3 - g(\mu_1, \mu_2)\right) d\mu_1 d\mu_2 \,, \tag{13}$$

where $g(\mu_1, \mu_2)$ gives the value of the dependent quantity $\mu_3$ in terms of $\mu_1$ and $\mu_2$. In exactly the same way we can account for systematic uncertainties, though various approaches are possible in this case (for an exhaustive analysis on how to include them we refer to the literature [3]).

## 2.3 Missing higher order uncertainties as a measurement problem in a Bayesian context

In the previous section we have briefly introduced the Bayesian probability framework and we have shown how it works with the aid of a simple example. We now specialize it to the problem of the determination of MHOUs, by following the idea of Cacciari and Houdeau [1].

The Cacciari-Houdeau framework tries to address the issue of estimating the MHOUs for a perturbative observable. The estimation of the uncertainty due to uncomputed perturbative corrections can be interpreted as the problem of determining our uncertainty on the convergence behavior of the series given the computed coefficients. Hence it belongs to the class of problems where the aim is to determine an unknown and uncertain parameter (which we suppose parameterizes the behavior of the series) rather

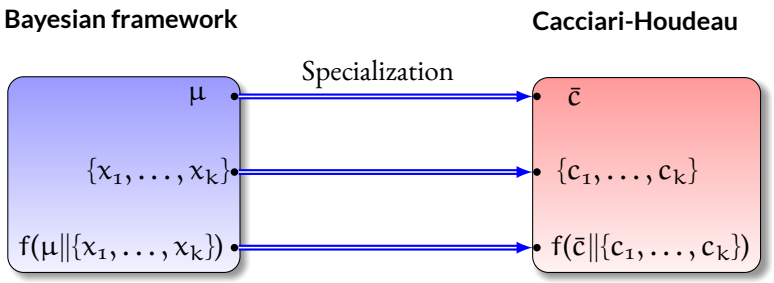


**Figure 2:** Schematic relation between the general elements of a Bayesian framework and their specialization in the Cacciari-Houdeau model.

than evaluating a fixed quantity by repeated experiments. Hence the Bayesian approach seems best suited for the task.

Suppose now that we are studying an observable whose perturbative expansion known up to order $k$ is given as

$$O_k = \sum_{n=1}^{k} \alpha_s^n c_n \,, \tag{14}$$

The core hypothesis around which the model is built is that the absolute values of the series coefficients $c_n$ share a common upper bound that we call $\bar{c}$. The true value of $\bar{c}$ is unknown and its role is equivalent to the $\mu$ parameter of the previous sections. Since we are in a Bayesian framework, we associate a prior to this unknown quantity and we update our "credibility" with the information coming from the known coefficients $\{c_1, \ldots, c_k\}$. The latter correspond to the measured values $x_i$ of the previous sections. We can think of them as probes for the value of $\bar{c}$. In figure 2 we graphically represent the logical relationship between the general Bayesian framework discussed in the previous section and the Cacciari-Houdeau model. The likelihood $f(c_n|\bar{c})$ is also part of the model definition. After having built the conditional density $f(\bar{c}|c_1, \ldots, c_k)$ by using Bayesian inference and $f(c_n|c_1, \ldots, c_k)$ for $n > k$, we can build the probability density for $\Delta_k = \sum_{n=k+1}^{\infty} \alpha_s^n c_n$ given the known coefficients, $f(\Delta_k|c_1, \ldots, c_k)$, which is exactly what quantifies our theoretical uncertainty due to missing higher order contributions.

It is important to underline that with this procedure we get a MHOU uncertainty interval intrinsically defined in terms of Bayesian credibility. Hence the interval has a full and coherent statistical interpretation that allows it to be readily used in other analyses, for example experimental ones, which is exactly one the reason that led to the creation of the model. A complete and detailed description of the Cacciari-Houdeau model follows in section 3.2.

# 3 ESTIMATIONS OF THEORETICAL UNCERTAINTIES IN QCD

We wish to survey two different approaches to the estimation of the MHOUs of a perturbatively calculated observable:

- the variation within a given range and around a chosen central value of the unphysical scales (i.e. the renormalization and the factorization scales) that appear in higher order perturbative calculations;
- the Bayesian approach introduced by Cacciari and Houdeau in [1], with its modification that will be discussed in section 3.3.

We now review how these two methods work, and also set the appropriate notations.

## 3.1 Uncertainty estimation by scale variation

The truncated perturbative expansion of an arbitrary observable $O$ at a fixed order will contain an unphysical higher-order dependence on some scales due to the renormalization procedures used in QFT calculations (e.g. renormalization or factorization scale, here all collectively denoted by $\mu$),

$$O_k(Q,\mu) = \sum_{n=l}^{k} \alpha_s^n(\mu) c_n(Q,\mu)\,, \tag{15}$$

where $Q$ is the characteristic hard scale and $l$ is the starting order in $\alpha_s$ of the processes. The standard approaches to estimate the MHOUs are all based on the idea of varying the scale $\mu$ in an interval $[Q/r, rQ]$, where $r$ is an arbitrary factor often chosen to be equal to 2. The values of the observable obtained at different scales are then used to derive an uncertainty interval according to a defined prescription.

This strategy to evaluate the uncertainties is based on the specific structure of the residual scale dependence at any given order. The latter is fixed by the renormalization group equation for the observable. It follows that all the terms that are added and do not cancel out between orders when the scales are varied have a structure that is the same of genuine higher order terms multiplied by a logarithm of the ratio of the new scale over the central one. This can be easily seen in the case of the renormalization scale variation. We assume that the only implicit dependence on the scale is in $\alpha_s$ and there are no other parameters (e.g. quark masses) that depend on the scale. Suppose we have an observable that can be expanded as in eq. (15). The evolution equation that governs the dependence on the renormalization scale for $\alpha_s$ is given by

$$\frac{d\alpha_s}{d\ln\mu^2} = \beta(\alpha_s) = -\alpha_s^2 \sum_{j=0}^{\infty} \alpha_s^j \beta_j\,, \tag{16}$$

where $\beta(\alpha_s)$ is the strong coupling beta-function. Due to the explicit structure of the coefficient $c_n$ dependence on $\mu$ (fixed by the RGE equation) the terms that depend on the scale at order less than $k$ cancel out. Then what is left is a higher order variation dominated by the term that comes from the product of the variation of $\alpha_s$ at the order $k$ times $c_k$, whose magnitude is then approximately given by $k\alpha_s^{k+1}\beta_0 c_k$. This term is indeed part of the genuine $(k+1)$-order contribution, where it comes from the loop correction diagrams that contribute to the $\alpha_s$ renormalization. Notice that at the same order in $\alpha_s$ there are also terms of the form $(k-j)\beta_j c_{k-j}$, with $0 < j \leqslant k$. However, due to the relative magnitude among the $\beta_j$ coefficients and assuming that all $c_n$ are of the same order, they can be considered subleading in the variation. We refer to the appendix of ref. [1] for more details.

A similar structure supports using factorization scale variation to estimate uncertainties in the case of observables with initial state hadrons (along with the independent variation of the renormalization scale). However the evolution equation for $\alpha_s$ is replaced by the Dokshitezer-Gribov-Lipatov-Altarelli-Parisi (DGLAP) equations and the role of the $\beta_i$ coefficients is assumed by the Altarelli-Parisi splitting functions.

In the community different recipes have been used to implement scale variation. Writing the uncertainty interval as $[O_k^-, O_k^+]$, around the central-scale value $O_k$ (not necessarily centered around it), the most common choices are:

1.
$$\begin{aligned} O_k^- &= \min\{O_k(Q, Q/r), O_k(Q, rQ), O_k(Q, Q)\}, \\ O_k^+ &= \max\{O_k(Q, Q/r), O_k(Q, rQ), O_k(Q, Q)\}. \end{aligned} \tag{17}$$

2.
$$O_k^- = \min_{\mu\in[Q/r, rQ]}\{O_k(Q,\mu)\}, \qquad O_k^+ = \max_{\mu\in[Q/r, rQ]}\{O_k(Q,\mu)\}. \tag{18}$$

3.
$$O_k^\pm = O_k \pm \frac{\delta_k}{2}, \tag{19}$$

where we have defined

$$\delta_n \equiv |O_k(Q, rQ) - O_k(Q, Q/r)|. \tag{20}$$

4. Same as eq. (19) but with

$$\delta_k \equiv \max_{\mu\in[Q/r, rQ]}\{O_k(Q,\mu)\} - \min_{\mu\in[Q/r, rQ]}\{O_k(Q,\mu)\}. \tag{21}$$

The main issue with the scale variation approach is that it does not provide a probability distribution for the uncertainty interval, which therefore has no statistical meaning. It is also worth noting that the common choice $r = 2$ is merely a convention, and that the value of the central scale around which to perform the variation is also largely arbitrary. Indeed, in some cases this central scale is deliberately chosen

away from the characteristic scale of the process to satisfy other criteria. For example, this is the case for Higgs production in gluon fusion where the central scale is often chosen equal to $m_H/2$ to mimic the result obtained when performing soft-gluon resummation [6], and because around this value the cross section shows reduced sensitivity to the scale choice and an improved convergence of the perturbative series [7].

Generalization to the case of two or more scales is straightforward and follows along the same lines. The most commonly used prescription, which we will also use in our study, is an extension of eq. (17), i.e. varying both the renormalization scale $\mu_r$ and the factorization one $\mu_f$ as indicated there, but with the additional constraint $1/r \leqslant \mu_r/\mu_f \leqslant r$, to avoid the appearance of unnaturally large logarithms.

## 3.2 The Cacciari-Houdeau Bayesian approach

As we have already seen in section 2.3, the approach of Cacciari and Houdeau [1] is a recently introduced Bayesian probability framework to compute MHOUs. It is based on various assumptions on the behavior of the coefficients of a series of the form

$$O_k(Q, Q) = \sum_{n=l}^{k} \alpha_s^n(Q) c_n(Q, Q) \equiv \sum_{n=l}^{k} \alpha_s^n c_n \,, \tag{22}$$

for a perturbative observable that starts at order $l$ of $\alpha_s$ and it is known up to order $k$. The unphysical scales have been set to the central value $Q$ and we have also implicitly defined $\alpha_s \equiv \alpha_s(Q)$ and $c_n \equiv c_n(Q, Q)$.

The model postulates as its basic assumption that all the perturbative coefficients have similar magnitudes. This can be quantitatively translated into the statement that all the perturbative coefficients $c_n$ share an upper bound to their absolute value that we denote $\bar{c}$. This and other assumptions are encoded into specific Bayesian priors and likelihoods, and in the choice of the expansion parameter, taken to be $\alpha_s$, and allow one to determine an uncertainty density profile (the posterior of the model) as a function of the size of the unknown remainder of the series $\Delta_k \equiv \sum_{n=k+1}^{\infty} \alpha_s^n c_n$. They are:

- The hypothesis that all the perturbative coefficients $\{c_l, c_{l+1}, c_{l+2}, \ldots\}$ are of the same order of magnitude, $\mathcal{O}(c_l) \simeq \mathcal{O}(c_{l+1}) \simeq \cdots$, is encoded in the use of a step function for the conditional density distribution of the coefficients on the hidden parameter $\bar{c}$

$$f(c_n|\bar{c}) = \frac{1}{2\bar{c}} \begin{cases} 1 & \text{if } |c_n| \leqslant \bar{c} \\ 0 & \text{if } |c_n| > \bar{c} \end{cases} \,. \tag{23}$$

  One could also use a density distribution that does not vanish anywhere, like a Gaussian distribution. The specific choice of eq. (23) was dictated by a requirement of simplicity in the original formulation and to ease the analytic study of the model.

- The density distributions of the perturbative coefficients when $\bar{c}$ is known are assumed to be independent

$$f(\{c_i, i \in I\}|\bar{c}) = \prod_{i \in I} f(c_i|\bar{c}) \,. \tag{24}$$

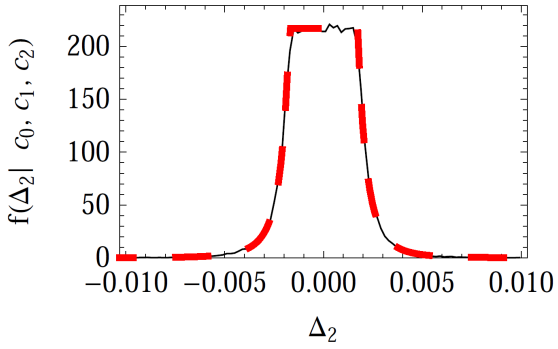


**Figure 3:** Plot of the posterior distribution for the $\Delta_2$ in the CH model, for a toy observable with $\bar{c}_k = 1$ and $\alpha_s = 0.1$ as shown in [1]. The red curve is the analytic approximation of eq. (26) while the black curve represents the exact result.

This implies that $\bar{c}$ is the only parameter that contains the information shared by the coefficients and that, when it is known, the residual uncertainties of the perturbative coefficients are then mutually independent.

- We do not have any information on the order of magnitude of the hidden parameter $\bar{c}$ as long as we have not computed any coefficient. In theory $\bar{c}$ could assume any positive real value and therefore all of its values for its order of magnitude are a priori equally probable. Therefore, a non-informative prior on the hidden parameter $\bar{c}$, a log-uniform distribution, is chosen

$$f_\epsilon(\bar{c}) = \frac{1}{2|\ln \epsilon|}\frac{1}{\bar{c}}\chi_{\epsilon\leqslant\bar{c}\leqslant 1/\epsilon}\,, \tag{25}$$

where $\epsilon$ is taken to zero at the end of the computation.

From these three hypotheses and with the use of Bayesian inference it is possible to derive the conditional densities $f(\bar{c}|c_1,\dots,c_k)$ and $f(c_n|c_1,\dots,c_k)$ for $n > k$. Finally, from these two densities it is possible to build the probability distribution for the residual theoretical uncertainty, $f(\Delta_k|c_1,\dots,c_k)$.

If the expansion parameter is sufficiently small, we can assume that the remainder of the series is dominated by the first unknown order, i.e. $\Delta_k \simeq \alpha_s^{k+1}c_{k+1}$. Then the posterior of the model for $\Delta_k$ can be computed analytically and expressed in a simple form

$$f(\Delta_k|c_1,\dots,c_k) \simeq \left(\frac{n_c}{n_c+1}\right)\frac{1}{2\alpha_s^{k+1}\bar{c}_{(k)}}\begin{cases} 1 & \text{if } |\Delta_k|\leqslant \alpha_s^{k+1}\bar{c}_{(k)} \\ \left(\frac{\alpha_s^{k+1}\bar{c}_{(k)}}{|\Delta_k|}\right)^{n_c+1} & \text{if } |\Delta_k|> \alpha_s^{k+1}\bar{c}_{(k)} \end{cases}, \tag{26}$$

where $\bar{c}_{(k)} \equiv \max(|c_1|,\cdots,|c_k|)$ and $n_c = k-1+1$ is the number of known perturbative coefficients. From eq. (26) and figure 3 it is possible to appreciate the characteristics of the posterior distribution for this model: a flat, central, plateau with power suppressed tails. The existence of such a probability density distribution for the uncertainty interval represents the main difference with the scale-variation procedure, that gives only an interval without a credibility profile.

In the same approximation, $\Delta_k \simeq \alpha_s^{k+1}c_{k+1}$, one can also calculate the smallest credibility interval

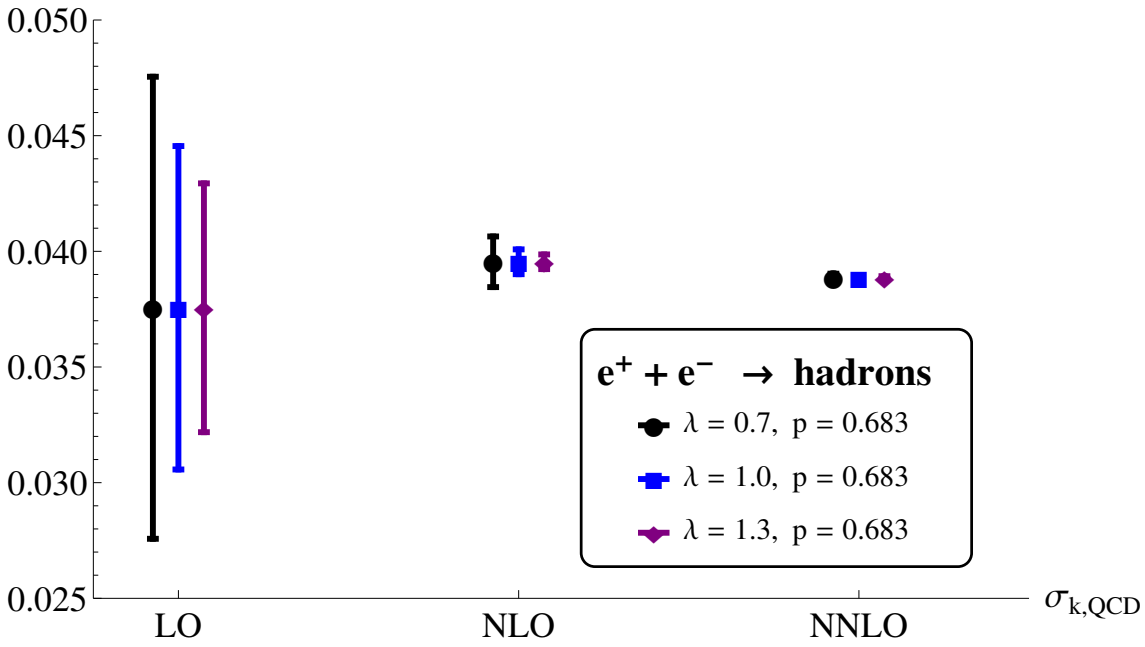


**Figure 4:** Effect of the $\lambda$ parameter on the uncertainty interval size.

for $\Delta_k$ with a DoB equal to $p\%$ (where $p\% \equiv p/100$ and $p \in [0, 100]$), i.e. such that $\Delta_k$ is expected to be contained within the interval $[-d_k^{(p)}, d_k^{(p)}]$ with $p\%$ credibility:

$$d_k^{(p)} = \begin{cases} \alpha_s^{k+1} \bar{c}_{(k)} \frac{n_c+1}{n_c} p\% & \text{if} \quad p\% \leqslant \frac{n_c}{n_c+1} \\ \alpha_s^{k+1} \bar{c}_{(k)} \left[(n_c+1)(1-p\%)\right]^{(-1/n_c)} & \text{if} \quad p\% > \frac{n_c}{n_c+1} \end{cases} . \tag{27}$$

## 3.3 The modified Cacciari-Houdeau approach ($\overline{\text{CH}}$)

The CH model described above relies on a specific form of the perturbative expansion, namely eq. (22). As a result, its estimation for the uncertainty is not invariant under a rescaling of the expansion parameter from $\alpha_s$ to $\alpha_s/\lambda$. In figure 4 we show the uncertainty bars for $e^+e^- \rightarrow$ hadrons for three different choices of $\lambda$.

Another connected issue is that, as we have seen in the previous section, the model assumes that the expansion parameter is such that all the perturbative coefficients $c_n$ are of the same order $\mathcal{O}(c_1) \simeq \mathcal{O}(c_{l+1}) \simeq \cdots$. A priori this could not be the case for the simple expansion in $\alpha_s$.

Attempts have been made to reformulate the model in a rescaling-invariant way to avoid both of these problems. Ultimately, none of them turned out to be satisfactory, to the extent that each required formulating priors much too informative, which shaped excessively the final posterior. We eventually settled instead on a slightly modified version of the CH model.

In the modified model, henceforth denoted as Modified Cacciari-Houdeau ($\overline{\mathbf{CH}}$), we rewrite the perturbative expansion in the form

$$O_k = \sum_{n=1}^{k} \frac{\alpha_s^n}{\lambda^n}(n-1)!\,\frac{\lambda^n c_n}{(n-1)!} \equiv \sum_{n=1}^{k} \left(\frac{\alpha_s}{\lambda}\right)^n (n-1)!\; b_n\,, \tag{28}$$

with

$$b_n \equiv \frac{\lambda^n c_n}{(n-1)!}\,, \tag{29}$$

and submit the new coefficients $b_n$ to the same priors originally used for the $c_n$. This leads to the uncertainty probability density profile

$$f(\Delta_k|b_1,\ldots,b_k) \simeq \left(\frac{n_c}{n_c+1}\right)\frac{1}{2k!\,(\alpha_s/\lambda)^{k+1}\bar{b}_k}\begin{cases} 1 & \text{if } |\Delta_k| \leqslant k!\left(\frac{\alpha_s}{\lambda}\right)^{k+1}\bar{b}_k \\ \left(\frac{k!(\alpha_s/\lambda)^{k+1}\bar{b}_k}{|\Delta_k|}\right)^{n_c+1} & \text{if } |\Delta_k| > k!\left(\frac{\alpha_s}{\lambda}\right)^{k+1}\bar{b}_k \end{cases}, \tag{30}$$

and to the credibility interval

$$d_k^{(p)} = \begin{cases} k!\left(\frac{\alpha_s}{\lambda}\right)^{k+1}\bar{b}_k\,\frac{n_c+1}{n_c}p\% & \text{if} \quad p\% \leqslant \frac{n_c}{n_c+1} \\ k!\,(\frac{\alpha_s}{\lambda})^{k+1}\bar{b}_k\,[(n_c+1)(1-p\%)]^{(-1/n_c)} & \text{if} \quad p\% > \frac{n_c}{n_c+1} \end{cases}. \tag{31}$$

The $(n-1)!$ factor, which represents the main modification with respect to the original CH model, can be justified on the ground that such a factor is expected to appear in higher order perturbative calculations, e.g. those in the large-$\beta_0$ limit and in connection with renormalons [8–11]. In appendix B we show that indeed removing the factorial term leads to worse performances of the model.

The factor $\lambda$ is free and needs to be determined a posteriori. The best choice for the rescaling factor $\lambda$ can be determined empirically by observing how the model fares in describing the uncertainties of observables that are known at a perturbative order beyond where we use the model. We will see that an optimal value turns out to be $\lambda \simeq 1$ for observables that do not involve hadrons in the initial state, while a value of $\lambda \simeq 0.6$ is favored in hadron-initiated processes. This method of determining $\lambda$ (further detailed below) brings of course some frequentist contamination in the Bayesian approach. We consider this drawback acceptable at the present stage, but we note that one could in principle further update the model instead, by introducing an additional prior for the value of $\lambda$ and thus avoid the frequentist contamination. The frequentist study on $\lambda$ performed in this work can then perhaps be used as a guide for the formulation of such an additional prior.

#### *Extension to hadronic observables*

The original CH model was formulated with non-hadronic observables[1] in mind. It is not a straightforward task to extend it to observables with initial state hadrons, henceforth denoted hadronic observables.

1 By non-hadronic observables we mean observables without hadrons in the initial states and therefore devoid of the dependence on the factorization scale

A generic hadronic observable (e.g. a total cross section) can be written as a convolution integral

$$O_k(\tau, Q) = \int_\tau^1 \frac{dz}{z} \mathcal{L}\left(\frac{\tau}{z}, Q\right) \sum_{n=l}^{k} \alpha_s^n C_n(z, Q) \equiv \mathcal{L}(Q) \otimes \sum_{n=l}^{k} \alpha_s^n C_n(Q)\,, \tag{32}$$

where $\mathcal{L}$ is the parton-parton luminosity, $C_n(Q)$ is the hard-scattering coefficient function, $\tau$ is an appropriate hadronic scaling variable and $Q$ is the characteristic energy scale of the process. All the unphysical renormalization and factorization scales are taken to be equal to $Q$, as in the non-hadronic case, and they are not explicitly shown. In eq. (32) the perturbative coefficient functions $C_n$ are distributions, and not simple numbers like the coefficients $c_n$ of the non-hadronic observables. This means that it is not possible to directly apply the $\overline{\text{CH}}$ method described in section 3.3 to hadronic observables of the form (32).

One can overcome this problem in two ways.

1. A first approach is to express the hadronic cross section as a series whose coefficients include the convolution with the parton-parton luminosities, i.e. we can rewrite eq. (32) in the form

$$O_k(\tau, Q) = \mathcal{L}(Q) \otimes \sum_{n=l}^{k} \alpha_s^n C_n(Q) \equiv \sum_{n=l}^{k} \left(\frac{\alpha_s}{\lambda_h}\right)^n (n-1)!\; H_n(\tau, Q)\,, \tag{33}$$

   where we have defined

$$H_n(\tau, Q) \equiv \frac{\lambda_h^n}{(n-1)!} \mathcal{L}(Q) \otimes C_n(Q)\,. \tag{34}$$

   One then proceeds like in the non-hadronic case, applying the Bayesian priors to the coefficients $H_n$. In practice, one is assuming that the non-perturbative physics contained in the parton-parton luminosity brings order by order roughly the same contribution, or more generally that its presence does not spoil the assumptions of the model. This is supposed also to be true from the perturbative contributions that come from DGLAP evolution. In our studies, to reflect these assumptions, we always use the same PDFs at all orders. This approach has also been adopted in a number of papers that have made use the original CH model, e.g. [12, 13].

   Note that in eq. (33) we have introduced a parameter $\lambda_h$ that is potentially different from the $\lambda$ employed in the expansion of non-hadronic observables.

2. A second approach consists in translating the observable to Mellin space, and write

$$O_k(N, Q) = \mathcal{L}(N+1) \sum_{n=l}^{k} \left(\frac{\alpha_s}{\lambda_h}\right)^n (n-1)!\; B_n(N, Q)\,, \tag{35}$$

   where

$$B_n(N, Q) \equiv \frac{\lambda_h^n}{(n-1)!} \int_0^1 dx\, x^{N-1}\, C_n(x, Q)\,. \tag{36}$$

   is the Mellin transform of the short-distance coefficient function $C_n$, rescaled by the usual factors adopted in $\overline{\text{CH}}$, and $\mathcal{L}(N+1)$ is the Mellin transform of the parton-parton flux. One then

observes that, if the Mellin inversion integral can be shown to be dominated by a single Mellin moment $N^*$, one can simply apply the priors of the $\overline{\text{CH}}$ approach to the short-distance *numbers* $B_n(N^*, Q)$ and find the relevant uncertainty, which can then be transported back to the full result by rescaling it appropriately.

Indeed, the dominant Mellin moment method is based on the following observation[14, 15]. Given the observable in Mellin space, the observable in the physical x-space is given by the inverse Mellin transform

$$O_k(\tau, Q) = \frac{1}{2\pi i}\int_{\bar{N}-i\infty}^{\bar{N}-i\infty} dN \tau^{-N} O_k(N, Q)\,. \tag{37}$$

We can rewrite eq. (37) as

$$O_k(\tau, Q) = \frac{1}{2\pi i}\int_{\bar{N}-i\infty}^{\bar{N}+i\infty} dN e^{E(\tau, N, Q)}\,, \tag{38}$$

where we have defined

$$E(\tau, N, Q) \equiv N \ln\left(\frac{1}{\tau}\right) + \ln O_k(N, Q) \tag{39}$$

and where $\bar{N}$ is larger than the real part of the rightmost singularity of $O_k(N, Q)$. We recall that $O_k(N, Q)$ has a singularity on the real positive axis because of the parton luminosity and to the right of this singularity it is a decreasing function of N, because the area below the curve $\tau^{N-1}O_k(\tau, Q)$ decreases as N increases. Therefore $E(\tau, N, Q)$ always has a minimum on the real positive axis at some point $N = N^*$. Hence the inversion integral is dominated by the region of N around $N^*$ and can be approximated by a saddle-point expansion of $E(\tau, N, Q)$ around $N^*$. Around the saddle point we have that

$$E(\tau, N, Q) \approx E(\tau, N^*, Q) + \frac{E''(\tau, N^*, Q)}{2!}(N - N^*)^2 + \mathcal{O}((N - N^*)^3)\,, \tag{40}$$

so that the Mellin inversion integral becomes

$$O_k(\tau, Q) \approx \frac{1}{2\pi i}\int_{N^*-i\infty}^{N^*+i\infty} dN e^{E(\tau, N^*, Q) + \frac{E''(\tau, N^*, Q)}{2!}(N-N^*)^2}\,. \tag{41}$$

We can then change the integration variable to $N = N^* + it$ and perform the Gaussian integration. The result is

$$O_k(\tau, Q) \approx \frac{1}{\sqrt{2\pi}} \frac{e^{E(\tau, N^*, Q)}}{\sqrt{E''(\tau, N^*, Q)}}\,. \tag{42}$$

This approach is viable because one can show that at least in some cases (see e.g. [14, 15]) such a dominant Mellin moment exists and eq. (42) gives a good approximation to the full result or at least of the k-factors, that ultimately are what the model uses in the determination of the behavior of the series.

The main limitation of this procedure, which a priori would be preferred over the first one because it does not contaminate the coefficients that are run through the Bayesian model with non-perturbative physics, is that it strongly relies on the predominance of not only a single Mellin moment but also a single production channel (e.g. gluon-gluon fusion in Higgs production at the LHC) at all orders. If this is not the case, the need to reweight the various dominant Mellin moments in the different parton channels will reintroduce contamination from non-perturbative physics.

A second, practical, limitation is that perturbative results are rarely available in Mellin space from public codes, limiting the straightforward application of this method to very few cases.

Because of the limitations of the Mellin moment method we will use the first approach in our study, but we will also present in appendix D two case studies for the Mellin moment method.

# 4 GLOBAL SURVEY RESULTS

In this chapter we try to assess the quality of the scale variation procedure and of the $\overline{\text{CH}}$ model by studying their performances as estimators of the MHOUs when applied to a set of observables. For every observable in the set we consider two quantities:

1. the size of the uncertainty predicted at a given perturbative order $n$ by the approach under consideration;

2. the known perturbative result for the same observable at order $n + 1$.

For each of the observables we then calculate the global success rate of the approach in predicting the uncertainty, i.e. the *fraction* of observables, for which the result of the perturbative order $n + 1$ actually falls within the uncertainty interval predicted by the model at order $n$ .

In the case of the Bayesian model we repeat the analysis described above for various values of $\lambda$ and DoB. This allows us to derive the optimal value of $\lambda$ to be used in the $\overline{\text{CH}}$ model, that is defined as the value of $\lambda$ for which the model has a global success rate which is most similar to the requested DoB, for every possible DoB.

In the case of the scale-variation method we vary the scaling factor $r$ defined in section 3.1. Since this method does not give statistically meaningful uncertainty intervals, we cannot determine an optimal value of $r$ from this analysis, like it is the case instead for $\lambda$ in the Bayesian approach. Rather, we can only assign an *a posteriori* heuristic confidence level (CL) value to the uncertainty intervals.

## 4.1 Setup

The observables used for the global survey have been divided into two groups.

A first group is composed of non-hadronic observables, defined as observables calculated from processes that do not include hadrons in the initial state. Table 1 gives the complete list, with the available perturbative accuracy (i.e. the maximum known QCD order) and a reference to original literature. To extract results for these non-hadronic observables we have used the values of the coefficients as given in the original references. If the zeroth order of these observables is entirely electroweak in nature, since we are interested in a perturbative expansion in powers of the strong coupling, we shall not include the first coefficient $c_0$ in the analysis when using the $\overline{\text{CH}}$ approach, as was the case in [1].

A second group contains hadronic observables, i.e. processes that involve initial-state hadrons and it is listed in table 2. In this case the perturbative coefficients were usually extracted from numerical results obtained by running the software package which implements the calculation of a given observable. In this case the leading order coefficient (i.e. the first one) is always also retained for the analysis with the $\overline{\text{CH}}$ approach, independently of its order in $\alpha_s$. It is also worth noting that, in order to avoid biasing

the analysis using different parton distribution functions (PDFs) at different orders, we will always use Next-to-Next-Leading Order (NNLO) PDFs at all orders.

All the coefficients and the specific parameters for the simulations are given in appendix A, in tables 11 and 12. For all our analyses we have used a private Mathematica code.

| Non-Hadronic observables | | | |
|---|---|---|---|
| Observable | Leading order in $\alpha_s$ | Highest known order in $\alpha_s$ | Reference |
| $R = \frac{\sigma(e^+e^- \to \text{hadr})}{\sigma(e^+e^- \to \mu^+\mu^-)}$ | 0 | 3 | [16] |
| Bjorken sum rule | 0 | 3 | [17] |
| GLS sum rule | 0 | 3 | [18] |
| $\Gamma(b \to ce\bar{\nu}_e)$ | 0 | 2 | [19] |
| $\Gamma(Z \to \text{hadr})$ | 0 | 4 | [20] |
| $\Gamma(Z \to b\bar{b})$ | 0 | 3 | [21] |
| 3-jets Thrust | 1 | 3 | [22] |
| 3-jets Heavy jet mass | 1 | 3 | |
| 3-jets Wide jet broadening | 1 | 3 | |
| 3-jets Total jet broadening | 1 | 3 | |
| 3-jets C parameter | 1 | 3 | |
| 3-to-2 jet transition | 1 | 3 | |
| $\gamma_{ns}^{(+)}(N=2)$ | 1 | 3 | [23] |
| $\gamma_{qq}(N=2)$ | 1 | 3 | |
| $\gamma_{qg}(N=2)$ | 1 | 3 | |
| $H \to b\bar{b}\vert_{m_b=0}$ | 0 | 4 | [24] |
| $H \to gg$ | 2 | 5 | [25] |
| $H \to \gamma\gamma$ | 0 | 2 | [26] |

**Table 1:** List of non-hadronic observables used in the global survey. Note that when the leading term is purely electroweak, this first coefficient, $c_0$ is not used when studying these non-hadronic observables in the Bayesian approach.

| Hadronic observables | | | |
|---|---|---|---|
| Observable | Leading order in $\alpha_s$ | Highest known order in $\alpha_s$ | Reference |
| $pp \to H$ at $\sqrt{s} = 8$ TeV | 2 | 4 | HIGLU [27], [28] |
| $b\bar{b} \to H$ associated production at $\sqrt{s} = 8$ TeV | 0 | 2 | bbh@nnlo [29] |
| $gg \to t\bar{t}$ at $\sqrt{s} = 8$ TeV | 2 | 4 | [30] |
| on-shell $pp \to Z + X \to e^+e^- + X$ at $\sqrt{s} = 8$ TeV | 0 | 2 | DYNNLO [31] |
| on-shell $p\bar{p} \to W^\pm + X \to e^\pm\nu_e + X$ at $\sqrt{s} = 8$ TeV | 0 | 2 | DYNNLO [31] |
| Higgs strahlung production (W/Z) at $\sqrt{s} = 8$ TeV | 0 | 2 | [32] |
| $b\bar{b}$ at $\sqrt{s} = 8$ TeV | 2 | 3 | MCFM |
| $Z + j$ at $\sqrt{s} = 8$ TeV | 1 | 2 | MCFM |
| $Z + 2j$ at $\sqrt{s} = 8$ TeV | 2 | 3 | MCFM[33] |
| $W^\pm + j$ at $\sqrt{s} = 8$ TeV | 1 | 2 | MCFM |
| $W^\pm + 2j$ at $\sqrt{s} = 8$ TeV | 2 | 3 | MCFM[33] |
| $ZZ$ at $\sqrt{s} = 8$ TeV | 0 | 1 | MCFM[34] |
| $WW$ at $\sqrt{s} = 8$ TeV | 0 | 1 | MCFM[34] |

**Table 2:** List of hadronic observables used in the global survey.

## 4.2 Results

*Scale Variation*

In this section we study the performance of the standard scale variation approach. One outcome of this analysis will be a heuristic confidence level (CL) for the uncertainty intervals given by scale variation, as a function of the scaling factor $r$ that sets the range over which the unphysical scales are varied, $\mu \in [Q/r, rQ]$.

In the non-hadronic case we have decided to test two of the prescriptions given in section 3.1, which are supposedly the most widely used ones: a) taking the maximum and the minimum of the cross sections obtained with $\mu = rQ$ or $\mu = Q/r$, as defined in eq. (17); b) taking the maximum and the minimum when scanning the whole interval of scales between $Q/r$ and $rQ$, as defined in eq. (18).

Results for the first prescription (i.e. only extreme values) are given in the left plot of figure 5. In this figure "LO" means that one evaluates the scale-variation uncertainty of the observable calculated up to the first known QCD order, the Leading Order (LO), whereas "NLO" means that the calculation of the observable is used up to second known QCD order. We observe that, at LO, the heuristic CL of the scale-variation uncertainty intervals for the conventional $r = 2$ value is of the order of 50%, and only reaches a 68% level for $r \simeq 3.5$. At larger values of $r$ the CL stabilizes around 80%. At NLO the CL is still of the order of 50% at $r = 2$ but it increases more rapidly with $r$ than at LO, and it is already around 68% for $r \simeq 2.5$-3 and it stabilizes again around 80%.

Results for the second scale-variation prescription (i.e. full scan) are given in the right plot of figure 5. While the LO results are very similar, the NLO heuristic CLs are of order 80% for $r = 3$-4 and then they are significantly larger, being of order 100% for $r > 5$. This behavior can probably be explained from the fact that at NLO the scale variation of an observable is usually non monotonic, and therefore a full scan captures better its overall variation than the evaluation of only two or three fixed points.

We perform the same study for the scale-variation uncertainties of hadronic observables. Since hadronic cross sections depend on two scales, the factorization and renormalization scales, we vary them independently to obtain the scale variation interval. As often done in the literature, we do not perform a full scan (too computationally expensive) but rather evaluate observables only at the center and at the extremes of a scale range, avoiding combinations that generate large logarithms, as explained at the end of section 3.1.

Figure 6 shows the results of the hadronic analysis. We have calculated the cross sections both using always NNLO PDFs (left) and order-matched ones (right), i.e. using LO PDFs at LO, NLO ones at NLO, etc. At every fixed order, the two choices are equivalent up to higher order terms. We have chosen to use the NNPDF2.3 PDF for NNLO and NLO, while at LO we used NNPDF2.1 since no NNPDF2.3 equivalent is available for the order-matched study, while the NNPDF2.3 NNLO set is used for the fixed NNLO PDF analysis. We used the strong coupling constant value as given by the PDF sets, for which we have $\alpha_s(m_Z) = 0.119$[1].

In both cases we see that, as common wisdom dictates, the LO scale variation is very poorly predictive of the true magnitude of the NLO result. At NLO the two prescriptions differ. Using always NNLO PDFs (left plot) we observe a 40% CL for the standard scale variation with $r = 2$. The 68% level is attained for $r$ between 3 and 4, and the CL then stabilizes around 90% CL for $r \geqslant 4$. The order-matched

1 In some cases, like for Higgs production in gluon fusion, the strong coupling is run at the central scale by the software that computes the cross section. In other cases the strong coupling is evolved using the facilities offered by LHAPDF.

PDF prescription shows a very small CL (less than 30%) for $r \leqslant 3$. The CL reaches 68% for $r$ a bit over 4 and then stabilizes around 75% for $r \geqslant 4.5$. Note that in the case of NNPDF the value of $\alpha_s$ is fixed at all orders and it is not allowed to float during the PDF fitting. This probably explains why the usually used order-matched prescription is a much worse player, since for equal values of $\alpha_s(Q)$, it misses higher-order contributions.

These two analyses for hadronic observables suggest that, in order to obtain a reasonably conservative uncertainty interval from scale variations, with a CL at least as large as 68%, in many cases one should use a rescaling factor $r$ equal at least to three or four.

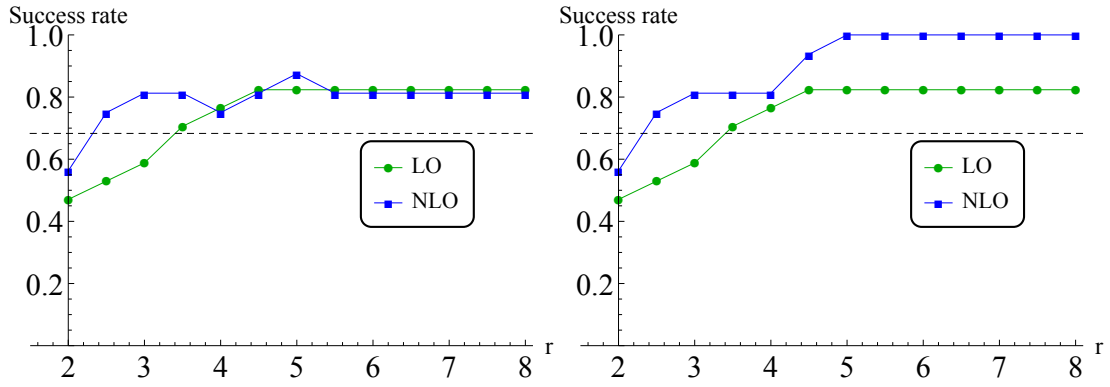


**Figure 5:** Fractions of observables within the uncertainty band found for scale variations between $\mu_R = Q/r$ and $\mu_R = rQ$; following the prescription of taking the values at the extremes of the intervals (left), taking the maximum and minimum of the values obtained by scanning the interval (right).

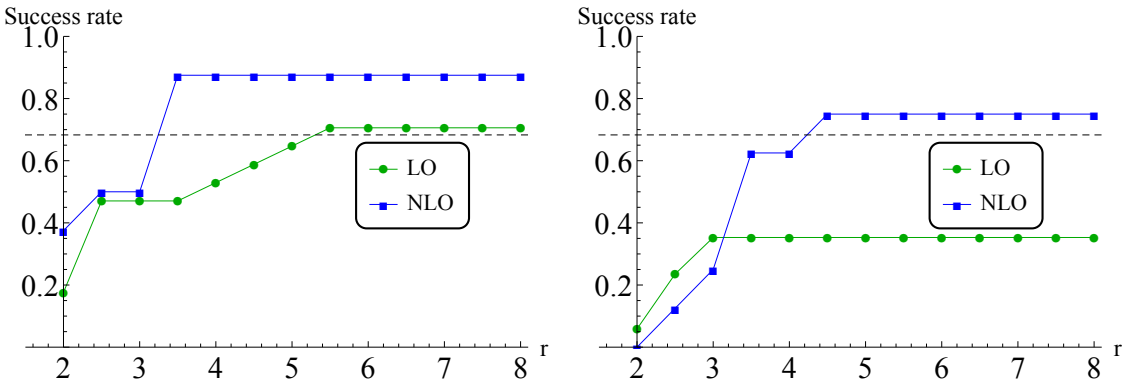


**Figure 6:** Scale-variation scan for processes with initial state hadrons: NNLO PDF (left), order-matched PDF (right). Combinations like $\mu_R = rQ$, $\mu_F = Q/r$ are not included.

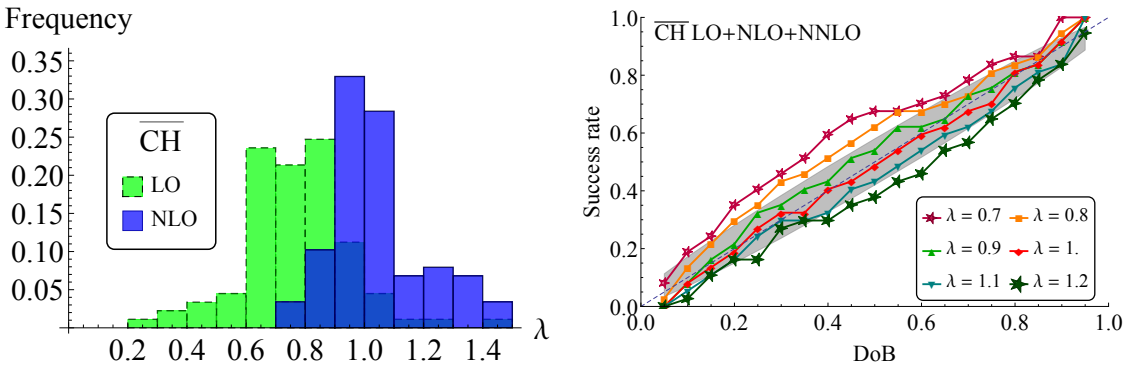


**Figure 7:** Non-hadronic survey: comparisons between DoB and actual success rate, to determine the most appropriate value for λ. Left, histogram of the optimal λ value obtained with a DoB scan. Right, plot of the success rate vs the requested DoB for six values of λ.

*The modified Cacciari-Houdeau model ($\overline{\text{CH}}$)*

For each of the sets of observables listed in table 1 and 2, we have also performed an analysis of the performance of the $\overline{\text{CH}}$ model in estimating the MHOUs. In this case the free parameter of the model is the λ factor that defines the expansion parameter of the perturbative series as written in eq. (28). The parameter λ plays a role analogous to that of r in the scale variation approach. However, since in the Bayesian model the widths of the uncertainty intervals are associated to specific credibility values, one can explicitly determine appropriate values for λ by asking that the model performs as expected, which means that success rate of the model should be roughly equal to the requested DoB.

We first study the non-hadronic observable case. We show the results of this analysis graphically in figure (7) in two different and complementary ways. Both plots include all the 18 non-hadronic observables. The right plot includes all the higher-order contributions up to NNLO, for a total of 37 elements, while the histogram represents only the LO and NLO analysis. To obtain the histogram in figure 7 (left), we vary the DoB between 0.05 and 0.95 in steps of 0.01. For each DoB value we determine the λ value which gives the best agreement with the condition DoB = success rate. The resulting λ values are plotted in a histogram. Values between 0.6 and 0.8 are preferred at LO, while $\lambda \simeq 1$ is favored at NLO level. The plot in figure 7 (right) shows instead how DoB and success rate compare, for different values of λ, in a global analysis of LO and NLO observables. We see that for values of λ in the 0.9-1.1 range the requested DoB agrees well with the observed success rate of the uncertainty prediction. Since we are interested in having a λ value that could be equally used both at LO and subsequent orders, it follows that our prescription is $\lambda \sim 0.9 - 1.1$. This frequentist-like determination of λ is itself subject to an uncertainty due to the finite size of the set of observables that we have used, which results in a statistical error on the observed success rate (see Appendix C for an extended description of the error determination procedure). This statistical error is displayed as a gray band in figure 7 (right). One can see how it roughly translates into a limiting precision of $\pm 0.2$ in the determination of λ.

We also perform the same analysis for the hadronic observables set given in table 2. Figure 8 (left) shows the histogram of the optimal values of $\lambda_h$ following a DoB scan, for the global set of hadronic observables. Smaller values than in the non-hadronic case are preferred, the histogram presenting a peak around $\lambda_h \simeq 0.5$. In figure 8 (right) we plot the success rate as a function of the DoB predicted by

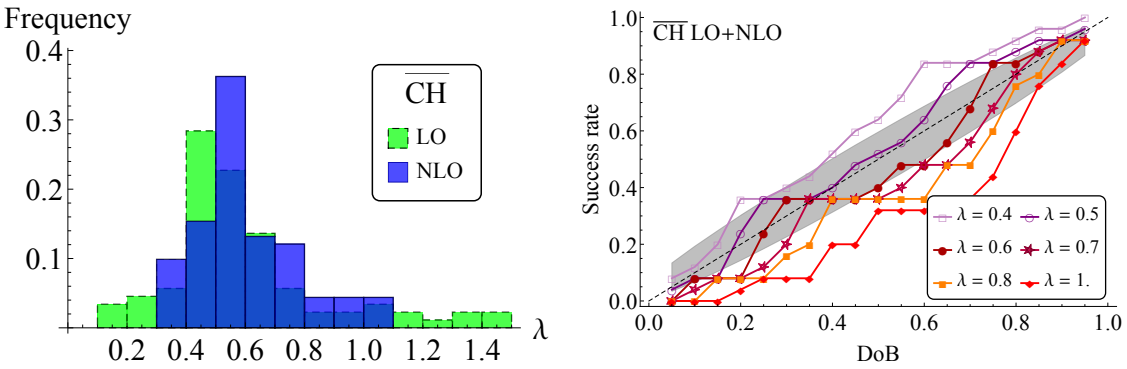


**Figure 8:** Hadronic survey: comparison between DoB and actual success rate to determine the most appropriate value for $\lambda$ for all hadronic observables.

$\overline{\text{CH}}$ for various values of $\lambda_h$ for all hadronic observables at LO and NLO. From this plot we see that $\lambda_h \simeq 0.5$ is preferred for a range of DoBs less than 50%, while for higher values of DoB a $\lambda_h$ around 0.6 is preferred. Since the most common use case for the model is characterized by the latter range of DoB (i.e. DoB = 68%,95%), we opt to take $\lambda_h = 0.6$ for our analysis.

Hence, the results of the analyses presented in this section allow us to 'tune' the $\overline{\text{CH}}$ as follows: we will use a parameter $\lambda = 1$ when considering non-hadronic observables (and we will not include in the analysis the $c_0$ coefficients), while we will use $\lambda_h = 0.6$ when considering hadronic observables[2].

2 It may be tempting to speculate that the smaller value of $\lambda$ in the hadronic case (and therefore a larger effective expansion parameter for the series) may be explained by the generally larger number of gluons involved in these processes, and therefore by an expansion parameter closer to $\alpha_s C_A$ than to $\alpha_s C_F$, but we will refrain from doing so.

# 5 BENCHMARK PROCESSES

In this section, we present the results for both the $\overline{\text{CH}}$ and the scale-variation prescription for some of the most relevant processes at leptonic and hadronic colliders. These include decay rates and production cross sections, most of them involving initial-state hadrons. We use the results obtained in the global survey (see section 4) to fix the parameters of the models. For observables without initial-state hadrons, the best-fit value for $\lambda$ in the $\overline{\text{CH}}$ model is 1, for the integrated-coefficient extension of the model to observables involving initial-state hadrons, the best fit value is $\lambda_h = 0.6$ . For the scale-variation prescription, $r \sim 2.5$ should be comparable to the 68% DoB for non-hadronic observables, while $r$ of $\mathcal{O}(3-4)$ should have the same role in the hadronic case. In addition, it is interesting to see how these prescriptions compare to the conventional scale variation with $r = 2$.

In light of these considerations, we compute the scale-variation intervals for $r = 2$ and $r = 4$ for all benchmark processes. On the other hand, for the $\overline{\mathbf{CH}}$ model we present the results for the 68% DoB and the 95% DoB intervals.

For every benchmark process we will show two different classes of plots:

1. An error-bar plot, where the x-axis represents the order of the observable, in power of $\alpha_s$, at which the calculation is done and the y-axis gives the corresponding value of the observable; error bars are shown by using a thick dark-blue line for the $\overline{\text{CH}}$ 68% DoB interval, while we use a thin light-blue line for the corresponding 95% DoB one. In red we plot the results for scale variation: the thick dark-red line corresponds to scale variation with a rescaling factor $r = 2$, while the thin light-red line is obtained with $r = 4$.

2. We show the posterior $f(\Delta_k|b_1, \ldots, b_k)$ for each order at which the observable is available. The profile of the distribution is plotted using a thick-blue line while a dark-blue (light-blue) filling is used to indicate the area under the distribution that corresponds to 68% (95%) DoB. For comparison we also plot the scale variation interval for $r = 2$ with a thin red line.

Finally, we also report a table, for every process, with the corresponding numerical values to appreciate quantitatively the width of the error intervals.

## 5.1 Higgs decays

The recent discovery of what appears to be a Higgs boson at the LHC has spurred a lot of activities to understand if its properties are or not the ones predicted by the Standard Model. The two first classes of observables that are the most readily accessible discriminants for this purpose, are Higgs production inclusive cross sections and decay rates. In this section we will focus on the latter, while we will show the result for the gluon fusion production mechanism in section 5.5 .

| $H \to gg$ | | | | | |
|---|---|---|---|---|---|
| Order | $\Gamma_k$[MeV] | $\overline{\text{CH}}$, 68% | $\overline{\text{CH}}$, 95% | $\text{SV}_{r=2}(\delta_k^-, \delta_k^+)$ | $\text{SV}_{r=2}$, DoB |
| $k = 2$ | 0.185 | $\pm 0.065$ | $\pm 0.420$ | $(-0.032, 0.044)$ | (19.2%, 26.0%) |
| $k = 3$ | 0.305 | $\pm 0.041$ | $\pm 0.105$ | $(-0.035, 0.040)$ | (29.0%, 32.6%) |
| $k = 4$ | 0.342 | $\pm 0.017$ | $\pm 0.031$ | $(-0.019, 0.012)$ | (38.5%, 24.5%) |
| $k = 5$ | 0.345 | $\pm 0.009$ | $\pm 0.015$ | $(-0.006, 0.0004)$ | (21.7%, 1.6%) |

**Table 3:** Analysis results for $H \to gg$. The meaning of the columns is described in the text at the beginning of the section. The layout of the table is the following: the first column is the perturbative order expressed in terms of the highest power $k$ of $\alpha_s$ that appears in the series expansion; in the second column we report the value of the observable computed with the central scales at that order; in the third and forth column we write the width of the interval computed by using the $\overline{\text{CH}}$ model for a DoB of 68% and 95% respectively; in the fifth column we show the results for the scale variation prescription for $r = 2$; in the last column we report the Bayesian DoB for the $r = 2$ scale-variation interval as computed in the $\overline{\text{CH}}$ model.

We focus our analysis on two specific decay channels: Higgs to two gluons and Higgs to two photons. The first one, while not particularly interesting at the LHC due to the huge QCD backgrounds, is computed up to N3LO and therefore it serves well as a showcase for the models; the second one, although characterized by small QCD corrections, is very important phenomenologically, due to its sensitivity to new charged particles and to the couplings of the Higgs to the top quark and the W boson.

*Higgs to two gluons*

The decay rate for the process $H \to gg$ at the k-th order in perturbative QCD is given by

$$\Gamma_k(H \to gg) = \sum_{n=2}^{k} \alpha_s^n c_n \tag{43}$$

In the numerical computation we have used $m_H = 125$ GeV as the central scale and the corresponding strong coupling constant value $\alpha_s(m_H) = 0.113$. Corrections are available up to $N^3LO$ and hence it is a perfect candidate for the study of the behavior of the perturbative QCD series. As the LO contribution is mediated by a loop process involving strongly interacting particles both running in the loop and in the final state, QCD corrections play a large role as can be seen in figure 9. The 68% DoB intervals obtained with the $\overline{\text{CH}}$ model correspond roughly to a scale-variation interval obtained with an $r$ between 2 and 4. Furthermore, the NLO is contained neither in the 68% DoB interval of the LO observable nor in the scale variation intervals with $r = 2$ or $r = 4$. This picture changes at higher orders. The observable at NNLO is within the 68% DoB interval of the $\overline{\text{CH}}$ model at NLO and also within the scale-variation interval for $r = 2$. The last contribution is contained in all plotted intervals. We can observe some features which were manifest in the global survey. According to the results for the scale-variation prescription, $r \sim 2 - 3$ corresponds to a CL of 68%. We observe that for the LO and NLO the interval size for the 68% DoB interval of the $\overline{\text{CH}}$ prescription is indeed a bit bigger than the $r = 2$ scale-variation interval and smaller than $r = 4$ one.

We report in table 3 the numerical results of the intervals. In general, we can see that scale-variation

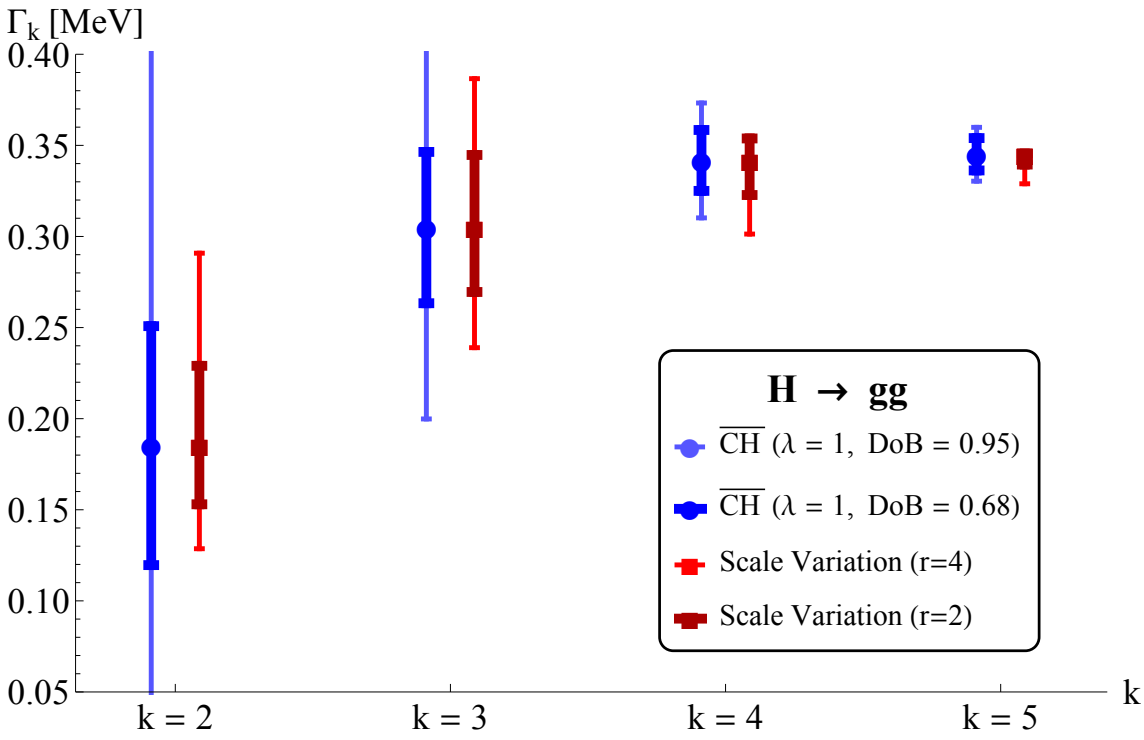


**Figure 9:** Size of the uncertainty interval at LO, NLO, NNLO and N3LO for $\overline{\text{CH}}$ with $\lambda = 1$, compared to those predicted by scale variation for the process $H \to gg$.

intervals are often very asymmetric while the $\overline{\text{CH}}$ intervals are by construction symmetric.

In figure 10 we show the results for the posterior distributions at all orders (thick blue line). In dark blue we fill the area that corresponds to the 68% DoB, while in light blue the one that corresponds to the 95% DoB. We also plot in red the scale variation interval for $r = 2$. We notice that the latter is always contained in the flat plateau of the Bayesian posterior. We also observe how the posterior distribution becomes more and more narrow as new orders are added. This especially reduces the size of the 95% DoB interval compared to the 68% DoB one.

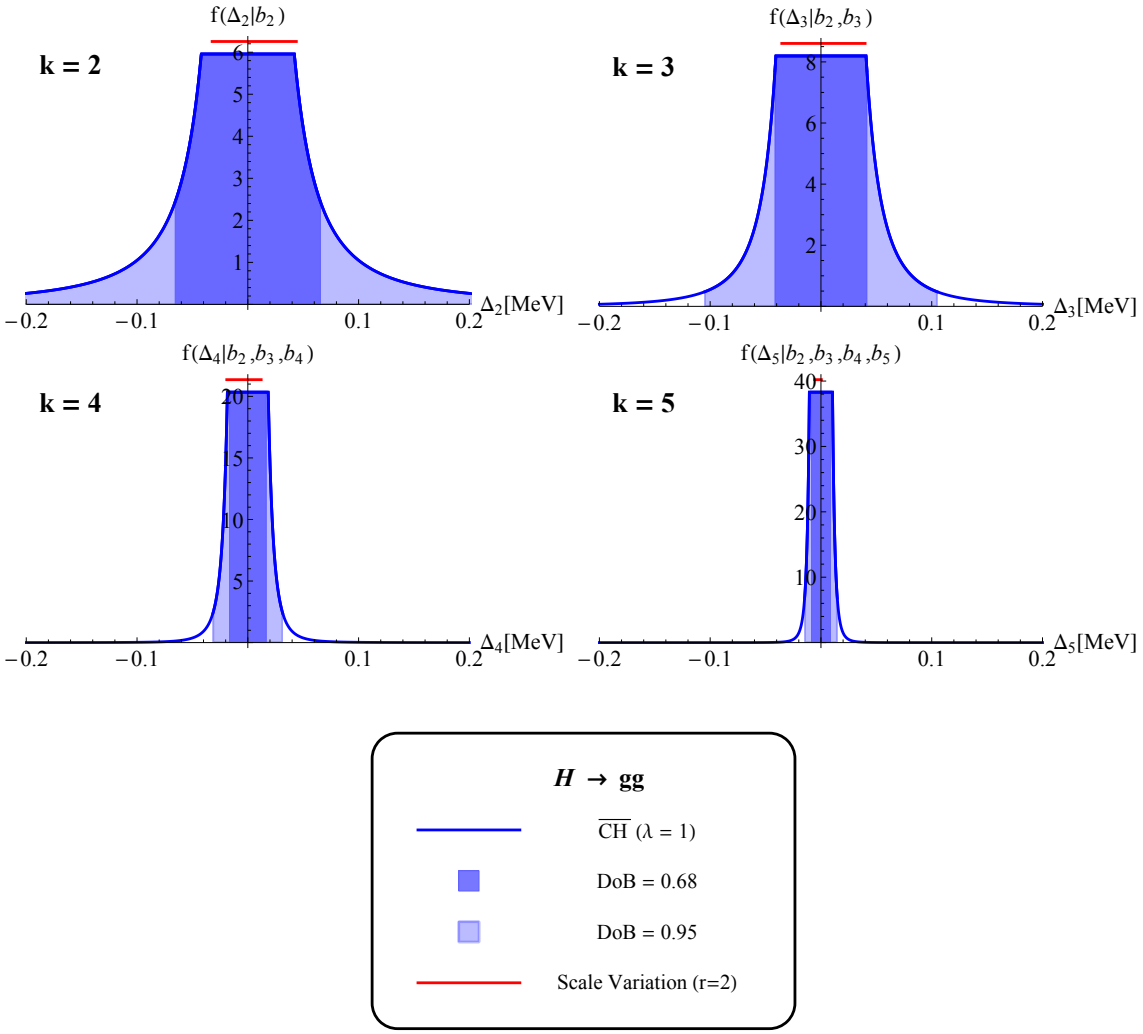


**Figure 10:** Posterior distribution of the Bayesian model for $\Delta_k = \sum_{n=k+1}^{\infty} \alpha_s^n c_n$ (blue solid), 68% DoB interval (blue fill), 95% DoB interval (light-blue fill), scale variation interval for $r = 2$ (red solid) for the process $H \to gg$.

| $H \to \gamma\gamma$ | | | | | |
|---|---|---|---|---|---|
| Order | $\Gamma_k$[KeV] | $\overline{\text{CH}}$, 68% | $\overline{\text{CH}}$, 95% | $SV_{r=2}(\delta_k^-, \delta_k^+)$ | $SV_{r=2}$ DoB |
| $k = 1$ | 9.548 | $\pm 0.030$ | $\pm 0.192$ | $(-0.015, 0.019)$ | $(20.1\%, 24.7\%)$ |
| $k = 2$ | 9.556 | $\pm 0.004$ | $\pm 0.011$ | $(-0.003, 0.001)$ | $(26.2\%, 7.3\%)$ |

**Table 4:** Analysis results for $H \to \gamma\gamma$. The meaning of the columns is described in the caption of table 3.

*Higgs to two photons*

The decay rate for Higgs to two photons is given by

$$\Gamma_k(H \to \gamma\gamma) = \sum_{n=0}^{k} \alpha_s^n c_n \tag{44}$$

The process is purely electroweak at LO, where the decay is mediated by a top-quark and a W-boson loop. QCD corrections are known up to $\mathcal{O}(\alpha_s^2)$.

Following our prescription for the applicability of the $\overline{\text{CH}}$ model to non-hadronic observables, we apply the model only to QCD corrections. We can see from figure 11 that in this case the scale-variation intervals with $r = 4$ have roughly the same size as the $\overline{\text{CH}}$ 68% DoB interval and that the $r = 2$ scale-variation interval is strikingly smaller than the latter, at variance with what it could have been predicted from the global survey.

We observe that the value of the observable at NLO is contained in the 68% DoB interval for $\overline{\text{CH}}$ and in the $r = 2$ interval for scale variation, reflecting the smallness of QCD corrections. Looking at the posterior distributions in figure 12, we note that the commonly used intervals for scale variation with $r = 2$ are always contained in flat plateau of the $\overline{\text{CH}}$ density distribution. In addition, the posterior plots show how the size of the 95% DoB interval is drastically reduced with respect to the 68% one, implying a good convergence of the perturbative series.

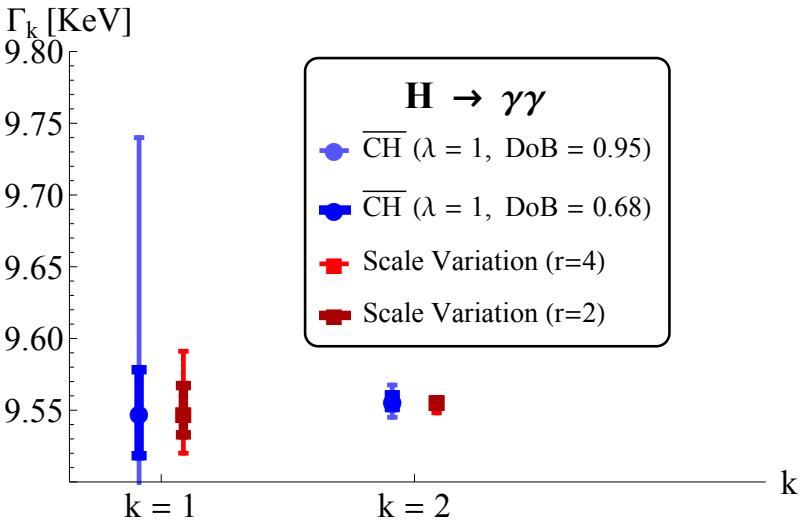


**Figure 11:** Size of the uncertainty interval at NLO and NNLO for $\overline{CH}$ with $\lambda = 1$, compared to those predicted by scale variation.

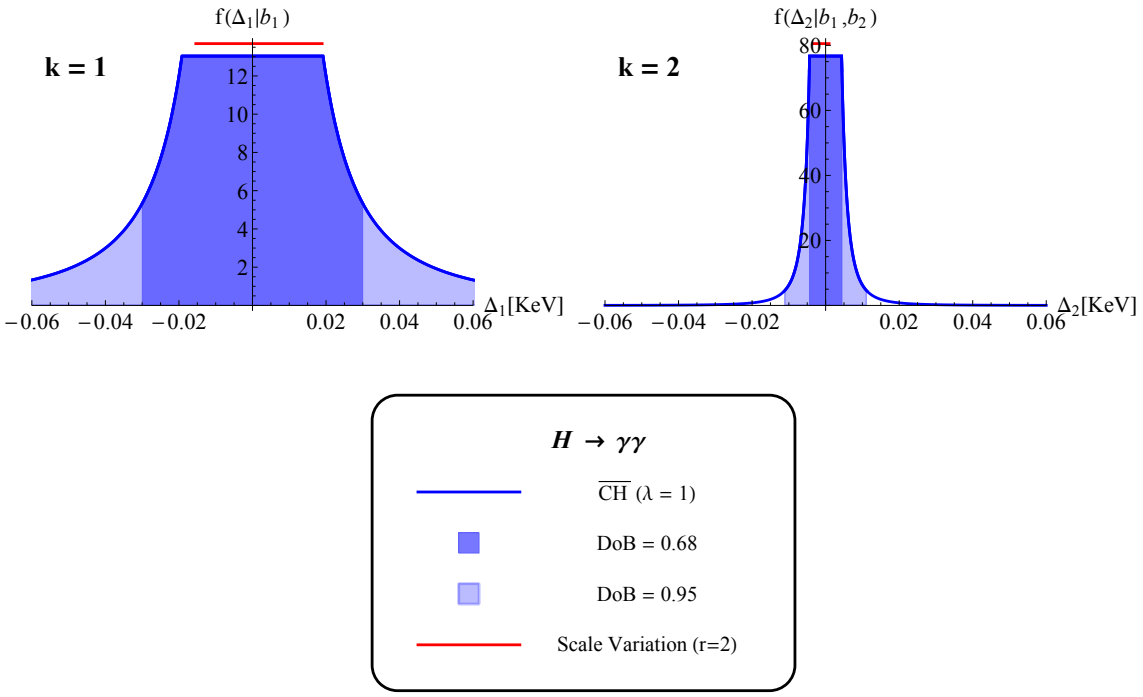


**Figure 12:** Posterior distribution of the Bayesian model for $\Delta_k = \sum_{n=k+1}^{\infty} \alpha_s^n c_n$ (blue solid), 68% DoB interval (blue fill), 95% DoB interval (light-blue fill), scale variation interval (red solid)

| $e^+e^- \to \gamma^* \to$ hadrons | | | | | |
|---|---|---|---|---|---|
| Order | $\sigma'_k$ | $\overline{\text{CH}}$, 68% | $\overline{\text{CH}}$, 95% | $\text{SV}_{r=2}(\delta_k^-, \delta_k^+)$ | $\text{SV}_{r=2}$ DoB |
| $k = 1$ | 0.03756 | $\pm 0.00693$ | $\pm 0.04432$ | $(-0.0035, 0.0044)$ | (20.0%, 24.9%) |
| $k = 2$ | 0.03955 | $\pm 0.00107$ | $\pm 0.00270$ | $(-0.00084, 0.00025)$ | (26.8%, 8.1%) |
| $k = 3$ | 0.03887 | $\pm 0.00034$ | $\pm 0.00063$ | $(-0.00032, 0.00006)$ | (32.7%, 5.8%) |

**Table 5:** Analysis results for hadroproduction in $e^+e^-$ collisions. The meaning of the columns is described in the caption of table 3.

## 5.2 Hadroproduction process in $e^+e^-$ collisions

In this section we re-propose the same analysis that was included in the original Cacciari-Houdeau paper [1], using the new $\overline{\text{CH}}$ model and comparing to SV also with $r = 4$.

The total cross section for the process $\sigma(e^+e^- \to \gamma^* \to \text{hadrons})$ is considered one of the standard candles of QCD physics and it is therefore an important test for our Bayesian model. To isolate QCD corrections, to which we would like to apply the model as per our prescription, we rewrite the observable in the following form

$$\sigma_k = \sigma_0 \left(1 + \sum_{n=1}^{k} c_i \alpha_s^n\right) . \tag{45}$$

We define the observable

$$\sigma'_k \equiv \sum_{n=1}^{k} c_n \alpha_s^n = \frac{\sigma_k}{\sigma_0} - 1 , \tag{46}$$

which we use to compare scale-variation and $\overline{\text{CH}}$ intervals. In table 5 we report the values of $\sigma'_k$, for $n_f = 5$ massless flavors. We have used $m_Z$ as the central scale choice and $\alpha_s(m_Z) = 0.118$.

In fig 13 we show the error bars for the $\overline{\text{CH}}$ model compared to the ones obtained with the scale-variation prescription. We see that scale variation with $r = 4$ leads to intervals comparable in size with the 68% DoB $\overline{\text{CH}}$ intervals and that the higher-order values of the observables are always contained in both the 68% DoB interval and the $r = 2$ scale-variation interval.

In figure 14 we plot the full density profile for this observable. We can see that the scale variation interval is always contained in the flat top section of the posterior distribution. As was the case for the previous two observables we observe that, with respect to the width of the plateau, the width of the 95% DoB interval is reduced in greater amount with respect to the corresponding 68% width, as the perturbative order increases.

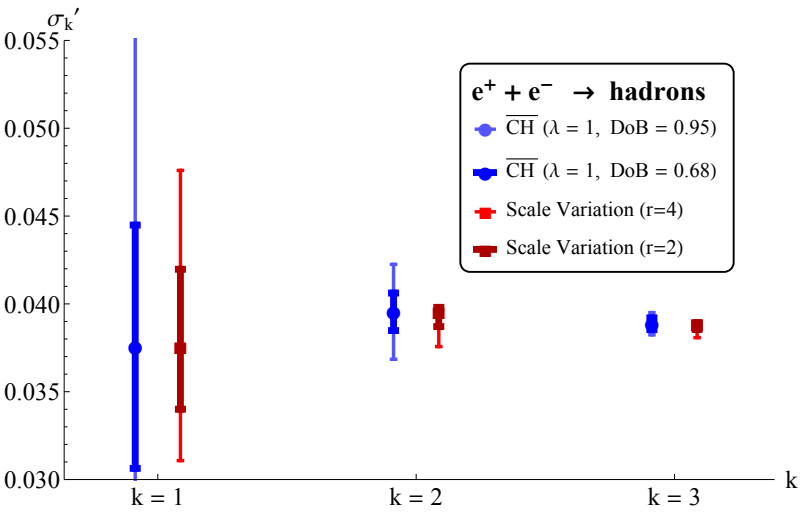


**Figure 13:** Size of the uncertainty interval at LO, NLO and NNLO for $\overline{\text{CH}}$ with $\lambda = 1$, compared to those predicted by scale variation for hadroproduction in $e^+e^-$ collisions.

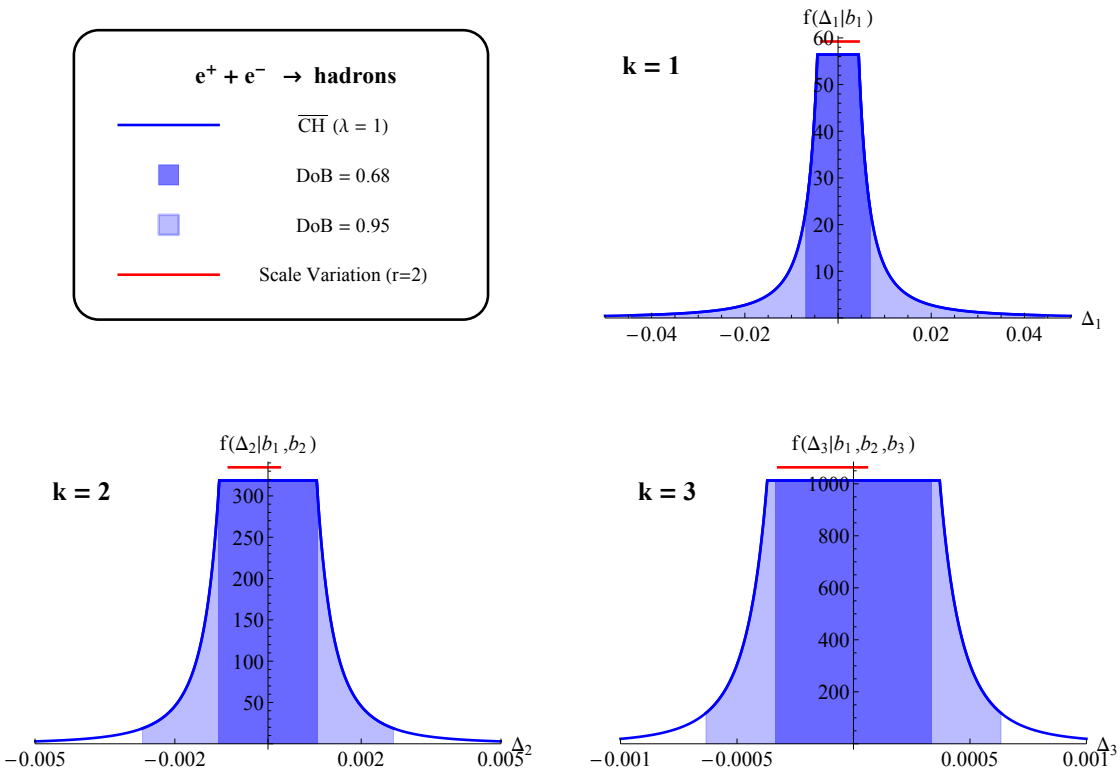


**Figure 14:** Posterior distribution of the Bayesian model for $\Delta_k = \sum_{n=k+1}^{\infty} \alpha_s^n c_n$ (blue solid), 68% DoB interval (blue fill), 95% DoB interval (light-blue fill), scale variation interval (red solid) for hadroproduction in $e^+e^-$ collisions.

| $pp \to W^+ \to e^+\nu_e$ | | | | | |
|---|---|---|---|---|---|
| Order | $\sigma_k$[nb] | $\overline{\text{CH}}$, 68% | $\overline{\text{CH}}$, 95% | $SV_{r=2}(\delta_n^-, \delta_n^+)$ | $SV_{r=2}$ DoB |
| k = 0 | 3.328 | $\pm$1.051 | $\pm$6.729 | $(-0.362, 0.319)$ | (13.4%, 11.9%) |
| k = 1 | 3.718 | $\pm$0.139 | $\pm$0.351 | $(-0.147, 0.095)$ | (35.7%, 23.2%) |
| k = 2 | 3.704 | $\pm$0.050 | $\pm$0.094 | $(-0.077, 0.061)$ | (45.5%, 40.9%) |

| $pp \to Z \to e^+e^-$ | | | | | |
|---|---|---|---|---|---|
| Order | $\sigma_k$[nb] | $\overline{\text{CH}}$, 68% | $\overline{\text{CH}}$, 95% | $SV_{r=2}(\delta_n^-, \delta_n^+)$ | $SV_{r=2}$ DoB |
| k = 0 | 0.4995 | $\pm$0.1548 | $\pm$0.9907 | $(-0.054, 0.047)$ | (13.6%, 12.0%) |
| k = 1 | 0.5574 | $\pm$0.0201 | $\pm$0.0507 | $(-0.020, 0.012)$ | (34.3%, 20.8%) |
| k = 2 | 0.5551 | $\pm$0.0071 | $\pm$0.0133 | $(-0.007, 0.010)$ | (36.0%, 43.4%) |

**Table 6:** Analysis results for $pp \to Z \to e^+e^-$ and $pp \to W^+ \to e^+\nu_e$. The meaning of the columns is described in the caption of table 3.

## 5.3 The Drell-Yan process at the LHC

Vector-boson production has large cross sections and clear signatures at hadron colliders like the LHC. Therefore, precise theoretical predictions including reliable estimates for theoretical uncertainties are important for precision measurements of the Standard Model and for new physics searches.

We have used the DYNNLO code [31] to obtain the cross section

$$\sigma_k(pp \to V) = \sum_{n=0}^{k} \alpha_s^n c_n \,, \tag{47}$$

where $V = W^+$ or $V = Z$, at the LHC with a center of mass energy of 8 TeV. For the computation we have used the NNLO NNPDF2.3 at all orders, with the corresponding values of $\alpha_s$, while the central scale has been set to the mass of the weak boson produced in the process. As already mentioned earlier, hadronic observables already show scale dependence through the PDFs at LO and we have decided to include the first coefficient, even if purely electroweak, also in the Bayesian analysis.

We observe a similar behavior for $W^+$ and $Z$ production as depicted in figures 15 and 17. The $\overline{\text{CH}}$ prescription with a DoB of 68% leads to larger intervals than the scale-variation prescription with the considered $r$ values at LO, the two prescriptions give similar intervals at NLO while at NNLO situation is inverted with the $\overline{\text{CH}}$ model with a CL of 68% yielding smaller intervals than the $r = 2$ scale variation.

Concerning the success rate, higher order corrections are always included in the previous order 68% DoB intervals for the $\overline{\mathbf{CH}}$ model at both NLO and NNLO while for for the $r = 2$ interval for scale variation this is valid only for the NNLO value.

Posterior distributions are reported in figure 16 and 18. We observe that also for this observable the scale variation intervals for $r = 2$ are contained in the flat plateau for LO and NLO, while they are not fully contained at NNLO. We also see that the good convergent behavior of the series is reflected in the narrowing of the posterior distribution.

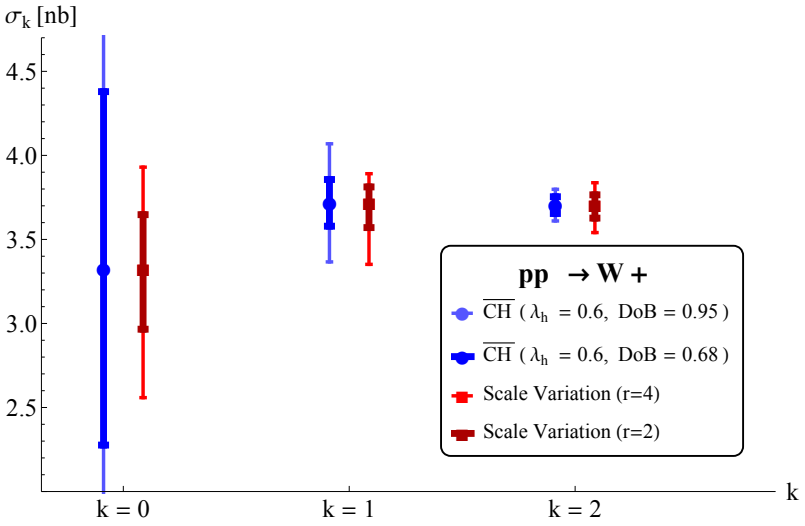


**Figure 15:** Size of the uncertainty interval at LO, NLO and NNLO for $\overline{\text{CH}}$ with $\lambda = 0.6$, compared to those predicted by scale variation for $pp \to W^+ \to e^+\nu_e$.

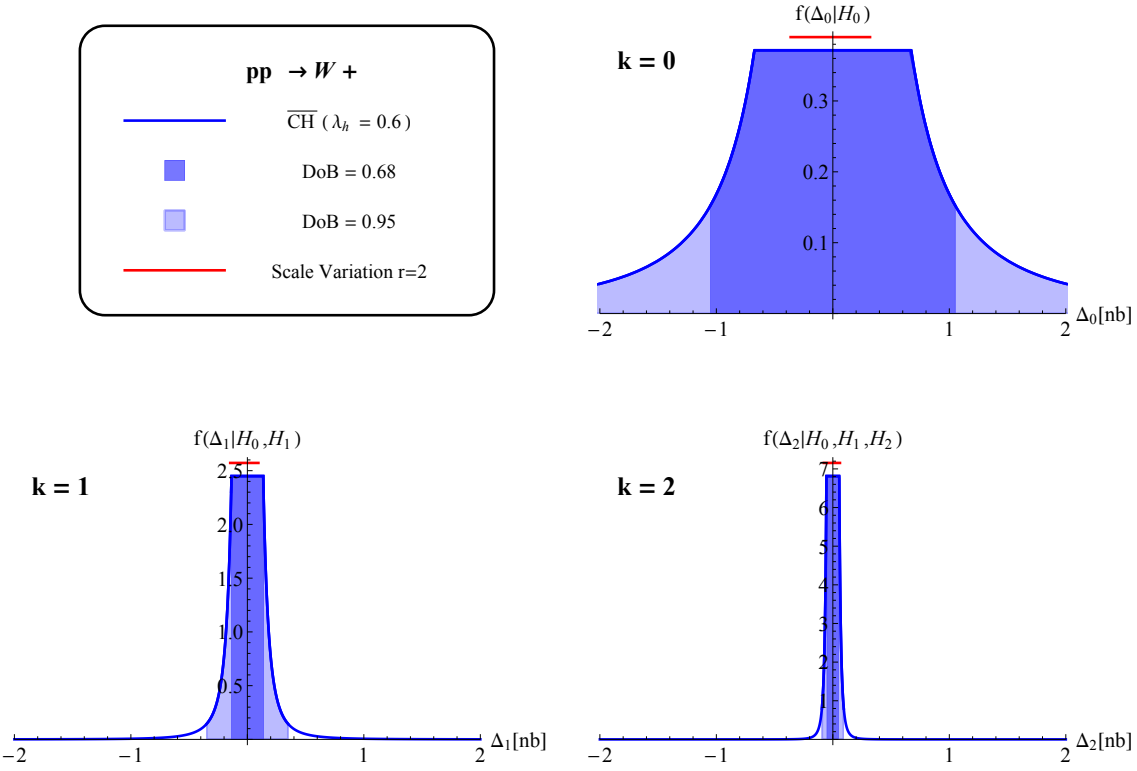


**Figure 16:** Posterior distribution of the Bayesian model for $\Delta_k = \sum_{n=k+1}^{\infty} \alpha_s^n c_n$ (blue solid), 68% DoB interval (blue fill), 95% DoB interval (light-blue fill), scale variation interval (red solid) $pp \to W^+ \to e^+\nu_e$.

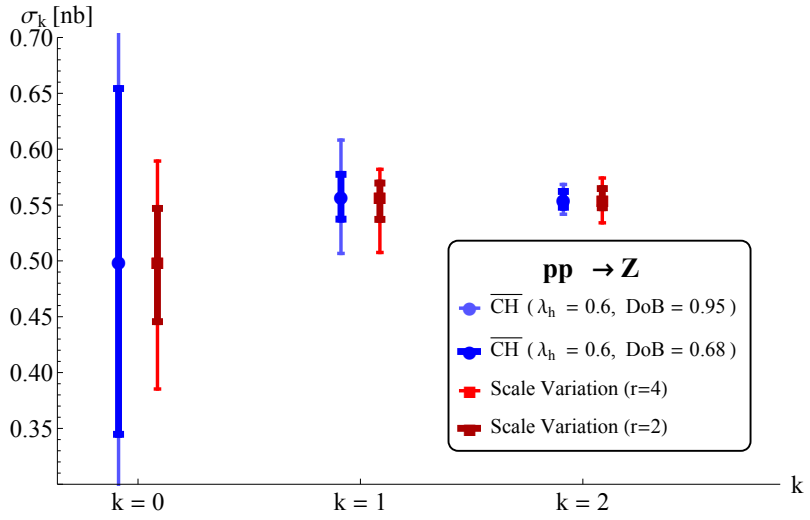


**Figure 17:** Size of the uncertainty interval at LO, NLO and NNLO for $\overline{\text{CH}}$ with $\lambda_h = 0.6$, compared to those predicted by scale variation for $pp \to Z \to e^+e^-$.

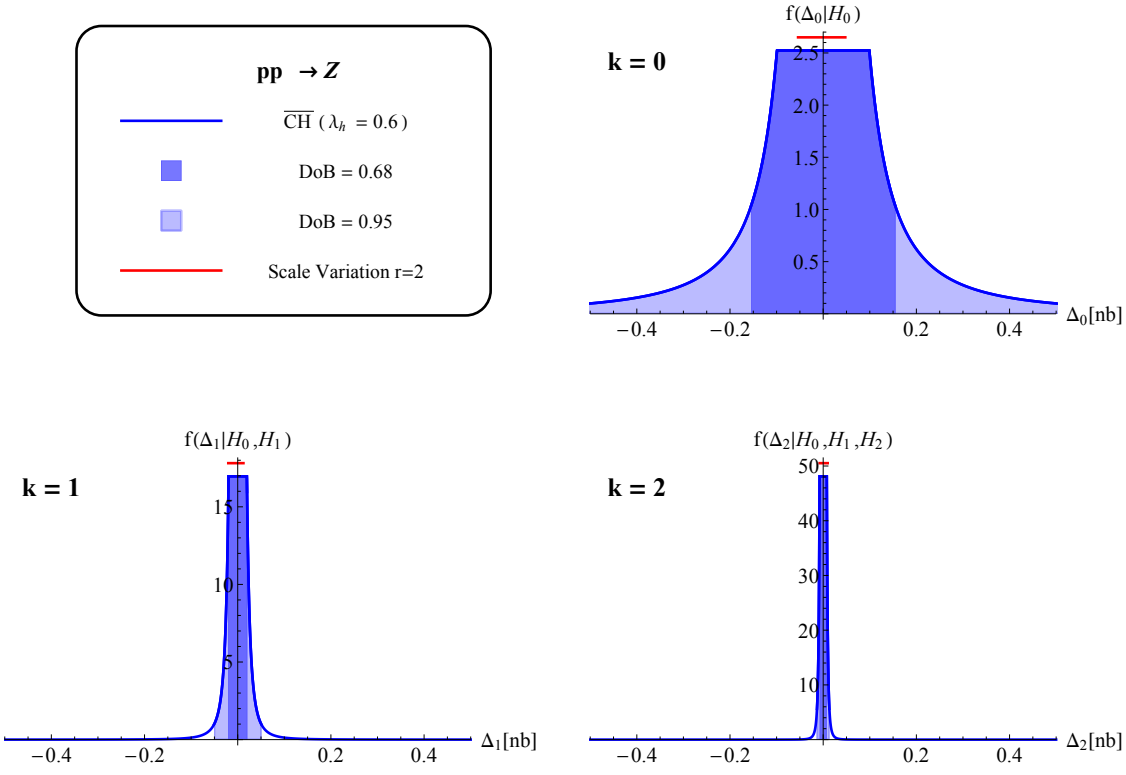


**Figure 18:** Posterior distribution of the Bayesian model for $\Delta_k = \sum_{n=k+1}^{\infty} c_n$ (blue solid), 68% DoB interval (blue fill), 95% DoB interval (light-blue fill), scale variation interval (red solid) for $pp \to Z \to e^+e^-$.

| $pp \to t\bar{t}$ | | | | | |
|---|---|---|---|---|---|
| Order | $\sigma_k$[pb] | $\overline{\text{CH}}$, 68% | $\overline{\text{CH}}$, 95% | $SV_{r=2}$ $(\delta_n^-, \delta_n^+)$ | $SV_{r=2}$ DoB |
| $k = 2$ | 146.32 | $\pm 82.61$ | $\pm 528.76$ | $(-34.32, 51.08)$ | $(16.2\%, 24.1\%)$ |
| $k = 3$ | 217.38 | $\pm 39.32$ | $\pm 99.46$ | $(-26.89, 26.94)$ | $(23.3\%, 23.3\%)$ |
| $k = 4$ | 244.36 | $\pm 25.24$ | $\pm 47.61$ | $(-13.52, 10.42)$ | $(18.2\%, 14.0\%)$ |

**Table 7:** Analysis results for $pp \to t\bar{t}$. The meaning of the columns is described in the caption of table 3.

## 5.4 $t\bar{t}$ production at the LHC

The cross section for top-quark-pair production at hadron colliders is now known up to NNLO [30]. This allows for an important comparison between theoretical prediction and experimental results at the LHC. Not only is top-pair production an important background process in BSM searches, but it is also an interesting observable by itself as a probe of the SM and for the precise measurement of the top-quark mass, one of the fundamental SM parameters needed to understand the stability of the EW vacuum. We used the tool `top++` to compute the cross sections at LO, NLO and NNLO for $\sqrt{s} = 8$ TeV at the LHC, with NNPDF2.3 NNLO PDF set used at all orders. We have always used the values of $\alpha_s$ coming from the PDF set and the top mass as the central scale for the process.

By looking at figure 19, we observe that the NLO cross section is contained in the LO 68% DoB interval of the $\overline{\text{CH}}$ prescription, while it is not contained in the scale-variation interval with $r = 2$. The NNLO cross section is outside both mentioned LO intervals but is within the 68% $\overline{\text{CH}}$ NLO intervals and nearly inside the $r = 2$ scale variation one. It is also worth mentioning that $\overline{\text{CH}}$ intervals with a DoB of 68% are similar in size to the scale-variation intervals with $r = 4$ for this observable. Scale-variation intervals with $r = 2$ are always contained in the $\overline{\text{CH}}$ 68% DoB intervals.

In figure 20 we show the posterior distribution for the $\overline{\textbf{CH}}$ model. We see that for this observable the scale variation result for $r = 2$ is always contained in the flat plateau. By comparing the shape of the distribution at different orders, one can appreciate the convergence behavior of the perturbative series.

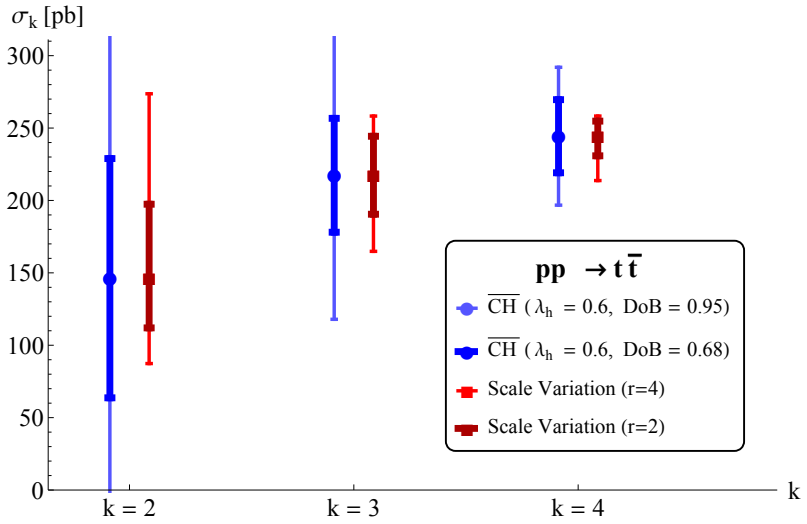


**Figure 19:** Size of the uncertainty interval at LO, NLO and NNLO for $\overline{\text{CH}}$ with $\lambda_h = 0.6$, compared to those predicted by scale variation for $pp \to t\bar{t}$.

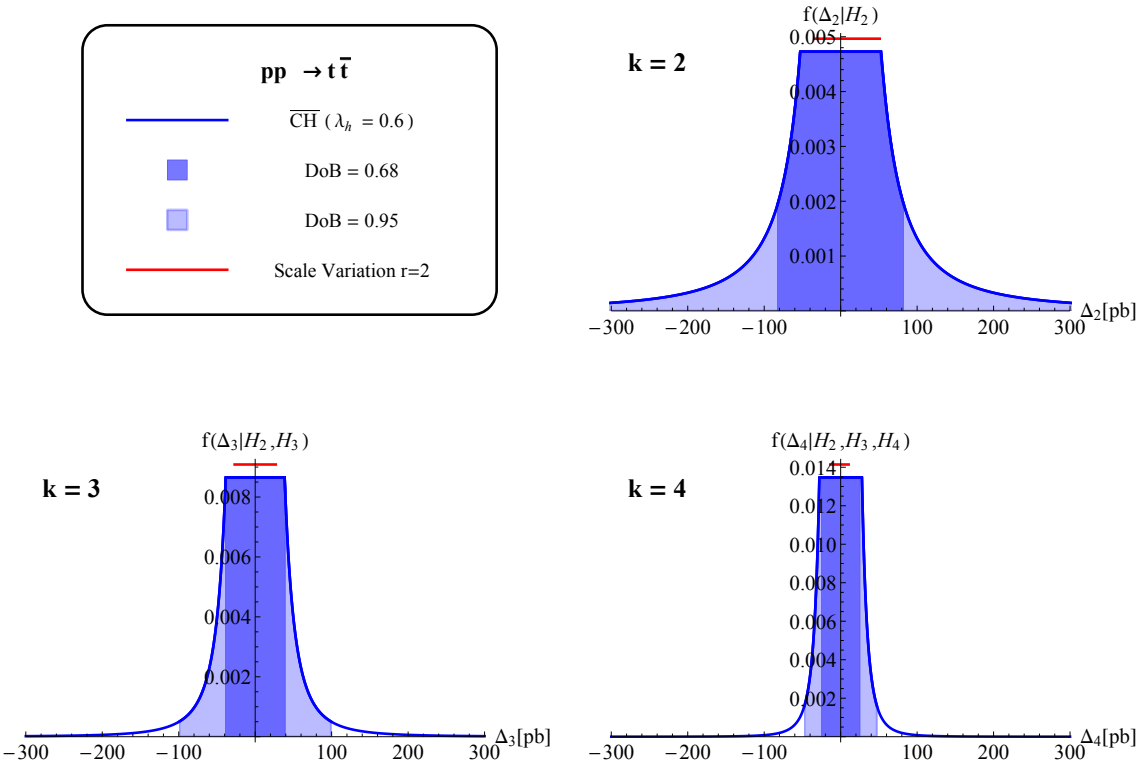


**Figure 20:** Posterior distribution of the Bayesian model for $\Delta_k = \sum_{n=k+1}^{\infty} \alpha_s^n c_n$ (blue solid), 68% DoB interval (blue fill), 95% DoB interval (light-blue fill), scale variation interval (red solid) for $pp \to t\bar{t}$.

| $pp \to H$ | | | | | |
|---|---|---|---|---|---|
| Order | $\sigma_k$[pb] | $\overline{CH}$, 68% | $\overline{CH}$, 95% | $SV_{r=2}\,(\delta_n^-, \delta_n^+)$ | $SV_{r=2}$ DoB |
| $k = 2$ | 5.6 | $\pm 3.35$ | $\pm 21.46$ | $(-0.98, 1.26)$ | $(11.39\%, 14.64\%)$ |
| $k = 3$ | 13.3 | $\pm 4.51$ | $\pm 11.42$ | $(-2.17, 2.74)$ | $(16.37\%, 20.69\%)$ |
| $k = 4$ | 18.37 | $\pm 3.52$ | $\pm 6.65$ | $(-2.06, 2.00)$ | $(19.88\%, 19.32\%)$ |

**Table 8:** Analysis results for $pp(gg) \to H$. The meaning of the columns is described in the caption of table 3.

## 5.5 Higgs boson production at the LHC

At hadronic colliders, the dominant production channel of the Higgs boson is gluon fusion. In this process the coupling of the Higgs to the gluons is mediated by a loop of colored particles. QCD corrections are known to be very large and the perturbative series is known to have a poorly-convergent behavior.

We compute the cross section for a 125 GeV Higgs at LHC with a center-of-mass energy of 8 TeV, using NNPDF2.3 as the PDF set at all orders. The values of $\alpha_s$ used in the hard scattering part of the cross section is given by $\alpha_s(m_Z) = 0.119$ and then evolved by HIGLU, giving a value of $\alpha_s(125.) \simeq 0.115$. The results have been obtained with HIGLU 4.0 for a top mass of 172.5 GeV and a bottom mass of 4.75 GeV.

We see from table 8 that the NLO contributions cause an increase of the cross section of 137% compared to LO and the NNLO contributions increase the cross section by another 37% compared to the NLO result.

Again, we compute the uncertainty intervals with the scale-variation prescription for $r = 2, 4$ and with the $\overline{CH}$ model with $\lambda_h = 0.6$. We show the results in figure 21. Scale variation with $r = 2$ does not seem to provide a reliable error estimate for this observable, since both the NLO and NNLO results are outside the bands computed at the previous order. We note on the other hand the following behavior for the $\overline{\mathbf{CH}}$ model: at LO the 68% DoB interval does not contain the NLO contribution; conversely, at NLO, the NNLO result is very close to the upper end of the 68% DoB band. In general we also observe that the 68% DoB intervals are comparable in size with scale variation intervals at $r = 4$.

To see how the 68% CL intervals compare to the 95% ones, we plot the posterior distribution in figure 22. We can see that just as for previous benchmark processes, the size of the 95% uncertainty intervals is reduced more drastically than the size of the 68% interval from LO to NNLO. We also note that the $r = 2$ intervals are always contained in the flat plateau part of the distribution at every order.

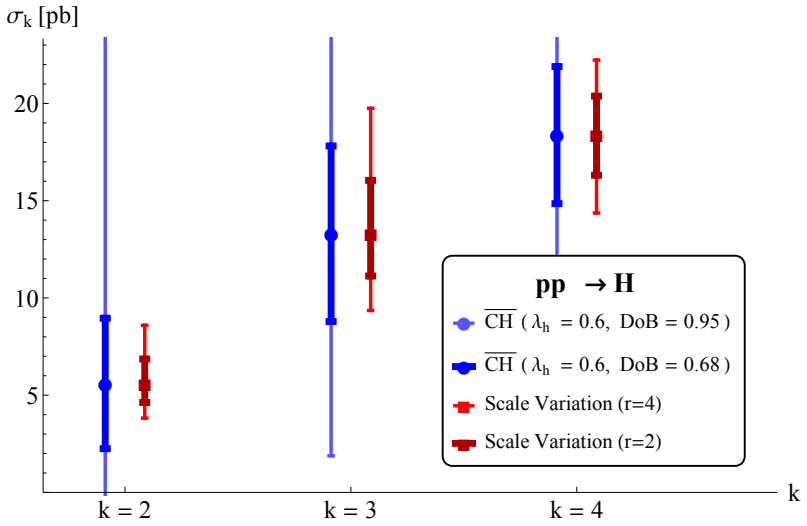


**Figure 21:** Size of the uncertainty interval at LO, NLO and NNLO for $\overline{CH}$ with $\lambda_h = 0.6$, compared to those predicted by scale variation.

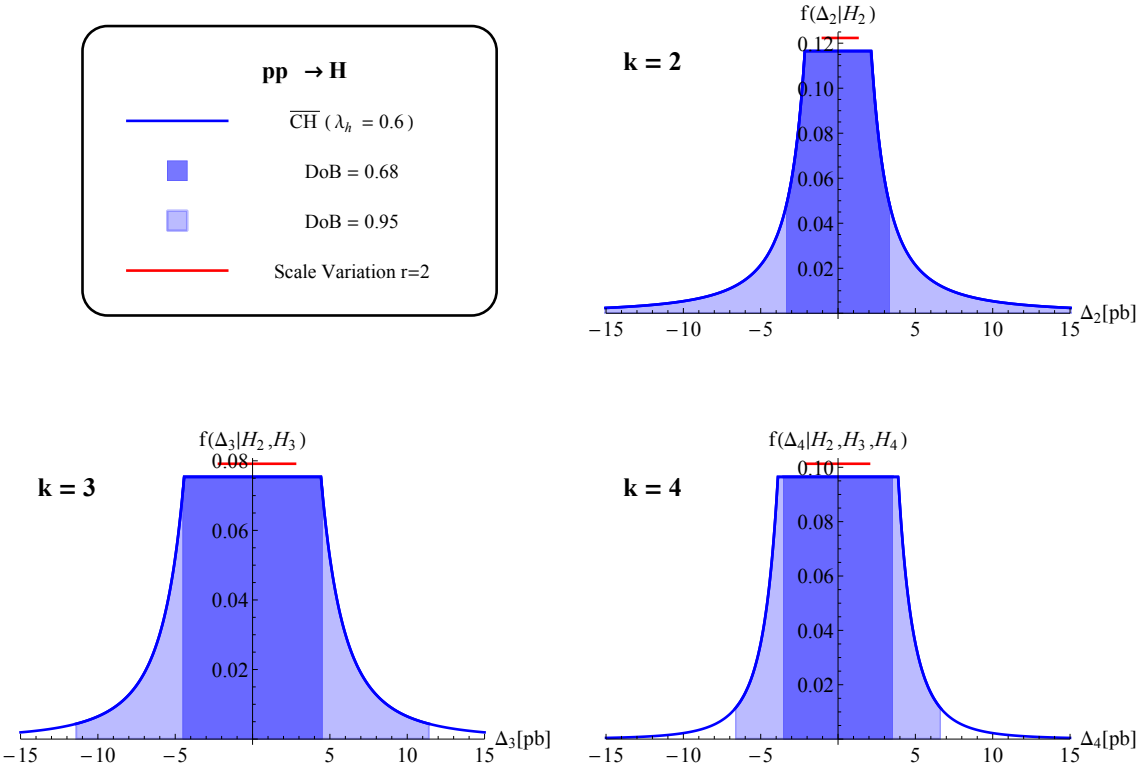


**Figure 22:** Posterior distribution of the Bayesian model for $\Delta_k = \sum_{n=k+1}^{\infty} \alpha_s^n c_n$ (blue solid), 68% DoB interval (blue fill), 95% DoB interval (light-blue fill), scale variation interval (red solid)

# 6 CONCLUSIONS AND OUTLOOKS

Now that we are entering the era of precision physics at the LHC, it will be extremely important to have not only a qualitative but also a quantitative control over uncertainties, both experimental and theoretical. With regard to the former, the community of the experimenters bears the responsibility of assessing them. Concerning the latter and focusing on the uncertainties coming from uncomputed higher order corrections, which are the object of our study, the theoretical community has relied for the past 20 years on a heuristic recipe, namely the scale-variation method. However this procedure is not built on robust theoretical foundations and it fails to provide a thorough statistical definition in term of Confidence Level (CL) of the intervals it provides. The latter is required to properly interpret the error bands and combine them with uncertainties of different origin. Moreover, up to this moment, there were no dedicated studies to understand its behavior on a wide set of observables.

The scope of this work was to improve our knowledge of the problem by performing a complete investigation of the commonly used prescription of scale variation and also by evaluating the performance of a much more modern method, the one introduced recently by Cacciari and Houdeau [1]. As a byproduct we also produced a modified version of the latter, which we named $\overline{\text{CH}}$ . We also extended the applications of the $\overline{\text{CH}}$ method to observables with initial state hadrons.

Hence we produced the first survey of the statistical behavior of these two methods. We moved along two complementary lines of analysis. First, we performed a global survey on a wide set of observables, categorized by their initial state being with or without initial state hadrons. Then we considered in details the results for a specific set of observables that we deemed significant from the phenomenological viewpoint.

With respect to the scale variation procedure, we have found that the factor of two usually used to determine the scale variation-range is not associated with a 68% heuristic-CL but with a lower value. This is true for the non-hadronic and, more markedly, for hadronic observables. A rescaling factor of the order of $3 - 4$ is probably a more conservative choice in both cases. It should be noticed that, with respect to Higgs specific observables, a similar conclusion was already reached in ref. [35, 36].

With regards to the Bayesian $\overline{\text{CH}}$ model, we have shown that it is capable of capturing the fundamental behavior of both non-hadronic and hadronic observables. While the general performance trend is good, it is probably possible to improve the model by restricting its definition (and tuning) to smaller (and more homogeneous) classes of observables. Moreover, our modification introduces in the model a new free parameter, $\lambda$, that needs to be determined with the aid of an external procedure. Indeed we used a frequentist analysis of the model performance to set it. However this introduces a frequentist contamination in the Bayesian framework that should probably be avoided for consistency. Naturally, a potential development is the replacement of the a posteriori determination of $\lambda$ with an ad-hoc Bayesian prior included in the model, with the aim of later marginalizing over it when computing the posterior distribution for the uncertainty interval. Other future developments include also the extension to differential observables, which is absolutely needed to fully exploit the phenomenological potential of the model.

Our conclusion is that for scale variation the commonly used factor of $r = 2$ can often lead to an underestimation of the real MHOU. Moreover, the newly introduced Bayesian framework by Cacciari and Houdeau, in its realization in the form of the $\overline{\text{CH}}$ model, provides an interesting alternative, being able to produce what appears to be a realistic estimation of the uncertainty intervals and, at the same time, a precise statistical interpretation in terms of Bayesian credibility. In light of this, it could be used to provide the estimation of missing higher order uncertainties alongside scale variation.

# Part II

## PRECISION HIGGS PHENOMENOLOGY AT THE LHC

We study the inclusive total cross section and the transverse momentum distribution of the Higgs boson at the LHC.

With respect to the former, we focus on the production of scalar and pseudoscalar Higgs bosons via gluon fusion and bottom-quark annihilation in the MSSM. Relying on the NNLO-QCD calculation implemented in the public code `SusHi` , we provide precise predictions for the Higgs-production cross section in six benchmark scenarios compatible with the LHC searches. We also provide a detailed discussion of the sources of theoretical uncertainty in our calculation. We examine the dependence of the cross section on the renormalization and factorization scales, on the precise definition of the Higgs-bottom coupling and on the choice of PDFs, as well as the uncertainties associated to our incomplete knowledge of the SUSY contributions through NNLO. In particular, a potentially large uncertainty originates from uncomputed higher-order QCD corrections to the bottom-quark contributions to gluon fusion.

On the other hand, the transverse momentum analysis is focused on the gluon fusion production process only. We present results in the SM, in the 2HDM and in the MSSM. We discuss the sources of uncertainties that arise during the computation of this observable in matched fixed order-resummed computations, with specific emphasis on the issues that derive from the inclusion of the bottom quark contribution. We discuss the problem in the SM and in the 2HDM. We will rely on the use of our `POWHEG-BOX` event generator and on the code `HRES` to perform the numerical analysis.

# 1 INTRODUCTION

The discovery of a scalar resonance with mass around 125.5 GeV by the ATLAS and CMS experiments at the Large Hadron Collider (LHC) [37, 38] puts new emphasis on the need for precise theoretical predictions for Higgs production and decay rates, both in the Standard Model (SM) and in plausible extensions of the latter such as the Minimal Supersymmetric Standard Model (MSSM). The role of these very accurate theoretical results is to be the basis for the ongoing investigations to determine the properties of the newly discovered resonance and to test its compatibility with the Higgs boson of the Standard Model (SM). In detail, the comparison between the experimental measurements and the theoretical predictions of the total production cross section and of the branching ratios in the different allowed decay channels will provide the basis to appreciate if and with which strength the new state couples to fermions and to the gauge bosons of the SM. Other studies target the kinematic of the decay products to try to distinguish among the various spin-parity combinations. Finally, further work will be necessary to clarify the nature of the scalar potential by measuring the accessible self-couplings of the Higgs bosons. The current status of these calculations is summarized in the reports of the LHC Higgs Cross Section Working Group (LHC-HXSWG) [39–41].

As we have already stressed in the first part of the thesis, a high degree of control over theoretical uncertainties is as important as the control over experimental ones. Our aim is therefore to provide a new insight on the theoretical uncertainties that enter the observables that are currently at the base of the experimental Higgs boson analysis. We will use state-of-the art results and computing tools to achieve this purpose.

The structure of the study is the following. At first, in chapter 2, we introduce briefly the three models whose Higgs sector observables we are going to study. This is needed to swiftly recall the physics behind our analysis and to fix the notation. Then, in chapter 3 we will delve briefly into the mechanisms of the two processes that we are going to study in detail, gluon fusion and bottom quark annihilation.

The first part of our original work is in chapter 4, where we present a precise study of scalar and pseudoscalar Higgs production in the MSSM. The chapter is divided according to the following structure.

In section 4.1 we show the predictions for the total inclusive cross section for Higgs production in six benchmark scenarios compatible with the LHC results, focusing in particular on a scenario with relatively light stops where the effect of the SUSY contributions can be significant.

In section 4.2 we provide a detailed discussion of the sources of theoretical uncertainty in the calculation of the total cross section for Higgs-boson production in the MSSM. We examine the dependence of the cross sections for gluon fusion and bottom-quark annihilation on the renormalization and factorization scales, on the precise definition of the Higgs-bottom coupling and on the choice of PDFs, as well as the uncertainty associated to our incomplete knowledge of the SUSY contributions through NNLO. In particular, we point out a potentially large uncertainty arising from uncomputed higher-order QCD corrections to the bottom-quark contributions to gluon fusion, which can affect the interpretation of the searches for the MSSM Higgs bosons in scenarios where their couplings to bottom quarks are enhanced with respect to the SM.

In chapter 5 we present the problem of computing the transverse momentum distribution of the Higgs boson in the SM, in the POWHEG-BOX framework. We will then present a thorough analysis of the so-called matching uncertainties for the computation of the transverse momentum spectrum of the Higgs boson. Our study has an emphasis on the issues that derive from the use of the matrix elements with full dependence of the quark masses. We rely on the use of our POWHEG-BOX event generator and on the code HRES to perform the numerical analysis. Next we study the same issues in the context of the two Higgs doublet model. Moreover we present our results for transverse momentum spectrum for the light, heavy and the pseudoscalar boson of the MSSM [39, 41], although we will leave the discussion of its uncertainties to a future study.

Finally, In chapter 6 we present our conclusions and sketch possible future areas of improvements.

In the appendix we report another possible technical approach to the problem of the inclusion of the complete quark amplitudes in the POWHEG-BOX and we list the cross sections and uncertainties for the production of the three neutral Higgs bosons in selected points of the parameter space for the light stop scenario that was the focus of the analysis in chapter 4.

# 2 THE HIGGS SECTOR

The problem of introducing mass terms for gauge bosons and chiral fermions in a gauge theory can be resolved using the so-called Higgs mechanism. In its simplest form, it involves the introduction of a scalar potential into the model Lagrangian, whose field (charged under the gauge symmetries that would be broken by the mass terms) acquires a non-zero vacuum expectation value. By suitably choosing the properties of the newly added scalar field and its interaction with matter fields, it is possible to generate the mass terms without violating the gauge symmetry of the original Lagrangian. We will now briefly review how this works in the SM, 2HDM and in the MSSM. For a complete review of these models we refer, for the SM and the MSSM to ref. [42] and ref. [43, 44] respectively; a complete introduction to the 2HDM can be found in ref. [45].

## 2.1 The Standard Model

The Standard Model (SM) is an $SU(3)_c \times SU(2)_L \times U(1)_Y$ gauge theory whose Lagrangian is given by

$$\mathcal{L}_{SM} = -\frac{1}{4} G^a_{\mu\nu} G^{\mu\nu}_a - \frac{1}{4} W^a_{\mu\nu} W^{\mu\nu}_a - \frac{1}{4} B_{\mu\nu} B^{\mu\nu} \tag{48}$$

$$+ \overline{L}_i i\not{D} L_i + \overline{e}_{Ri} i\not{D} e_{Ri} + \overline{Q}_i i\not{D} Q_i + \overline{u}_{Ri} i\not{D} u_{Ri} + \overline{d}_{Ri} i\not{D} d_{Ri}. \tag{49}$$

where $D_\mu$ is the $SU(3)_c \times SU(2)_L \times U(1)_Y$ covariant derivative; the field strength tensor for the gluon is $G^a_{\mu\nu}$, the one for the $W$ field is $W^a_{\mu\nu}$ and the one for the B field is $B_{\mu\nu}$. The summation over the index $i$ is intended to be over the families. The matter content of the theory is the following: $L_i$ is the leptonic left handed $SU(2)$ doublet; $e_{Ri}$ is the leptonic right handed $SU(2)$ singlet; $Q_i$ is the quark left handed $SU(2)$ doublet; $u_{Ri}$ and $d_{Ri}$ are the right handed $SU(2)$ singlet for up-type and down-type quark respectively. There are no right handed neutrinos in the SM. While it would be possible to introduce mass terms for the quarks if the only gauge symmetry present would be $SU(3)_c$, it is impossible to introduce mass terms for the gauge bosons and for the chiral fermions (i.e. fermions whose left handed and right handed component lives in different representation of the gauge group) without violating the $SU(2)_L \times U(1)_Y$ gauge symmetry of the Lagrangian. The Higgs mechanism addresses this issue. In the SM it is implemented in its simplest form, with the introduction of a single $SU(2)$ doublet of scalars field

$$\Phi = \begin{pmatrix} \phi^+ \\ \phi^0 \end{pmatrix}, \quad Y_\phi = +1\,. \tag{50}$$

We can then add the scalar doublet to the SM by adding the following terms to the original Lagrangian

$$\mathcal{L}_S = (D^\mu \Phi)^\dagger (D_\mu \Phi) - \mu^2 \Phi^\dagger \Phi - \lambda (\Phi^\dagger \Phi)^2\,, \tag{51}$$

where the covariant derivative is given by

$$D_\mu \Phi = \left( \partial_\mu - i g \tau^a W_\mu^a - i g' \frac{Y_q}{2} B_\mu \right) \Phi \,. \tag{52}$$

Here $B_\mu$ is the gauge field of the $U(1)_Y$ group (with generator $Y_q/2$) while the $W_\mu^a$ are the gauge fields of the $SU(2)_L$ gauge group (with generator $\tau^a = \sigma^a/2$, where $\sigma^a$ are the Pauli matrix). We denote with $g'$ and $g$ respectively the coupling constant of the $U(1)_Y$ and $SU(2)_L$ gauge group. If we take $\mu^2 < 0$ the neutral component (with respect to the electric charge $Q = T_3 + Y_\Phi/2$ where $T_3$ is the third component of the isospin) of the scalar doublet develops a non-zero vacuum expectation value (vev)

$$\langle \Phi \rangle_0 \equiv \langle 0 | \Phi | 0 \rangle = \begin{pmatrix} 0 \\ \frac{v}{\sqrt{2}} \end{pmatrix} \text{ with } v = \left( -\frac{\mu^2}{\lambda} \right)^{1/2} . \tag{53}$$

We then expand the scalar doublet around the vev $v$ , at first order, by writing it in terms of four fields $\theta_{1,2,3}(x)$ and $H(x)$:

$$\Phi(x) = \begin{pmatrix} \theta_2 + i\theta_1 \\ \frac{1}{\sqrt{2}}(v + H) - i\theta_3 \end{pmatrix} \simeq e^{i\theta_a(x)\tau^a(x)/v} \begin{pmatrix} 0 \\ \frac{1}{\sqrt{2}}(v + H(x)) \end{pmatrix} . \tag{54}$$

We then perform a gauge transformation and move to the unitary gauge to isolate the physical degrees of freedom. After doing so we have

$$(\Phi(x))_{\text{unitary gauge}} = e^{-i\theta_a(x)\tau^a} \Phi(x) = \frac{1}{\sqrt{2}} \begin{pmatrix} 0 \\ v + H(x) \end{pmatrix} . \tag{55}$$

The $H(x)$ is the remaining physical degree of freedom, i.e. the Higgs boson. We can now substitute the expansion in the kinetic term of eq. (51), obtaining

$$|D_\mu \Phi|^2 = \frac{1}{2}(\partial_\mu H)^2 + \frac{1}{8} g^2 (v + H)^2 |W_\mu^1 + i W_\mu^2|^2 + \frac{1}{8}(v + H)^2 |g W_\mu^3 - g' B_\mu|^2 \,. \tag{56}$$

We now rewrite this expression in terms of the fields $W_\mu^\pm$, $Z_\mu$ and $A_\mu$, defined by

$$W^\pm = \frac{1}{\sqrt{2}}(W_\mu^1 \mp i W_\mu^2) \,, \tag{57}$$

$$Z_\mu = \frac{g W_\mu^3 - g' B_\mu}{\sqrt{g^2 + g'^2}} \,, \tag{58}$$

$$A_\mu = \frac{g W_\mu^3 + g' B_\mu}{\sqrt{g^2 + g'^2}} \,. \tag{59}$$

We have then

$$|D_\mu \Phi|^2 = \frac{1}{2}(\partial_\mu H)^2 + \left[ \left( \frac{g}{2} \right)^2 W^{\mu +} W_{\mu -} + \frac{1}{2} \frac{(g^2 + g'^2)}{4} Z^\mu Z_\mu \right] (v + H)^2 \tag{60}$$

After expanding the last terms, we can isolate the mass terms for the $W^{\pm}_{\mu}$ and the $Z_{\mu}$ bosons, which now have acquired masses equal to

$$M_W = \frac{1}{2} v g \,, \qquad M_Z = \frac{1}{2} v \sqrt{g^2 + g'^2} \tag{61}$$

while the photon is still massless, accordingly to our desire to keep the $U(1)_Q$ symmetry unbroken. From the same Lagrangian we can extract the couplings of the Higgs boson to vector bosons. They are, written in terms of the masses of the particle coupled to the Higgs:

$$g_{HVV} = 2\frac{M_V^2}{v} \qquad g_{HHVV} = 2\frac{M_V^2}{v^2} \tag{62}$$

As we can see, the coupling is proportional to the mass: the more massive particles couple more strongly to the Higgs boson.

The generation of the fermion masses is achieved by writing Yukawa interaction terms with $\Phi$ (for the type-down quarks and the leptons) and with the isodoublet $\tilde{\Phi} = i\tau_2 \Phi^*$ (for the up-type quarks). For every fermion generation one introduces the following Yukawa Lagrangian:

$$\mathcal{L}_F = -\lambda_e \, \bar{L} \, \Phi \, e_R - \lambda_d \, \bar{Q} \, \Phi \, d_R - \lambda_u \, \bar{Q} \, \tilde{\Phi} \, u_R \; + \; h.c. \tag{63}$$

To get the masses and the couplings of the fermions to the Higgs, we have to expand the Higgs field around its vev. For example, taking the electron field one obtains the following relevant term:

$$-\frac{1}{\sqrt{2}} \lambda_e \, (\bar{\nu}_e, \bar{e}_L) \begin{pmatrix} 0 \\ v + H \end{pmatrix} e_R \; = \tag{64}$$

$$= -\frac{1}{\sqrt{2}} \, \lambda_e \, (v + H) \, \bar{e}_L \, e_R \tag{65}$$

The value $m_e = \frac{\lambda_e \, v}{\sqrt{2}}$ is identified as the mass of the particle. Repeating the same for the first generation quarks we have:

$$m_u = \frac{\lambda_u \, v}{\sqrt{2}} \qquad m_d = \frac{\lambda_d \, v}{\sqrt{2}} \tag{66}$$

From the same Lagrangian we can extract the couplings of the fermions to the Higgs boson. We have in general that:

$$g_{Hff} = \frac{m_f}{v} \tag{67}$$

With the same isodoublet of scalar fields we have therefore generated the masses of the weak vector bosons and of the fermions. The $SU(2)xU(1)$ gauge symmetry is now spontaneously broken or hidden, while the $U(1)_Q$ and the $SU(3)_C$ symmetry are still unbroken.

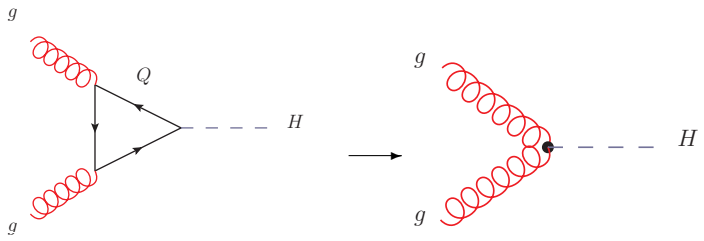


**Figure 23:** Leading order diagram for gluon fusion in the SM (left) and in the HQEFT where the top quark has been integrated out (right).

### 2.1.1 Heavy quark effective Lagrangian for the Higgs-gluons coupling

Since the Higgs boson is not charged under the color gauge group $SU(3)_c$, it does not interact with gluons directly. Indeed its coupling to the gluons is mediated by a loop of color-charged fermions, i.e. quarks. Since, as we have seen above, in the SM the coupling of the fermions to the Higgs boson is proportional to the mass, the main contribution comes from the heaviest colored fermion, the top quark. We will see in chapter 3 that the most important Higgs boson production at hadronic collider is indeed gluon initiated, due to the very high gluon parton luminosity. This process, called gluon fusion, is already described by one loop diagrams at first order in perturbation theory. It is possible to simplify the calculation by introducing a Heavy Quark Effective Field Theory (HQEFT) where the top quark degrees of freedom are integrated out from the Lagrangian and leave an effective operator that couples directly the Higgs to the gluons,

$$\mathcal{L}_{\text{HQEFT}} = \frac{\alpha_s}{12\pi}\frac{H}{v}\,\text{Tr}\left[G^a_{\mu\nu}G^a_{\mu\nu}\right] . \tag{68}$$

By following this approach, gluon fusion starts as a tree level process and the computation simplifies significantly. However this approximation loses validity as soon as the other relevant scales of the process reach the top quark threshold. For inclusive production this happens when the mass of the Higgs reaches the $2 \times m_t$ threshold. It is found however that even beyond the threshold it is possible to use this approximation for NLO and NNLO corrections, by rescaling the result by a factor $LO(\text{top})/LO(m_t \to \infty)$ with good accuracy with respect to the full SM result. For differential distributions the validity range is again limited by the top mass scale: as soon as one of the scales (for example the $p_T$) reaches it, deviations from the HQEFT start to appear.

## 2.2 The Two Higgs Doublet Model

The two Higgs Doublet Model (2HDM) is one of the simplest extension of the SM. At the Lagrangian level, the only difference is an extended scalar sector, with two $SU(2)_L$ doublets instead of one. The motivations behind it are numerous ranging from axion models (it is possible to impose the Peccei-Quinn $U(1)$ symmetry to the Lagrangian only if the latter contains two doublets) to the baryon asymmetry of the Universe (the 2HDM model provides additional sources of CP violation). Finally it could also be taken as an effective implementation of the Higgs sector of the MSSM, which indeed has the same

structure as we will see in section 2.3. The most general formulation of the 2HDM contains fourteen additional parameters and can have CP-conserving, CP-violating and charge-violating minima. For our purpose, we make several simplifying assumptions: CP is conserved in the Higgs sector, CP is not spontaneously broken and finally we impose discrete symmetries to remove from the scalar potential all quartic terms that are odd in either of the doublets (though we will keep open the possibility of softly broken them by considering all possible real quadratic coefficients). Hence, calling $H_1$ and $H_2$ two Higgs doublets with hypercharge +1 we have that the scalar potential is given by

$$\begin{aligned} V_0 = {} & m_{11}^2 H_1^\dagger H_1 + m_{22}^2 H_2^\dagger H_2 - m_{12}^2 \left( H_1^\dagger H_2 + H_2^\dagger H_1 \right) + \frac{\lambda_1}{2} \left( H_1^\dagger H_1 \right)^2 + \frac{\lambda_1}{2} \left( H_2^\dagger H_2 \right)^2 \\ & + \lambda_3 H_1^\dagger H_1 H_2^\dagger H_2 + \lambda_4 H_1^\dagger H_2 H_2^\dagger H_1 + \frac{\lambda_5}{2} \left[ \left( H_1^\dagger H_2 \right)^2 + \left( H_2^\dagger H_1 \right)^2 \right] \end{aligned} \tag{69}$$

where all parameters are real. The two complex scalar doublets can be explicitly decomposed in eight fields

$$H_i = \begin{pmatrix} H_i^+ \\ (v_i + \rho_i + i\eta_i)/(\sqrt{2}) \end{pmatrix}, \; i = 1, 2 \tag{70}$$

where we have supposed that the two doublets get a non-zero vacuum expectation value

$$\langle H_1 \rangle_0 \equiv \langle 0 | H_1 | 0 \rangle = \begin{pmatrix} 0 \\ \frac{v_1}{\sqrt{2}} \end{pmatrix}, \quad \langle H_2 \rangle_0 \equiv \langle 0 | H_2 | 0 \rangle = \begin{pmatrix} 0 \\ \frac{v_2}{\sqrt{2}} \end{pmatrix}. \tag{71}$$

Three of the eight fields are eaten by the $W^\pm$ and $Z$ gauge bosons to acquire mass. The remaining five degrees of freedom appear in the physical spectrum. Hence the latter contains a charged scalar, two neutral CP-even scalars and one neutral CP-odd scalar. We now proceed to diagonalize the mass matrices of the physical degree of freedoms. Given the above minimization condition, we have that the mass matrix for the charged Higgs sector is given by

$$\mathcal{L}_{\phi^\pm,\text{mass}} = \left[ m_{12}^2 - (\lambda_4 + \lambda_5) v_1 v_2 \right] \; (H_1^- , H_2^-) \begin{pmatrix} \frac{v_2}{v_1} & -1 \\ -1 & \frac{v_1}{v_2} \end{pmatrix} \begin{pmatrix} H_1^+ \\ H_2^+ \end{pmatrix}. \tag{72}$$

One of the eigenvalues of the mass matrix is zero: this corresponds to the would-be electrically charged Goldstone boson $G^\pm$ which is going to get eaten by the $W^\pm$ bosons. The other eigenvalue is the mass of the charged Higgs field: $m_\pm^2 = \left[ m_{12}^2/(v_1 v_2) - (\lambda_4 + \lambda_5) \right] (v_1^2 + v_2^2)$. The pseudoscalar mass matrix is instead given by

$$\mathcal{L}_{\eta,\text{mass}} = \left[ m_{12}^2/(v_1 v_2) - 2\lambda_5 \right] \; (\eta_1 , \eta_2) \begin{pmatrix} v_2^2 & -v_1 v_2 \\ -v_1 v_2 & v_1^2 \end{pmatrix} \begin{pmatrix} \eta_1 \\ \eta_2 \end{pmatrix}. \tag{73}$$

Again, one of the eigenvalues of the mass matrix is zero, corresponding to the would-be Goldstone boson that gets eaten by the $Z$ boson. The other eigenvalue corresponds to the mass of the physical pseudoscalar state, $m_A^2 = [m_{12}^2/(v_1 v_2) - 2\lambda_5](v_1^2 + v_2^2)$. The rotation angle that diagonalizes the mass matrices of

the charged and pseudoscalar fields is the same and it is usually called $\beta$. It is linked to the vacuum expectation values of the two Higgs doublets by the following fundamental relation

$$\tan\beta = \frac{v_2}{v_1} \tag{74}$$

Finally, for the mass matrix of the scalar states, we have

$$\mathcal{L}_{\rho,\text{mass}} = -(\rho_1\,,\rho_2)\begin{pmatrix} m_{12}^2\frac{v_2}{v_1} + \lambda_1 v_1^2 & -m_{12}^2 + (\lambda_3+\lambda_4+\lambda_5)\,v_1v_2 \\ -m_{12}^2 + (\lambda_3+\lambda_4+\lambda_5)\,v_1v_2 & m_{12}^2\frac{v_1}{v_2} + \lambda_2 v_2^2 \end{pmatrix}\begin{pmatrix}\rho_1\\ \rho_2\end{pmatrix}. \tag{75}$$

The rotation angle that diagonalizes the matrix is conventionally called $\alpha$ and it is another important phenomenological parameter.

It is important to notice that if we redefine the original doublets as

$$H_1' = \cos\beta H_1 + \sin\beta H_2 \tag{76}$$
$$H_2' = -\sin\beta H_1 + \cos\beta H_2 \tag{77}$$
$$\tag{78}$$

one finds that

$$\langle H_1'\rangle_0 \equiv \langle 0|H_1'|0\rangle = \begin{pmatrix} 0 \\ \frac{v}{\sqrt{2}}\end{pmatrix}, \quad \langle H_2'\rangle_0 \equiv \langle 0|H_2'|0\rangle = \begin{pmatrix} 0 \\ 0\end{pmatrix}. \tag{79}$$

where $v = \sqrt{v_1^2+v_2^2}$, as in the SM. The two diagonalization angles $\alpha$ and $\beta$ parametrize the way that the couplings to gauge bosons and fermions are rescaled with respect to the SM. Indeed we can write $v_1 = v\cos\beta$ and $v_2 = v\sin\beta$. We have now that the eigenstates of the neutral sector mass matrices are:

- For the pseudoscalar sector

$$G^0 = \eta_1\cos\beta + \eta_2\sin\beta \tag{80}$$
$$A = \eta_1\sin\beta - \eta_2\cos\beta. \tag{81}$$

- For the neutral scalar sector

$$h = \rho_1\sin\alpha - \rho_2\cos\alpha \tag{82}$$
$$H = -\rho_1\cos\alpha - \rho_2\sin\alpha. \tag{83}$$

On the other hand, the SM-like Higgs boson would be

$$H^{SM} = \rho_1\cos\beta + \rho_2\sin\beta = h\sin(\alpha-\beta) - H\cos(\alpha-\beta) \tag{84}$$

It can be demonstrated that one can choose without loss of generality to take $v_1$ and $v_2$ as non-negative real numbers, thus having a $\beta$ angle in first quadrant. On the other hand, in the 2HDM, the angle $\alpha$ can

be taken either in the fourth or in the first quadrant.

The most general form of the Yukawa couplings of the quarks to the two Higgs doublets is given by

$$\mathcal{L}_Y = (y_1)_{ij}\,\bar{\psi}_i\psi_j H_1 + (y_2)_{ij}\,\bar{\psi}_i\psi_j H_2. \tag{85}$$

where the $\psi_i$ are four-component Dirac spinors and the sum over the indices $i$ and $j$ is understood to be over the quark generations. The mass matrix for the quarks is then given by

$$M_{ij} = (y_1)_{ij}\,\frac{v_1}{\sqrt{2}} + (y_2)_{ij}\,\frac{v_2}{\sqrt{2}}. \tag{86}$$

In the most general form of the 2HDM, the two matrices $y_1$ and $y_2$ will not be simultaneously diagonalizable. In this case, the neutral Higgs scalars will mediate tree-level flavor changing neutral currents (FCNC), at variance with the SM. Due to experimental results, which put high constraints on this processes, this is not desirable. It was demonstrated by Paschos, Glashow and Weinberg (PGW) that a necessary and sufficient condition for the absence of FCNC at tree level is that all fermions of a given charge and helicity transform according to the same irreducible representation of $SU(2)$, corresponds to the same eigenvalue of $T_3$ and that a basis exists such that they receive contributions in the mass matrix from a single source. This is already true in the SM. In the 2HDM the same requirement can be enforced by introducing symmetries (discrete or continuous).

In the quark case we have only two possibilities. The first one, the so-called "type I" 2HDM, all quarks couple to one of the Higgs doublets, which by convention is taken to be $H_2$. It can be constructed by requiring a discrete $H_1 \to -H_1$ symmetry. The other possibility is the "type II" 2HDM, where the $Q = 2/3$ right-handed quarks couple to one Higgs doublet, conventionally $H_2$, and the $Q = -1/3$ right handed quarks couple instead to $H_1$. It can be obtained by imposing the $H_1 \to -H_1$ and $d_R^i \to -d_R^i$ discrete symmetry to the Lagrangian or by other requirements like supersymmetry.

Regarding the leptons, there are various possibilities, all allowed by the PGW theorem: the conventional one is that right handed leptons have the same symmetry as the $d_R^i$ and therefore they couple to the same Higgs as $Q = -1/3$ quarks; in the "lepton specific" model we have that the right handed quarks couple to $H_2$ while right handed leptons to $H_1$; in the "flipped" model right handed with $Q = 2/3$ and right handed leptons couple to $H_2$ while right handed quarks with charged $Q = -1/3$ couple to $H_1$.

We can then write the Yukawa part of the Lagrangian in the following way

$$\begin{aligned}\mathcal{L}_{\text{Yukawa}} = &- \sum_{f=u,d,l} \frac{m_f}{v}\left(\lambda_f^h \bar{f} f h + \lambda_f^H \bar{f} f H - i\lambda_f^A \bar{f}\gamma_5 f A\right) \\ &- \left\{\frac{\sqrt{2}V_{ud}}{v}\bar{u}\left(m_u\lambda_u^A P_L + m_d\lambda_d^A P_R\right) d H^+ + \frac{\sqrt{2}m_l\lambda_l^A}{v}\nu\bar{u}_L l_R H^+ + \text{h.c.}\right\}.\end{aligned} \tag{87}$$

All the cases discussed above can be then expressed in terms of various values for the $\lambda$ parameters. The explicit values are given in table 9.

With respect to the couplings to two gauge bosons, in all varieties of 2HDM we the couplings is the SM one rescaled by a factor $\sin(\beta-\alpha)$ for h and by a factor $\cos(\alpha-\beta)$ for H. Instead the couplings of A to two gauge bosons vanishes.

For the type II 2HDM, a particularly important parameter point choice for phenomenological reasons is the so called decoupling limit. We have that when $\alpha = \beta - \pi/2$ the couplings of h to fermions and

| Higgs couplings in the 2HDM | | | | |
|---|---|---|---|---|
| Coupling | Type I | Type II | Lepton specific | Flipped |
| $\lambda_u^h$ | $\cos\alpha/\sin\beta$ | $\cos\alpha/\sin\beta$ | $\cos\alpha/\sin\beta$ | $\cos\alpha/\sin\beta$ |
| $\lambda_d^h$ | $\cos\alpha/\sin\beta$ | $-\sin\alpha/\cos\beta$ | $\cos\alpha/\sin\beta$ | $-\sin\alpha/\cos\beta$ |
| $\lambda_u^H$ | $\sin\alpha/\sin\beta$ | $\sin\alpha/\sin\beta$ | $\sin\alpha/\sin\beta$ | $\sin\alpha/\sin\beta$ |
| $\lambda_d^H$ | $\sin\alpha/\sin\beta$ | $\cos\alpha/\cos\beta$ | $\sin\alpha/\sin\beta$ | $\cos\alpha/\cos\beta$ |
| $\lambda_u^A$ | $\cot\beta$ | $\cot\beta$ | $\cot\beta$ | $\cot\beta$ |
| $\lambda_d^A$ | $-\cot\beta$ | $\tan\beta$ | $-\cot\beta$ | $\tan\beta$ |
| $\lambda_l^h$ | $\cos\alpha/\sin\beta$ | $-\sin\alpha/\cos\beta$ | $-\sin\alpha/\cos\beta$ | $\cos\alpha/\sin\beta$ |
| $\lambda_l^H$ | $\sin\alpha/\sin\beta$ | $\cos\alpha/\cos\beta$ | $\cos\alpha/\cos\beta$ | $\sin\alpha/\sin\beta$ |
| $\lambda_l^A$ | $-\cot\beta$ | $\tan\beta$ | $\tan\beta$ | $-\cot\beta$ |
| $\lambda_V^h$ | $\sin(\beta-\alpha)$ | $\sin(\beta-\alpha)$ | $\sin(\beta-\alpha)$ | $\sin(\beta-\alpha)$ |
| $\lambda_V^H$ | $\cos(\beta-\alpha)$ | $\cos(\beta-\alpha)$ | $\cos(\beta-\alpha)$ | $\cos(\beta-\alpha)$ |
| $\lambda_V^A$ | 0 | 0 | 0 | 0 |

**Table 9:** Rescaling factors for the couplings to quarks (top section), leptons (middle section) and to two gauge bosons (bottom section) for the neutral Higgs bosons in four different types of 2HDM.

gauge bosons are equal to the SM ones and the H coupling to two gauge bosons goes to zero. If the mass of H and A are much heavier than h, one can integrates out these two fields from the Lagrangian and recover the SM as an effective theory.

## 2.3 The Minimal Supersymetric Standard Model

The Minimal Supersymmetric Standard Model (MSSM) is the simplest supersymmetric extension of the SM. Its gauge group is the same as the SM one, $SU(3)_c \times SU(2)_L \times U(1)_Y$, the particle content is composed of the SM fermions (three generations of quarks and leptons without right handed neutrinos) and their spin zero counterparts. Moreover, R-parity is assumed and supersymmetry is broken with the explicit addition of soft-breaking[1] terms to the Lagrangian. In the MSSM the Higgs sector is enlarged. Indeed, the requirement of the holomorphicity of the superpotential, to respect supersymmetry, and of the cancellation of the anomalies, dictates the introduction of two $SU(2)_L$ doublet Higgs, with opposite hypercharges. The structure of the interactions – and therefore also of the SUSY-conserving masses after spontaneous breaking of the EW symmetry – between these two doublets and the matter fields is contained into superpotential. In its simplest form, hypothesizing R-parity conservation, we can write it as

$$W = h_e H_1 L E^c + h_d H_1 Q D^c + h_u Q H_2 U^c - \mu H_1 H_2 \tag{88}$$

1 The soft breaking of supersymmetry does not spoil the cancellation of quadratic divergences in radiative corrections

where $Q, U^c, D^c$ are the quark superfields, $L, E^c$ are the lepton superfields and $H_1, H_2$ are the two Higgs superfields. Soft SUSY-breaking mass and interaction terms for MSSM scalars are on the other hand contained in the scalar potential

$$\begin{aligned}\mathcal{L}_{\text{soft}-\text{breaking}} = & m_{H_1}^2 H_1^\dagger H_1 + m_{H_2}^2 H_2^\dagger H_2 + m_Q^2 Q^\dagger Q + m_L^2 L^\dagger L \\ & + m_u^2 \tilde{u}_R^* \tilde{u}_R + m_d^2 \tilde{d}_R^* \tilde{d}_R + m_e^2 \tilde{e}_R^* \tilde{e}_R \\ & + \left(T_e H_1 L \tilde{e}_R^* + T_d H_1 Q \tilde{d}_R^* + T_u Q H_2 \tilde{u}_R^* + B_\mu H_1 H_2 + \text{h.c.}\right). \end{aligned} \tag{89}$$

In all these expressions we have left implicit the summation over families and the contraction of $SU(2)_L$ and $SU(3)_C$ indices. Finally, the Lagrangian also contains the soft SUSY-breaking mass terms for the gauginos, the superpartners of the gauge bosons

$$\mathcal{L}_G = \frac{1}{2}\left(M_1 \tilde{b}\tilde{b} + M_2 \tilde{w}\tilde{w} + M_3 \tilde{g}\tilde{g}\right) + \text{h.c.}\,. \tag{90}$$

With respect to the Higgs sector, if we keep only the neutral component of the two Higgs doublets, we have that the resulting expression for the tree level Higgs scalar potential is

$$V_0 = m_1^2 |H_1^0|^2 + m_2^2 |H_2^0|^2 + B_\mu (H_1^0 H_2^0 + \text{h.c.}) + \frac{g^2 + g'^2}{8}\left(|H_1^0|^2 - |H_2^0|^2\right)^2 \tag{91}$$

where $m_1^2 = m_{H_1}^2 + |\mu|^2$ and $m_2^2 = m_{H_2}^2 + |\mu|^2$ while $g$ and $g'$ are the $SU(2)_L$ and $U(1)_Y$ gauge coupling constant. The first three terms in this expression come from $W$ and $\mathcal{L}_{\text{soft}-\text{breaking}}$ while the last one is a D-term contribution. The two Higgs doublets acquire non-zero vacuum expectation values, $v_1$ and $v_2$, which can be assumed to be real and positive without loss of generality once it is defined, as we do, to have $B_\mu$ real and non-negative (this is always possible by reabsorbing the phases in the fields). We can then decompose the two doublets as

$$H_1^0 = \frac{1}{\sqrt{2}}\left(v_1 + S_1 + iP_1\right), \quad H_2^0 = \frac{1}{\sqrt{2}}\left(v_2 + S_2 + iP_2\right) \tag{92}$$

Exactly as in the SM case, we can then replace the Higgs fields in the Lagrangian with this expression to find the values for the gauge bosons and fermions masses. Indeed we have $m_W^2 = g^2 v^2/4$ and $m_Z^2 = (g^2 + g'^2)v^2/4$, where we have defined $v^2 \equiv v_1^2 + v_2^2$. For the fermions, we have that up-type quarks get masses in the form of $m_u = h_u \frac{v_2}{\sqrt{2}}$, while down type quarks and charged leptons have $m_{d,e} = h_{d,e}\frac{v_1}{\sqrt{2}}$, where here $h_i$ is one of the eigenvalues of the $i$ Yukawa matrix.

At variance with the SM, here the masses of the physical spectrum of Higgs bosons are not arbitrary parameters and they are determined by the model. We have that the mass matrix for the pseudoscalar state is diagonalized by an angle $\beta$ such that $\tan\beta = v_2/v_1$. Of the two eigenstates of the mass matrix, one, $G^0$ is the would-be Goldstone boson which is eaten by the $Z$ boson to acquire mass, while the other is a physical pseudoscalar state with a tree level mass equals to

$$m_A^2 = \frac{B_\mu}{\cos\beta \sin\beta}. \tag{93}$$

The same angle $\beta$ diagonalizes also the charged components of the two Higgs doublets. Of the four

eigenstates, two, $G^{\pm}$, are the two would-be Goldstone bosons that get eaten by the two $W^{\pm}$, while the other two, $H^{\pm}$ are physical states with masses $m^2_{H^{\pm}} = m^2_A + m^2_W$.

On the other hand, with respect to the CP-even neutral Higgs, we first use the minimum condition of the tree level Higgs potential $V_0$ to replace the two parameter $m_1^2$ and $m_2^2$ with a combination of $m_A^2$ and $\tan\beta$. We can then rewrite the tree-level mass matrix, in the $(S_1, S_2)$ basis, as

$$\mathcal{M}_0 = \begin{pmatrix} m_A^2 \sin^2\beta + m_Z^2 \cos^2\beta & -(m_A^2 + m_Z^2)\sin\beta\cos\beta \\ -(m_A^2 + m_Z^2)\sin\beta\cos\beta & m_A^2\cos^2\beta + m_Z^2\sin^2\beta \end{pmatrix}. \tag{94}$$

The matrix is diagonalized by an angle $\alpha$ given by

$$\tan 2\alpha = \left(\frac{m_A^2 + m_Z^2}{m_A^2 - m_Z^2}\right)\tan 2\beta \tag{95}$$

Its eigenstates are called $h$ and $H$. The lightest one, $h$, at tree level cannot be heavier than $m_Z^2\cos^2 2\beta < m_Z^2$. However the mass of $h$ receives huge radiative corrections which allow its value to be pushed up to and to be compatible with the observed one of $\sim 125.5$ GeV.

We now take a look at how the couplings between the Higgs and the SM fields are changed in the MSSM, where the role of the SM Higgs boson is shared by the two scalars $h$ and $H$. With respect to the gauge bosons, we have

$$g_{hVV} = \frac{2m_V^2}{v}\sin(\beta-\alpha), \quad g_{HVV} = \frac{2m_V^2}{v}\cos(\beta-\alpha), \tag{96}$$

while the couplings to the quarks and leptons are given by

$$g_{huu} = \frac{\cos\alpha}{\sin\beta}\frac{m_u}{v}, \quad g_{hdd,hee} = -\frac{\sin\alpha}{\cos\beta}\frac{m_{d,e}}{v} \tag{97}$$

$$g_{Huu} = \frac{\sin\alpha}{\sin\beta}\frac{m_u}{v}, \quad g_{Hdd,hee} = \frac{\cos\alpha}{\cos\beta}\frac{m_{d,e}}{v} \tag{98}$$

The pseudoscalar instead does not couple to two gauge bosons, while its couplings to quarks and leptons are given by

$$g_{Auu} = \cot\beta\frac{m_u}{v}, \quad g_{Add,Aee} = \tan\beta\frac{m_{d,e}}{v} \tag{99}$$

Also in the MSSM, as was the case in the 2HDM, we can tune the parameters to have the decoupling of H and A from fermions and gauge bosons. When $m_A \gg m_Z$, the mixing angle in the CP-even sector becomes $\alpha \simeq \beta - \pi/2$. Then we have that $m_h \simeq m_Z|\cos 2\beta|$ and the couplings of $h$ to SM fermions and gauge bosons become SM-like. In the same limit, the mass of the heaviest scalar becomes $m_H \simeq m_A$, the couplings of H to gauge bosons vanish and the ones to two up-type (down-type) SM fermions are suppressed (enhanced) by a $\tan\beta$ factor. In other words, in this limit we have a light SM-like Higgs boson with a heavy and mass-degenerates multiplet (H,A,$H^{\pm}$) decoupled from the gauge bosons.

With respect to the sfermions, the Higgs Yukawa couplings matrices $(h_e, h_d, h_u)$ introduce another source of mass terms beside the ones coming from the soft-SUSY breaking terms $(m_Q^2, m_L^2, m_U^2, m_D^2, m_E^2)$ and the trilinear interaction terms $(T_e, T_d, T_u)$ already present in $\mathcal{L}_{\text{soft}-\text{breaking}}$. We notice that the trilin-

ear couplings and $\mu$ introduce a mixing between the superpartners of the right-handed and left-handed SM fermions. The physical degrees of freedom are the eigenstates of the result $6 \times 6$ mass matrices. For our consideration, we will neglect any intergeneration mixing. In this case, the only mixing to be taken into account is the one between the superpartners of the left-handed and right-handed squarks. Under this assumption, we can decompose the trilinear Higgs-squark interactions in a production of two flavor-diagonal matrices, $T_q = h_q A_q$, with $q = u, d$. Hence we have that the mass matrices for the third generation squarks, in $(\tilde{q}_L, \tilde{q}_R)$, are

$$\mathcal{M}_{\tilde{t}} = \begin{pmatrix} m_Q^2 + m_t^2 + (\frac{1}{2} - \frac{2}{3}\sin^2\theta_W) m_Z^2 \cos 2\beta & m_t(A_t - \mu \cot\beta) \\ m_t(A_t - \mu\cot\beta) & m_U^2 + m_t^2 + \frac{2}{3}\sin^2\theta_W m_Z^2 \cos 2\beta \end{pmatrix} \tag{100}$$

and

$$\mathcal{M}_{\tilde{b}} = \begin{pmatrix} m_Q^2 + m_b^2 - (\frac{1}{2} - \frac{1}{3}\sin^2\theta_W) m_Z^2 \cos 2\beta & m_b(A_b - \mu \tan\beta) \\ m_b(A_b - \mu\tan\beta) & m_D^2 + m_t^2 - \frac{1}{3}\sin^2\theta_W m_Z^2 \cos 2\beta \end{pmatrix} \tag{101}$$

where the soft-SUSY breaking masses $m_Q$, $m_U$, $m_D$, $A_t$ and $A_b$ are the entries $(3,3)$ in the corresponding and now diagonal (in flavor space) matrices, while $\theta_W$ is the Weinberg angle. The rotation angles that diagonalize the two matrices are $\theta_{\tilde{t}}$ and $\theta_{\tilde{b}}$ respectively for the stop and sbottom matrices. The eigenstates are denoted with $(\tilde{t}_1, \tilde{t}_2)$ and $(\tilde{b}_1, \tilde{b}_2)$. The mixing term (i.e. the off-diagonal entry in the mass matrix) is related to the mixing angle with the following relation

$$\sin 2\theta_t = \frac{2 m_t X_t}{m_{\tilde{t}_1}^2 - m_{\tilde{t}_2}^2}, \qquad \sin 2\theta_b = \frac{2 m_b X_b}{m_{\tilde{b}_1}^2 - m_{\tilde{b}_2}^2} \tag{102}$$

where we have defined $X_t = A_t - \mu \cot\beta$ and $X_b = A_b - \mu\tan\beta$.

Finally, the two Higgs superpartners, the higgsinos, mix with the superpartners of the $SU(2)_L \times U(1)_Y$ gauge bosons. With respect to the charges higgsinos and winos, the latter defined as $\tilde{w}^{\pm} = (w^1 \mp i\tilde{w}^2)$, we have

$$\mathcal{M}_{\text{charginos}} = -\begin{pmatrix} -i\tilde{w} & \tilde{h}_1^- \end{pmatrix} \begin{pmatrix} M_2 & g\frac{v_2}{\sqrt{2}} \\ g\frac{v_1}{\sqrt{2}} & \mu \end{pmatrix} \begin{pmatrix} -i\tilde{w}^+ \\ \tilde{h}_2^+ \end{pmatrix} + \text{h.c.}\,. \tag{103}$$

where we have been using a two-component formalism for the spinors. The matrix $\mathcal{M}_{\text{charginos}}$ is diagonalized by two unitary matrices $U$ and $V$ such that

$$U^* \mathcal{M}_{\text{charginos}} V^\dagger = \begin{pmatrix} m_{\chi_1^\pm} & 0 \\ 0 & m_{\chi_2^\pm} \end{pmatrix}. \tag{104}$$

The two two-component physical chargino states are given by

$$\chi_i^+ = V_{ij} \begin{pmatrix} -i\tilde{w}^+ \\ \tilde{h}_2^+ \end{pmatrix}_j, \quad \chi_i^- = U_{ij} \begin{pmatrix} -i\tilde{w}^- \\ \tilde{h}_1^- \end{pmatrix}_j, \tag{105}$$

with $m_{\chi_i^+} \leqslant m_{\chi_i^-}$. If we take all the entries in the chargino mass matrix as real, we have that then also

$U$ and $V$ are real matrices. However the eigenvalues of chargino mass matrices should then be allowed to take on negative signs.

The neutral gauginos, $\tilde{b}$ and $\tilde{w}^0$, mix with the neutral higgsinos $\tilde{h}_1^0$ and $\tilde{h}_2^0$. The mass matrices, in the two-component spinor formalism, can be written as

$$\mathcal{M}_{\text{neutralinos}} = -\frac{1}{2}\left(-i\tilde{b} \;\; -i\tilde{w}^0 \;\; \tilde{h}_1^0 \;\; \tilde{h}_2^0\right)\begin{pmatrix} M_1 & 0 & -g'\frac{v_1}{2} & g'\frac{v_2}{2} \\ 0 & M_2 & g\frac{v_1}{2} & -g\frac{v_2}{2} \\ -g'\frac{v_1}{2} & g\frac{v_1}{2} & 0 & -\mu \\ g'\frac{v_2}{2} & -g\frac{v_2}{2} & -\mu & 0 \end{pmatrix}\begin{pmatrix} -i\tilde{b} \\ -i\tilde{w}^0 \\ \tilde{h}_1^0 \\ \tilde{h}_2^0 \end{pmatrix}. \quad (106)$$

The neutralino mass matrix is diagonalized by a single unitary matrix $N$. We have then that the physical eigenstates are given by

$$\chi_i^0 = N_{ij}\begin{pmatrix} -i\tilde{b} \\ -i\tilde{w}^0 \\ \tilde{h}_1^0 \\ \tilde{h}_2^0 \end{pmatrix}. \quad (107)$$

As in the case of charginos, if we assume that all the entries in the neutralino mass matrix are real and we allow the eigenvalues to pick up negative signs, we have that also the diagonalization matrix $N$ is itself real.

The gluino, being a singlet under $SU(2)_L \times U(1)_Y$ and not mixing with any other fermion, has a tree-level mass that coincides with the Soft-SUSY breaking mass, $m_{\tilde{g}} = M_3$.

# 3 HIGGS PRODUCTION PROCESSES

The main production processes at hadron colliders are: gluon fusion, where the Higgs is produced by coupling to gluons through a loop of colored particles (figure 24a); vector boson fusion, where the Higgs is produced in the fusion of two weak bosons (figure 24b); Higgs-bremsstrahlung where the Higgs is emitted from a weak boson produced in a Drell-Yan process (figure 24c); quark-associated production, where the Higgs boson is produced in association with two quarks in the final state (figure 24d). The relative importance of these processes in the SM can be seen from figure 25. In the next few sections, we focus only on the two Higgs production processes that we have studied during our work, the gluon fusion and bottom associated production processes. While the former is important both in the SM and its extension, due to the very large gluon luminosity at the LHC, the latter assumes an important – and possibly dominant – role only in beyond SM models where the bottom Yukawa coupling is enhanced. This is the case of the MSSM, for which we indeed provide a thorough analysis.

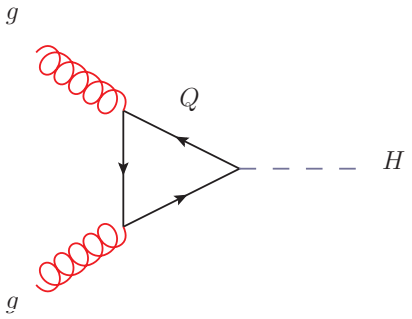


**(a)** Gluon fusion

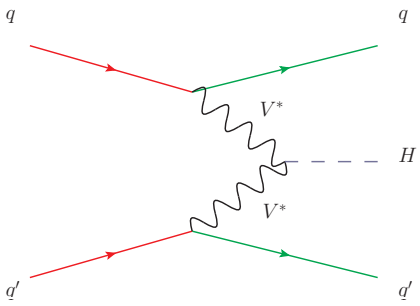


**(b)** Vector boson fusion

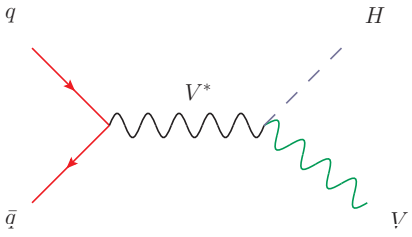


**(c)** Higgs-strahlung

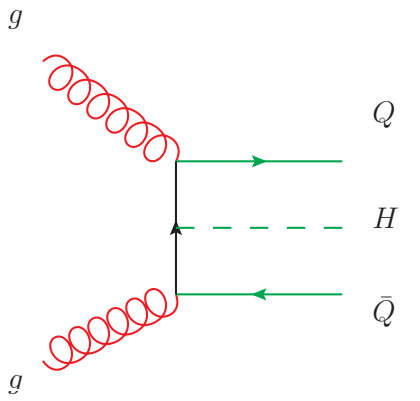


**(d)** Quark associated production

**Figure 24:** Main production channels at hadronic colliders

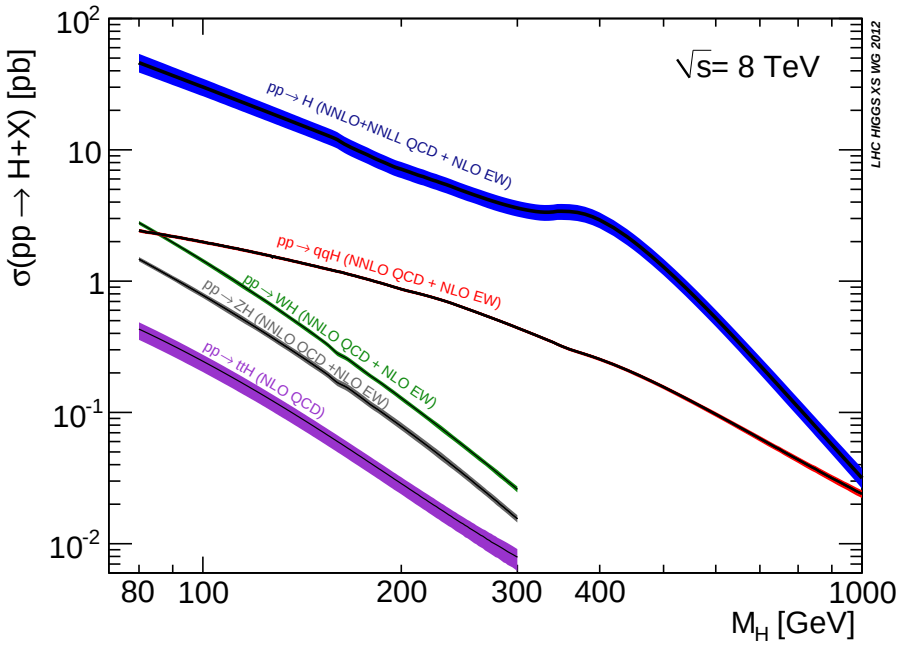


**Figure 25:** Total cross section for the four main Higgs production processes at the LHC, $\sqrt{s} = 8$ TeV in the SM.

## 3.1 Gluon fusion

### 3.1.1 Standard model

In the SM, the main production mode of the Higgs boson at hadron colliders is the gluon fusion subprocess. Here the coupling of the Higgs boson to the gluons is mediated by a loop of colored particles. Since in the SM the coupling of a particle to the Higgs boson is proportional to its mass, the largest contribution comes from a top quark loop. The gluon fusion cross section is very well approximated by a heavy quark effective field theory (HQEFT), where the mass of the top quark is taken to infinity. The latter is then integrated out from the Lagrangian, leaving an effective operator which couples the Higgs boson to two, three and four gluons, as have seen in section 2.1.1. The coupling of the Higgs boson to gluons is then proportional to the Fermi constant and the strong coupling, but is independent of all the Yukawa couplings. In this approach, corrections up to the next-to-next-to-leading order (NNLO) QCD are available [7, 46]. Recently estimations of the next-to-next-to-next-to-leading order (N3LO) QCD contributions have appeared in the literature [47]. The calculation using the complete SM Lagrangian, accounting then for finite mass effects from the top and for the bottom contribution, was done up to NLO-QCD [48]. The inclusion of the complete contribution from the top, bottom and charm quark gives a suppression of $\mathcal{O}(-5\%)$, for a light Higgs of mass around $m_H = 125$ GeV. Moreover finite top-mass effects at NNLO-QCD have been estimated and found to be of the order $\mathcal{O}(1\%)$ [27, 49–51]. Quark mass effects, as we will see, impart also a non-trivial change in the shape of the transverse momentum distribution of the Higgs boson. The presence of various sources of theoretical uncertainty (uncomputed higher order corrections, PDF and $\alpha_s$ uncertainties) affects the prediction for the total cross section in a larger way than mass effects, making their appreciation quite challenging. Available are also soft-gluon

resummation effects [52]; the first-order electroweak (EW) contributions [53–57] and estimates of the mixed QCD-EW contributions [58].

*The cross section at NLO in the SM*

We now briefly recall the explicit structure of the cross section. This allows us to introduce the theoretical elements that are used in the computational tools used in the study. Moreover, we will point out where exactly the differences between the HQEFT and the full calculation appear.

The hadronic cross section for an Higgs of mass $m_H$ at hadronic center-of-mass energy of $\sqrt{s}$ in gluon fusion can be written as

$$\begin{aligned}\sigma(h_1 + h_2 \to H + X) &= \sum_{a,b} \int_0^1 dx_1 dx_2 \; f_{a,h_1}(x_1, \mu_F^2)\, f_{b,h_2}(x_2, \mu_F^2) \times \\ &\quad \times \int_0^1 dz\, \delta\left(z - \frac{\tau_H}{x_1 x_2}\right) \hat{\sigma}_{ab}(z)\,, \end{aligned} \tag{108}$$

where $\tau_H = m_h^2/s$, $\mu_F$ is the factorization scale, $f_{a,h_i}(x, \mu_F^2)$, the parton density of the colliding hadron $h_i$ for the parton of type $a$, ($a = g, q, \bar{q}$) and $\hat{\sigma}_{ab}$ the cross section for the hard partonic subprocess $ab \to H + X$ at the partonic center-of-mass energy $\hat{s} = x_1 x_2 s = m_h^2/z$. The latter can be written as :

$$\hat{\sigma}_{ab}(z) = \sigma^{(0)}\, z\, G_{ab}(z)\,, \tag{109}$$

where

$$\sigma^{(0)} = \frac{G_\mu \alpha_s^2(\mu_R^2)}{128\sqrt{2}\pi} \left| \sum_{i=t,b} \frac{\mathcal{G}_{1/2}^{(1l)}}{2} \right|^2 \tag{110}$$

is the Born-level contribution. The sum is defined over the quarks that run in the triangle loop. The explicit form of LO the matrix element amplitude is

$$\mathcal{G}_{1/2}^{(1l)} = -4y_{1/2}\left[2 - \left(1 - 4y_{1/2}\right) H(0, 0, x_{1/2})\right]\,, \tag{111}$$

where we have defined

$$y \equiv \frac{m_q^2}{m_h^2}, \qquad x \equiv \frac{\sqrt{1-4y} - 1}{\sqrt{1-4y} + 1} \tag{112}$$

The amplitude in eq. (111) is defined in terms Harmonic Polylogarithms (HPLs). HPLs are a class of special functions which can be used to express amplitudes in a form which is particularly suited for numerical evaluation by computer programs. Indeed they are used in our implementation of the gluon fusion process in the POWHEG-BOX framework. Following the standard notation, we have that $H(0, 0, z)$ labels a HPL of weight 2 that results to be[1]

$$H(0, 0, z) = \frac{1}{2}\log^2(z)\,. \tag{113}$$

1 All the analytic continuations are obtained with the replacement $-m_h^2 \to -m_h^2 - i\epsilon$

In the heavy quark mass limit, where $m_q \to \infty$, $\mathcal{G}_{1/2}^{(1l)}$ tends to $-4/3$.
Up to NLO terms, we can write

$$G_{ab}(z) = G_{ab}^{(0)}(z) + \frac{\alpha_s(\mu_R^2)}{\pi} G_{ab}^{(1)}(z)\,, \tag{114}$$

with

$$G_{ab}^{(0)}(z) = \delta(1-z)\,\delta_{ag}\,\delta_{bg}\,, \tag{115}$$

$$G_{gg}^{(1)}(z) = \delta(1-z)\left[C_A\,\frac{\pi^2}{3} + \beta_0 \ln\left(\frac{\mu_R^2}{\mu_F^2}\right) + \mathcal{G}^{(2l)}\right] + P_{gg}(z)\ln\left(\frac{\hat{s}}{\mu_F^2}\right) + C_A\,\frac{4}{z}\,(1-z+z^2)^2\,\mathcal{D}_1(z) + C_A\,\mathcal{R}_{gg}\,, \tag{116}$$

$$G_{q\bar{q}}^{(1)}(z) = \mathcal{R}_{q\bar{q}}\,, \tag{117}$$

$$G_{qg}^{(1)}(z) = P_{gq}(z)\left[\ln(1-z) + \frac{1}{2}\ln\left(\frac{\hat{s}}{\mu_F^2}\right)\right] + \mathcal{R}_{qg}\,. \tag{118}$$

At NLO we have the following contributions

- The $gg$ channel (Eq. (116)) involves virtual and real corrections. The former, regularized by the infrared singular part of the cross section $gg \to Hg$, are displayed in the first row of Eq. (116) where $\beta_0 = (11\,C_A - 2\,n_f)/6$, with $n_f$ the number of active quark flavors, is the first coefficient in the expansion of the $\beta$-function for the strong coupling $\alpha_s$. The function $\mathcal{G}^{(2l)}$ containing the mass-dependent contribution of the two-loop virtual corrections, can be cast in the following form:

$$\mathcal{G}^{(2l)} = 2\,\mathrm{Re}\left(\frac{\mathcal{G}_{1/2}^{(2l)}}{\mathcal{G}_{1/2}^{(1l)}}\right) \tag{119}$$

  where $\mathcal{G}_{1/2}^{(2l)}$ contains the two-loop contributions. Explicit analytic expressions for $\mathcal{G}_{1/2}^{(2l)}$ given in terms of HPLs can be found in ref. [51]. In the case of single heavy quark $\mathcal{G}_{1/2}^{(2l)}$ becomes independent of the renormalized mass chosen and goes to $-3/2\,C_F + 5/2\,C_A = 11/2$, that can be also obtained via an effective theory calculation [48]. The second row of Eq. (116) contains the non-singular contribution from the real gluon emission in the gluon fusion process where

$$\mathcal{D}_i(z) = \left[\frac{\ln^i(1-z)}{1-z}\right]_+ \tag{120}$$

  are the plus distributions and

$$P_{gg}(z) = 2\,C_A\,\left[\mathcal{D}_0(z) + \frac{1}{z} - 2 + z(1-z)\right] \tag{121}$$

is the LO Altarelli-Parisi splitting function. The function $\mathcal{R}_{gg}$ can be written as

$$\mathcal{R}_{gg} = \frac{1}{z(1-z)} \int_0^1 \frac{dv}{v(1-v)} \left\{ \frac{8\,z^4 \left|\mathcal{A}_{gg}(\hat{s},\hat{t},\hat{u})\right|^2}{\left|\mathcal{G}_{1/2}^{(1l)}/2\right|^2} - (1-z+z^2)^2 \right\}, \tag{122}$$

where $\hat{t} = -\hat{s}(1-z)(1-v)$, $\hat{u} = -\hat{s}(1-z)v$. The explicit expression for $|\mathcal{A}_{gg}(s,t,u)|^2$, which represents the unsubtracted real emission matrix element, can be found in [51]. In the $m_q \to \infty$ limit we have $\mathcal{R}_{gg} \to -11(1-z)^3/(6z)$.

- The $q\bar{q} \to Hg$ annihilation channel, Eq. (117), can be written as

$$\mathcal{R}_{q\bar{q}} = \frac{128}{27} \frac{z\,(1-z)\,\left|\mathcal{A}_{q\bar{q}}(\hat{s},\hat{t},\hat{u})\right|^2}{\left|\mathcal{G}_{1/2}^{(1l)}/2\right|^2}, \tag{123}$$

with the expression for $\mathcal{A}_{q\bar{q}}(s,t,u)$ again found in [51]. In the limit of heavy quark we have $\mathcal{R}_{q\bar{q}} \to 32(1-z)^3/(27z)$.

- Finally we consider the quark-gluon scattering channel, $qg \to qH$. In Eq. (118) $P_{gq}$ is the LO Altarelli-Parisi splitting function

$$P_{gq}(z) = C_F\,\frac{1+(1-z)^2}{z}, \tag{124}$$

while the function $\mathcal{R}_{qg}$ can be written as

$$\begin{aligned}\mathcal{R}_{qg} \;=\; & C_F \int_0^1 \frac{dv}{(1-v)} \left\{ \frac{1+(1-z)^2v^2}{[1-(1-z)v]^2} \frac{2\,z\left|\mathcal{A}_{qg}(\hat{s},\hat{t},\hat{u})\right|^2}{\left|\mathcal{G}_{1/2}^{(1l)}/2\right|^2} - \frac{1+(1-z)^2}{2z} \right\} \\ & + \frac{1}{2} C_F z, \end{aligned} \tag{125}$$

where

$$\mathcal{A}_{qg}(\hat{s},\hat{t},\hat{u}) = \mathcal{A}_{qq}(\hat{t},\hat{s},\hat{u}). \tag{126}$$

In the HQEFT limit we have that $\mathcal{R}_{qg} \to 2\,z/3 - (1-z)^2/z$.

*The cross section at NNLO in the HQEFT*

The cross section at NNLO is known only in the HQEFT, only the top contribution is therefore known. At this order, the coefficient function has the form

$$G_{ab}(z) = G_{ab}^{(0)}(z) + \frac{\alpha_s(\mu_R^2)}{\pi} G_{ab}^{(1)}(z) + \left(\frac{\alpha_s(\mu_R^2)}{\pi}\right)^2 G_{ab}^{(2)}(z). \tag{127}$$

The contributions at this order are

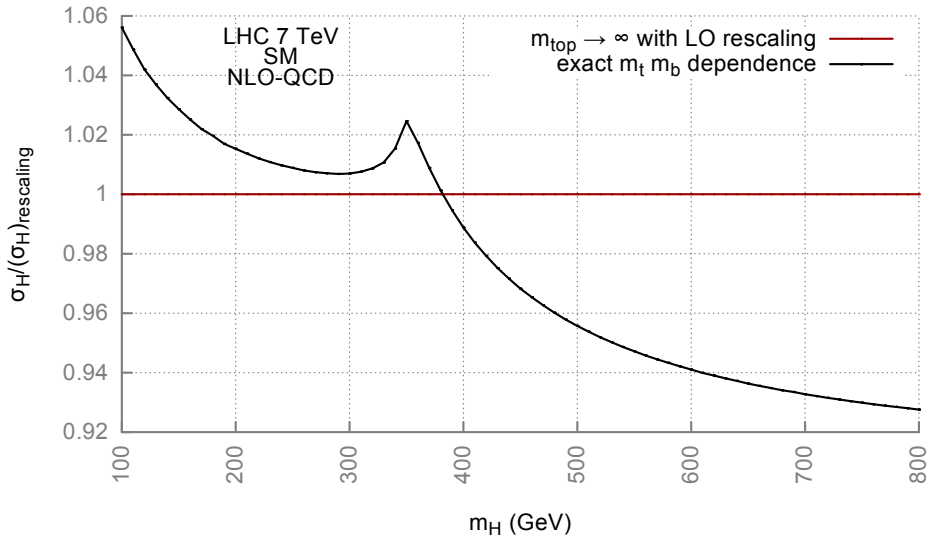


**Figure 26:** Relative difference between the gluon fusion total cross section in the SM (black) and the one in the HQEFT with LO rescaling (red).

- $G^{(2)}_{gg}(z)$ contains the two loop virtual diagrams for the subprocess $gg \to H$; the one loop real emission diagram for subprocess $gg \to Hg$; the tree level double real emission diagrams for $gg \to Hgg$ and $gg \to Hq\bar{q}$.
- $G^{(2)}_{qg}(z)$ contains the one loop correction to the process $gq \to Hq$; the tree level double real emission diagrams for the subprocess $gq \to Hgq$.
- $G^{(2)}_{q\bar{q}}(z)$ contains the one loop correction to the process $q\bar{q} \to Hg$; the tree level double real emission diagrams for $q\bar{q} \to Hgg$ and $q\bar{q} \to Hq\bar{q}$.
- The new channel $G^{(2)}_{qq'}(z)$ appears at this order. Its contribution comes from the tree level diagrams for double parton emission $qq' \to Hqq'$.

Complete expressions for these contributions can be found in the literature, see ref. [7, 46].

*Range of validity of the HQEFT*

As we have seen in subsection 2.1.1, in the SM it is possible to define an effective field theory (HQEFT) where the top quark degree of freedom is integrated out of the Lagrangian and the gluons couple directly to the Higgs field through an effective operator. In this approximation, as we have seen in the section above, the computation and the expressions for the gluon fusion cross section simplify significantly. It is known that the total cross section computed in the HQEFT and rescaled by the factor $k = LO(m_t, m_b)/LO(m_t \to \infty)$ gives a good approximation of the complete result. In figure 26 we show the quality of the numerical agreement at NLO between the result in the HQEFT rescaled by the factor $k$ (red line) with respect to the SM one, with both the top and bottom contributions included (black line). We observe that the HQEFT approximation is remarkably good, since in a mass range from

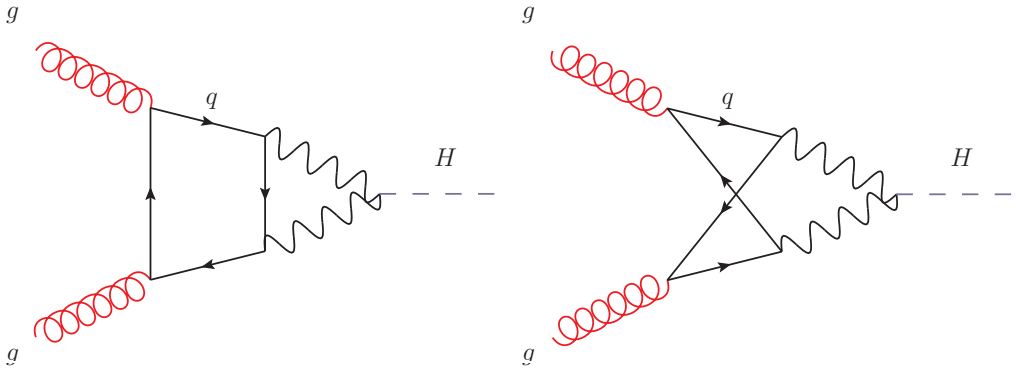


**Figure 27:** Example of two topologies contributing to the EW corrections at two loop order

100 to 800 the NLO top and bottom effects give a deviation of at most +4% for $m_h = 100$ GeV and about −7% for $m_H = 800$ GeV.

*Electro-Weak corrections*

In the SM the dominant EW corrections to the gluon fusion production cross-section come from light fermion contributions. These are given by two-loop diagrams which consist of a quark loop which couples to the Higgs particle through electroweak gauge bosons. In this way, light colored fermions can contribute to the process, avoiding their direct Higgs coupling suppression due to their low masses. The contribution from electroweak corrections that we include is obtained by: summing over the diagrams over the first two generations of quarks; adding the bottom quark contribution by the including the diagrams with the Z boson only, which is by itself finite and gauge invariant. The $\delta_{ew}$ correction factor is given by:

$$\delta_{ew} = \frac{2\alpha}{|\mathcal{G}_{1/2}^{(1l)}|^2}\left[\mathrm{Re}(\mathcal{G}_{1/2}^{(1l)})\mathrm{Re}(\mathcal{G}_{lf}^{2l}) + \mathrm{Im}(\mathcal{G}_{1/2}^{(1l)})\mathrm{Im}(\mathcal{G}_{lf}^{2l})\right] \tag{128}$$

where

$$\mathcal{G}_{lf}^{2l} = \frac{(m_W - i\Gamma_W/2)^2}{4\pi s^2 m_H^2}\left[\frac{2}{c^4}\left(\frac{5}{4} - \frac{7}{3}s^2 + \frac{22}{9}s^4\right)A_1(x_Z) + 4A_1(x_W)\right] \tag{129}$$

. We have also defined:

$$s^2 = \sin^2\theta_W \qquad c^2 = 1 - s^2 \tag{130}$$

$$x_W = -\frac{m_H^2}{(m_W - i\Gamma_W/2)^2} \qquad x_Z = -\frac{m_H^2}{(m_Z - i\Gamma_Z/2)^2} \tag{131}$$

The function $A_1$ is defined in ref. [54]. The top quark contribution can produce significant effects if the Higgs boson being considered is heavy. Indeed, as can been seen from figure 28, the light quarks approximation is valid only within specific mass ranges.

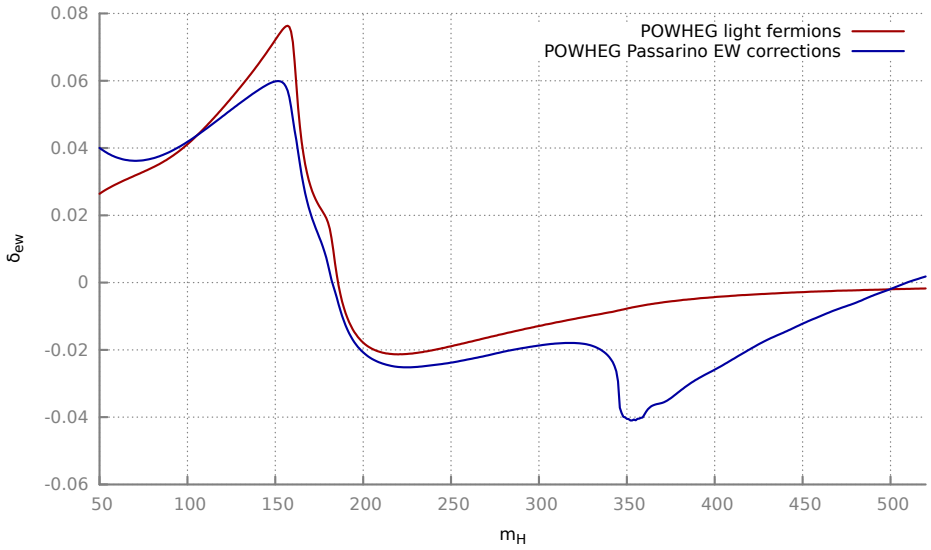


**Figure 28:** The $\delta_{EW}$ contributions across the Higgs mass range 50-520 GeV as calculated by POWHEG in its two possible mode of operation: contributions from light fermions only or full correction with top contribution included [56].

### 3.1.2 2HDM

As we have seen in section 2.2, the difference between the SM and the 2HDM is an enlarged scalar sector which results in a broader physical spectrum of Higgs bosons, consisting in two neutral CP-even scalars, $h$ and $H$, one neutral CP-odd scalar and two charged scalars, $H^{\pm}$. The couplings of the physical states to the matter fields and to the gauge boson are different from the ones in the SM. They can indeed deviate quite enough and lead, for some parameter choices, to gluon fusion cross sections dominated by the bottom quark, at variance with the SM where the cross section is always top dominated. The bottom-quark contributions are subject to large QCD corrections enhanced by powers of $\ln(m_\phi^2/m_b^2)$, where $\phi$ denotes a generic Higgs boson, and so far they have been computed only at the NLO [27, 49–51]. As a result, the uncomputed higher-order QCD corrections to the bottom-quark contributions can become the dominant source of uncertainty in the cross section for the production of heavy 2HDM Higgs bosons in gluon fusion. The cross section for the production of $h$ and $H$ can be simply obtained by introducing an appropriate rescaling factor $\lambda$ in the expressions that were introduced in the previous subsection for the SM, to account for the modified Yukawa coupling. For example, we have at LO

$$\sigma^{(0)} = \frac{G_\mu \alpha_s^2(\mu_R^2)}{128\sqrt{2}\pi}\left|\sum_{i=t,b}\frac{g_{1/2}^{(1l)}}{2}\right|^2 \to \frac{G_\mu \alpha_s^2(\mu_R^2)}{128\sqrt{2}\pi}\left|\sum_{i=t,b}\lambda_i\frac{g_{1/2}^{(1l)}}{2}\right|^2 \tag{132}$$

The rescaling factor $\lambda_i$ are analogously introduced at NLO and NNLO. Their explicit form was given in table 9. For pseudoscalar production, the structure of the cross section is the same, although the explicit form of the matrix elements is different [27].

### 3.1.3 MSSM

As outlined in section 2.3, the Higgs sector of the MSSM consists of two SU(2) doublets, $H_1$ and $H_2$, whose relative contribution to electroweak symmetry breaking is determined by the ratio of vacuum expectation values of their neutral components, $\tan\beta \equiv v_2/v_1$. The spectrum of physical Higgs bosons is richer than in the SM, consisting of two neutral scalars, h and H, one neutral pseudoscalar, A, and two charged scalars, $H^{\pm}$. The couplings of the MSSM Higgs bosons to matter fermions differ from those of the SM Higgs, and they can be considerably enhanced or suppressed depending on $\tan\beta$. For the neutral Higgs bosons, one of the most important production process is still gluon fusion. However, the coupling of the Higgs boson to the gluon is mediated by loops involving not only the top and bottom quarks but also from loops their superpartners, the stop and sbottom squarks.

If the third-generation squarks have masses around one TeV or even larger, their contributions to the gluon-fusion process are suppressed, and a sufficiently accurate determination of the cross section can be achieved by rescaling the SM results for the top- and bottom-quark contributions by appropriate Higgs-quark effective couplings, exactly as was done in the 2HDM case. If, on the other hand, some of the squarks have masses of the order of a few hundred GeV – a scenario not yet excluded by the direct searches at the LHC – a precise calculation of the contributions to the gluon-fusion cross section from diagrams involving squarks becomes mandatory. The NLO-QCD contributions to scalar production arising from diagrams with colored scalars and gluons were first computed in the vanishing-Higgs-mass limit (VHML) in ref. [59], and the full Higgs-mass dependence was included in later calculations [50, 51, 60]. For what concerns pseudoscalar production, the NLO-QCD contributions arising from diagrams with quarks and gluons are known [27, 49–51] while diagrams involving only squarks and gluons do not contribute to the gluon-fusion process due to the structure of the pseudoscalar couplings to squarks. In contrast, a full calculation of the contributions to either scalar or pseudoscalar production arising from two-loop diagrams with quarks, squarks and gluinos – which can involve up to five different particle masses – is still missing. Calculations based on a combination of analytic and numerical methods were presented in refs. [61, 62], but neither explicit analytic formulae nor public computer codes implementing the results of those calculations have been made available so far.

Approximate results for the quark-squark-gluino contributions can however be obtained assuming the presence of some hierarchy between the Higgs mass and the masses of the particles running in the loops. If the Higgs boson is lighter than all the particles in the loops, it is possible to expand the result in powers of the Higgs mass, with the first term in the expansion corresponding to the VHML. This limit was adopted in refs. [63–65] for the calculation of the top-stop-gluino contributions to scalar production and in refs. [66, 67] for the analogous calculation of pseudoscalar production. Refs. [65, 67] also discussed the reliability of the VHML by considering the next term in the expansion in the Higgs mass.

While an expansion in the Higgs mass is a viable approximation in the computation of the top-stop-gluino contributions to the production of the lightest scalar h, it might not be applicable to the production of the heaviest scalar H and of the pseudoscalar A, if their mass is comparable to the mass of the top quark. Moreover, an expansion in the Higgs mass is certainly useless in the calculation of the bottom-sbottom-gluino contributions, due to the presence of a light bottom quark. All of these limitations can, however, be overcome with an expansion in inverse powers of the superparticle masses. Since it does not assume any hierarchy between the Higgs mass and the mass of the quark in the loop, such an expansion is applicable to both top-stop-gluino and bottom-sbottom-gluino contributions, as long as the squarks

and the gluino are heavier than the considered Higgs boson and the top quark. Results for scalar production based on an expansion in the superparticle masses were presented in refs. [68–70], and analogous results for pseudoscalar production were presented in ref. [67].

In a significant part of the MSSM parameter space, the couplings of the heavier neutral Higgs bosons H and A to bottom quarks are enhanced by $\tan\beta$ with respect to the corresponding coupling of the SM Higgs, while their couplings to top quarks are suppressed by $\tan\beta$. When that is the case, the bottom-quark contributions to the gluon-fusion process – which for a SM-like Higgs with mass around 125.5 GeV amount to roughly 7% of the cross section – can dominate over the top-quark contributions. As in the 2HDM case, the fact that these contributions are known only up to NLO can become one of the dominant source of uncertainty in the computation of the cross section.

*The structure of the cross section at NLO*

Using the same formalism that we have used in the SM case, we can write the structure of the cross section for scalar and pseudoscalar Higgs production in the MSSM. The hadronic cross section for an Higgs $\phi = h, H, A$ of mass $m_\phi$ at hadronic center-of-mass energy of $\sqrt{s}$ in gluon fusion can be written as

$$\begin{aligned}\sigma(h_1 + h_2 \to \phi + X) \;=\; & \sum_{a,b} \int_0^1 dx_1 dx_2 \; f_{a,h_1}(x_1, \mu_F^2)\, f_{b,h_2}(x_2, \mu_F^2) \times \\ & \times \int_0^1 dz\, \delta\left(z - \frac{\tau_\phi}{x_1 x_2}\right) \hat{\sigma}_{ab}(z)\,, \end{aligned} \tag{133}$$

where $\tau_\phi = m_\phi^2/s$, $\mu_F$ is the factorization scale, $f_{a,h_i}(x, \mu_F^2)$, the parton density of the colliding hadron $h_i$ for the parton of type $a$, ($a = g, q, \bar{q}$) and $\hat{\sigma}_{ab}$ the cross section for the hard partonic subprocess $ab \to H + X$ at the partonic center-of-mass energy $\hat{s} = x_1 x_2 s = m_\phi^2/z$. The latter can be written as :

$$\hat{\sigma}_{ab}(z) = \sigma^{(0)}\, z\, G_{ab}(z)\,, \tag{134}$$

where now we have

$$\sigma^{(0)} = \frac{G_\mu \alpha_s^2(\mu_R^2)}{128\sqrt{2}\pi} \left| \sum_{i=t,b} \lambda_i \frac{\mathcal{G}_{1/2}^{(1l)}}{2} + \sum_{i=\tilde{t},\tilde{b}} \tilde{\lambda}_i \frac{\mathcal{G}_0^{(1l)}}{2} \right|^2 \tag{135}$$

as the Born-level contribution. In the case of CP-even scalar production, i.e. $\phi = h, H$, we also have, besides the sum over the quarks that run in the triangle loop with the rescaled coupling $\lambda_i$, the contribution from the squarks, whose coupling is parametrized by $\tilde{\lambda}_i$ and whose leading order matrix element is given by

$$\mathcal{G}_0^{(1l)} = 4 y_0 \left[1 + 2\, y_0\, H(0, 0, x_0)\right] \tag{136}$$

We have defined analogously to the quark case the two variables

$$y \equiv \frac{m_{\tilde{q}}^2}{m_h^2}, \qquad x \equiv \frac{\sqrt{1 - 4y} - 1}{\sqrt{1 - 4y} + 1} \tag{137}$$

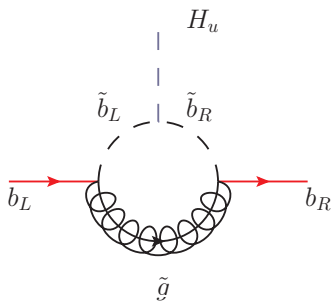


**Figure 29:** Example of tan β enhanced Feynman diagram that can be resummed in an effective Higgs-bottom-bottom coupling.

and we recall that

$$H(0,0,z) = \frac{1}{2}\log^2(z)\,. \tag{138}$$

In the case of pseudoscalar $\phi = A$ production, $\tilde{\lambda}_i = 0$, since there are no LO diagrams with squarks running in the loop. Though the global structure of the NLO contribution is the same as the one that enters the equivalent SM contribution, SUSY-QCD corrections show up in several terms

- $\mathcal{G}^{(21)}$ contains not only the two loop corrections to diagrams with quarks and gluons, but also the two loop diagrams with squarks and gluons and the ones with squarks and gluino. The computation of the latter is extremely difficult due to high number of scales present in the diagrams and it is now available only in approximated form, as was discussed above.

- The real terms $\mathcal{R}_{gg}$,$\mathcal{R}_{qg}$,$\mathcal{R}_{q\bar{q}}$ also include the contribution from one loop diagrams with squarks and the emission of one additional parton besides the SM ones.

*The structure of the cross section beyond NLO-QCD*

In order to improve the accuracy of the MSSM prediction for the gluon-fusion cross section, and to allow for a meaningful comparison with the SM prediction, several contributions beyond the NLO in QCD should be included. The NNLO-QCD contributions to scalar production arising from diagrams with top quarks and the subset of EW contributions arising from diagrams with light quarks can be obtained from the corresponding SM results with an appropriate rescaling of the Higgs couplings to quarks and to gauge bosons. The NNLO-QCD top-quark contributions to pseudoscalar production have also been computed [71]. Approximate results beyond the NLO in QCD also exist for the contributions of diagrams involving superparticles. A first estimate of the NNLO-QCD contributions of diagrams involving stop squarks was presented in ref. [72], and an approximate calculation of those contributions, assuming the VHML and specific hierarchies among the superparticle masses, was recently presented in refs. [73, 74]. Furthermore, a subset of potentially large tan β-enhanced contributions from diagrams involving sbottom-gluino or stop-chargino loops can be resummed in the LO cross section by means of an

effective Higgs-bottom coupling [75–77]. Indeed this amounts to replacing the MSSM bottom Yukawa coupling $\lambda_b^i$ $i = h, H, A$ with

$$\lambda'^{h}_{b} = \frac{\lambda_b^h}{1+\Delta_b}\left(1 - \Delta_b \frac{\cot\alpha}{\tan\beta}\right), \tag{139}$$

$$\lambda'^{H}_{b} = \frac{\lambda_b^H}{1+\Delta_b}\left(1 + \Delta_b \frac{\tan\alpha}{\tan\beta}\right), \tag{140}$$

$$\lambda'^{A}_{b} = \frac{\lambda_b^A}{1+\Delta_b}\left(1 - \Delta_b \frac{1}{\tan^2\beta}\right) \tag{141}$$

where $\Delta_b$ contains the resummation of higher order sbottom contributions coming from diagrams as the one in figure 29.

## 3.2 Bottom quark associated production

The computation of Higgs boson production in association with bottom quarks can be performed in two ways. The first one is by using the so-called the four-flavor scheme (4FS), where one does not consider the bottom quarks as partons in the proton, the process is initiated by two gluons or by a light quark-antiquark pair, and the cross section is known at the NLO in QCD [78]. This is the same scheme that one uses when computing top-quark associated production. However, while in the top associated case the top mass and the Higgs boson mass can be considered of the same magnitude, in the case of the bottom quark we have that the ratio $m_b/m_H$ can be quite sizable and therefore more attention should be reserved to collinear logarithms of the form $\ln(m_b/m_H)$. A way to address this issue is to use the five-flavor scheme (5FS), where the bottom quarks are in the initial partonic state. The cross section in this case is known up to the NNLO in QCD [29, 79]. The use of bottom-quark parton density functions (PDFs) in the 5FS indeed allows to resum terms enhanced by $\ln(m_\phi^2/m_b^2)$ that would arise in the 4FS when one or both bottom quarks are collinear to the incoming partons. For our studies we limited ourselves to the 5FS computation.

### 3.2.1 Standard Model

In the SM the cross section is extremely small and the process is usually not even considered feasible for an experimental search. However we briefly recall here the basic structure of the cross section up to NNLO in the 5FS, since it will be the same also in the 2HDM and in the MSSM. The bottom is always assumed to be massless, aside from the Yukawa coupling. The hadronic cross section for an Higgs of mass $m_H$ at hadronic center-of-mass energy of $\sqrt{s}$ can be written as

$$\begin{aligned}\sigma(h_1 + h_2 \to (b\bar{b})H + X) \;=\; & \sum_{a,b}\int_0^1 dx_1 dx_2 \; f_{a,h_1}(x_1,\mu_F^2)\, f_{b,h_2}(x_2,\mu_F^2) \times \\ & \times \int_0^1 dz\, \delta\left(z - \frac{\tau_H}{x_1 x_2}\right) \hat{\sigma}_{ij}(z)\,,\end{aligned} \tag{142}$$

where $\tau_H = m_H^2/s$, $\mu_F$ is the factorization scale, $f_{a,h_i}(x, \mu_F^2)$, the parton density of the colliding hadron $h_i$ for the parton of type $a$, $(a = g, q, \bar{q})$ and $\hat{\sigma}_{ij}$ the cross section for the hard partonic subprocess $ij \to H + X$ at the partonic center-of-mass energy $\hat{s} = x_1 x_2 s = m_\phi^2/z$. The partonic cross section can then be written as

$$\hat{\sigma}_{ij}(z) = \sigma_0 \Delta_{ij}(z), \tag{143}$$

where the normalization factor is given by

$$\sigma_0 = \frac{\pi}{12} \frac{1}{m_H^2}. \tag{144}$$

We can then expand $\Delta(z)$ as a series in $\alpha_s$. Up to NNLO we have

$$\Delta_{ij}(z) = \Delta_{ij}^{(0)}(z) + \frac{\alpha_s}{\pi} \Delta_{ij}^{(1)}(z) + \left(\frac{\alpha_s}{\pi}\right)^2 \Delta_{ij}^{(2)}(z). \tag{145}$$

In details we have:

- The $b\bar{b}$ subprocess.
  $\Delta_{b\bar{b}}^{(0)}(z)$ contains the tree level, purely electroweak, bottom quark annihilation process $b\bar{b} \to H$.
  $\Delta_{b\bar{b}}^{(1)}(z)$ contains contributions coming from the one loop corrections to the tree level diagrams and the contributions from the real emission process $b\bar{b} \to Hg$. At NNLO, to compute $\Delta_{ij}^{(2)}(z)$, we have also to include tree level diagrams for the $b\bar{b} \to Hgg$, $b\bar{b} \to Hq\bar{q}$ and $b\bar{b} \to Hb\bar{b}$ subprocess.

- The $bg$ subprocess.
  The subprocess appears at NLO, contributing at three level to the $\Delta_{bg}^{(1)}(z)$ correction to the coefficient function. At NNLO, $\Delta_{bg}^{(2)}(z)$ includes the one loop corrections to the $bg \to Hb$ subprocess and the tree level emission diagram $bg \to Hgb$.

- At NNLO we have also the tree level contributions to $\Delta_{ij}^{(2)}(z)$ from the following subprocess:$bb \to Hbb$; $bq \to Hbq$; $gg \to Hgg$; $q\bar{q} \to Hb\bar{b}$.

Complete expressions for the coefficient function can be found in [29].

### 3.2.2 2HDM

For large values of the tan β parameter, in the type II 2HDM, bottom associated production can be sizable and even be bigger than gluon fusion. The global structure of the cross section is the same as in the SM, with the only difference being in the Yukawa coupling of the Higgs to the bottom quark. It can be demonstrated that the cross section for the pseudoscalar Higgs boson is the same as the one for its CP-even counterparts. Therefore the cross section can be computed starting from the SM one

and then rescaling it with the appropriate factor to match the 2HDM Yukawa coupling, by making the substitution

$$\sigma_0 = \frac{\pi}{12}\frac{1}{m_H^2} \to \frac{\pi}{12}\frac{\lambda_b^2}{m_\phi^2} \tag{146}$$

where $\lambda_b$ is the rescaling factor for the bottom Yukawa.

### 3.2.3 MSSM

As in the 2HDM, when the couplings to bottom quarks are sufficiently enhanced, the production of MSSM Higgs bosons through bottom-quark annihilation dominates over gluon fusion. As in the case of gluon fusion, the tan β-enhanced contributions from diagrams involving superpartners can be resummed in the LO result by means of an effective Higgs-bottom coupling. The remaining one-loop contributions from superpartners have been found to be small [80]. We can then obtain the cross section by making, as in the 2HDM case, the following substitution

$$\sigma_0 = \frac{\pi}{12}\frac{1}{m_H^2} \to \frac{\pi}{12}\frac{\lambda_b^2}{m_\phi^2} \tag{147}$$

where $\lambda_b$ is the rescaling factor for the bottom Yukawa. The latter can also be made to include the resummed tan β-enhanced contributions, using the same formulas reported at the end of subsection. 3.1.3.

# 4 TOTAL INCLUSIVE CROSS SECTION FOR HIGGS PRODUCTION IN THE MSSM

In this section we discuss the production of scalar and pseudoscalar Higgs bosons via gluon fusion and bottom-quark annihilation in the MSSM. Relying on the NNLO-QCD calculation implemented in the public code SusHi, we provide precise predictions for the Higgs-production cross section in six benchmark scenarios compatible with the LHC searches. We also provide a detailed discussion of the sources of theoretical uncertainty in our calculation. We examine the dependence of the cross section on the renormalization and factorization scales, on the precise definition of the Higgs-bottom coupling and on the choice of PDFs, as well as the uncertainties associated to our incomplete knowledge of the SUSY contributions through NNLO. In particular, a potentially large uncertainty originates from uncomputed higher-order QCD corrections to the bottom-quark contributions to gluon fusion.

## 4.1 Higgs boson production in viable MSSM scenarios

Since no superparticles have been found during the first run of the LHC, Higgs boson studies are as important as direct-search efforts to pin down the exclusion regions of the MSSM parameter space. In our study we focused on the total inclusive cross section, carefully specializing our computations to scenarios that are not yet excluded by other constraints. Precise predictions of the cross section allow to test the compatibility of the discovered neutral scalar resonance with the corresponding MSSM one and also to restrict the MSSM parameter space by using the experimental limits on the production of the other Higgses of the model.

### 4.1.1 The tools

A considerable effort has been devoted over the years to making the existing calculations of Higgs production available to the physics community in the form of public computer codes. In the case of the SM, NNLO-QCD predictions of the total cross section for gluon fusion, including various refinements such as EW corrections and finite top-mass effects, are provided, e.g., by `HIGLU` [28], `ggh@nnlo` [81], `HNNLO` [82] and `iHixs` [83]. The code `bbh@nnlo` [84] provides instead a NNLO-QCD prediction of the total cross section for Higgs production in bottom-quark annihilation in the 5FS. For what concerns the production of MSSM Higgs bosons via gluon fusion, `HIGLU` implements the results of ref. [60] for the NLO-QCD contributions arising from diagrams with squarks and gluons, as well as the results of refs. [76, 77] for the resummation of the tan β-enhanced squark contributions in an effective Higgs-bottom coupling. More recently, two codes that compute the cross section for Higgs production including approximate results for the contributions of diagrams with quarks, squarks and gluinos have become available. As described in ref. [85], the NLO-QCD [51, 65, 67, 68, 70] and EW [54, 57] contributions to Higgs-boson production via gluon fusion in the SM and in the MSSM have been implemented in a

module for the so-called POWHEG-BOX [86], a framework for consistently matching NLO-QCD computations of matrix elements with parton-shower Monte Carlo generators, avoiding double counting and preserving the NLO accuracy of the calculation. The code SusHi [87] computes the cross section for Higgs-boson production in both gluon fusion and bottom-quark annihilation, in the SM, in the 2HDM and in the MSSM. In the case of gluon fusion, SusHi includes the exact results of ref. [49] for the NLO-QCD contributions of two-loop diagrams with top and bottom quarks, and the approximate results of refs. [64, 67, 70] and refs. [67, 68] for the NLO-QCD contributions of two-loop diagrams with stop and sbottom squarks, respectively. The NLO-QCD contributions of one-loop diagrams with emission of an additional parton are taken from ref. [69]. The NNLO-QCD contributions from diagrams with top quarks are included via a call to ggh@nnlo, and the corresponding contributions from diagrams with stop squarks are estimated following ref. [72]. Finally, the known SM results for the EW contributions [54, 56, 57] are adapted to the MSSM by rescaling the Higgs couplings to top quarks and to gauge bosons. In the case of bottom-quark annihilation, SusHi obtains from bbh@nnlo the NNLO-QCD result valid in the SM, then rescales it by an effective Higgs-bottom coupling that accounts for the tan $\beta$-enhanced squark contributions [75, 76].

### 4.1.2 The benchmark scenarios

The discovery of a neutral scalar with mass around 125.5 GeV puts the studies of the Higgs sector of the MSSM in an entirely new perspective. In order to remain viable, a point in the MSSM parameter space must now not only pass all the experimental bounds on superparticle masses, but also lead to the prediction of a scalar with mass, production cross section and decay rates compatible with those measured at the LHC. In particular, the relatively large mass of the SM-like scalar discovered at the LHC implies either stop masses of the order of 3 TeV – which would result in a negligible stop contribution to the production cross section – or a large value of the left-right mixing term in the stop mass matrix (see, e.g., refs. [88, 89]). In the latter case, at least one of the stops could have a mass as low as a few hundred GeV, and induce a significant contribution to the gluon-fusion cross section. In view of these considerations, we will focus on the set of MSSM scenarios compatible with the LHC findings that has recently been proposed in ref. [90].

The SM parameters entering our calculations include the Z-boson mass $m_Z = 91.1876$ GeV, the $W$-boson mass $m_W = 80.398$ GeV, the Fermi constant $G_F = 1.16637 \times 10^{-5}$ and the strong coupling constant $\alpha_s(m_Z) = 0.119$ [91]. For the masses of the top and bottom quarks we take the pole mass $m_t = 173.2$ GeV [92] and the SM running mass (in the $\overline{\text{MS}}$ scheme) $m_b(m_b) = 4.16$ GeV [93].

At the tree level, the MSSM neutral scalar masses $m_h$ and $m_H$ and the scalar mixing angle $\alpha$ can be computed in terms of $m_Z$, tan $\beta$ and the pseudoscalar mass $m_A$ only. However, the radiative corrections to the tree-level predictions can be substantial, and they bring along a dependence on all of the other MSSM parameters. To compute the masses and the couplings of Higgs bosons and superparticles in a given point of the MSSM parameter space we use the public code FeynHiggs [94], which includes the full one-loop [95] and dominant two-loop [96–100] corrections to the neutral Higgs masses. Since the theoretical uncertainty of the Higgs-mass calculation in FeynHiggs has been estimated to be of the order of 3 GeV [101],[1] we consider as phenomenologically acceptable the points in the MSSM parameter

1 To reduce this uncertainty, it would be necessary to include in the mass calculation the remaining two-loop effects [102] and at least the dominant three-loop effects [103, 104]. Note also that there is an additional uncertainty of approximately 1 GeV

| Scenario | $M_S$ [GeV] | $X_t$ [GeV] | $\mu$ [GeV] | $M_2$ [GeV] |
|---|---|---|---|---|
| $m_h^{max}$ | 1000 | 2000 | 200 | 200 |
| $m_h^{mod+}$ | 1000 | 1500 | 200 | 200 |
| $m_h^{mod-}$ | 1000 | −1900 | 200 | 200 |
| *light stop* | 500 | 1000 | 400 | 400 |
| *light stau* | 1000 | 1600 | 500 | 200 |
| *tau-phobic* | 1500 | 3675 | 2000 | 200 |

**Table 10:** Choices of MSSM parameters for the benchmark scenarios proposed in ref. [90].

space where FeynHiggs predicts the existence of a scalar with mass between 122.5 GeV and 128.5 GeV and with approximately SM-like couplings to gauge bosons.

In addition to $\tan\beta$ and $m_A$, the MSSM parameters most relevant to the prediction of the masses and production cross sections of the Higgs bosons are: the soft SUSY-breaking masses for the stop and sbottom squarks, which for simplicity we set all equal to a common mass parameter $M_S$; the soft SUSY-breaking gluino mass $m_{\tilde{g}}$; the soft SUSY-breaking Higgs-squark-squark couplings $A_t$ and $A_b$; the superpotential Higgs-mass parameter $\mu$. In our convention for the sign of the latter, the left-right mixing terms in the stop and sbottom mass matrices are $X_t \equiv A_t - \mu\cot\beta$ and $X_b \equiv A_b - \mu\tan\beta$, respectively. It should be noted that in our analysis the soft SUSY-breaking squark masses and trilinear couplings are expressed in an "on-shell" (OS) renormalization scheme, as described in refs. [96, 97] for the stop sector and in refs. [68, 98, 99] for the sbottom sector. Since the two-loop calculation of the Higgs masses implemented in FeynHiggs and the NLO-QCD calculation of the production cross section implemented in SusHi employ the same OS scheme, the input values of the soft SUSY-breaking parameters can be passed seamlessly from the Higgs-mass calculation to the cross-section calculation. Concerning the parameters $\tan\beta$, $\mu$ and $m_A$, their definition is relevant to the Higgs-mass calculation only. In particular, $\tan\beta$ and $\mu$ are expressed in the $\overline{\text{DR}}$ scheme, at a renormalization scale that FeynHiggs takes by default equal to $m_t$, while $m_A$ is identified with the pole mass of the pseudoscalar. Finally, the choice of renormalization scheme for $m_{\tilde{g}}$ amounts to a higher-order effect, because the gluino mass enters only the two-loop part of the corrections.

A detailed description of the six benchmark scenarios adopted in our analysis can be found in the paper where they were originally proposed, ref. [90]. All of the scenarios are characterized by relatively large values of the ratio $X_t/M_S$, ensuring that the mass of the SM-like Higgs falls within the required range without the need for extremely heavy stops. In addition, the masses of the gluino and of the first-two-generation squarks are set to 1.5 TeV, large enough to evade the current ATLAS [105, 106] and CMS [107–109] bounds. The prescriptions of ref. [90] for the parameters $M_S$, $X_t$, $\mu$ and for the soft SUSY-breaking wino mass $M_2$ are listed in table 10. We vary the parameters $\tan\beta$ and $m_A$ within the ranges

$$2 \leqslant \tan\beta \leqslant 50\,, \qquad 90\,\text{GeV} \leqslant m_A \leqslant 1\,\text{TeV}\,. \tag{148}$$

In all scenarios the Higgs-sbottom-sbottom coupling $A_b$ is set equal to $A_t$, the left-right mixing of the first-two-generation squarks is neglected and the bino mass $M_1$ is obtained from the GUT relation $M_1/M_2 = (5/3)(m_Z^2/m_W^2 - 1)$, with the exception of the fourth scenario where we set $M_1 =$

stemming from the uncertainty of the SM input parameters, especially $m_t$.

340 GeV.[2] Finally, the choices of ref. [90] for the soft SUSY-breaking parameters in the slepton sector have a very small impact on the predictions for the Higgs masses and production cross sections, therefore we do not report them here.

The fourth scenario in table 10, denoted as *light stop*, deserves a special discussion. In this scenario the two stop masses are 324 GeV and 672 GeV; the sbottom masses depend on $\tan\beta$, but the lightest sbottom is always heavier than 450 GeV, while the heaviest one is always lighter than 550 GeV. With such relatively low masses, loops involving squarks can give a sizable contribution to the cross section for Higgs production, but we have to worry about the exclusion bounds from the LHC. Indeed, the ATLAS and CMS collaborations have presented preliminary results for the searches of direct stop- and sbottom-pair production, based on the full 8-TeV data sample, considering the decay chains

$$\tilde{t}_1 \to t\,\chi_1^0 \to b\,W\,\chi_1^0 \;\; [110, 111]\,, \qquad \tilde{t}_1 \to b\,\chi_1^\pm \to b\,W\,\chi_1^0 \;\; [110, 111]\,, \qquad \tilde{t}_1 \to c\,\chi_1^0 \;\; [112, 113]\,,$$

$$\tilde{b}_1 \to b\,\chi_1^0 \;\; [107, 114]\,, \qquad\qquad \tilde{b}_1 \to t\,\chi_1^\pm \to t\,W\,\chi_1^0 \;\; [105, 108]\,.$$

The allowed values of the stop and sbottom masses depend on the chargino and neutralino masses, as well as on the branching ratios for the different squark decays. With the choice of parameters in table 10, $M_2 = \mu = 400$ GeV, together with $M_1 = 340$ GeV, the masses for the lightest chargino and neutralino have a mild dependence on $\tan\beta$, but they stay within the ranges $m_{\chi_1^\pm} \approx 341 - 346$ GeV and $m_{\chi_1^0} \approx 316 - 320$ GeV for $\tan\beta > 10$. In this case the lightest stop decays almost entirely through the loop-induced, flavor-violating channel $\tilde{t}_1 \to c\,\chi_1^0$. This channel has been investigated by ATLAS [112] and CMS [113], but the resulting bounds only reach to values of $m_{\tilde{t}_1}$ around 250 GeV. For the lightest sbottom, the two-body decays $\tilde{b}_1 \to \tilde{t}_1\,W$ and $\tilde{b}_1 \to b\,\chi_j^0$ (with $j$ up to 3 or 4) are kinematically open. The direct decay of $\tilde{b}_1$ to the lightest neutralino would be constrained by the searches in refs. [107, 114], but i) that channel is never dominant in the considered range of parameters and ii) the experimental bounds only reach to values of $m_{\chi_1^0}$ below 280 GeV. Finally, the heaviest stop and sbottom can decay through a multitude of channels, and their direct decays to $\chi_1^0$ or $\chi_1^\pm$ are significantly suppressed.

### 4.1.3 Cross section for Higgs production

We are now ready to present our precise predictions for the production of MSSM Higgs bosons at the LHC. As mentioned earlier, we rely on the code `SusHi` ,[3] which includes all of the available NLO-QCD contributions to the gluon-fusion process, supplemented with the known SM results for the NNLO-QCD contributions in the heavy-top limit and for the EW contributions (both adapted to the MSSM by appropriately rescaling the Higgs couplings). While the results implemented in `SusHi` for the NNLO-QCD top contributions are strictly valid only for a Higgs mass below the top threshold, $m_\Phi < 2\,m_t$, a comparison with the NLO results suggests that they provide a decent approximation also for larger values of the Higgs mass [115, 116]. The NNLO-QCD contributions from stop loops are estimated following ref. [72], i.e., neglecting the contributions of three-loop diagrams but retaining the NNLO contributions that arise from the product of lower-order terms. We have also checked that, when all of the NNLO-QCD contributions are omitted, the results of `SusHi` for the gluon-fusion cross section agree with

2 The choice $M_1 = 350$ originally proposed in ref. [90] would result in a stop LSP for $\tan\beta \gtrsim 20$.

3 For a detailed description of the cross-section calculation implemented in `SusHi` we refer to the code's manual [87].

those of the calculation implemented in the POWHEG-BOX [85], which includes the same NLO-QCD and EW contributions. For what concerns the bottom-quark annihilation process, SusHi includes the NNLO-QCD results valid in the SM within the 5FS, also rescaled by the effective Higgs-bottom couplings of the MSSM.

In our study, we fix the center-of-mass energy of the proton-proton collisions to 8 TeV. While the numerical value of the total cross section for Higgs production does obviously depend on the collision energy, we have checked that the relative importance of the various contributions to the production processes and their qualitative behavior over the MSSM parameter space do not change substantially if we set the energy to 13 TeV. By default, we use the MSTW2008 set of PDFs [117], and we fix the renormalization and factorization scales entering the gluon-fusion cross section to $\mu_R = \mu_F = m_\phi/2$ [6, 7], where $\phi = \{h, H, A\}$ denotes the considered Higgs boson. For bottom-quark annihilation, the central values of the scales are chosen as $\mu_R = m_\phi$ and $\mu_F = m_\phi/4$ [29, 79, 118]. In the calculation of the gluon-fusion cross section we relate the bottom Yukawa coupling to the pole mass $M_b$, computed at the three-loop level [119] from the input value for the running mass, $m_b(m_b)$. In the case of bottom-quark annihilation, on the other hand, we relate the bottom Yukawa coupling to $m_b(m_\phi)$, in turn obtained from $m_b(m_b)$ via four-loop renormalization-group evolution [120]. In both cases, the $\tan\beta$-enhanced SUSY corrections to the relation between mass and Yukawa coupling of the bottom quark are included following refs. [75, 76]. The theoretical uncertainties associated to the choice of PDFs, to the variation of the renormalization and factorization scales and to the definition of the bottom Yukawa coupling will be discussed in detail in section 4.2.

In figures 30 and 31 we show the total cross section – i.e., the sum of gluon fusion and bottom-quark annihilation – for the production of the scalars (h, H) and of the pseudoscalar (A), respectively, as contour plots in the $m_A - \tan\beta$ plane. For the other MSSM parameters, we adopt the *light-stop* scenario described in section 4.1.2.MSSM and SM Tables for the numerical values of the cross section (and the corresponding uncertainties) in all of the six benchmark scenarios are given in the appendix. In the two plots of figure 30, referring to h (left) and H (right) production, the red lines are contours of equal mass for the corresponding scalar. In this scenario, the prediction for the mass of the lightest scalar reaches a maximum of 123.8 GeV at large $\tan\beta$. The heaviest-scalar mass grows with $m_A$, and we show only the contour corresponding to 126 GeV to avoid clutter (for large $m_A$, the contours are roughly at $m_H \approx m_A$ and independent of $\tan\beta$). The x-axis of the plot for h production ends at $m_A = 300$ GeV because, for larger values, the cross section becomes essentially independent of $m_A$. The x-axis of the plots for H and A ends at $m_A = 500$ GeV because the expansion in the SUSY masses used to approximate the two-loop squark contributions in SusHi becomes unreliable when the Higgs mass approaches the lowest squark-mass threshold, which in the *light-stop* scenario corresponds to $2\, m_{\tilde{t}_1} \approx 650$ GeV. The theoretical uncertainty associated with this approximation will be discussed in section 4.2.4.

The qualitative behavior of the cross sections in figures 30 and 31 can be easily interpreted considering the relations between the scalar and pseudoscalar masses in the MSSM Higgs sector, and how each of the Higgs bosons couples to the top and bottom quarks (the squark contributions are generally subdominant, as will be discussed below). In the so-called decoupling limit, $m_A \gg m_Z$, the lightest scalar h has SM-like couplings to quarks, while its mass is essentially independent of $m_A$ and, for $\tan\beta \gtrsim 10$, depends only weakly on $\tan\beta$. The cross section for h production (left plot in figure 30) varies very little in this region, and differs from the SM result for a Higgs boson of equal mass only because of the squark contributions to the gluon-fusion process. For $m_A \lesssim 130$ GeV, on the other hand, the couplings of h

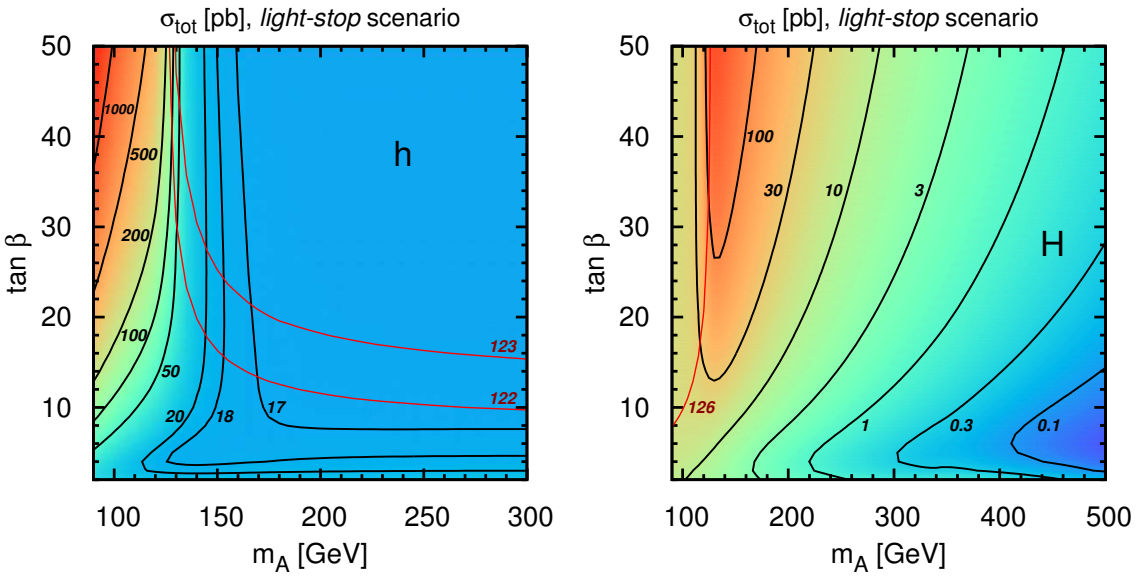


**Figure 30:** Total cross section in pb for the production of h (left) and H (right), as a function of $m_A$ and tan β in the *light-stop* scenario. The solid red lines are contours of equal mass for each scalar.

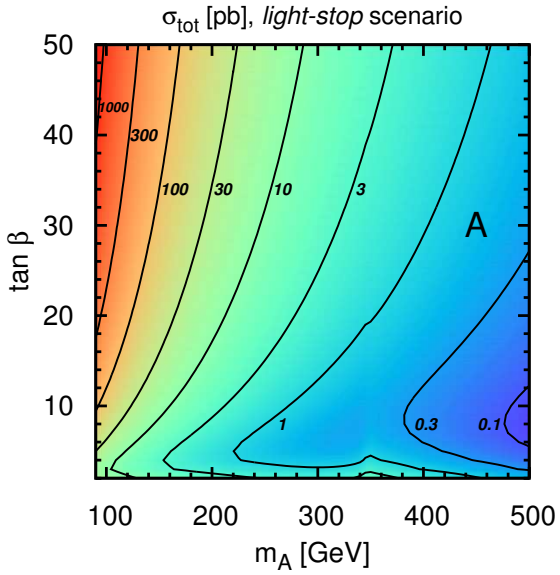


**Figure 31:** Total cross section in pb for the production of the pseudoscalar A.

to top (bottom) quarks are non-standard, being suppressed (enhanced) by $\tan\beta$. In this narrow region the total cross section for h production is dominated by the contributions of the diagrams that involve the Higgs-bottom coupling, and it grows significantly with $\tan\beta$.

The behavior of the cross section for H production in the $m_A$ – $\tan\beta$ plane (right plot in figure 30) is different from – and somewhat complementary to – the one for h production. In the strip where $m_A \lesssim 130$ GeV, the heaviest scalar has a mass around 125 GeV and significant couplings to both top and bottom quarks, and the cross section for its production grows with $\tan\beta$. For larger $m_A$, on the other hand, $m_H$ grows together with $m_A$, and the couplings of H to top (bottom) quarks are suppressed (enhanced) by $\tan\beta$. The total cross section for H production is therefore dominated, already for moderate $\tan\beta$, by the contributions of the diagrams that involve the Higgs-bottom coupling. The latter grow significantly with $\tan\beta$, but decrease with $m_A$, being suppressed by powers of the ratio $m_b^2/m_H^2$. Finally, the pseudoscalar couplings to top (bottom) quarks are suppressed (enhanced) by $\tan\beta$ for all values of $m_A$. Therefore, the behavior of the cross section for A production in the $m_A$ – $\tan\beta$ plane, see figure 31, resembles the behavior of h production when $m_A \lesssim 130$ GeV, and the one of H production for larger $m_A$: in both cases, the cross section grows with $\tan\beta$, but decreases with $m_A$.

To disentangle the effects of the two main production channels for the MSSM Higgs bosons, we show in figures 32 and 33 the ratio between the gluon-fusion cross section and the sum of gluon-fusion and bottom-quark-annihilation cross sections in the *light-stop* scenario, again as contour plots in the $m_A$ – $\tan\beta$ plane. Predictably, the plots reflect the behavior of the coupling of the considered Higgs boson to bottom quarks. The left plot in figure 32 shows that, when $m_A$ is large enough that the couplings of the lightest scalar are SM-like, gluon fusion is by far the dominant process for h production, and the contribution of bottom-quark annihilation amounts only to a few percent. Only in the strip with $m_A \lesssim 130$ GeV and $\tan\beta \gtrsim 8$, where the coupling of h to bottom quarks is sufficiently enhanced by $\tan\beta$, does bottom-quark annihilation become the dominant process. Conversely, bottom-quark annihilation gives the largest contribution to the cross section for H production (right plot in figure 32) when $m_A \gtrsim 130$ GeV and $\tan\beta \gtrsim 6$, while in the case of A production (figure 33) the cross section is dominated by bottom-quark annihilation already for $m_A \gtrsim 100$ GeV, as long as $\tan\beta \gtrsim 5 - 8$.

To assess the relevance of the squark contributions to the gluon-fusion cross section in the *light-stop* scenario, we show in figures 34 and 35 the ratio of the total gluon-fusion cross section over the cross section computed including only the contributions of quarks (with appropriate rescaling of the Higgs-quark couplings). The left plot of figure 34 shows that – in this scenario characterized by relatively light squarks – the interference between the top and stop contributions can reduce the cross section for h production by as much as 20% in the decoupling region with large $m_A$ and $\tan\beta$. Remarkably, in this region the partial NNLO-QCD contributions from stop loops that we include following ref. [72] account by themselves for a 6% suppression of the cross section. The theoretical uncertainty associated to these contributions will be discussed in section 4.2.4. For what concerns H production (right plot of figure 34), the squark contributions reduce the cross section by up to 30% for low values of $m_A$, and the suppression becomes even stronger with increasing pseudoscalar mass. In particular, near the lower-right corner of the plot, where $m_A \gtrsim 420$ GeV and $\tan\beta$ ranges between 6 and 20, the interference between the quark and squark contributions induce a suppression of the cross section by 70 – 80%. In this region the top contribution is suppressed by $\tan\beta$, while the bottom contribution is suppressed by $m_b^2/m_H^2$ and only moderately enhanced by $\tan\beta$, so they both become comparable in size with the stop contribution. The resulting gluon-fusion cross section is rather small, of the order of a few femtobarns.

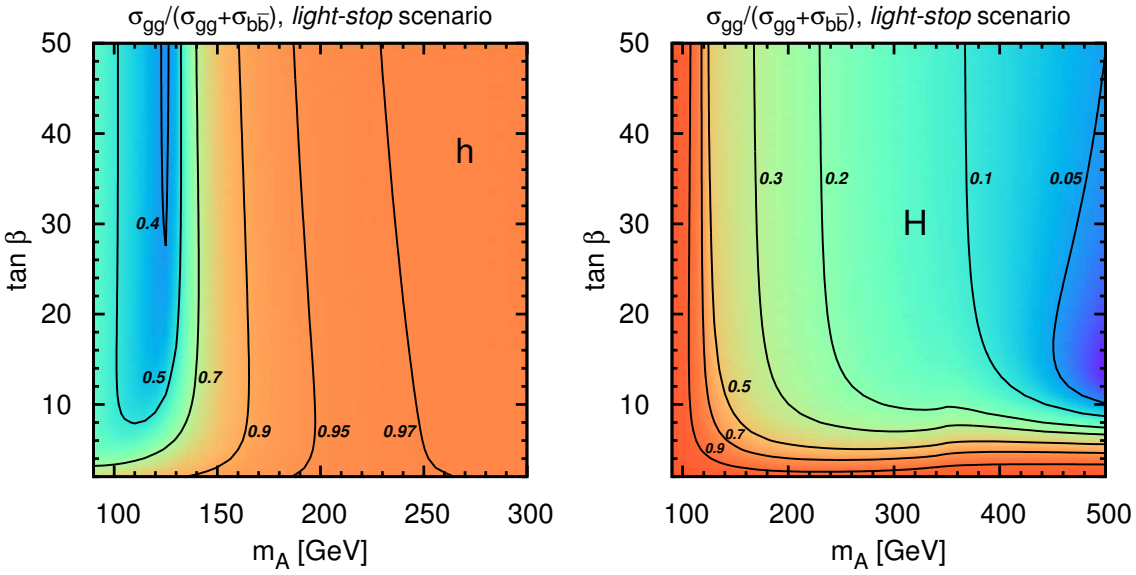


**Figure 32:** Ratio of gluon-fusion cross section over total cross section for the production of h (left) and H (right), as a function of $m_A$ and tan β in the *light-stop* scenario.

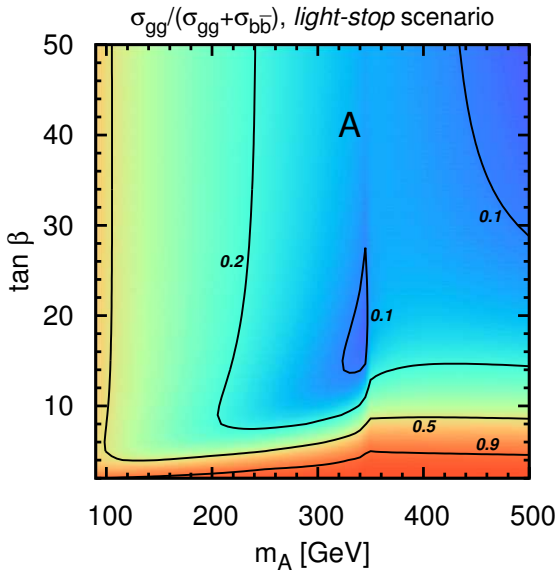


**Figure 33:** Same as figure 32 for the production of the pseudoscalar A.

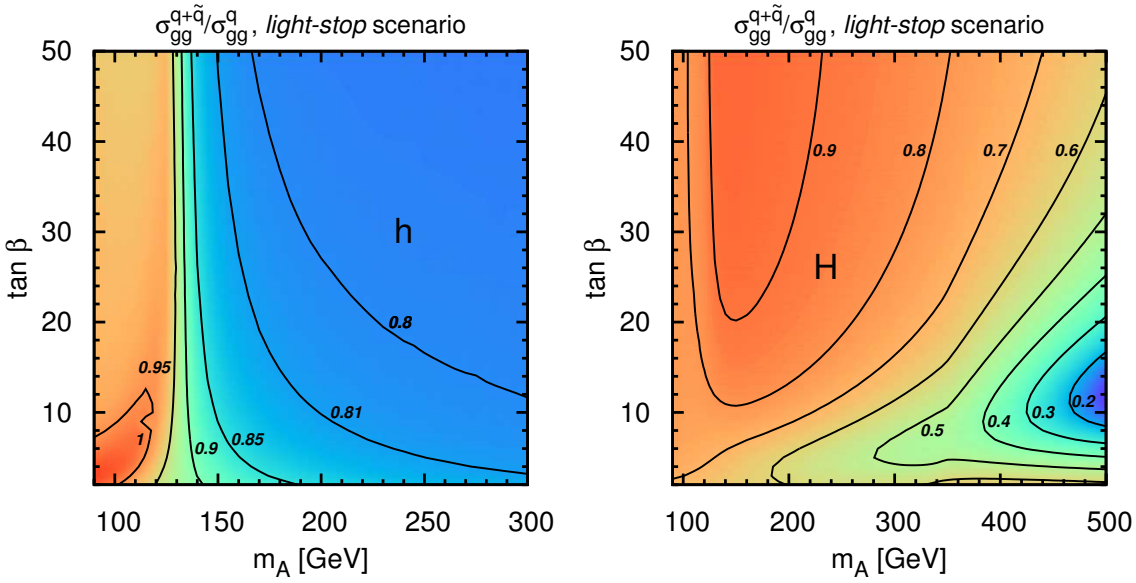


**Figure 34:** Ratio of gluon-fusion cross section for the production of h (left) and H (right) over the corresponding cross section neglecting squark contributions, as a function of $m_A$ and tan β in the *light-stop* scenario.

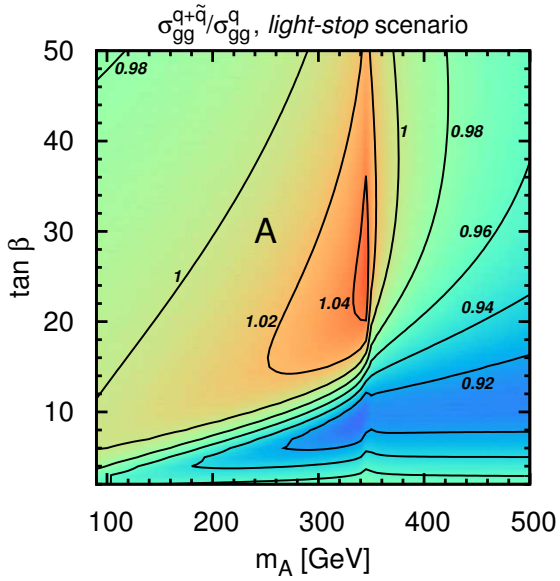


**Figure 35:** Same as figure 34 for the production of the pseudoscalar A.

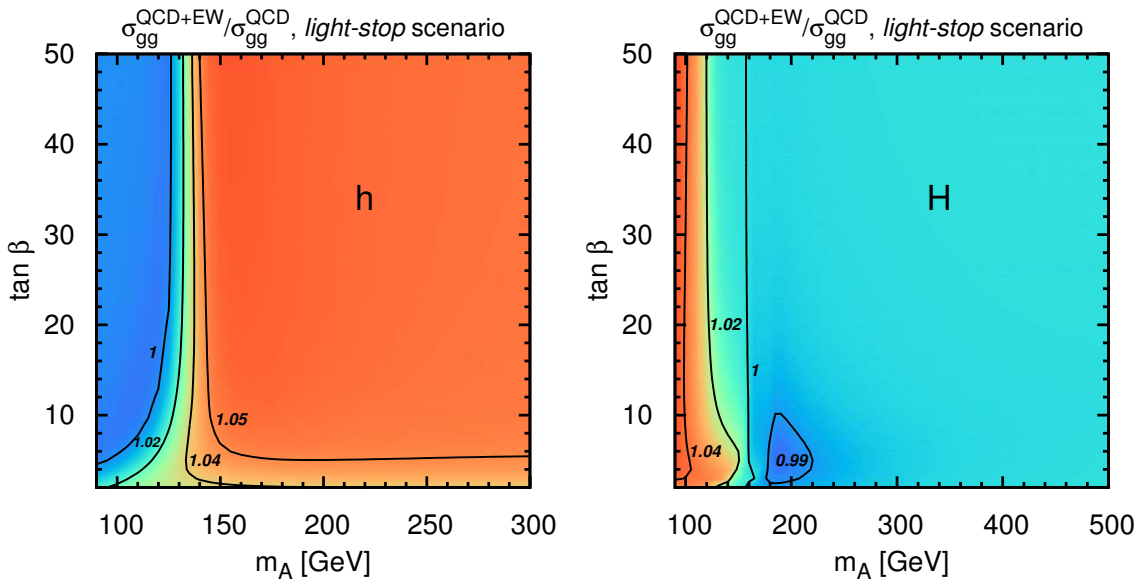


**Figure 36:** Ratio of gluon-fusion cross section for the production of h (left) and H (right) over the corresponding cross section neglecting EW contributions, as a function of $m_A$ and tan β in the *light-stop* scenario.

Finally, figure 35 shows that, in the case of A production, the effect of the squark contributions on the cross section for gluon fusion in the *light-stop* scenario is always less than 10%. This is due to the fact that the pseudoscalar couples only to two different squark-mass eigenstates, while gluons couple only to pairs of the same squarks. Therefore, there is no squark contribution to the gluon-fusion process at the LO, and the whole effect in figure 35 arises from two-loop diagrams.

For a SM Higgs boson sufficiently lighter than the top threshold, the EW corrections to gluon fusion are well approximated [56, 57] by the contributions of two-loop diagrams in which the Higgs couples to EW gauge bosons, which in turn couple to the gluons via a loop of light quarks (including the bottom). In `SusHi` , these contributions are incorporated in the MSSM calculation of the gluon-fusion cross section by rescaling the two-loop EW amplitude given in ref. [57] with the appropriate Higgs-gauge boson couplings.[4] In figure 36 we investigate the impact of the light-quark EW contributions on the production of the scalars h and H, plotting the ratio of the gluon-fusion cross sections computed with and without those contributions, in the $m_A$ – tan β plane for the *light-stop* scenario. The figure shows that the EW corrections tend to increase the cross section, and their impact depends mainly on the strength of the coupling of the considered scalar to gauge bosons. In the case of h production (left plot) the EW corrections become fairly constant, around 6%, in the region of sufficiently large $m_A$ where the lightest scalar has SM-like couplings. Conversely, in the case of H production (right plot) the EW corrections reach a comparable value only in the strip of very low $m_A$, and they quickly drop below 1% as soon as $m_A \gtrsim 150$ GeV. On the other hand, since the pseudoscalar does not couple to two gauge bosons at tree level, there are no EW contributions from light-quark loops to its production.

For what concerns the remaining sources of EW corrections to gluon fusion, those arising from two-loop diagrams involving top quarks are known to be small for a SM-like Higgs with mass around 125

4 In fact, `SusHi` implements two alternative procedures for including the EW contributions in the total cross section for gluon fusion. We follow the one described in eq. (37) of the code's manual [87].

GeV [56], while in the case of H and A they are suppressed in most of the parameter space by the small (or vanishing) Higgs couplings to top quarks and to gauge bosons. On the other hand, the EW corrections involving the bottom Yukawa coupling, which have not yet been computed because they are negligible for the SM Higgs, could become relevant for the production of H and A. In addition, a full computation of the EW corrections should include the contributions of diagrams involving superparticles. The non-decoupling SUSY effects that dominate at large $\tan\beta$ are indeed included in an effective Higgs-bottom coupling, as discussed in section 4.2.2, but the remaining contributions, so far uncomputed, could become relevant if some of the superparticles are relatively light.

Results for the Higgs-production cross section in the other benchmark scenarios listed in table 10 can be found in the appendix. In the four scenarios denoted as $m_h^{\text{max}}$, $m_h^{\text{mod+}}$, $m_h^{\text{mod}-}$ and *light stau*, the couplings of the Higgs bosons to top and bottom quarks and to gauge bosons are rather similar to the ones in the *light-stop* scenario. Thus, the discussion given above for the qualitative behavior in the $m_A - \tan\beta$ plane of the total cross section, of the EW corrections and of the relative importance of gluon fusion and bottom-quark annihilation applies to those four scenarios as well. However, all of the third-generation squarks have masses around 1 TeV, therefore the impact of the SUSY contributions on the gluon-fusion cross section is considerably smaller than in the case of the *light-stop* scenario. The suppression of the cross section for h production in the decoupling limit never goes beyond 6%. For what concerns H production, the effect of the interference between quark and squark contributions becomes significant only for very large $m_A$ and moderate $\tan\beta$, where the gluon-fusion cross section is tiny anyway. The largest effect, a suppression by 30 – 40%, is found in the *light-stau* scenario for $m_A \gtrsim 850$ GeV and $10 \lesssim \tan\beta \lesssim 20$, where the cross section is of the order of a tenth of a femtobarn. The SUSY contributions to A production, already small in the *light-stop* scenario because they only arise at two loops, are further suppressed in the $m_h^{\text{max}}$, $m_h^{\text{mod+}}$, $m_h^{\text{mod}-}$ and *light-stau* scenarios.

In the last scenario in table 10, denoted as *tau-phobic*, the MSSM parameters are arranged in such a way that, for certain values of $m_A$ and $\tan\beta$, the radiative corrections to the $(1,2)$ element of the CP-even Higgs mass matrix suppress significantly the mixing angle $\alpha$, so that the coupling of h to taus – which is proportional to $\sin\alpha$ – is in turn suppressed with respect to its SM value. However, the couplings of the scalars to top and bottom quarks are modified as well, in particular the coupling of h to bottom quarks is suppressed. As a result, in the *tau-phobic* scenario the behavior in the $m_A - \tan\beta$ plane of the various contributions to the Higgs-production cross section differs from the one found in the other scenarios. The total cross section for h production shows some enhancement with $\tan\beta$ even for large values of $m_A$, while for small $m_A$ the total cross section for H production has a milder dependence on $\tan\beta$ than in the other scenarios. Also, the suppression of the h coupling to bottom quarks makes the contribution of bottom-quark annihilation to h production smaller than in the other scenarios. Finally, the *tau-phobic* scenario is characterized by third-generation squark masses around 1.5 TeV, and by a value of the superpotential Higgs-mass parameter, $\mu = 2$ TeV, much larger than in the other scenarios. Since $\mu$ enters the couplings of the Higgs bosons to squarks, the impact of the SUSY contributions on the cross section for scalar production is – despite the heavier squarks – somewhat larger than in the $m_h^{\text{max}}$, $m_h^{\text{mod+}}$, $m_h^{\text{mod}-}$ and *light-stau* scenarios, and in the case of pseudoscalar production it is even larger than in the *light-stop* scenario.

## 4.2 Sources of theoretical uncertainty

Like any other quantity evaluated perturbatively, the cross sections for Higgs production in gluon fusion and bottom-quark annihilation suffer from an intrinsic theoretical uncertainty due to the truncation at finite order in the coupling constants. Typically, the residual dependence on the renormalization and factorization scales is used as an estimate of this uncertainty. In section 4.2.1 we discuss our study of the scale dependence of the cross sections.

In addition, there are sources of uncertainty that are more specific to the Higgs-production processes considered in this study. As we discuss in section 4.2.2, one of the most important sources of uncertainty in the production of Higgs bosons with non-standard couplings to quarks is the dependence of the cross section on the precise definition of the bottom-quark mass and Yukawa coupling. The numerical difference between the pole bottom mass and the running mass computed at a scale of the order of the Higgs mass is more than 40%, and – in a fixed-order calculation of the cross sections – the effect of such a large variation cannot be compensated by the large logarithms that are induced at NLO by counterterm contributions. Furthermore, it is well known that the relation between the bottom mass and the corresponding Yukawa coupling is affected by potentially large, $\tan\beta$-enhanced SUSY corrections that must be properly resummed. The dependence of the cross sections on the details of the resummation procedure constitutes a further source of uncertainty.

In section 4.2.3 we discuss the uncertainties associated to the choice of PDF sets. We also investigate the issue of consistency between the pre-defined value of the bottom mass in the PDFs and the value of the mass used to extract the bottom Yukawa coupling.

Finally, in section 4.2.4 we discuss two sources of uncertainty arising from our incomplete knowledge of the SUSY contributions to gluon fusion. In particular, we assess the validity of the expansion in inverse powers of the SUSY masses used to approximate the contributions of two-loop diagrams involving superparticles. We also estimate the uncertainty associated to the fact that `SusHi` does not include the contributions of three-loop diagrams involving superparticles.

### 4.2.1 Scale dependence of the cross section

In this section we study the dependence of the cross section for Higgs production on the renormalization scale $\mu_R$ at which the relevant couplings in the partonic cross section are expressed, and on the factorization scale $\mu_F$ entering both the PDFs and the partonic cross section. We recall that, although the complete result for the hadronic cross section does not depend on $\mu_R$ and $\mu_F$, its approximation at a given perturbative order retains a dependence on those scales, which is formally one order higher than the accuracy of the calculation. In a given calculation at fixed order, the two scales are arbitrary, and they are typically fixed at some central values $\bar{\mu}_R$ and $\bar{\mu}_F$ characteristic of the hard scattering process. The variation of the scales around their central values provides an estimate of the size of the uncomputed higher-order contributions.

We discuss separately the cases of gluon fusion (section 4.2.1) and of bottom-quark annihilation (section 4.2.1). In the former, $\mu_R$ denotes the scale at which we express the strong gauge coupling entering the partonic cross section already at the LO, while in the latter it denotes the scale at which we express both the bottom Yukawa coupling entering at the LO and the strong gauge coupling entering at the NLO. We postpone to section 4.2.2 a discussion of the dependence of the gluon-fusion cross section on the scale at

which we express the bottom Yukawa coupling.

*Gluon fusion*

The natural hard scale in the production of a Higgs boson $\phi$ is obviously of the order of $m_\phi$. In our study of gluon fusion we take $\bar{\mu}_R = \bar{\mu}_F = m_\phi/2$ as central values for the renormalization and factorization scales, because, with this choice, the cross section shows a reduced sensitivity to scale variations and an improved convergence of the perturbative expansion [7]. Moreover, it has been observed that this choice allows to mimic the effects of soft-gluon resummation in the total cross section [6].

We study the impact of the scale variation around the central choice $(\bar{\mu}_R, \bar{\mu}_F)$ following the LHC-HXSWG prescription [39]: we consider seven combinations of renormalization and factorization scales, defined as the set $C_\mu$ of the pairs $(\mu_R, \mu_F)$ obtainable from the two sets $\mu_R = \{m_\phi/4,\ m_\phi/2,\ m_\phi\}$ and $\mu_F = \{m_\phi/4,\ m_\phi/2,\ m_\phi\}$, with the additional constraint that $1/2 \leqslant \mu_R/\mu_F \leqslant 2$ (i.e., we treat the variations of the ratio $\mu_R/\mu_F$ on the same footing as the variations of the individual scales, discarding the two pairs where the ratio varies by a factor of four around its central value). We then determine the maximal and minimal values of the cross section on the set $C_\mu$,

$$\sigma^- \equiv \min_{(\mu_R,\,\mu_F)\,\in\, C_\mu} \{\sigma(\mu_R, \mu_F)\}\,, \qquad \sigma^+ \equiv \max_{(\mu_R,\,\mu_F)\,\in\, C_\mu} \{\sigma(\mu_R, \mu_F)\}\,, \tag{149}$$

and define the relative scale uncertainty of the cross section as $\Delta_\mu \equiv \Delta^+_\mu - \Delta^-_\mu$, where

$$\Delta^+_\mu \equiv \frac{\sigma^+ - \sigma(\bar{\mu}_R, \bar{\mu}_F)}{\sigma(\bar{\mu}_R, \bar{\mu}_F)}\,, \qquad \Delta^-_\mu \equiv \frac{\sigma^- - \sigma(\bar{\mu}_R, \bar{\mu}_F)}{\sigma(\bar{\mu}_R, \bar{\mu}_F)}\,. \tag{150}$$

In figures 37 and 38 we show the contours of equal $\Delta_\mu$ for scalar and pseudoscalar production in the $m_A$ – $\tan\beta$ plane, fixing the MSSM parameters as in the *light-stop* scenario. The qualitative features of the plots can be understood by considering that the top, bottom, SUSY and EW contributions to the gluon-fusion cross section are known at different orders in the perturbative expansion. In particular, the top contribution is included in `SusHi` with full mass dependence through $\mathcal{O}(\alpha_s^3)$ (i.e., NLO) and in the VHML at $\mathcal{O}(\alpha_s^4)$ (i.e, NNLO). Its residual scale dependence amounts to an $\mathcal{O}(\alpha_s^5)$ effect, with the exception of some mass-dependent effects at $\mathcal{O}(\alpha_s^4)$, which are known to be numerically small [121]. The bottom and sbottom contributions are included at the NLO and they account for an $\mathcal{O}(\alpha_s^4)$ effect. The stop contributions are included through the NNLO, see section 4.2.4, but their effect on scale dependence is also of $\mathcal{O}(\alpha_s^4)$ because we neglect the genuine three-loop terms. Finally, while the EW corrections are computed at $\mathcal{O}(\alpha\alpha_s^2)$, their inclusion as a fully factorized term at the NLO causes their effect on scale variation to be of $\mathcal{O}(\alpha\alpha_s^4)$, numerically very small. As a consequence of the varying accuracy of the different contributions, the scale uncertainty for the production of a given Higgs boson depends on which contribution plays the dominant role in the considered region of the $m_A$ – $\tan\beta$ plane. The uncertainty is lowest, around 10 – 20%, where the top contribution dominates: this is the case for h production (left plot in figure 37) in the decoupling region, where the uncertainty stabilizes to roughly 16% at large $m_A$ (i.e., slightly smaller than the 18% we obtain for the same Higgs mass in the SM); for H production (right plot in figure 37) in the strip with $m_A \lesssim 120$ GeV, as well as when $\tan\beta \lesssim 10$ and $m_A \lesssim 400$ GeV; for A production (figure 38) in the strip with $\tan\beta \lesssim 10$. In contrast, the scale uncertainty exceeds 20% in the regions where the bottom contribution is enhanced or downright dominant: at large $\tan\beta$ for H

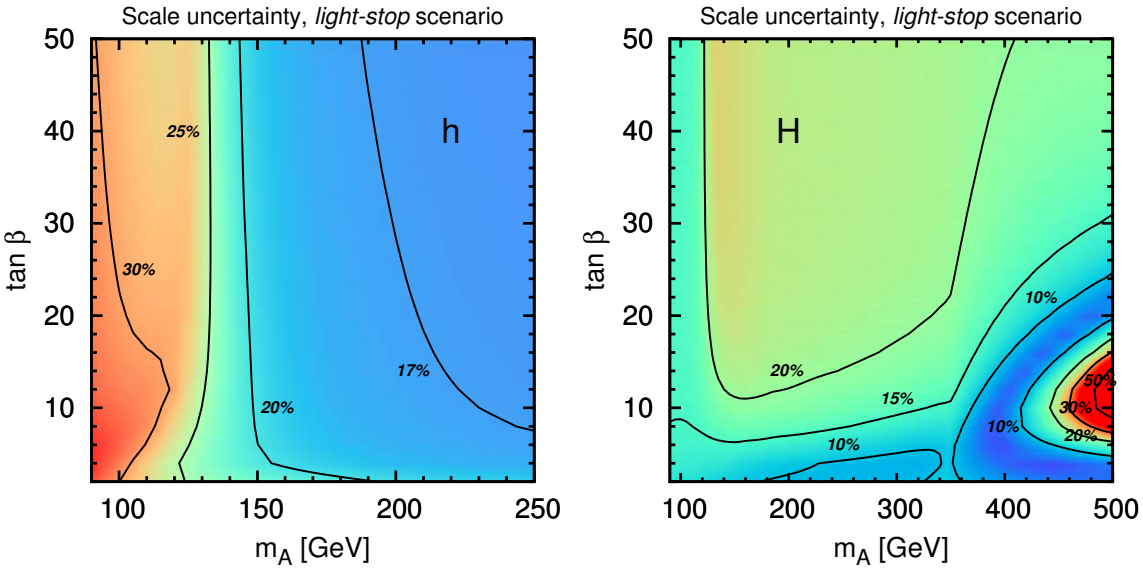


**Figure 37:** Relative scale uncertainty $\Delta_\mu$ (in percent) for h production (left) and H production (right) in gluon fusion.

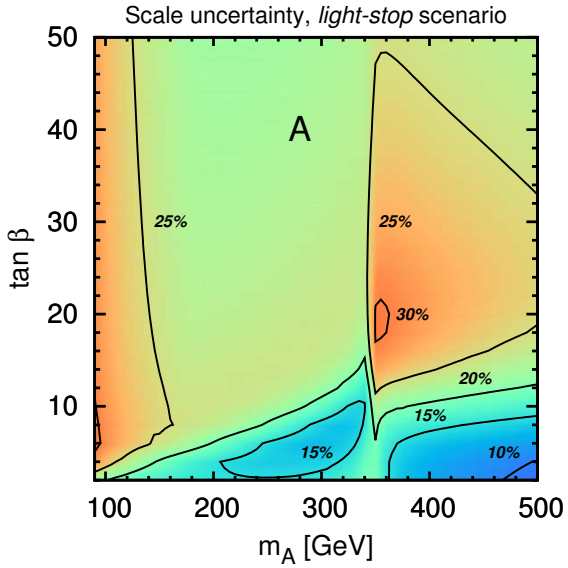


**Figure 38:** Same as figure 37 for the production of the pseudoscalar A.

and A production, and at small $m_A$ for h production.

The plots for H and A production in figures 37 and 38 show additional structures. In the case of H production, the scale uncertainty becomes very large for $8 \lesssim \tan\beta \lesssim 16$ and $m_A \gtrsim 460$ GeV. As appears from figure 34, this region is characterized by a significant cancellation between the top, bottom and stop contributions to the gluon-fusion amplitude, resulting in a very small NLO cross section and an enhanced sensitivity to higher-order effects. In the case of A production, the structure visible for $m_A \approx 350$ GeV is associated to the cusp-like behavior of the top contribution to the gluon-fusion amplitude around the threshold $m_A = 2\, m_t$. Another feature of H and A production, partially overshadowed by the structures described above, is a tendency towards smaller scale uncertainties for larger pseudoscalar (and hence scalar) masses. This is due to the fact that the strong gauge coupling – which controls the size of the higher-order effects that we are estimating – is evaluated at a scale proportional to the mass of the considered Higgs boson, and gets smaller when the scale increases.

The other scenarios were studied following the same procedure, and the results are qualitatively similar. However, for h production, the scale dependence in the decoupling region is similar to, or even bigger than, the one in the SM. For H production, due to the different interplay of quark and squark contributions, the cancellations that in the *light-stop* scenario cause the region of very large uncertainty for $8 \lesssim \tan\beta \lesssim 16$ and $m_A \gtrsim 460$ GeV occur at higher values of $m_A$.

Finally, a study of independent variations of the renormalization and factorization scales shows that, in a large fraction of the parameter space, the former yield a much larger uncertainty than the latter. The factorization-scale uncertainty is smaller in size than the renormalization-scale uncertainty already at the LO, and it is further reduced by the inclusion of higher-order terms.

#### *Bottom-quark annihilation*

In SusHi , the cross section for Higgs production in bottom-quark annihilation is implemented at NNLO-QCD in the 5FS. Our default choice for the central scales is $\bar{\mu}_R = m_\phi$ and $\bar{\mu}_F = m_\phi/4$, following the observation that radiative corrections are particularly small for this value of the factorization scale [29, 79, 118]. To study the uncertainty associated to the variation of the scales, we consider seven combinations corresponding to all possible pairings of $\mu_R = \{m_\phi/2, m_\phi, 2\, m_\phi\}$ and $\mu_F = \{m_\phi/8, m_\phi/4, m_\phi/2\}$, with the additional constraint that $2 \leqslant \mu_R/\mu_F \leqslant 8$ (again, we discard the two pairs with the largest variation of $\mu_R/\mu_F$ around its central value, which in this case is 4 ). We then determine the scale uncertainty $\Delta_\mu$ in analogy to eqs. (149) and (150).

Differently from the case of gluon fusion, the scale uncertainty of bottom-quark annihilation depends very weakly on $\tan\beta$. This is due to the fact that, in eq. (150), the $\tan\beta$-dependence of the cross section via the effective Higgs-bottom coupling cancels out in the ratio, leaving only a mild, indirect dependence – only for scalar production – via the value of the Higgs mass that determines $\mu_R$ and $\mu_F$.

In figures 39 and 40 we show the scale dependence of the cross section for scalar and pseudoscalar production, respectively, as a function of $m_A$ in the *light-stop* scenario with $\tan\beta = 20$. In the upper part of each plot, the solid line denotes the cross section for bottom-quark annihilation computed with the central scale choice $(\bar{\mu}_R, \bar{\mu}_F)$, while the yellow band around the solid line is delimited by the maximal and minimal cross sections $\sigma^+$ and $\sigma^-$, defined in analogy to eq. (149). The lower part of each plot shows the relative variation of the cross section with respect to the central value (i.e., the total width of the yellow band corresponds to $\Delta_\mu$). While the values of the total cross section do of course depend on

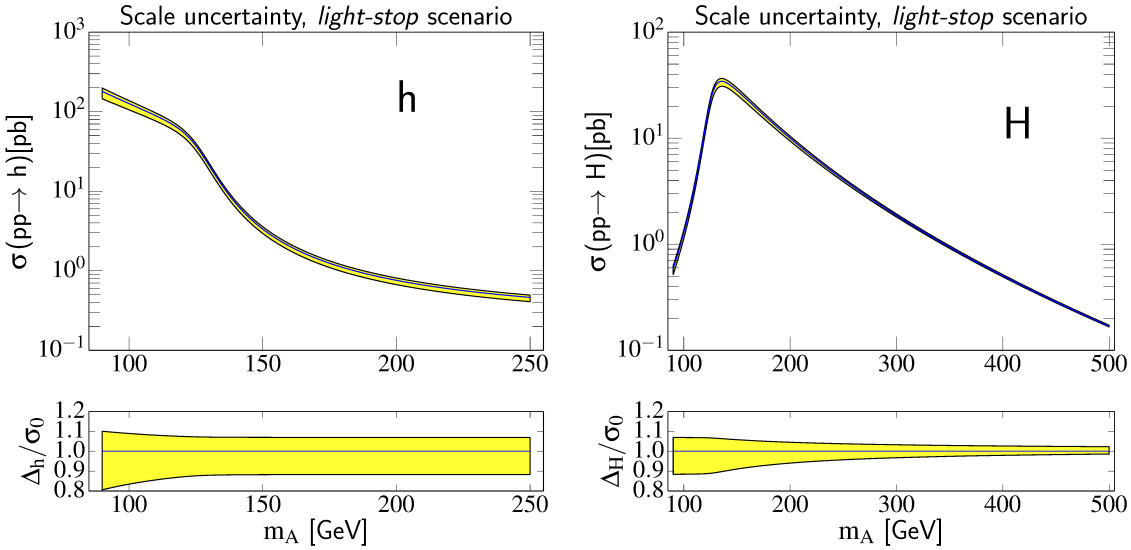


**Figure 39:** Scale uncertainty of the cross section for h production (left) and H production (right) in bottom-quark annihilation, in the *light-stop* scenario with $\tan\beta = 20$.

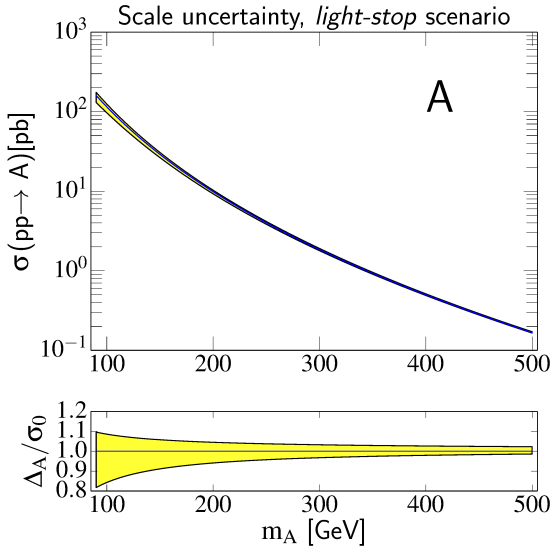


**Figure 40:** Same as figure 39 for the production of the pseudoscalar A.

the chosen benchmark scenario, the relative scale variation is essentially the same in all scenarios, due to the above-mentioned cancellation of the dependence on the effective Higgs-bottom coupling.

The left plot in figure 39 shows that the relative scale uncertainty of the cross section for $h$ production can be as large as 30% for low values of $m_A$, then it stabilizes to roughly 18% in the decoupling region where $m_h$ becomes independent of $m_A$. In contrast, the relative scale uncertainty of the cross section for the production of H (right plot in figure 39) and A (figure 40) decreases as $m_A$ (and hence $m_H$) increases. As already mentioned for the case of gluon fusion, this behavior is due to the fact that the higher-order effects that we are estimating are controlled by the strong gauge coupling, and the latter decreases when the scale at which it is computed, which is proportional to the Higgs mass, increases.

Finally, an independent variation the renormalization and factorization scales shows that, in this case, the dominant uncertainty is given by the dependence on the factorization scale.

### 4.2.2 Definition of the Higgs-bottom coupling

In the production of a SM-like Higgs boson, the contribution of bottom-quark annihilation and the effect of the bottom-quark loops in gluon fusion amount to a few percent of the total cross section. Therefore, in that case the theoretical uncertainty associated to the definition of the Higgs coupling to bottom quarks is negligible compared to other sources of uncertainty. On the other hand, this uncertainty becomes significant in scenarios where the Higgs-bottom coupling is enhanced with respect to its SM counterpart, $Y_b^{SM} = \sqrt{2}\, m_b/v$ (here $v \approx 246$ GeV). In the MSSM the tree-level couplings of the neutral Higgs bosons to bottom quarks are modified as follows:

$$Y_b^h = -\frac{\sin\alpha}{\cos\beta}\, Y_b^{SM}\,, \qquad Y_b^H = \frac{\cos\alpha}{\cos\beta}\, Y_b^{SM}\,, \qquad Y_b^A = \tan\beta\, Y_b^{SM}\,, \tag{151}$$

where $\alpha$ is the mixing angle in the CP-even Higgs sector. In the decoupling limit, $m_A \gg m_Z$, the mixing angle simplifies to $\alpha \approx \beta - \pi/2$, so that the coupling of $h$ to bottom quarks is SM-like, while the couplings of H and A are both enhanced by $\tan\beta$.

In this section we discuss two issues that affect the precise definition of the Higgs-bottom couplings: the first concerns the choice of renormalization scheme – and scale – for the bottom mass from which the couplings are extracted; the second concerns higher-order effects in the procedure through which the $\tan\beta$-enhanced SUSY contributions are resummed in effective Higgs-bottom couplings.

#### *Scheme and scale dependence of the bottom mass*

The parameter $m_b$ enters the expression for the gluon-fusion amplitude with two distinct roles: as the actual mass of the bottom quarks running in the loops, and as a proxy for the Higgs-bottom coupling $Y_b^\phi$, where $\phi = \{h, H, A\}$. The numerical value of $m_b$ depends strongly on the renormalization scheme and scale: an $\overline{MS}$ mass $m_b(m_b) = 4.16$ GeV corresponds to a pole mass $M_b = 4.92$ GeV at three-loop level, whereas evolving $m_b(m_b)$ up to a scale of the order of the typical energy of the gluon-fusion process decreases significantly its value. For example, if we evolve at four-loop level the bottom mass up to the scale at which we express the strong gauge coupling, $\mu_R = m_\phi/2$, we obtain $m_b(m_\phi/2) = 2.93$ GeV for $m_\phi = 125$ GeV. While any change in the definition of the bottom mass and Yukawa coupling entering the one-loop part of the amplitude is formally compensated for, up to higher orders,

by counterterm contributions in the two-loop part, the numerical impact of such strong variations on the prediction for the gluon-fusion cross section can be significant.

To illustrate this point, we identify the mass of the bottom quarks in the loops with the pole mass $M_b$, and consider the dependence of the gluon-fusion cross section on the prescription for the Higgs-bottom coupling $Y_b^\phi$, focusing on $\phi = \{h, H\}$. In the *light-stop* scenario with $m_A = 130$ GeV and $\tan\beta = 40$, where both Higgs scalars are relatively light and have enhanced couplings to the bottom quark, the effect of extracting $Y_b^\phi$ from the $\overline{\text{MS}}$ mass $m_b(m_b)$ instead of the pole mass $M_b$ leads to a 17% decrease in the cross section for $h$ production, and a 24% decrease in the cross section for $H$ production. The use of $m_b(m_\phi/2)$ would instead decrease the cross section for $h$ production by 34%, and the one for $H$ production by 51%, with respect to the values obtained with $M_b$. As a second example, we take the *light-stop* scenario with $m_A = 300$ GeV and $\tan\beta = 10$, where the lightest scalar $h$ has SM-like couplings to quarks. In this case the cross section for $h$ production varies by less than 2% when choosing among the three options discussed above for the definition of $Y_b^h$. For the heaviest scalar $H$, on the other hand, the changes in the cross section relative to the value derived with $M_b$ amount to $-22\%$ and $-50\%$ when $Y_b^H$ is extracted from $m_b(m_b)$ and $m_b(m_H/2)$, respectively.

The strong sensitivity of the production of non-standard Higgs bosons on the choice of renormalization scheme (and scale) for the bottom mass and Yukawa coupling has been discussed in the past, see e.g. refs. [27, 83, 122]. However, unlike many other processes for which there are theoretical arguments in favor of one or the other choice, for Higgs production in gluon fusion we are not aware of any such arguments that go beyond heuristic. As was already noted in ref. [27], the options of relating $Y_b^\phi$ to $M_b$ or to $m_b(m_b)$ might seem preferable to the one of using $m_b(m_\phi/2)$, in that they lead to smaller two-loop contributions. If in the one-loop part of the amplitude for scalar production we identify the mass of the bottom quark with $M_b$ and the bottom Yukawa coupling with $m_b(\mu_b)$, where $\mu_b$ is a generic renormalization scale, the contribution of diagrams with bottom quarks and gluons to the two-loop part of the amplitude reads

$$\mathcal{A}_b^{2\ell}(\tau) \;\propto\; C_F \left[\mathcal{F}_{C_F}(\tau) + \mathcal{F}_{1/2}^{1\ell}(\tau)\left(1 - \frac{3}{4}\ln\frac{m_b^2}{\mu_b^2}\right)\right] + C_A\,\mathcal{F}_{C_A}(\tau)\,, \tag{152}$$

where $C_F = 4/3$ and $C_A = 3$ are color factors, $\tau = 4\,m_b^2/m_\phi^2$, and we omit an overall multiplicative factor. Truncating the functions at the first order in an expansion in powers of $\tau$, one finds [51]

$$\mathcal{F}_{1/2}^{1\ell}(\tau) \;=\; -2\tau\left(1 - \frac{1}{4}L_{b\phi}^2\right) + \mathcal{O}(\tau^2)\,, \tag{153}$$

$$\mathcal{F}_{C_F}(\tau) \;=\; -\tau\left[5 + \frac{9}{5}\zeta_2^2 - \zeta_3 - (3 + \zeta_2 + 4\,\zeta_3)\,L_{b\phi} + \zeta_2\,L_{b\phi}^2 + \frac{1}{4}L_{b\phi}^3 + \frac{1}{48}L_{b\phi}^4\right] + \mathcal{O}(\tau^2)\,, \tag{154}$$

$$\mathcal{F}_{C_A}(\tau) \;=\; -\tau\left[3 - \frac{8}{5}\zeta_2^2 - 3\,\zeta_3 + 3\,\zeta_3\,L_{b\phi} - \frac{1}{4}(1 + 2\,\zeta_2)\,L_{b\phi}^2 - \frac{1}{48}L_{b\phi}^4\right] + \mathcal{O}(\tau^2)\,, \tag{155}$$

with

$$L_{b\phi} \;\equiv\; \ln(-4/\tau) \;=\; \ln(m_\phi^2/m_b^2) - i\,\pi\,. \tag{156}$$

The equations above show that the two-loop bottom contribution to the gluon-fusion amplitude contains powers of $\ln(m_\phi^2/m_b^2)$, and that the choice $\mu_b = m_b$ does eliminate some of the logarithmically enhanced terms. Similarly, relating the coupling entering the one-loop part of the amplitude to the

pole mass $M_b$ eliminates the whole piece proportional to $\mathcal{F}_{1/2}^{1\ell}(\tau)$ in eq. (152). Each of the two remaining terms, $C_F\,\mathcal{F}_{C_F}(\tau)$ and $C_A\,\mathcal{F}_{C_A}(\tau)$, also contains powers of $\ln(m_\phi^2/m_b^2)$, but for realistic values of $m_\phi$ the two terms largely cancel out against each other, resulting in a small two-loop contribution from bottom quarks. However, such cancellation should be considered accidental: there is no argument suggesting that it persists at higher orders in QCD, or that it is motivated by some physical property of the bottom contribution to gluon fusion. To illustrate this point, we can consider the case of Higgs decay to two photons: the one-loop bottom contribution to the amplitude has the same structure as the corresponding contribution to gluon fusion, but the two-loop bottom-gluon contribution is obtained from eq. (152) by dropping the term proportional to $C_A$, which originates from diagrams with three- and four-gluon interactions. In that case no significant cancellation occurs, and the amplitude is not minimized when $Y_b^\phi$ is extracted from $m_b(m_b)$ or $M_b$. In fact, it was also noted in ref. [27] that the two-loop bottom-gluon contribution to the amplitude for Higgs decay to photons is minimized when the one-loop contribution is fully expressed in terms of $m_b(m_\phi/2)$.

In the case of the Higgs coupling to photons, the problems related to the ambiguity in the definition of $Y_b^\phi$ have been solved with a resummation of the leading and next-to-leading logarithms of the ratio $m_\phi^2/m_b^2$ [123]. Until a similar calculation is performed for the Higgs coupling to gluons, there is no obvious reason to favor one choice of renormalization scheme (and scale) for the bottom Yukawa coupling over the others. In our study we choose to relate the coupling to the pole mass $M_b$, and we consider the difference between the results obtained using $M_b$ and those obtained using $m_b(m_\phi/2)$ as a measure of the uncertainty associated with the uncomputed higher-order QCD corrections. For the production of a SM-like Higgs with mass around 125.5 GeV, this procedure – also advocated by the LHC-HXSWG in ref. [39] – results in an uncertainty of 1 – 2% in the gluon-fusion cross section. On the other hand, as we show in figures 41 and 42 for scalar and pseudoscalar production in the *light-stop* scenario, the cross section could be reduced by more than 60% in the regions of the $m_A$ – $\tan\beta$ plane where the gluon-fusion process is dominated by the bottom-quark contribution. It is however worth recalling that, as shown in figures 32 and 33, in such regions the total cross section for Higgs production is dominated by bottom-quark annihilation. In the 5FS, the cross section for the latter process is known at the NNLO in QCD [29, 79], and it is free of large logarithms of the ratio $m_\phi^2/m_b^2$ when $Y_b^\phi$ is related to $m_b(m_\phi)$. The theoretical uncertainty of the cross section for bottom-quark annihilation associated to reasonable variations around this scale choice is already included in the uncertainty bands shown in figures 39 and 40 in the previous section.

#### *Resummation of* $\tan\beta$*-enhanced corrections*

It is well known that, in the MSSM, loop diagrams involving superparticles induce $\tan\beta$-enhanced corrections to the couplings of the Higgs bosons to bottom quarks [124]. If all superparticles are considerably heavier than the Higgs bosons they can be integrated out of the MSSM Lagrangian, leaving behind a two-Higgs-doublet model with effective Higgs-bottom couplings

$$\widetilde{Y_b}^h = \frac{Y_b^h}{1+\Delta_b}\left(1-\Delta_b\,\frac{\cot\alpha}{\tan\beta}\right), \quad \widetilde{Y_b}^H = \frac{Y_b^H}{1+\Delta_b}\left(1+\Delta_b\,\frac{\tan\alpha}{\tan\beta}\right), \quad \widetilde{Y_b}^A = \frac{Y_b^A}{1+\Delta_b}\left(1-\Delta_b\,\cot^2\beta\right), \tag{157}$$

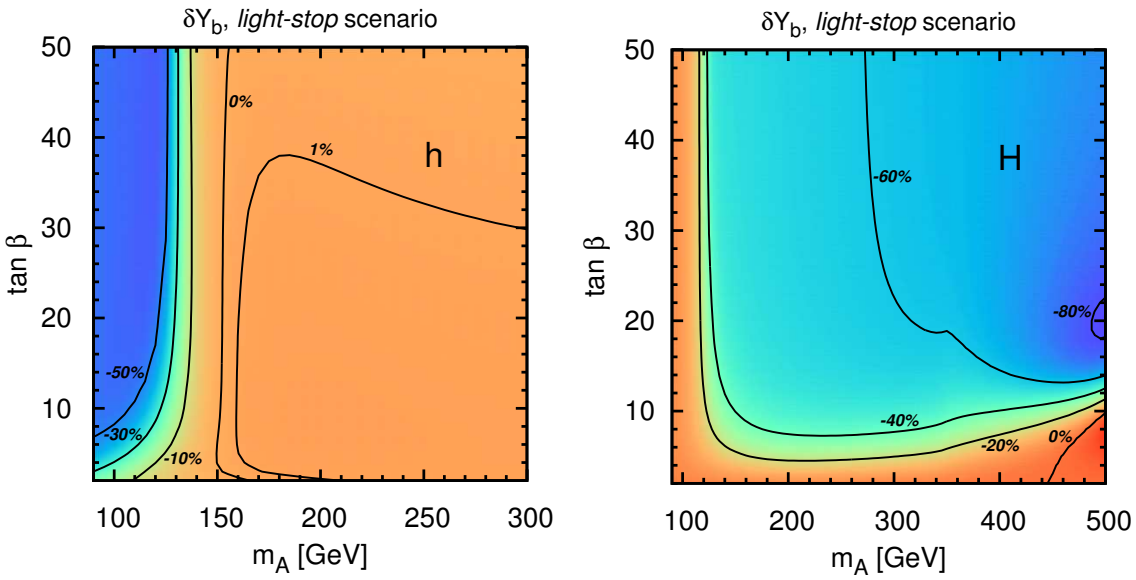


**Figure 41:** Variation (in percent) of the gluon-fusion cross section for the production of $h$ (left) and $H$ (right) when the Higgs-bottom coupling $Y_b^\phi$ is extracted from $m_b(m_\phi/2)$ instead of $M_b$, as a function of $m_A$ and $\tan\beta$ in the *light-stop* scenario.

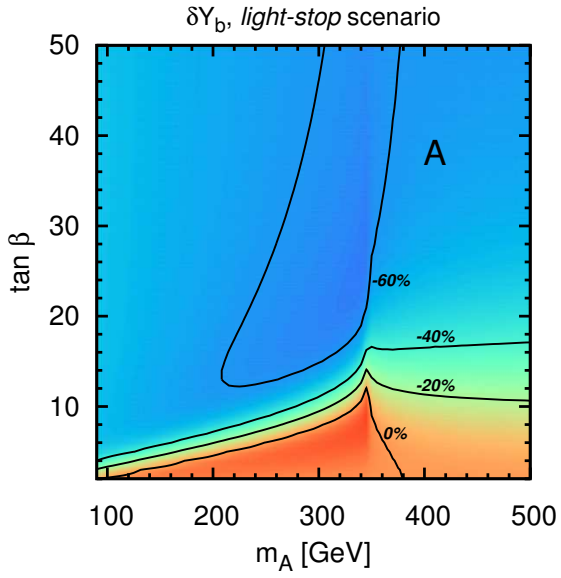


**Figure 42:** Same as figure 41 for the production of the pseudoscalar $A$.

where $Y_b^\Phi$ are the tree-level Higgs-bottom couplings defined in eq. (151), and, retaining only the $\mathcal{O}(\alpha_s)$ contribution from diagrams with sbottoms and gluinos, the $\tan\beta$-enhanced term $\Delta_b$ reads

$$\Delta_b = \frac{2\,\alpha_s}{3\,\pi}\,\frac{m_{\tilde{g}}\,\mu\,\tan\beta}{m^2_{\tilde{b}_1}-m^2_{\tilde{b}_2}}\left(\frac{m^2_{\tilde{b}_1}}{m^2_{\tilde{b}_1}-m^2_{\tilde{g}}}\ln\frac{m^2_{\tilde{b}_1}}{m^2_{\tilde{g}}}-\frac{m^2_{\tilde{b}_2}}{m^2_{\tilde{b}_2}-m^2_{\tilde{g}}}\ln\frac{m^2_{\tilde{b}_2}}{m^2_{\tilde{g}}}\right). \tag{158}$$

In the limit $m_A \gg m_Z$, where $\cot\alpha \approx -\tan\beta$, the superparticle contributions encoded in $\Delta_b$ decouple from the coupling of the lightest scalar, while the couplings of the heaviest scalar and of the pseudoscalar are both rescaled by a factor $(1-\Delta_b\,\cot^2\beta)/(1+\Delta_b)$.

In refs. [75, 76] it was shown that, in the calculation of processes that involve the Higgs-bottom couplings, the $\tan\beta$-enhanced corrections can be resummed to all orders in the expansion in powers of $\Delta_b$ by inserting the effective couplings of eq. (157) in the lowest-order amplitude for the considered process. In the case of gluon fusion, this amounts to using $\widetilde{Y_b}^\Phi$ in the bottom contribution to the one-loop part of the amplitude. However, when this resummation procedure is combined with the actual calculation of the superparticle contributions to the one- and two-loop amplitude for gluon fusion, care must be taken to avoid double counting. To this effect, we must subtract from the full result for the two-loop amplitude the contribution obtained by replacing $\widetilde{Y_b}^\Phi$ in the resummed one-loop amplitude with the $\mathcal{O}(\Delta_b)$ term of the expansion of $\widetilde{Y_b}^\Phi$ in powers of $\Delta_b$. Depending on the choice of renormalization scheme for the parameters in the sbottom sector, additional $\tan\beta$-enhanced terms could be induced in the two-loop amplitude by the counterterm of the Higgs-sbottom coupling that enters the sbottom contribution to the one-loop amplitude. To avoid the occurrence of large two-loop corrections, which would put the validity of the perturbative expansion into question, we employ for the sbottom sector the OS renormalization scheme described in ref. [68].

An ambiguity in the procedure for the resummation of the $\Delta_b$ terms concerns the treatment of the Higgs-bottom couplings entering the two-loop part of the gluon-fusion amplitude. The difference between the results obtained using either $Y_b^\Phi$ or $\widetilde{Y_b}^\Phi$ in the two-loop part is formally of higher order, i.e., it amounts to three-loop terms that are suppressed by a factor $A_b/(\mu\tan\beta)$ with respect to the dominant three-loop terms of $\mathcal{O}(\Delta_b^2)$ accounted for by the resummation. Nevertheless, in our study we choose to identify the Higgs-bottom couplings in both the one- and two-loop parts of the amplitude with $\widetilde{Y_b}^\Phi$. We found that this choice allows us to reproduce – after an expansion in powers of $\Delta_b$ – the three-loop result that can be inferred from ref. [76], where the sub-dominant terms proportional to $A_b$ were also resummed in the effective couplings.

For large values of $\tan\beta$, the factor $\Delta_b$ can even become of order one, unless the superpotential parameter $\mu$ is suppressed with respect to the soft SUSY-breaking masses. The effect of the SUSY correction on the effective Higgs-bottom couplings depends crucially on the sign of $\Delta_b$. For positive $\Delta_b$ the correction suppresses the couplings, reducing the overall relevance of the bottom contribution to gluon fusion. On the other hand, for negative $\Delta_b$ the correction enhances the couplings, which diverge as $\Delta_b$ approaches $-1$. As a consequence, when $\Delta_b$ is large and negative the result for the gluon-fusion cross section is extremely sensitive to the precise value of $\Delta_b$, and a refined calculation of the latter becomes mandatory to reduce the uncertainty associated to the bottom contribution.

The first obvious step to improve the calculation of $\Delta_b$ consists in including other one-loop contributions that are not shown in eq. (158). In particular, the diagrams with stops and charginos induce a

contribution, controlled by the top Yukawa coupling, that can be comparable in size with the $\mathcal{O}(\alpha_s)$ contribution in eq. (158). In our numerical analysis we use by default the full one-loop result for $\Delta_b$ as computed by `FeynHiggs`, which allows us to resum in our prediction for the Higgs-production cross section also the tan $\beta$-enhanced corrections of electroweak origin.

Another improvement in the calculation would come from the inclusion of the dominant two-loop contributions to $\Delta_b$, which have been computed in ref. [77] but are not yet implemented in `FeynHiggs`. Indeed, it was shown in ref. [77] that the one-loop result for $\Delta_b$ is particularly sensitive to changes in the renormalization scales at which the strong-gauge and top-Yukawa couplings are expressed, and that the inclusion of the two-loop contributions stabilizes this scale dependence. In particular, both the one-loop sbottom-gluino and stop-chargino contributions to $\Delta_b$ vary by roughly $\pm 10\%$ when the renormalization scales are lowered or raised by a factor of two around their central values, which are chosen as the average of the masses of the relevant superparticles. We can therefore estimate the uncertainty of the gluon-fusion cross section associated to the one-loop computation of $\Delta_b$ by varying by $\pm 10\%$ the result provided by `FeynHiggs`.

In general, the impact of the uncertainty of $\Delta_b$ on the total uncertainty of the gluon-fusion cross section depends on the considered point in the MSSM parameter space. As was the case also for the scheme and scale dependence of $Y_b^\Phi$ discussed in the previous section, the $\Delta_b$ uncertainty can be significant only if the bottom contribution to the cross section is substantially enhanced with respect to the SM case. For illustration, we consider again the *light-stop* scenario with $m_A = 130$ GeV and $\tan\beta = 40$, where both Higgs scalars have enhanced couplings to bottom quarks. The superpotential parameter $\mu$ has positive sign, and the $\Delta_b$ corrections suppress the effective couplings $\widetilde{Y_b}^\Phi$. We find that the cross sections for $h$ and $H$ production in gluon fusion increase by 4% and 7%, respectively, if the value of $\Delta_b$ is reduced by 10%, while they decrease by 4% and 6%, respectively, if $\Delta_b$ is increased by 10%. The effect is larger if $\mu$ is taken negative, so that the $\Delta_b$ corrections enhance the effective couplings. In that case the dependence on $\Delta_b$ is reversed: if we consider the same point in the *light-stop* scenario but flip the sign of $\mu$, the cross sections for $h$ and $H$ production in gluon fusion decrease by 17% and 16%, respectively, when $|\Delta_b|$ is reduced by 10%, while they increase by 23% and 21%, respectively, when $|\Delta_b|$ is increased by 10%.

Finally, we stress that a similar uncertainty affects the cross section for Higgs production via bottom-quark annihilation, where the tree-level amplitude is computed in terms of the effective couplings $\widetilde{Y_b}^\Phi$. Also in this case, we can estimate the uncertainty by varying by $\pm 10\%$ the value of $\Delta_b$ provided by `FeynHiggs`.

### 4.2.3 Uncertainties from the PDFs and $\alpha_s$

The prediction for the total cross section at hadron level is affected by our imperfect knowledge of the proton PDFs. This uncertainty has different sources: the PDFs cannot be computed from first principles but they rather have to be fitted from data, and the experimental error of the latter affects the outcome of the fit and propagates to the prediction of any observable. Also, the choices related to the fitting methodology and to the mathematical representation of the PDFs induce an ambiguity in the results, as can be appreciated by comparing the PDF parameterizations provided by three collaborations that perform a global fit of low- and high-energy data: MSTW2008 [117], CT10 [125] and NNPDF2.3 [126]. These uncertainties will be discussed in section 4.2.3, together with the parametric dependence of the

cross section on the value of the strong coupling constant. Another source of uncertainty is related to the available perturbative-QCD information on the scattering processes from which the PDFs are extracted. Among these perturbative effects, an issue that is particularly relevant in the case of Higgs production via bottom-quark annihilation is the consistent inclusion of the bottom-mass effects in the evolution of the PDFs according to the DGLAP equations. The transition between four and five active flavors in the proton occurs at a matching scale that is set equal to the bottom mass. The bottom density in the proton depends parametrically on this matching scale, which in turn affects the predictions for the cross section. The phenomenological implications of this issue will be discussed in detail in section 4.2.3. A systematic discussion of further sources of theoretical uncertainty – such as, e.g., the dependence of the PDFs on the choice of renormalization and factorization scale in the matrix elements that are used to perform the fit – is not yet available in the literature, and goes beyond the scope of this study.

*Combination of PDF and $\alpha_s$ uncertainties*

The uncertainty associated to the experimental errors of the data from which the PDFs are extracted is represented by the PDF collaborations with the introduction of $N_R$ different PDF sets (replicas), all equivalent from the statistical point of view in the description of the data. Any observable has to be computed $N_R$ times with the different sets, and the spread of the results can be interpreted as the error induced by the PDF due to the data and to the fitting methodology. The replicas are determined by the PDF collaborations following the Hessian (for MSTW2008 and CT10) or the Monte Carlo (for NNPDF2.3) approaches, and the PDF error has to be computed accordingly. In QCD the cross sections are also affected by a parametric uncertainty associated to the input value of the strong coupling constant. This dependence is particularly relevant in the gluon-fusion cross section, which is proportional to $\alpha_s^2$ at the LO and is subject to very large QCD corrections, of $\mathcal{O}(\alpha_s^3)$, at the NLO. Each PDF collaboration recommends a different central value for $\alpha_s(m_Z)$, generating a spread of the central predictions for the Higgs-production cross section. The combination of the PDF and $\alpha_s$ uncertainties (henceforth, PDF+$\alpha_s$) and their correlation was first discussed in ref. [127]. A conservative approach to combine the different predictions obtained using the MSTW2008, CT10 and NNPDF2.3 PDF sets is known as PDF4LHC recipe, and it amounts to taking the envelope of the PDF+$\alpha_s$ uncertainty bands of the three collaborations, where for each group the preferred $\alpha_s(m_Z)$ central value is adopted [128]. Following this reference we take $\Delta\alpha_s = \pm 0.0012$ for the experimental error on the strong coupling constant.

Due to the very steep behavior of the PDFs for increasing values of the final-state invariant mass, the gluon-fusion process receives its dominant contribution from the threshold production region, with a very important role played by the virtual corrections and by the universal, factorizable, soft-gluon corrections. Consequently, the cross section is dominated by the LO-kinematics configurations also at higher perturbative orders. At the LO, the gluon-fusion cross section depends on the rapidity of the Higgs boson only through the PDFs, therefore the relative size of the PDF+$\alpha_s$ uncertainty does not depend on the details of the partonic process, but only on the value of the Higgs-boson mass. As a consequence, the relative PDF+$\alpha_s$ uncertainty, for a given value of the Higgs mass, can be read directly from the tables of the SM predictions reported in the appendix B of the latest LHC-HXSWG report [41]. Differences with respect to the SM predictions may originate from hard, process-dependent radiative corrections, but their impact on the relative PDF+$\alpha_s$ uncertainty is at the sub-percent level.

To assess the PDF+$\alpha_s$ uncertainty of the cross section for Higgs production in bottom-quark annihilation we adopt again the PDF4LHC recipe. The bottom density in the proton does not have an intrinsic

component, but it is generated dynamically, via gluon splittings, by the DGLAP evolution of the PDFs. Therefore, the uncertainties of the bottom and gluon PDFs are strongly correlated.

Similarly to the case of gluon fusion, for a given value of the Higgs mass the relative PDF+$\alpha_s$ uncertainty of the cross section for bottom-quark annihilation differs very little between the SM and the MSSM, because the radiative corrections involving SUSY particles affect the kinematics of the process only at higher orders.[5] We find that the uncertainty has an almost constant behavior when the mass $m_\Phi$ of the produced Higgs boson is lighter than 300 GeV, and that it increases for larger mass values: for example, at the NNLO, the PDF+$\alpha_s$ uncertainty of the cross section for bottom-quark annihilation amounts to $\pm 6/6/8/21\%$ for $m_\Phi = 124/300/500/1000$ GeV.

*Bottom-mass dependence of the PDFs*

The calculation of hadronic cross sections involves the convolution of the partonic cross sections with the PDFs, which have an intrinsic dependence on the bottom mass. For example, the central set of MSTW2008 [117], which we use as default for our analysis, assumes a pole mass $M_b = 4.75$ GeV. Converted to the $\overline{\text{MS}}$ mass via a three-loop QCD calculation, this corresponds to $m_b(m_b) = 4.00$ GeV, which differs both from the value recommended by the LHC-HXSWG, $m_b(m_b) = 4.16$ GeV [91, 93], and from the current PDG value, $m_b(m_b) = 4.18$ GeV [129].

In addition to their dependence through the PDFs, the cross sections for Higgs production also depend on the bottom mass at the partonic level, i.e., through the bottom Yukawa coupling, the bottom-quark propagators and the phase space. In the regions of the MSSM parameter space where the bottom-quark contributions to Higgs production are enhanced, it becomes vital to evaluate the partonic cross sections with the correct input value for the bottom mass, which, as mentioned above, may not necessarily correspond to the value used in the PDFs. In this section we will examine the uncertainty that arises when we choose the bottom mass entering the partonic cross sections independently from the PDF set.

The MSTW2008 PDFs come in seven sets obtained with $M_b$ ranging from 4 GeV to 5.5 GeV in steps of 0.25 GeV. In ref. [130] the MSTW collaboration studied the sensitivity of the PDFs on the value of the bottom mass, showing that the PDFs for the gluon and for the four lightest quarks are almost insensitive to $M_b$, whereas the bottom PDF exhibits quite a strong dependence. As shown in figure 6 of ref. [130], a variation by $\pm 0.5$ GeV around the central value $M_b = 4.75$ GeV leads to changes in the bottom PDF that exceed the 90% C.L. uncertainty, even for the relatively large value of the factorization scale relevant to Higgs production, $\mu_F \approx 100$ GeV.

The cross section for Higgs production via gluon fusion is mostly sensitive to the gluon PDF, and receives only a small contribution, starting at the NLO, from diagrams with initial-state bottom quarks. As a result, when we evaluate the gluon-fusion cross section with the seven PDF sets – while fixing the bottom mass in the partonic cross section – we find that the result changes only at the per mil level, independently of the phenomenological scenario under consideration. We conclude that, for this process, the formal inconsistency of choosing different values for the bottom mass in the partonic cross section and in the PDFs induces only a negligible uncertainty.

In contrast, the hadronic cross section for Higgs production in bottom-quark annihilation, when computed in the 5FS, depends directly on the bottom PDF. As a result, we expect this process to show

5 In SusHi the SUSY corrections to bottom-quark annihilation enter only through the effective couplings $\widetilde{Y_b}^{\Phi}$, therefore our estimate of the PDF+$\alpha_s$ uncertainty for a given Higgs mass is exactly the same in the SM and in the MSSM.

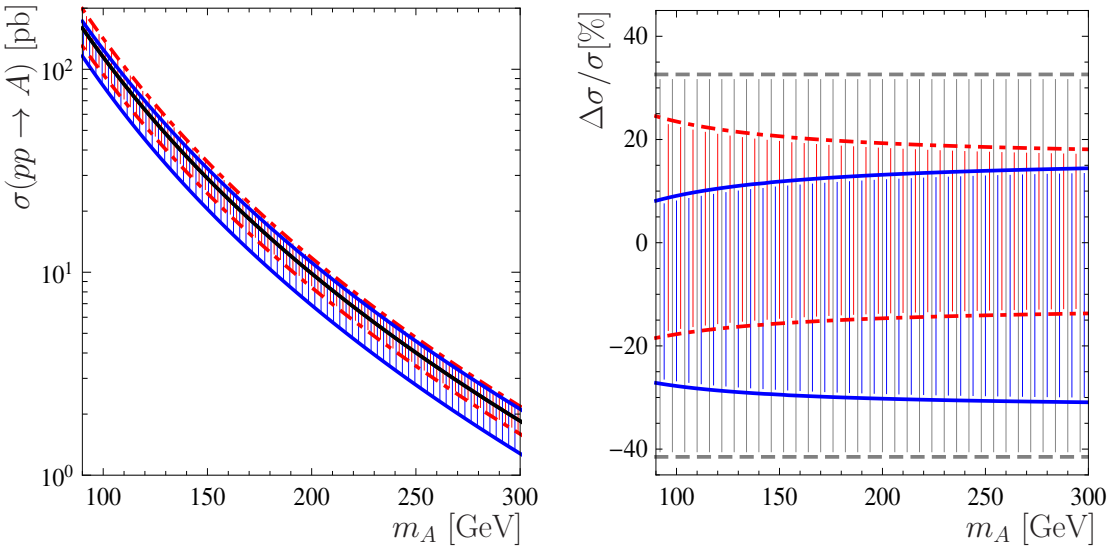


**Figure 43:** (Left) Cross section for pseudoscalar Higgs production in bottom-quark annihilation as a function of $m_A$ for the *light-stop* scenario with $\tan\beta = 20$. (Right) Relative variation of the cross section for different choices of the pole bottom mass used in the PDFs and of the running mass used in the partonic cross section. Red: PDF variation, $\widetilde{Y}_b^A$ fixed; black: PDF fixed, $\widetilde{Y}_b^A$ varies; blue: PDF and $\widetilde{Y}_b^A$ vary simultaneously.

a significant dependence on the value of the bottom mass used in the PDFs, and the issue of consistency with the bottom mass used in the definition of the bottom Yukawa coupling becomes unavoidable.

In figure 43 we investigate the bottom-mass dependence of the hadronic cross section for pseudoscalar production in bottom-quark annihilation (we find similar behaviors for the production of the scalars, both light and heavy). The plot on the left shows the hadronic cross section as a function of the pseudoscalar mass $m_A$, in the *light-stop* scenario with $\tan\beta = 20$. As in section 4.1, the renormalization and factorization scales are set to $\mu_R = m_A$ and $\mu_F = m_A/4$. The central (black) solid line in the left plot is computed with our default settings, namely we use the PDF set with $M_b = 4.75$ GeV and we relate the Yukawa coupling $\widetilde{Y}_b^A$ to $m_b(m_A)$, which we obtain from the input $m_b(m_b) = 4.16$ GeV via renormalization-group evolution. The plot on the right of figure 43 represents the variation of the cross section relative to this default setting, when we change the bottom mass in the PDFs and/or in the Yukawa coupling.

In both plots, the red band between dot-dashed lines indicates the spread in the cross section obtained with the extreme PDF sets – corresponding to $M_b = 4$ GeV and $M_b = 5.5$ GeV, respectively – with $\widetilde{Y}_b^A$ fixed to the default value. As expected, the impact of the bottom mass used in the PDFs is significant: it amounts to about $(+20/-15)\%$ at large $m_A$, with larger values of $M_b$ corresponding to smaller cross sections. This anti-correlation is a consequence of the fact that, for larger bottom masses, the reduced available phase space for the splitting of gluons into bottom pairs leads to a suppression of the bottom PDF. On the other hand, the bottom Yukawa coupling is directly correlated with the magnitude of the cross section. Simultaneously adjusting the bottom mass entering the bottom Yukawa coupling and the one entering the bottom PDF should therefore lead to some degree of compensation between these two effects.

Converting the pole-mass values $M_b = 4$ GeV and $M_b = 5.5$ GeV to the $\overline{\text{MS}}$ scheme at three-loop level, one obtains $m_b(m_b) = 3.32$ GeV and $m_b(m_b) = 4.69$ GeV, respectively. Using these numbers to calculate $\widetilde{Y_b}^A$ while fixing the PDF set to the default (i.e., the set with $M_b = 4.75$ GeV) results in the gray band between dashed lines in the right plot of figure 43. It turns out that this band is about twice as large as the red band arising from PDF variation. However, the gray band is rather asymmetric, because the pole mass $M_b = 4.75$ GeV for the default PDF set corresponds at the three-loop level to $m_b(m_b) = 4.00$ GeV, which is significantly smaller than our default input for $\widetilde{Y_b}^A$, i.e. $m_b(m_b) = 4.16$ GeV. The net effect on the cross section of a simultaneous variation of the bottom mass in the PDFs and in $\widetilde{Y_b}^A$, shown as a blue band between solid lines in both the left and the right plots, is thus also asymmetric, and it is of the order of $(+15/-30)\%$ at large $m_A$.

Our procedure to estimate the uncertainty of the cross section for bottom-quark annihilation arising from the bottom-mass dependence of the PDFs is similar to the one in ref. [122]. We fix the bottom Yukawa coupling to the value implied by $m_b(m_b) = 4.16$ GeV, as recommended by the LHC-HXSWG, and we use as uncertainty the spread in the cross section caused by the variation of $M_b$ in the PDFs around the central value of 4.75 GeV. However, the full variation of $\pm 0.75$ GeV allowed by the MSTW2008 PDFs, which would correspond to the red band in figure 43, seems overly conservative for our purposes. A variation of $\pm 0.25$ GeV is in fact sufficient to encompass the value $M_b = 4.92$ GeV, which corresponds at the three-loop level to the recommended $\overline{\text{MS}}$ mass $m_b(m_b) = 4.16$ GeV. This variation finally leads to an estimate of the uncertainty of about $\pm 6\%$. A similar estimate is obtained from NNPDF2.1 [131], which also provides PDF sets with different values of $M_b$.

#### 4.2.4 Higher-order SUSY contributions to gluon fusion

In this section we discuss two sources of uncertainty affecting the SUSY contributions to the cross section for gluon fusion. The first is the validity of the expansion in the heavy superparticle masses of the two-loop SUSY contributions; the second is the impact of the three-loop SUSY contributions that are not included in `SusHi` .

##### *Validity of the expansion in the SUSY masses*

The results implemented in `SusHi` for the two-loop stop contributions to lightest-scalar production rely on the VHML, while the results for the remaining two-loop SUSY contributions rely on expansions in inverse powers of the superparticle masses. The latter include terms up to $\mathcal{O}(m_\Phi^2/M^2)$, $\mathcal{O}(m_t^2/M^2)$, $\mathcal{O}(m_b/M)$ and $\mathcal{O}(m_Z^2/M^2)$, where $m_\Phi$ denotes a Higgs mass and $M$ denotes a generic superparticle mass. Therefore, the validity of the results for the two-loop SUSY contributions is limited to the region where the mass of the produced Higgs boson is smaller than the lowest-lying SUSY-particle threshold of the Feynman diagrams involved. In all of the six benchmark scenarios considered in our study, the lightest-scalar mass lies comfortably below this limit. Since we consider $m_A \leqslant 1$ TeV, the same applies also to the masses of the heaviest scalar and of the pseudoscalar in the five scenarios in which the squark masses are themselves of the order of 1 TeV. In the *light-stop* scenario, on the other hand, the lowest-lying SUSY threshold is at $2\, m_{\tilde{t}_1} \approx 650$ GeV, hence our need to limit our analysis to $m_A \leqslant 500$ GeV.

To assess the quality of our approximation in the vicinity of the threshold, we multiply the two-loop stop and sbottom contributions to the gluon-fusion amplitude by test factors $t_{\tilde{q}} \equiv \mathcal{A}_{\tilde{q}_1}^{1\ell}/\mathcal{A}_{\tilde{q}_1}^{1\ell,\,\text{exp}}$,

with $\tilde{q} = \{\tilde{t}, \tilde{b}\}$. Specifically, $\mathcal{A}^{1\ell}_{\tilde{q}_1}$ is the lightest-squark contribution to the one-loop part of the scalar-production amplitude including the full mass dependence, while $\mathcal{A}^{1\ell,\,\mathrm{exp}}_{\tilde{q}_1}$ includes only the leading $\mathcal{O}(m^{-2}_{\tilde{q}_1})$ terms in the expansion in the lightest-squark mass. Assuming that the expanded two-loop contributions deviate from the full ones by an amount comparable to that seen in the one-loop contributions, the variation in the gluon-fusion cross section resulting from the introduction of the test factors can be considered as an estimate of the uncertainty associated to the expansion in the SUSY masses.

The contour plots in figure 44 show the effect of introducing these test factors on the cross section for the production of the heaviest scalar (left plot) and of the pseudoscalar (right plot) in the *light-stop* scenario. In the case of H production, the variation of the cross section at large $m_A$ amounts to a few percent when $\tan\beta$ is sufficiently large, but it can exceed 20% when $8 \lesssim \tan\beta \lesssim 16$. As can be seen in the right plot of figure 34, in this region the one-loop quark and squark contributions to the gluon-fusion amplitude largely cancel each other, with the result that the total cross section becomes small and particularly sensitive to variations in the two-loop contributions. This sensitivity to higher-order effects manifests also as the large scale uncertainty, up to 50%, visible in the right plot of figure 37. In the case of A production, on the other hand, no such cancellations occur, because the squarks do not contribute to the one-loop amplitude for gluon fusion.[6] The variation of the cross section at large $m_A$ is therefore limited to a few percent even for moderate $\tan\beta$.

We performed the same analysis on the other five benchmark scenarios, where the squark masses are of the order of 1 TeV. As expected, we found that the effect of rescaling the two-loop SUSY contributions by test factors $t_{\tilde{q}}$ is much smaller than in the *light-stop* scenario, and it is certainly negligible when compared to the scale uncertainty of the cross section. In particular, in the *tau-phobic* scenario – where the squark contributions to the gluon-fusion amplitude are enhanced by the large value of the parameter $\mu$ – the effect on H production reaches the few-percent level only when $m_A$ approaches 1 TeV, for moderate $\tan\beta$. In the remaining four scenarios the effect is even smaller.

#### *The SUSY contributions at the NNLO*

The QCD corrections to the gluon-fusion cross section are large, typically exceeding 100% at the energy of the LHC. In the SM, an excellent approximation to these corrections is obtained in the VHML (or heavy-top limit) [7, 46, 121], where a perturbative K-factor is calculated in the effective theory that results from neglecting the bottom Yukawa coupling and integrating out the top quark, leaving behind a point-like Higgs-gluon interaction term $\mathcal{L}_{ggH} = -(1/4v)\, C(\alpha_s)\, H G_{\mu\nu} G^{\mu\nu}$, with $v \approx 246$ GeV. The Wilson coefficient

$$C(\alpha_s) = C^{(0)} + \frac{\alpha_s}{\pi} C^{(1)} + \left(\frac{\alpha_s}{\pi}\right)^2 C^{(2)} \tag{159}$$

accounts for heavy particles that mediate the Higgs-gluon coupling in the underlying theory. In the SM, this is just the top quark; it is easy to see, though, that the inclusion of stop squarks (and gluinos) only affects $C(\alpha_s)$, while the form of $\mathcal{L}_{ggH}$ remains unchanged. A comparison with the full result at the NLO suggests that, within the SM, the VHML provides a decent approximation of the NNLO top contributions also for rather large Higgs masses [115, 116]. Therefore, `SusHi` includes the NNLO effects in the cross sections for the production of all three neutral Higgs bosons of the MSSM.

6 For the same reason, we cannot define test factors analogous to $t_{\tilde{q}}$ in terms of the pseudoscalar-production amplitude. To estimate the accuracy of the mass expansion for A production we use the same test factors $t_{\tilde{q}}$ as for H production.

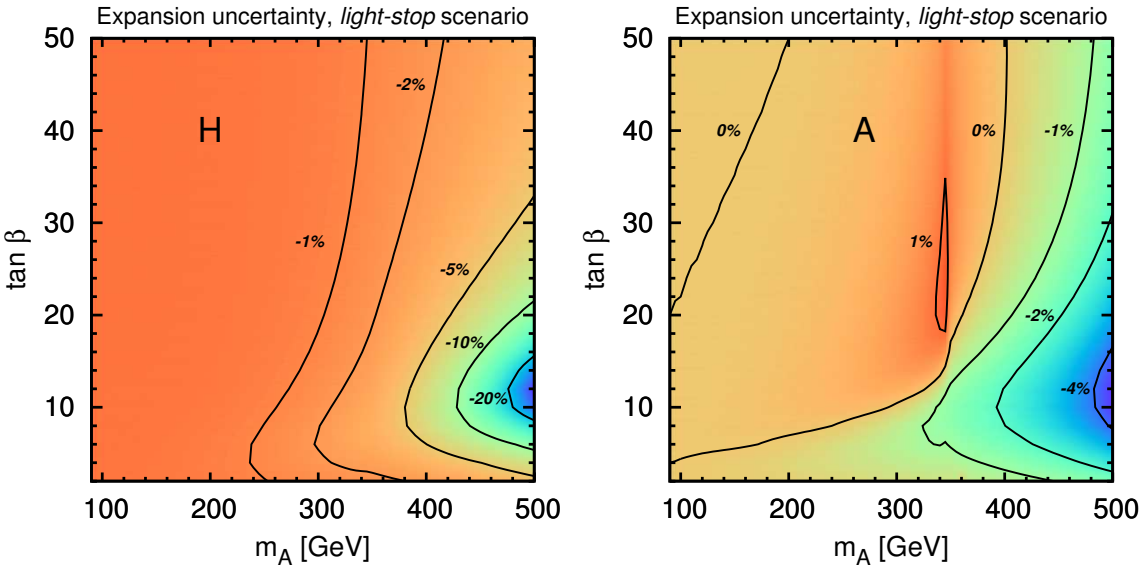


**Figure 44:** Variation of the gluon-fusion cross section for the production of H (left) and A (right) in the *light-stop* scenario when the two-loop SUSY contributions are rescaled by $t_{\tilde{q}} \equiv \mathcal{A}^{1\ell}_{\tilde{q}_1}/\mathcal{A}^{1\ell,\,\mathrm{exp}}_{\tilde{q}_1}$.

Within the effective theory, the K-factor at the NNLO takes the form

$$K = 1 + \frac{\alpha_s}{\pi}\frac{1}{C^{(0)}\Sigma^{(0)}}\left[C^{(0)}\Sigma^{(1)} + 2\,C^{(1)}\Sigma^{(0)} + \frac{\alpha_s}{\pi}\left(C^{(0)}\Sigma^{(2)} + 2\,C^{(1)}\Sigma^{(1)} + (C^{(1)})^2\Sigma^{(0)} + 2\,C^{(2)}\Sigma^{(0)}\right)\right], \tag{160}$$

where $\Sigma^{(n)}$ is the $n^{\mathrm{th}}$-order term in the perturbative expansion of the hadronic cross section based on $\mathcal{L}_{ggH}|_{C(\alpha_s)\equiv 1}$. Note that, in the NNLO part of the K-factor in eq. (160), the only genuine three-loop term that depends on the underlying theory is $C^{(2)}$. This observation was exploited in ref. [72] to derive an estimate of the NNLO top/stop contribution to the gluon-fusion cross section in the MSSM. In particular, it was shown that the final result depends only very weakly on the numerical value of $C^{(2)}$. Consequently, once the two-loop stop contributions are included in $C^{(1)}$, the unknown three-loop stop contributions to $C^{(2)}$ induce an uncertainty in the cross section much smaller than the residual uncertainty derived from scale variation. It was suggested to use the top contribution $C^{(2)}_t$ for the whole $C^{(2)}$, and to estimate the related uncertainty by varying that coefficient within the interval $[0, 2\,C^{(2)}_t]$.

In ref. [72] the hadronic cross section was obtained, in analogy to the SM NNLO result, by reweighting its exact LO expression with the K-factor of eq. (160):

$$\sigma^{\mathrm{NNLO}} = K\,|\mathcal{A}^{1\ell}_{t\tilde{t}}|^2\,\Sigma_0\,, \tag{161}$$

where $\mathcal{A}^{1\ell}_{t\tilde{t}} \equiv \mathcal{A}^{1\ell}_t + \mathcal{A}^{1\ell}_{\tilde{t}}$ is the one-loop amplitude including both the top and stop contributions with the exact Higgs-mass dependence (in particular, $\mathcal{A}^{1\ell}_{t\tilde{t}} \to C^{(0)}$ in the VHML, i.e. for $m_\Phi \to 0$). However, as was discussed also in the previous section, there exist so-called *gluophobic* regions of the

MSSM parameter space in which the top and stop contributions to the amplitude can cancel each other to a large extent. Since the precise values of the MSSM parameters where this cancellation is maximal differ between the full calculation and the VHML, the ratio $|\mathcal{A}_{t\bar{t}}^{1\ell}|/C^{(0)}$ entering the cross section – see eqs. (160) and (161) – can become spuriously large when $C^{(0)} \approx 0$. In order to evade this effect, we replace $C^{(0)}$ in eq. (159) with $\mathcal{A}_{t\bar{t}}^{1\ell}$. This leads to the following expression for the cross section:

$$\begin{aligned}\sigma^{\text{NNLO}} &= |\mathcal{A}_{t\bar{t}}^{1\ell}|^2\,\Sigma^{(0)} + \frac{\alpha_s}{\pi}\left(|\mathcal{A}_{t\bar{t}}^{1\ell}|^2\,\Sigma^{(1)} + 2\,C^{(1)}\,\Sigma^{(0)}\,\text{Re}\,\mathcal{A}_{t\bar{t}}^{1\ell}\right) \\ &+ \left(\frac{\alpha_s}{\pi}\right)^2\left[|\mathcal{A}_{t\bar{t}}^{1\ell}|^2\,\Sigma^{(2)} + 2\left(C^{(1)}\,\Sigma^{(1)} + C^{(2)}\,\Sigma^{(0)}\right)\text{Re}\,\mathcal{A}_{t\bar{t}}^{1\ell} + (C^{(1)})^2\,\Sigma^{(0)}\right]. \qquad (162)\end{aligned}$$

This formula applies to both MSSM scalars. The effective Lagrangian for the gluonic interaction of the pseudoscalar involves an additional operator which contributes at the NNLO [71], but it can be treated in a completely analogous way.

In `SusHi`, the NNLO top and stop contributions to the gluon-fusion cross section in the VHML are isolated by subtracting from the $\sigma^{\text{NNLO}}$ in eq. (162) the same quantity truncated at the NLO (and computed with NLO PDFs). The result is then added to the full NLO cross section, which accounts also for the bottom and sbottom contributions and for the known Higgs-mass dependence of the two-loop amplitude. The 6% suppression of the cross section for the production of a SM-like scalar induced by the NNLO stop contributions in the *light-stop* scenario – see section 4.1.3 – can be ascribed to the effect of the term $2\,C^{(1)}\,\Sigma^{(1)}\,\text{Re}\,\mathcal{A}_{t\bar{t}}^{1\ell}$ in the second line of eq. (162). Indeed, the large value of the (normalized) NLO term of the cross section in the effective theory, $\Sigma^{(1)}/\Sigma^{(0)} \approx 26$, compensates for the suppression by $\alpha_s/\pi$, with the result that the effect of the two-loop stop contribution to $C^{(1)}$ at the NNLO is roughly as large as the corresponding effect at the NLO.

To assess the uncertainty arising from the fact that we neglect the three-loop SUSY contributions to $C^{(2)}$, we make use of a recent calculation of those contributions in the VHML [73, 74]. The calculation is based on an expansion of the relevant Feynman diagrams in terms of certain hierarchies among the different masses, similar to the strategy that was pursued in ref. [104] for the calculation of the 3-loop corrections to the Higgs mass in the MSSM. The results of ref. [74] are available in the form of a `Mathematica` file, which provides the basis for the expansion of $C^{(2)}$ in various hierarchies of the masses $m_{\tilde{t}_1}$, $m_{\tilde{t}_2}$, $m_{\tilde{g}}$, $m_t$, and $m_{\tilde{q}}$, combined with expansions in differences of these masses. Following an algorithm suggested in ref. [74], these expansions should allow one to derive a numerical approximation for $C^{(2)}$ in any viable MSSM scenario.

Applying this approach to the scenarios defined in table 10, we find that the deviation of the whole $C^{(2)}$ from the top contribution $C_t^{(2)}$ is rather small, and the second-order coefficient certainly stays within the range $[0,\, 2\,C_t^{(2)}]$. Varying $C^{(2)}$ within this interval, we estimate that the effect of the three-loop SUSY contributions to the gluon-fusion cross section does not exceed 1% in all of the scenarios considered in this study. It is therefore a viable strategy to follow ref. [72] and set $C^{(2)} = C_t^{(2)}$, attributing an uncertainty of $\pm 1\%$ to the final result for the cross section.

# 5 THE TRANSVERSE MOMENTUM SPECTRUM OF THE HIGGS BOSON IN GLUON FUSION

The computation of the transverse momentum distribution of the Higgs boson requires particular attention. In the region of small $p_T$ the presence of large $\log(p_T/m_H)$ terms spoils the accuracy of the fixed order results. To have a physically meaningful prediction these logarithms have to be resummed. In the HQEFT framework, the corrections up to NLO-QCD have been analytically computed and matched with the resummation at NNLL accuracy. The results have been originally implemented in the computer code HqT [132] and later in the parton Monte Carlo software HRES [133]. In the context of matched NLO[1] computation with Parton Shower (PS) Monte Carlo event generators, which implement the resummation at LL algorithmically, the result in the HQEFT has been available for a long time. More recently, the exact matrix elements retaining the full dependence on the quark masses have been implemented in POWHEG [85] and also MC@NLO , allowing for the inclusion of the bottom quark contribution. An analytic approach to include the latter has been presented in ref. [82] and in ref. [134], using the same theoretical framework originally developed for HqT.

## 5.1 Considerations on the resummed computation of the transverse momentum distribution

### 5.1.1 Analytic resummation and the collinear limit

The Higgs boson acquires a transverse momentum $p_T$ because of its recoil against QCD radiation. In fixed-order perturbation theory the emission of initial state massless gauge bosons yields, in the collinear limit, a logarithmic divergence of the Higgs transverse momentum distribution, signaling a breakdown of the perturbative approach, with an effective expansion parameter $\alpha_s(p_T)\log(p_T/m_H) \sim 1$ in the phase space region of vanishing $p_T$. The analytic resummation to all orders of the terms $(\alpha_s(p_T)\log(p_T/m_H))^n$ is performed by exploiting the universal properties of QCD radiation in the collinear limit and restores an acceptable physical behavior (the Sudakov suppression) of the Higgs transverse momentum distribution in the limit $p_T \to 0$.

In the collinear limit $p_T \to 0$ the amplitude for the real emission process $gg \to gH$ diverges and can be written as $\mathcal{M}_{exact} = \mathcal{M}_{div}/p_T + \mathcal{M}_{reg}$. The second term can be neglected and it is possible to recognize that $\mathcal{M}_{div}$ is proportional to the Born amplitude times the appropriate radiation term. This factorization of the amplitude, after $\mathcal{M}_{reg}$ has been neglected, is the starting point for the resummation of the collinear emission to all orders. Indeed, we can iterate this factorization in the case of the amplitude for the emission of $n$ additional partons. In parameter space, this procedure leads to a factorized expression with $n$ divergent emission factors times a term proportional to the Born amplitude. The ex-

1 In the context of NLO+PS computation, NLO is the order of normalization of the distribution. The transverse momentum spectrum is at LO, since at Born level in gluon fusion the Higgs boson has no transverse momentum.

pression for the approximated amplitude describing the emission of up to $n$ partons can be cast in the form of an exponential series, which can thus be summed to all orders. The resummation procedure is valid (accurate and explicitly demonstrated) if and only if the $\mathcal{M}_{reg}$ term can be neglected.

The resummed partonic cross section has a factorized structure given by the product of a universal exponential factor that accounts for the resummation to all orders of the logarithmically divergent terms, multiplied by a process dependent function, that describes the details of the hard scattering process. This factorization requires the introduction of a scale $\mu_{res}$, called resummation scale. The latter defines the region where the resummation is applied and it is usually set to a value between 0 and the hard-scattering scale, e.g. the Higgs boson mass. A customary choice in the literature is $\mu_{res} = m_h/2$. The precise choice of this value will be further discussed in the next sections.

The matching procedure requires that the integral of the Higgs transverse momentum distribution be equal to a constant, which is conventionally set to the value of the fixed order total cross section. This constraint holds exactly for any choice of $\mu_{res}$, so that any variation of the resummation scale modifies the shape of the distribution but not its integral and yields thus a correlation between low- and high-$p_T$ regions.

### 5.1.2 Numerical resummation in the NLO+PS framework

Another approach to the resummation of terms enhanced by the factor $\log(p_T/m_H)$ is the one obtained in the context of Parton Shower (PS) Monte Carlo, where the multiple emission of partons is numerically simulated via the Shower algorithm. The matching between fixed order NLO-QCD results and the PS has been discussed in [86, 135] and it is implemented in several tools regularly used in the experimental analyses. In a sufficiently general way we can write the matching formula as

$$d\sigma = \bar{B}^s(\Phi_B)d\Phi_B \left\{ \Delta^s_{t_o} + \Delta^s_t \frac{R^s(\Phi)}{B(\Phi_B)} d\Phi_r \right\} + R^f d\Phi + R_{reg} d\Phi. \tag{163}$$

The phase space is factorized into the product of the Born and the real emission components, $d\Phi = d\Phi_B\, d\Phi_r$. The Born squared matrix element is denoted by B while $\bar{B}$ is the NLO normalization factor. The latter is defined as

$$\bar{B}^s(\Phi_B) = B(\Phi_B) + \hat{V}_{fin}(\Phi_B) + \int \hat{R}^s(\Phi_B, \Phi_r) d\Phi_r \,. \tag{164}$$

In this formula $\hat{V}_{fin}$ represents the UV- and IR-regularized virtual contribution. We use the hat to indicate that an amplitude has been IR-regularized. The partonic subprocesses with the emission of an additional real parton can be split in two groups: those that are divergent in the limit of collinear emission, called $R_{div}$, and the ones that are instead regular, $R_{reg}$. We can further subdivide the squared matrix elements of the divergent subprocesses in two parts:

$$R_{div} = R^s + R^f. \tag{165}$$

The term $R^s$ contains the collinear singularity of $R_{div}$, while $R^f$ is a finite remainder. Finally, we use the symbol $\Delta^s_t$ for the Sudakov form factor, with $t$ as the showering ordering variable:

$$\Delta^s_{\bar{t}} = e^{-\int \frac{dt}{t} \frac{R^s}{B} d\Phi_r \theta(t-\bar{t})} . \tag{166}$$

The splitting of $R_{div}$ in eq. (165) is defined up to a finite part that can be reabsorbed in $R^s$. In the literature two different choices have been adopted: in POWHEG $R^s = R_{div}$, while in MC@NLO $R^s \propto \alpha_s P_{ij} B$ is proportional to the product of the Born matrix elements times the relevant Altarelli-Parisi splitting functions.

It is interesting to observe that different definitions for $R^s$ generate higher-order effects in the matched differential cross section. The possibility of defining the finite part $R^f$ in an arbitrary way can be exploited to parameterize the uncertainties related to the matching procedure as we will see in section 5.6.

## 5.2 POWHEG-BOX implementation of $gg \to \phi$

In this section we briefly discuss our implementation of the gluon-fusion Higgs production process in the POWHEG-BOX framework, following closely ref. [85] (see also ref. [136, 137]).

The generation of the hardest emission is done in POWHEG by specializing eq. (163) to the gluon fusion process:

$$\begin{aligned} d\sigma &= \bar{B}(\bar{\Phi}_1)\, d\bar{\Phi}_1 \left\{ \Delta\left(\bar{\Phi}_1, p_T^{min}\right) + \Delta\left(\bar{\Phi}_1, p_T\right) \frac{R\left(\bar{\Phi}_1, \Phi_{rad}\right)}{B\left(\bar{\Phi}_1\right)} d\Phi_{rad} \right\} \\ &+ \sum_q R_{q\bar{q}}\left(\bar{\Phi}_1, \Phi_{rad}\right) d\bar{\Phi}_1 d\Phi_{rad} . \end{aligned} \tag{167}$$

In the equation above the variables $\bar{\Phi}_1 \equiv (M^2, Y)$ denote the invariant mass squared and the rapidity of the Higgs boson, which describe the kinematics of the Born (i.e., lowest-order) process $gg \to \phi$. The variables $\Phi_{rad} \equiv (\xi, y, \phi)$ describe the kinematics of the additional final-state parton in the real emission processes. In particular, denoting by $k_2'$ the momentum of the final-state parton in the partonic center-of-mass frame, or

$$k_2' = k_2'^0 (1, \sin\theta \sin\phi, \sin\theta \cos\phi, \cos\theta), \tag{168}$$

we have

$$k_2'^0 = \frac{\sqrt{s}}{2}\xi, \qquad y = \cos\theta , \tag{169}$$

where $s$ is the partonic center-of-mass energy squared.

Finally, the last term in eq. (167) describes the effect of the $q\bar{q} \to \phi g$ channel, which has been kept apart in the generation of the first hard emission because it does not factorize into the Born cross section times an emission factor.

We now discuss the various terms appearing in eq. (167) in more detail. We have:

$$\begin{aligned}\bar{B}(\bar{\Phi}_1) &= B_{gg}(\bar{\Phi}_1) + V_{gg}(\bar{\Phi}_1) \\ &+ \int d\Phi_{rad} \left\{ \hat{R}_{gg}(\bar{\Phi}_1, \Phi_{rad}) + \sum_q \left[ \hat{R}_{gq}(\bar{\Phi}_1, \Phi_{rad}) + \hat{R}_{qg}(\bar{\Phi}_1, \Phi_{rad}) \right] \right\} + \text{c. r.}\end{aligned} \tag{170}$$

where

$$B_{gg}(\bar{\Phi}_1) = \mathcal{B}_{gg}(\bar{\Phi}_1)\, \mathcal{L}_{gg}\,, \tag{171}$$

$$V_{gg}(\bar{\Phi}_1) = \mathcal{V}_{gg}(\bar{\Phi}_1)\, \mathcal{L}_{gg}\,, \tag{172}$$

$$\hat{R}_{gg}(\bar{\Phi}_1, \Phi_{rad}) = \hat{\mathcal{R}}_{gg}(\bar{\Phi}_1, \Phi_{rad})\, \mathcal{L}_{gg}\,, \tag{173}$$

$$\hat{R}_{gq}(\bar{\Phi}_1, \Phi_{rad}) = \hat{\mathcal{R}}_{gq}(\bar{\Phi}_1, \Phi_{rad})\, \mathcal{L}_{gq}\,, \tag{174}$$

$$\hat{R}_{qg}(\bar{\Phi}_1, \Phi_{rad}) = \hat{\mathcal{R}}_{qg}(\bar{\Phi}_1, \Phi_{rad})\, \mathcal{L}_{qg}\,, \tag{175}$$

with $\mathcal{L}_{ab}$ the luminosity for the partons $a$ and $b$. In eq. (170) " c. r." denotes the collinear remnants multiplied by the relevant parton luminosity. The remnants are the finite leftovers after the subtraction of the initial-state collinear singularities into the parton distribution function is performed, and their explicit expressions are given in eqs. (2.36), (2.37) and (3.7)–(3.10) of ref. [136].

The function $\mathcal{B}_{gg}(\bar{\Phi}_1)$ in eq. (171) represents the squared matrix element of the Born contribution to the process, averaged over colors and helicities of the incoming gluons, and multiplied by the flux factor $1/(2M^2)$. It is given by

$$\mathcal{B}_{gg}(\bar{\Phi}_1) = \frac{G_\mu\, \alpha_s^2(\mu_R^2) M^2}{256\sqrt{2}\,\pi^2} \left| \mathcal{G}^{1\ell} \right|^2\,, \tag{176}$$

where $\mathcal{G}$ is the form factor for the coupling of the Higgs boson with two gluons, whose explicit form depends on the particle content of the model considered and will be detailed in the following sections. It is decomposed in one- and two loop parts as

$$\mathcal{H} = \mathcal{G}^{1\ell} + \frac{\alpha_s}{\pi}\, \mathcal{G}^{2\ell} + \mathcal{O}(\alpha_s^2)\,. \tag{177}$$

The regularized two-loop virtual contributions are contained in

$$\mathcal{V}_{gg}(\bar{\Phi}_1) = \frac{\alpha_s}{\pi} \left[ C_A \frac{\pi^2}{3} + \beta_0 \ln\left(\frac{\mu_R^2}{\mu_F^2}\right) + 2\,\mathrm{Re}\left(\frac{\mathcal{G}^{2\ell}}{\mathcal{G}^{1\ell}}\right) \right] \mathcal{B}_{gg}(\bar{\Phi}_1)\,. \tag{178}$$

In the equation above, $\mu_R$ and $\mu_F$ are the renormalization and factorization scale, respectively, $C_A = N_c$ ($N_c$ being the number of colors), and $\beta_0 = (11\, C_A - 2\, N_f)/6$ ($N_f$ being the number of active flavors) is the one-loop beta function of the strong coupling.

The hatted functions $\hat{\mathcal{R}}_{ij}$ in eqs. (173)–(175) are the Frixione, Kunst and Signer [138, 139] infrared-subtracted counterparts of $\mathcal{R}_{ij}$

$$\hat{\mathcal{R}}_{ij}(\bar{\Phi}_1, \Phi_{rad}) = \frac{1}{\xi} \left\{ \frac{1}{2} \left(\frac{1}{\xi}\right)_+ \left[ \left(\frac{1}{1-y}\right)_+ + \left(\frac{1}{1+y}\right)_+ \right] \right\} \left[ (1-y^2)\, \xi^2\, \mathcal{R}_{ij}(\bar{\Phi}_1, \Phi_{rad}) \right]\,, \tag{179}$$

where $\mathcal{R}_{ij}$ are the squared amplitudes, averaged over the incoming helicities and colors and multiplied by the flux factor $1/(2s)$, for the NLO partonic subprocesses ($gg \to \phi g, gq \to \phi q, qg \to q\phi$):

$$\mathcal{R}_{gg}(\bar{\Phi}_1, \Phi_{rad}) = \frac{3\, G_\mu\, \alpha_s^3\, M^8}{\sqrt{2}\,\pi\, 2\, s} \frac{|\mathcal{A}_{gg}(s,t,u)|^2}{stu}\,, \tag{180}$$

$$\mathcal{R}_{gq}(\bar{\Phi}_1, \Phi_{rad}) = -\frac{G_\mu\, \alpha_s^3\, M^4}{\sqrt{2}\,\pi\, 6\, s} \frac{s^2+u^2}{(s+u)^2\, t}\, |\mathcal{A}_{qg}(s,t,u)|^2\,, \tag{181}$$

$$\mathcal{R}_{qg}(\bar{\Phi}_1, \Phi_{rad}) = -\frac{G_\mu\, \alpha_s^3\, M^4}{\sqrt{2}\,\pi\, 6\, s} \frac{s^2+t^2}{(s+t)^2\, u}\, |\mathcal{A}_{qg}(s,u,t)|^2\,, \tag{182}$$

where $s = M^2/(1-\xi)$, $t = -(s/2)\,\xi\,(1+y)$ and $u = -(s/2)\,\xi\,(1-y)$.

The complete real matrix elements that enter the POWHEG Sudakov form factor, eq. (166), read

$$R(\bar{\Phi}_1, \Phi_{rad}) = R_{gg}(\bar{\Phi}_1, \Phi_{rad}) + \sum_q \left[R_{gq}(\bar{\Phi}_1, \Phi_{rad}) + R_{qg}(\bar{\Phi}_1, \Phi_{rad})\right]\,, \tag{183}$$

$$B(\bar{\Phi}_1) = B_{gg}(\bar{\Phi}_1)\,, \tag{184}$$

where the functions $R_{ab}$ are the non-infrared-subtracted counterparts of eqs. (173)–(175). The probability for the emission of the first and hardest parton is described with the exact matrix element in all the phase space regions.

Finally, the contribution of the $q\bar{q} \to \phi g$ channel is

$$R_{q\bar{q}}(\bar{\Phi}_1, \Phi_{rad}) = \mathcal{R}_{q\bar{q}}(\bar{\Phi}_1, \Phi_{rad})\, \mathcal{L}_{q\bar{q}}, \tag{185}$$

with

$$\mathcal{R}_{q\bar{q}}(\bar{\Phi}_1, \Phi_{rad}) = \frac{4\, G_\mu\, \alpha_s^3\, M^4}{\sqrt{2}\,\pi\, 9\, s} \frac{t^2+u^2}{(t+u)^2\, s}\, |\mathcal{A}_{q\bar{q}}(s,t,u)|^2\,. \tag{186}$$

The functions $\mathcal{A}_{gg}$, $\mathcal{A}_{qg}$ in eqs. (180)–(182) and $\mathcal{A}_{q\bar{q}}$ in eq. (186) are the same that appear in section 3.1.1.

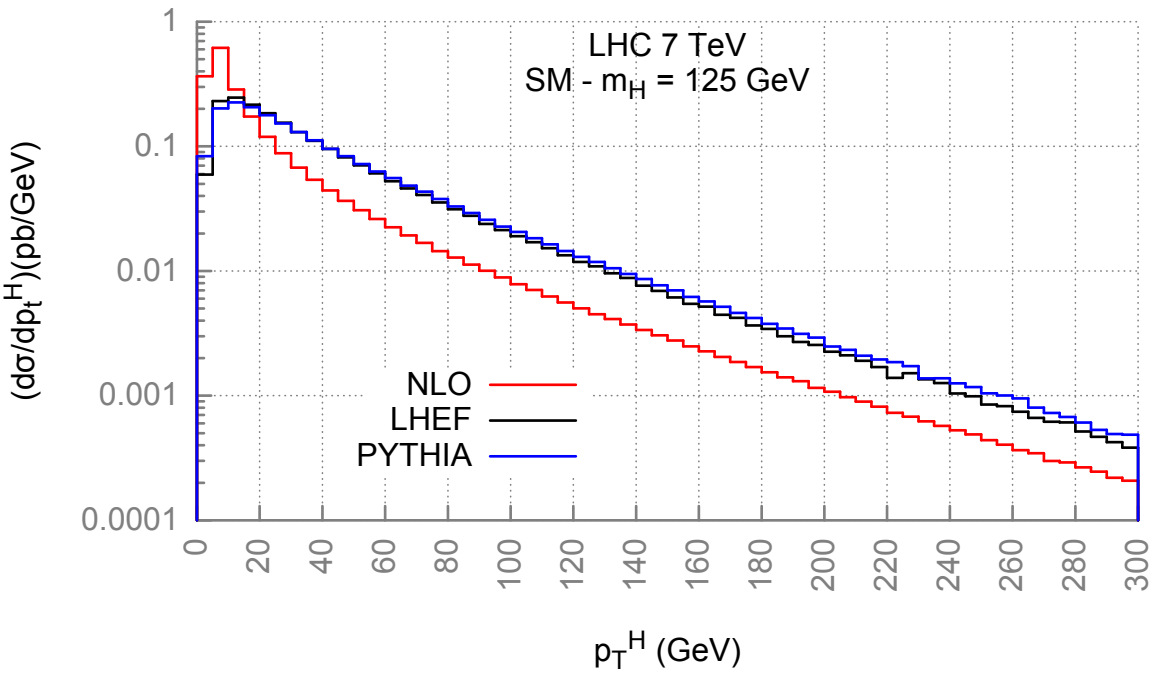


**Figure 45:** Transverse momentum distribution of the Higgs boson in the gluon fusion production. In red we plot the distribution at fixed order, in black at LHEF level and in blue after showering with PYTHIA.

## 5.3 The transverse momentum spectrum of the Higgs boson in the SM

We now use our POWHEG-BOX implementation to study the $p_T^H$ spectrum in the SM for an Higgs boson with mass $m_H = 125$ GeV. We use the MSTW2008 PDF set and the value of $\alpha_s$ associated with it, $m_t = 172.5$ GeV and $m_b = 4.75$ GeV. The renormalization and factorization scale are always assumed equal to $m_H$. In figure 45 we plot the transverse momentum of the Higgs boson in three approximations. In red we show the fixed order calculation obtained with POWHEG at NLO. The distribution tends to diverge in the $p_T^H \to 0$ limit due to the potentially large terms of the form $\log(p_T^H/m_H)$ that need to be resummed[2]. The black curve represents the distribution at the Les Houches Event File (LHEF) level. LHEF is a standardized file format used by MC event generators to write event records to files, with the aim of helping interoperability between the software used in the field. In our case it stores the events after the emission of the first, hardest, radiated parton. This result is not properly physical, however it can be used to appreciate the effect of the POWHEG Sudakov form factor. Indeed, we can see here that the Sudakov form factor has already restored the physical behavior of the distribution, with the distribution going to zero in the $p_T^H \to 0$ limit. The effect of subsequent emissions can be seen by looking at the blue curve, which represents the $p_T^H$ distribution after the full showering of the events by PYTHIA. The distribution after parton shower, in absence of acceptance cuts, has the same qualitative features of the LHEF one, though there are some quantitative differences due to the additional emission of radiation by

2 In this plot the collinear divergence of the real matrix amplitudes is already subtracted, moreover the first bin contains also the NLO virtual corrections to properly normalize the distribution to the NLO total inclusive cross section

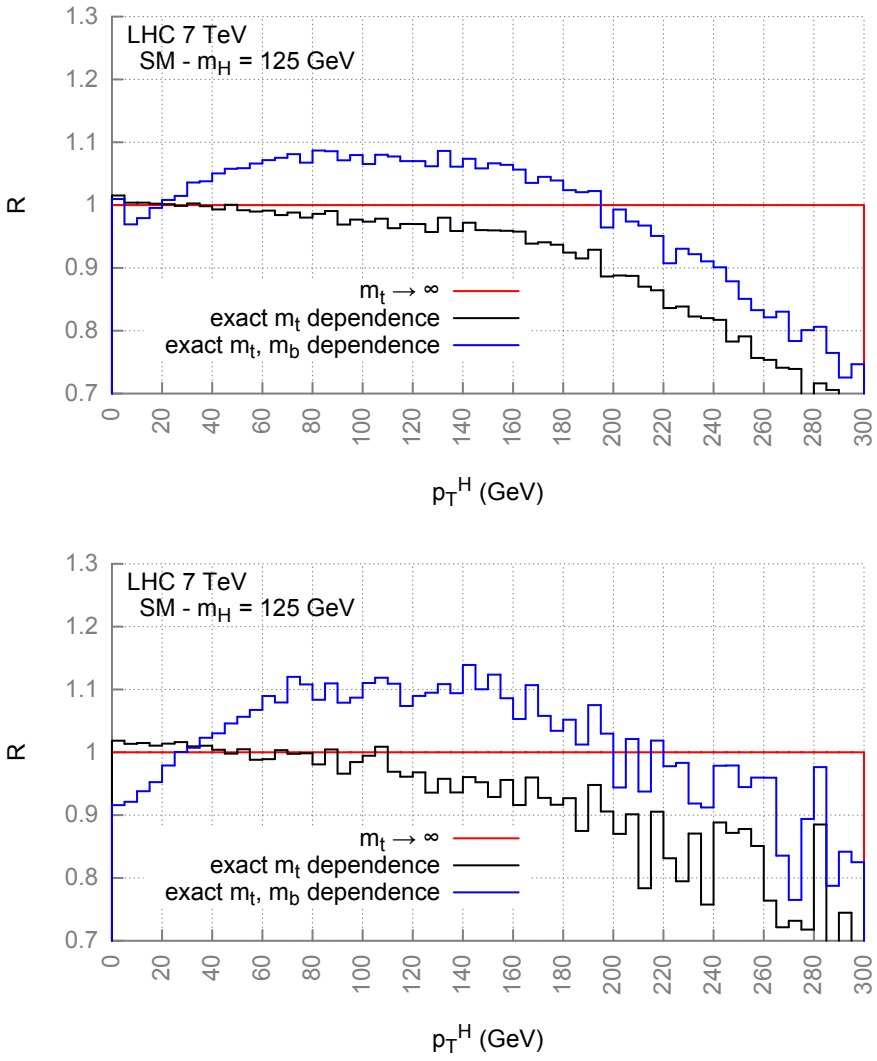


**Figure 46:** Ratio of the shape between the normalized $p_T^H$ distribution in the SM with top and bottom (blue) and only top (black) running in the loops with the one obtained in the HQEFT (red) at NLO (top) and after showering (bottom).

the shower.

### 5.3.1 Top-mass effects and inclusion of the bottom contribution

As we have pointed out in subsection 2.1.1, in the SM the HQEFT gives a good approximation of the total inclusive cross section for Higgs production in gluon fusion. However in the case of the $p_T^H$ differential distribution the situation is more complex. In figure 46 we plot in blue the ratio of the shape[3] of

3 By shape of the distribution we mean the distribution normalized to one, i.e. the distribution divided by the total cross section at NLO.

transverse momentum distribution computed in the SM with the top and bottom quark running in the loops with respect to the one in the HQEFT; to separate the effects of the two quarks, in black we show the ratio of the shape computed just with the top quark contribution included to the HQEFT one; on the top we show the plot at NLO while on the bottom the curves are computed after the showering of the events with PYTHIA.

At NLO, we can see that top quark effects start to be relevant once we come close to the top mass threshold and result in a suppression of the differential cross section. The introduction of the bottom quark, which adds another mass scale to the process, yields a suppression of the low-$p_T^H$ tail of the distribution up to an intermediate scale of about 80 GeV; after, the top quark influence starts to be dominant and we recover the same shape of the case where only the top quark is running in the loop. It is important to stress that in the SM the bottom quark bends the shape of the distribution through the interference term with the top quark in the full amplitude.

From the right plot we can observe that the resummation of the collinear logarithms in the POWHEG-BOX +PS framework enhances the effects already observed at fixed order. This behavior can be explained in the following terms. As can be read from eq. (163), the probability of emitting the Higgs in association with a parton depends on the product $\Delta \times R/B$, where R is the squared matrix element for real-parton emission, B is the Born amplitude, and $\Delta$ is the Sudakov factor, which in turn is exponentially suppressed by R/B, see eq. (166). In the HQEFT case, the emission probability is computed in terms of the ratio $R(t,\infty)/B(t,\infty)$. For small $p_T^H$, the Sudakov factor with exact top and bottom mass dependence, $\Delta(t+b,\mathrm{exact})$, used in our implementation is smaller than the corresponding factor $\Delta(t,\infty)$ in the HQEFT, because $R(t+b,\mathrm{exact})/B(t+b,\mathrm{exact}) > R(t,\infty)/B(t,\infty)$. This inequality holds for two reasons: first, the $p_T^H$ distribution is proportional to R, and $R(t+b,\mathrm{exact}) > R(t,\infty)$ for $p_T^H < 200$ GeV [140]; second, the inclusion of the bottom contribution reduces the LO cross section with respect to the result obtained in the HQEFT [27]. Thus, as shown in the right plot, for small $p_T^H$ the Sudakov factor suppresses the $p_T^H$ distribution by almost 10% with respect to the result obtained in the current H implementation. Since the emission probability is also directly proportional to the ratio R/B, starting from $p_T^H \simeq 30$ GeV this factor prevails over the Sudakov factor, and the distribution with exact dependence on the quark masses becomes larger than the one in the HQEFT by up to $\sim 15\%$. Finally, for $p_T^H \gtrsim m_t$ the inclusion of the full top-mass dependence leads to a negative correction, similar to the one already observed in the pure NLO-QCD calculation. The inclusion of multiple gluon emission with the PYTHIA QCD-PS (lower panels) does not change dramatically – in the absence of acceptance cuts – the results obtained including only the hardest emission.

A comparison with MC@NLO shows that the specific structure of the Sudakov form factor is instrumental to the way the effect of the bottom loops is propagated to the final resummed distribution. Indeed we can see from figure 47 that when the Sudakov form factor is proportional to the Altarelli-Parisi splitting function, the final distribution will not show a suppression for small $p_T^H$ and the enhancement in the intermediate region is suppressed with respect to the fixed order result. It is also interesting to point out that on the other hand for the top quark only the two codes yield a similar distortion of the shape. Finally, at variance with POWHEG , in the high-$p_T^H$ tail the NLO behavior is recovered.

These differences between the two codes are an indication of the complexity of the problem, that now includes four mass scales: one at the top mass; one at the Higgs mass; one at the bottom mass; and one which is the $p_T$ of the emitted gluon. The appearance of the bottom mass scale changes the collinear behavior of the real emission amplitude that, as we have seen in section 5.1.1, determines the choice of

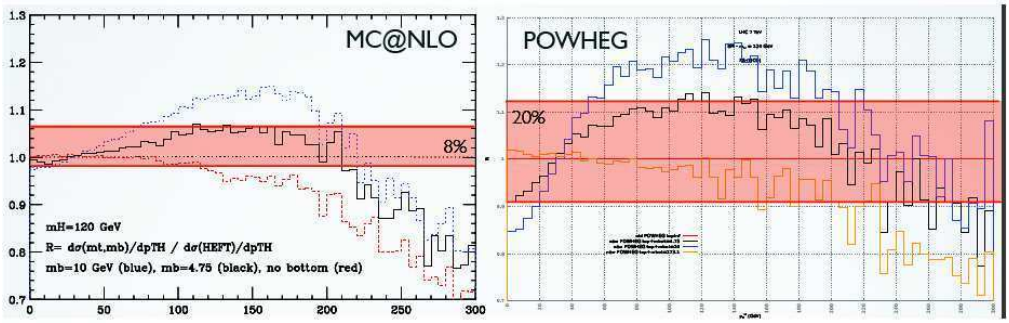


**Figure 47:** Ratio between the transverse momentum distribution in the SM over the one in the HQEFT as computed by MC@NLO (left) and POWHEG (right), for different values of the bottom mass (from a talk by S.Frixione).

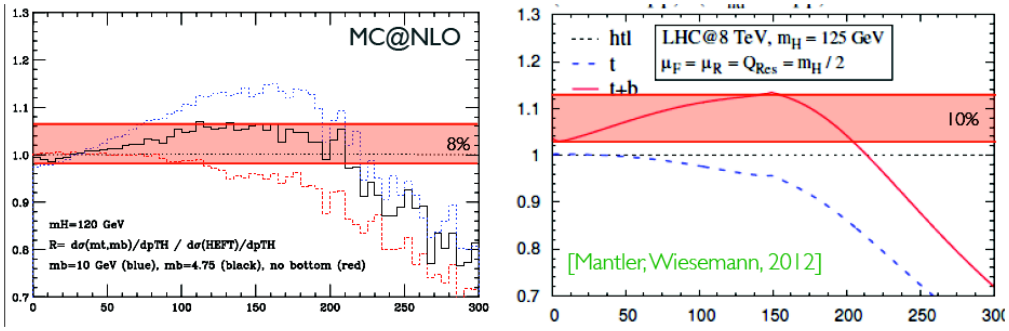


**Figure 48:** Ratio between the transverse momentum distribution in the SM over the one in the HQEFT as computed by MC@NLO (left) and by Mantler et al. [134] (right), for both the top-only and the top-and-bottom case (from a talk by S.Frixione).

the appropriate resummation scale for the process. In their default configuration the two codes differ significantly in the way they fix the latter. In POWHEG the bottom scale is dynamically and automatically included by the usage of the real matrix element in the POWHEG Sudakov form factor; in MC@NLO the default choice for the resummation scale is fixed and of the order of $m_H/2$ and therefore there is no accounting for the bottom mass scale. Indeed, one obtains the same result of MC@NLO if an analytic resummation with the same scale choice is performed [134], as can be seen from figure 48, with a variation band of the order of 10% for the inclusion of both the top and bottom quark, to be compared with a 8% band for MC@NLO . In the case of the inclusion of only the top quark contribution, we see that again the analytic resummation yields the same results as POWHEG and MC@NLO .

It is important to stress that all these discrepancies between the codes are due to higher-order effects and that formally all the results from POWHEG and MC@NLO have the same accuracy. Recently, a multi-scale approach to the problem has been proposed in ref. [82]. In chapter 5.6 we will also address the issue of the choice of multiple resummation scales more in detail, starting from the study the collinear behavior of the real emission amplitude, and we will compare with the results of ref. [82]. Finally, in appendix E we report of another approach to the study of the inclusion of the top mass effects and of the bottom contribution in POWHEG , based on the idea of including them at fixed order, to compare more closely with what happens with the standard MC@NLO configuration.

## 5.4 The transverse momentum spectrum in the 2HDM

As we have seen in section 2.2, the 2HDM is characterized by the fact that the coupling of the Higgs boson to the quarks can be enhanced/suppressed significantly. We want to understand how a modification of the *relative* importance of the coupling of the top and bottom quark changes the shape of the transverse momentum distribution. The kind of 2HDM befit for this purpose is type-II. At this level we are not interested in a phenomenological study of the 2HDM, we will therefore take the neutral scalar mixing angle equals to $\alpha = -\pi/4$ for the light Higgs $h$ and $\alpha = \pi/4$ for the heavy Higgs $H$. This implies an equal rescaling factor for the coupling of the quarks to the two Higgses, with respect to the dependence on $\alpha$. Hence, we can assume that the only dependence left on the 2HDM parameters is the one from $\tan\beta$: for large values of $\tan\beta$, the bottom coupling will be enhanced, while for values of $\tan\beta$ less than one it is the top quark coupling that will be enhanced. We study the change of the shape of the distribution for a light Higgs, $m_h = 125$ GeV, and a heavy Higgs with $m_H = 500$ GeV, for $\tan\beta = 40$ and $\tan\beta = 0.1$.

In figure 49 we show the results in the bottom enhanced scenario ($\tan\beta = 40$). For a light Higgs we observe that raising the bottom coupling and suppressing the top one corresponds to an enhancement of the low-end of $p_T^h$ distribution for a Higgs of $m_h = 125$ GeV, while it tends to slightly suppress the same region for $m_H = 500$ GeV. It is important to underline that in this case, at variance with the SM, the dominant effect of the bottom does not come from the interference term with the top amplitude but from the pure squared modulus amplitude. In figure 50 we plot on the other hand the results for the case where the top is enhanced and the bottom suppressed. We see again that in the light Higgs case this yields an enhancement for low $p_T^h$. In the case of the heavy Higgs, no substantial difference is observed.

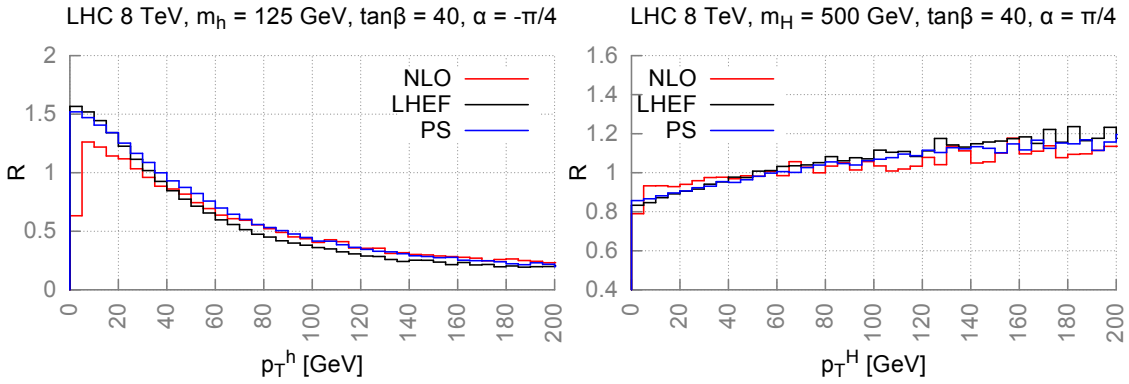


**Figure 49:** Shape ratio for the transverse momentum distribution in the 2HDM for $\tan\beta = 40$, in the case of a Higgs of $m_h = 125$ GeV (left) and of $m_H = 500$ GeV (right) with respect to the one of SM Higgs of equal mass. In red we show the the result at NLO, in blue the result after showering of the events. The computations is performed at the LHC with $\sqrt{s} = 8$ TeV.

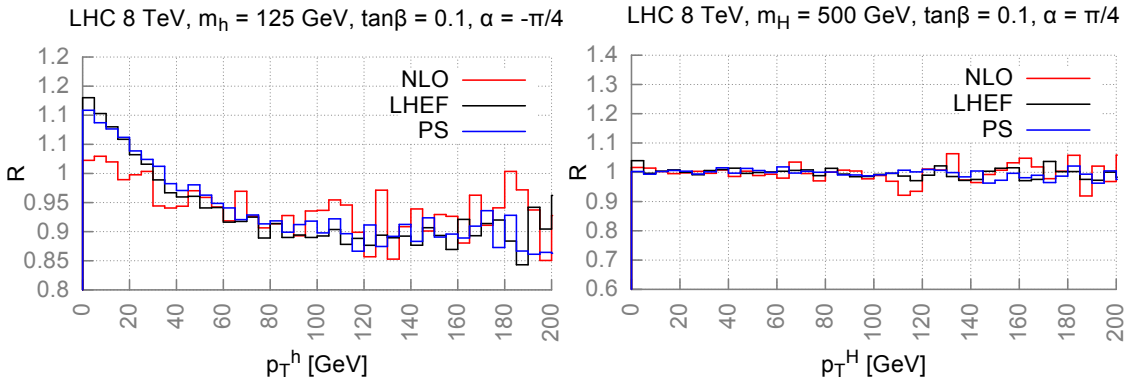


**Figure 50:** Shape ratio for the transverse momentum distribution in the 2HDM for $\tan\beta = 0.1$, in the case of a Higgs of $m_h = 125$ GeV (left) and of $m_H = 500$ GeV (right) with respect to the one of SM Higgs of equal mass. In red we show the the result at NLO, in blue the result after showering of the events. The computations is performed at the LHC with $\sqrt{s} = 8$ TeV.

## 5.5 The transverse momentum spectrum in the MSSM

As for the type-II 2HDM, there are regions of the MSSM parameter space where the Higgs coupling to bottom quarks is enhanced. For the correspondent parameter choices we expect the transverse-momentum distribution of a scalar produced via gluon fusion to be distorted with respect to the corresponding distribution of a SM Higgs boson [141–143]. We now report the results that we published in ref. [41] for h and H, with the addition of the the corresponding curve for the pseudoscalar A.

In order to investigate the changes to the $p_T^\phi$ distribution that occur in the MSSM, we consider the point in the *light stop* scenario with $M_A = 130$ GeV and $\tan\beta = 40$, characterized by the fact that both scalars have non-standard couplings to quarks and masses in the vicinity of the LHC signal (indeed, FeynHiggs predicts $M_h = 122.4$ GeV and $M_H = 129.3$ GeV). This point is likely to be already excluded by the ATLAS and CMS searches for neutral Higgs bosons decaying into $\tau^+\tau^-$ pairs, but it can still provide a useful illustration of the expected size of this kind of effects. The simulations are run for the LHC with $\sqrt{s} = 8$ TeV. We used the MSTW2008-NLO PDF set and its corresponding values of $\alpha_s$.

In figures 51 we show the ratio of the transverse-momentum distribution for a MSSM scalar produced via gluon fusion over the corresponding distribution for a SM Higgs with the same mass. The plot on the left refers to the lightest scalar h, while the plot on the right refers to the heaviest scalar H. In figure 52 we plot the same quantity for a MSSM pseudoscalar Higgs boson.

In each plot, the continuous (red) line represents the ratio of distributions computed at NLO by `SusHi` , while the two histograms are computed with the `POWHEG` implementation of gluon fusion of [85], modified by the adoption of the on-shell renormalization scheme for the squark parameters and the inclusion of the results of [70] for the squark contributions to H production. In particular, the solid (black) histogram represents the ratio of distributions computed in a pure (i.e., fixed-order) NLO calculation, while in the dashed (blue) histogram the distributions are computed with our `POWHEG-BOX` implementation. As parton-shower we used PYTHIA[144]).

The plots in 51 and 52 show that, in this point of the MSSM parameter space, the enhancement of the Higgs-bottom coupling results in both an enhancement of the total cross section and a distortion of the transverse-momentum distribution, in particular for the heaviest scalar H (note the difference in the scale between the left and the right plot). The effect of the resummation in `POWHEG` and the unitarity constraint implemented in the matching procedure of NLO matrix elements with parton shower make the transverse-momentum distribution of the Higgs bosons harder. The comparison between the solid and dashed histograms shows that for h this effect is somewhat stronger than in the SM, while for H it is somewhat weaker. On the other hand for the pseudoscalar we see that the distribution is softer than the corresponding SM one.

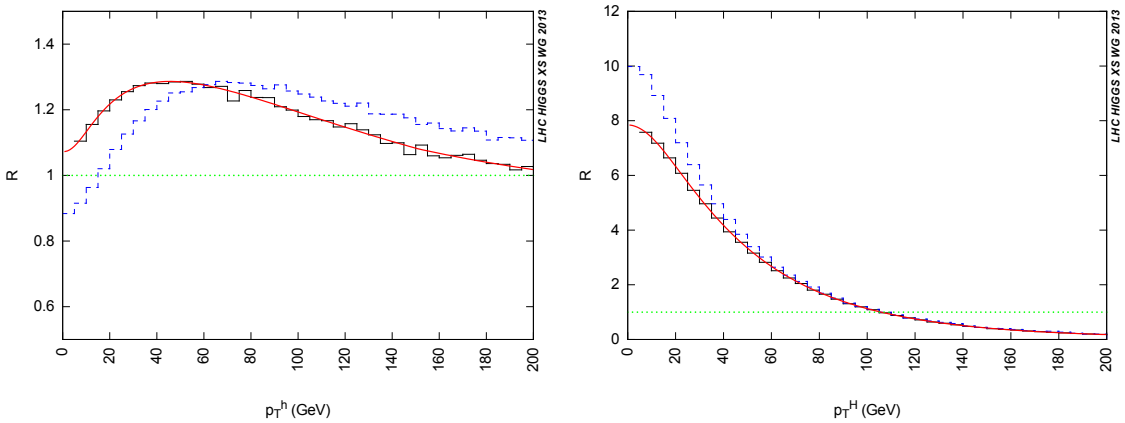


**Figure 51:** Ratio of the transverse-momentum distribution for the MSSM scalar h (left) or H (right) over the distribution for a SM Higgs with the same mass, in the *light stop* scenario with $M_A = 130$ GeV and $\tan\beta = 40$. The meaning of the different curves is explained in the text.

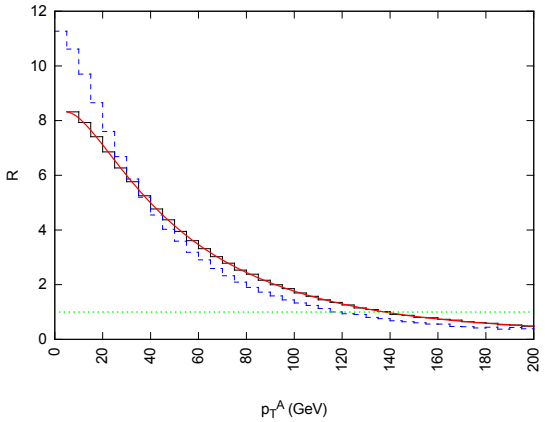


**Figure 52:** Ratio of the transverse-momentum distribution for the MSSM pseudoscalar A over the distribution for a SM Higgs with the same mass, in the *light stop* scenario with $M_A = 130$ GeV and $\tan\beta = 40$. The meaning of the different curves is explained in the text.

## 5.6 The choice of the resummation scale and uncertainty estimation

### 5.6.1 The role of the damping factor $h$ in the POWHEG-BOX framework

We have seen in subsection 5.1.2 that there is an ambiguity in the definition of the finite part of the real matrix element that enters the Sudakov form factor in the POWHEG formalism. Indeed, in the POWHEG-BOX framework, the separation between $R^s$ and $R^f$ can be achieved in a dynamical way using the $D_h$ damping factor, that is defined as

$$D_h = \frac{h^2}{h^2 + (p_T)^2}. \tag{187}$$

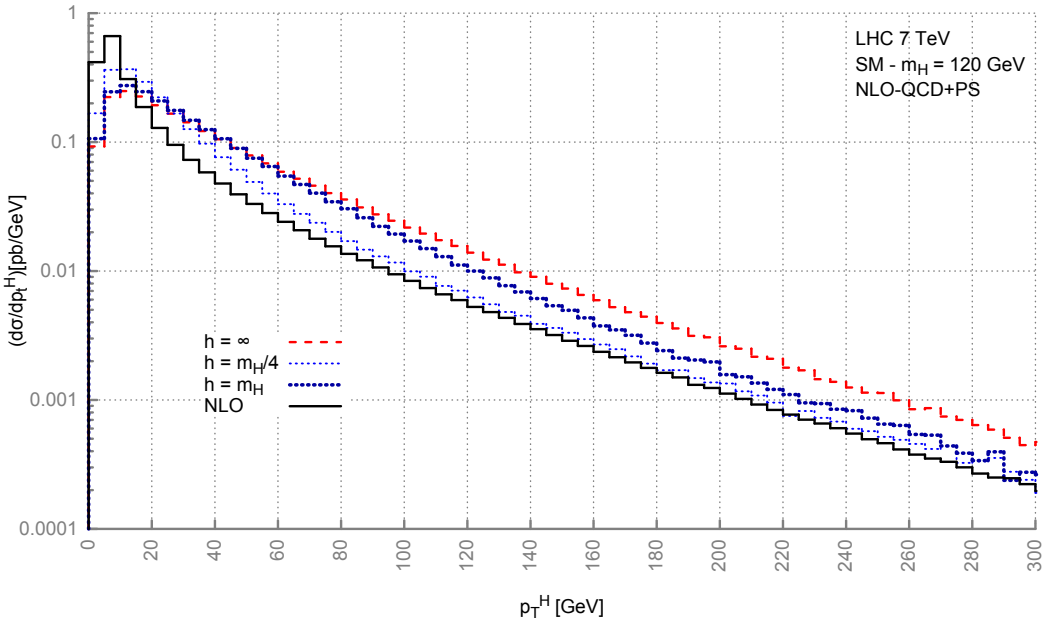


**Figure 53:** Dependence of the Higgs transverse momentum distribution on the value of the scale $h$ used in the damping factor $D_h$. In dashed-red we plot the result with the standard configuration; in black we have the fixed order result; with the thin- (thick-) blue dots we represents the results with h equal to $m_H/4$ ($m_H$).

The divergent and the regular part of $R_{div} = R^s + R^f$ are then recast in the following form

$$R^s = \frac{h^2}{h^2 + (p_T)^2} R_{div}\,, \qquad R^f = \frac{(p_T)^2}{h^2 + (p_T)^2} R_{div}. \tag{188}$$

The role of the scale $h$ is to separate the low transverse-momentum region from the high one and it therefore specifies the range of momenta for which the Sudakov form factor is possibly different than 1. In the limit of $p_T \to 0$ we obtain that $R^s \to R_{div}$ and that $R^f \to 0$. In this limit the effect of multiple parton radiation is sizable, because of the Sudakov form factor suppression. On the other hand, when $p_T \gg h$ we have $R^s \to 0$ and $R_f \to R_{div}$ and the Sudakov form factor tends to 1. In this latter regime the emission of a real parton is described at fixed order by the pure matrix elements $R^f = R_{div}$.

The differential distribution generated according to eq. (163) contains higher order terms due to the product of $\bar{B} \times R^s$. Indeed in the large $p_T$ region we have

$$\begin{aligned} d\sigma &= \bar{B}(\Phi_B) d\Phi_B \left\{ \Delta_{t_0} + \Delta_t \frac{R^s(\Phi)}{B(\Phi_B)} d\Phi_r \right\} + R^f d\Phi + R_{reg} d\Phi \\ &\approx \bar{B}(\Phi_B) \frac{R^s(\Phi)}{B(\Phi_B)} d\Phi + R^f d\Phi + R_{reg} d\Phi \\ &\equiv K(\Phi_B) R^s(\Phi) d\Phi + R^f d\Phi + R_{reg} d\Phi, \\ K(\Phi_B) &:= \frac{\bar{B}(\Phi_B)}{B(\Phi_B)} = 1 + \mathcal{O}(\alpha_s). \end{aligned} \tag{189}$$

Originally the factor $D_h$ was introduced to dampen the $R^s$ contribution at large $p_T$ and to recover the exact NLO result in this kinematic region.

In figure 53, it is possible to observe how well the resummed distribution recovers the NLO behavior in the high-$p_T$ region for various values of the scale $h$. We see as expected that the lower the value of $h$, the lower the value of $p_T$ at which this happens.

The total NLO cross-section is always preserved for any value of $h$, as can checked by integrating eq. (163) over the whole phase space. This property implies in turn that the low- and high-$p_T$ region of the differential cross section are correlated. Any increase of the distribution at low-$p_T$ translates in a decrease of the high-$p_T$ tail and vice versa.

The role effectively played by scale $h$ is analogous to the one described in subsection 5.1.1 for the resummation scale $\mu_{res}$: indeed, for $p_T < h$ or for $p_T < \mu_{res}$ the Sudakov suppression yields a regular behavior of the Higgs transverse momentum distribution, whereas for $p_T$ larger than these scales the fixed-order description is recovered. It should however be remarked that $\mu_{res}$ and $h$ have a completely different origin. The resummation scale $\mu_{res}$ necessarily appears as the scale at which the resummation is defined and the factorization of the partonic cross section implemented; the damping factor $D_h$ is instead a convenient $p_T$-dependent parameterization of the ambiguity in the definition of $R^s$.

### 5.6.2 The $gg \to Hg$ subprocess

As we have recalled in subsection 5.1.1 and subsection 5.1.2, to properly resum the collinear logarithms we should be in a kinematic region where the collinear approximation accurately describes the emission process. We now try to study this issue in a specific subprocess, namely $gg \to Hg$. This subprocess gives the dominant contribution to the gluon fusion channel for Higgs production.

#### *Helicity amplitudes and kinematic variables*

We consider now the amplitude for this process in two approximations: the exact expression, $\mathcal{M}$, and its collinear divergent part $\mathcal{M}_{div}/p_T$. We define the ratio $C(p_T)$

$$C(s, p_T, m_H^2) = \frac{|\mathcal{M}(s, p_T, m_H^2)|^2}{|\mathcal{M}_{div}(s, m_H^2)/p_T|^2}\,, \tag{190}$$

which represents how the exact squared matrix element differs from its collinear approximation as a function of $p_T$. We observe that by construction we have that $\lim_{p_T \to 0} C(p_T) = 1$.

The regular part of the amplitude becomes non negligible with respect to its collinear counterpart for values of $\bar{p}_T$ such that

$$|C(s, \bar{p}_T, m_H^2) - 1| > \bar{C}. \tag{191}$$

To fix the setup of our study we choose $\bar{C} = 0.1$. This value is arbitrary, but its order of magnitude can be justified in the framework of a QCD calculation, since the size of the terms without a collinear logarithmic enhancement is $\alpha_s$ times a coefficient of order 1.

The amplitude of the process $gg \to Hg$ is a function of two independent kinematic variables, e.g. $s$ and $p_T$. The production of a final state with a definite $p_T$ requires a minimum value for $s$ of

$$s_{min} = m_H^2 + 2(p_T)^2 + 2p_T\sqrt{(p_T)^2 + m_H^2}. \tag{192}$$

We study the behavior of the amplitude as a function of $p_T$ for $s = s_{min} + s_{soft}$, where $s_{soft} = (100\ \text{GeV})^2$ is necessary to avoid the soft divergence and focus only on the collinear behavior. The choice of a value of $s$ close to $s_{min}$ is phenomenologically motivated by the strong PDF suppression in the hadronic cross section for increasing partonic $s$.

The scattering process is described by eight helicity amplitudes $\mathcal{M}^{\lambda_1,\lambda_2,\lambda_3}(s, p_T, m_H^2)$, where $\lambda_1 = \pm 1$, $\lambda_2 = \pm 1$ are the helicities of the two incoming gluons and $\lambda_3 = \pm 1$ is the helicity for the outgoing one. The amplitudes are not all independent: indeed parity conservation implies that

$$\mathcal{M}^{\lambda_1,\lambda_2,\lambda_3}(s, p_T, m_H^2) = -\mathcal{M}^{-\lambda_1,-\lambda_2,-\lambda_3}(s, p_T, m_H^2), \tag{193}$$

leaving four independent amplitudes, $\mathcal{M}^{+++}$, $\mathcal{M}^{++-}$, $\mathcal{M}^{-+-}$ and $\mathcal{M}^{-++}$, whose complete expressions can be found for example in ref. [145]. We reorganize them as follows

$$\mathcal{M}^{\lambda_1,\lambda_2,\lambda_3}(s, p_T, m_H^2) = \mathcal{M}_{div}^{\lambda_1,\lambda_2,\lambda_3}(s, m_H^2)/p_T + \mathcal{M}_{reg}^{\lambda_1,\lambda_2,\lambda_3}(s, p_T, m_H^2) \tag{194}$$

and we use this decomposition to compute the unpolarized squared matrix elements exactly or in the collinear approximation.

*Case study: the Standard Model*

In the Standard Model the full amplitude is the sum of a top and a bottom contribution. The results for the variable $C(s, p_T^H, m_H^2)$ for a Higgs boson with $m_H = 125$ GeV and $m_H = 500$ GeV are shown in figure 54. We plot in red and green the behavior of the amplitudes computed including only the top or the bottom. In black we show the behavior of the full amplitude that includes the sum of the top and bottom contribution. In the same figure, for $m_H = 125$ GeV, we plot in blue the results obtained in the HQEFT.

We first discuss the impact of the regular terms in the case of a light Higgs. We compare the results obtained for the only-top case with the exact matrix elements with the ones in the HQEFT; we observe that in both models a deviation by more than 10% from the collinear approximation occurs for $p_T > 55$ GeV. This effect should thus not be interpreted as a top mass effect; the latter becomes visible for $p_T > 170$ GeV. From the analysis of the helicity amplitudes, we observe that this deviation from the collinear approximation stems from $\mathcal{M}^{-+-}$. For the bottom quark, the deviation from the collinear approximation starts from $p_T$ greater than 20 GeV, when the bottom loops are resolved by the emitted gluons. In the case of the full amplitude with the sum of the top and bottom quarks contributions, it is known that in the SM there is a negative interference between the two groups of diagrams, which accidentally tends to cancel the regular terms, extending the range of validity of the collinear approximation. This accidental cancellation depends on the specific values of the quark masses and of the couplings in the SM. Hence, it is more conservative to read the deviation from the collinear regime by studying the top and bottom cases separately.

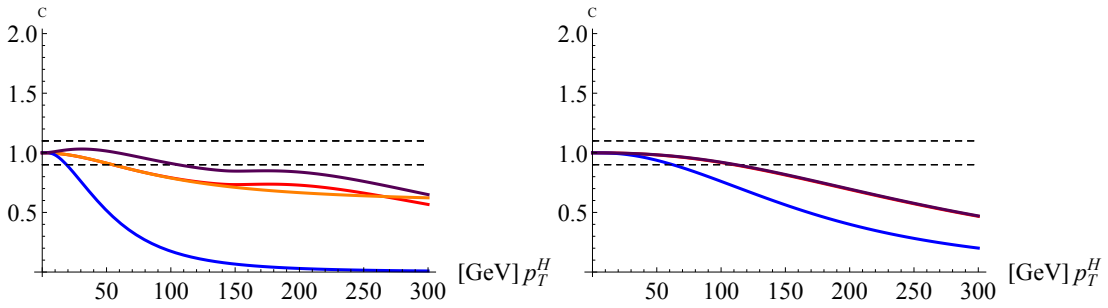


**Figure 54:** Effect of the regular part of the amplitude compared to the collinear approximation on the sum of the three collinear divergent helicity amplitudes, for a light Higgs of $m_H = 125$ GeV (left) and for a heavy Higgs of $m_H = 500$ GeV (right). In red we plot the curve obtained with the top quark running in the loop, in orange the one in the HQEFT, in blue the bottom quark one and in purple the sum of the top and bottom quark amplitudes.

In the case of a heavy Higgs, the scale of the process is set by the mass of the boson, $m_h = 500$ GeV, all the quark loops are fully resolved and a HQEFT approximation of the amplitude is not valid. The amplitude that includes only the top-quark diagrams deviates from its collinear approximation for $p_T$ greater than 120 GeV [4]. Instead, the amplitude that includes only the bottom-quark diagrams deviates from its collinear approximation for $p_T$ greater than 60 GeV.

### 5.6.3 SM phenomenology

The resummation procedure is constrained by the correctness of the collinear approximation for the matrix elements. In the previous section we have tried to find a procedure to quantitatively assess the goodness of this approximation by looking at the behavior of the helicity amplitudes. However there is always bound to be a degree of arbitrariness in defining the acceptable region; in our case this is represented by our choice to set $\bar{C} = 0.1$ in eq. (191).

We now want to perform an assessment of the uncertainties associated with the ambiguity linked to the scale choice. We will use the analytic results, computed by Grazzini et al. [82] and provided in the public code HRES [133] as comparison. As we have seen in subsection 5.1.1 the analytic resummation procedure requires the introduction of a resummation scale. Analogously to what happens with the renormalization and factorization scales, the physical results do not depend upon $\mu_{res}$, but the truncation to a fixed order of the perturbative expansion leaves a residual dependence on it, which can be used to express the uncertainty of the matching procedure between the resummed and the fixed-order results; a variation of this scale in the interval $[\mu_{res}/2, 2\mu_{res}]$ is conventionally adopted.

We compare the analytic results with the one obtained in the NLO+PS POWHEG-BOX framework by our gluon fusion event generator. We first show explicitly how it is possible to introduce the two separate scales, one for the top and one for the bottom quark, in this framework; then we estimate the matching uncertainties, by varying the value $h$ which enters the damping factor $D_h$ around the central values. While the most conservative approach is to take two separate scales for the top and the bottom contri-

4 We remark that the collinear regime is not defined by an absolute value of the variable $\bar{p_T}$, but it is better characterized in terms of the ratio $r = \bar{p_T}/m_h$; in the case under discussion (only top diagrams) we find $r \simeq 1/4$ whereas for $m_h = 125$ GeV we have $r \simeq 1/2$.

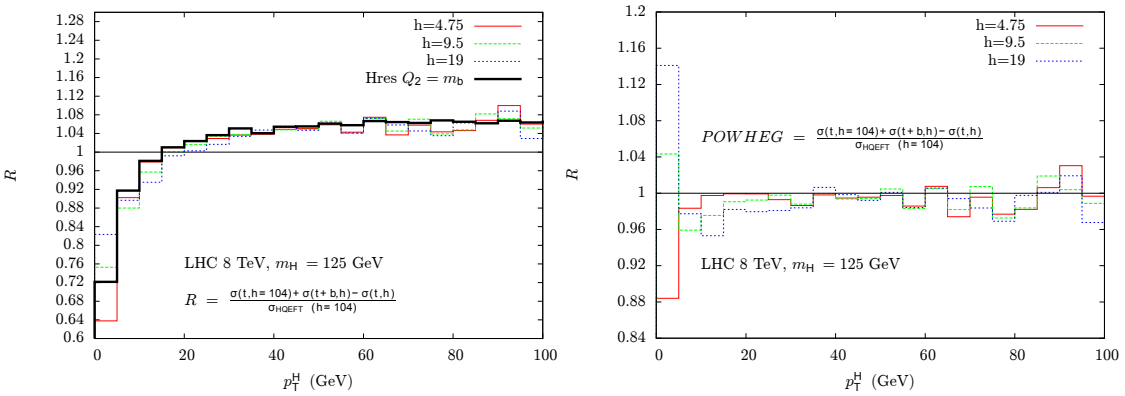


**Figure 55:** On the left mass effects in HRES and in the POWHEG-BOX for $m_H = 125$ GeV; on the right relative deviation of POWHEG with respect to HRES in the same case.

butions, we also show the results obtained by taking just one single scale (read from the combined top and bottom amplitude) since, as we will see, in the SM case it provides a quite good approximation. The single case approach is useful when trying to study the behavior of the distribution for many different configurations since the runtime of a single simulation can be sizable.

In the numerical analysis we used $m_{top} = 172.5$ GeV, $m_{bot} = 4.75$ GeV and the PDF sets MSTW2008-68cl with their corresponding values of $\alpha_s(m_Z)$. We chose $\mu_R = \mu_F = m_H$ as the renormalization and factorization scales. Unless stated otherwise, we used PYTHIA8 with the tune AU-CT10 to shower the POWHEG-BOX events. The center of mass energy at the LHC has been assumed to be $\sqrt{s} = 8$ TeV.

#### *Comparison of* POWHEG *and* HRES *in the two-scale approach*

As we have shown in section 5.6.2, the presence of the bottom quark in the amplitude makes the gluon fusion a four-scale problem from the point of view of the resummation of collinear algorithms. In ref. [82] Grazzini et al proposed a new prescription to account for this. We show here our recipe to implement the same reasoning in the POWHEG-BOX framework, complemented with the choice of the scales for the processes that comes from our study of the helicity amplitudes. We rewrite the squared matrix element as:

$$|\mathcal{M}(\text{top}+\text{bot})|^2 = |\mathcal{M}(\text{top})|^2 + [|\mathcal{M}(\text{top}+\text{bot})|^2 - |\mathcal{M}(\text{top})|^2] \ . \tag{195}$$

where we have put in round bracket the quarks that run in the loops of the diagram. The square brackets contain the top-bottom interference and the square of the modulus of the bottom amplitude. We recall that in the POWHEG language, the resummation effects via Parton Shower (PS) are damped above the scale $h$, by the factor $D_h$ as defined in eq. (187). Moreover by construction the total cross section does not depend on the value of $h$. This allows us to write the following equation

$$\sigma(\text{top}+\text{bot}) = \sigma(\text{top}, h = h_t) + [\sigma(\text{top}+\text{bot}, h = h_b) - \sigma(\text{top}, h = h_b)] \ , \tag{196}$$

where we have introduced the notation $\sigma(q, h)$ to indicate the total cross section evaluated with the quark $q$ in the internal loops and where $h$ is the scale that enters the damping factor $D_h$. This equa-

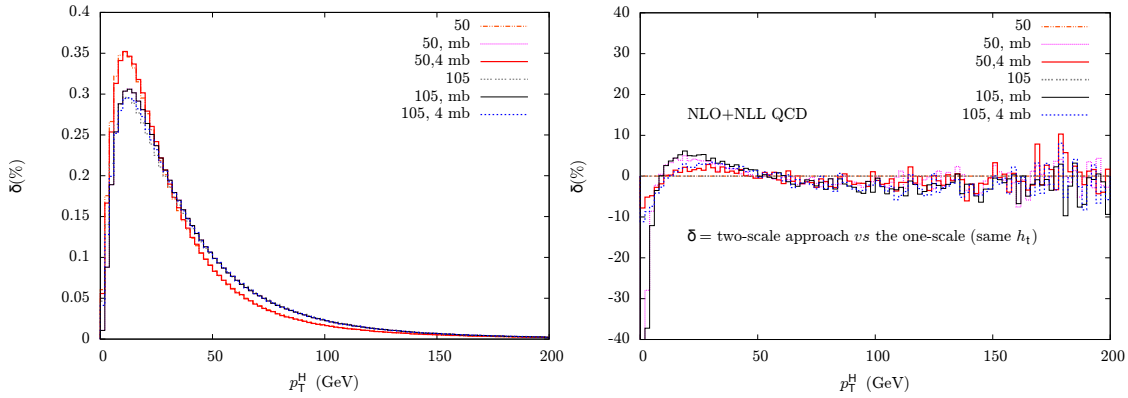


**Figure 56:** Mass effects in POWHEG in the two and in the one-scale approach. Higgs transverse momentum distribution (left plot) computed with different choices of the scales; relative deviation of the two-scale approach with respect to the one-scale results obtained with $h = h_t = m_H/1.2$ (right).

tion is trivial for the total cross section, however it can and should also be used to compute differential observables, specifically the Higgs boson transverse momentum. We derive the values for the scales $h_t$ and $h_b$ from our analysis of the helicity amplitudes. We can see from figure 54 that in the case of only top-loop diagrams, the resummation can be safely applied up to a scale $h_t$ comparable to the Higgs mass. Indeed common choices are $h_t = m_H/2$, or, following the LHC-HXSWG recommendation [40], $h_t = m_H/1.2$. In ref. [82], it is proposed to use $m_{bot}$ as the central value for the scale that limits the inclusion of the resummation effects for the bottom amplitude contributions, whereas from figure 54 we can read that in the only-bottom case, the scale at which the collinear approximation fails at the 10% level is of the $\mathcal{O}(20)$ GeV, i.e. $h_b \simeq 4m_{bot}$. We will compare, in the following, these two options for the bottom-related part of the amplitude. A similar subdivision was studied in ref. [82] and then implemented in HRES . In figure 55, left plot, we compare the predictions obtained with HRES with those computed with the POWHEG-BOX . We plot the ratio of the Higgs transverse momentum distribution with the full description that includes quark mass effects according to eq. (195) divided by one computed in the HQEFT, in order to estimate the effect of the inclusion of the full mass dependent amplitude for the top and the bottom quark. With different colors we show the results obtained with different choices of the scale $h_b$, with fixed $h_t = m_H/1.2$. Also in the HQEFT results we use the same $h_t$. In black we plot the analogous results obtained with the code HRES for a choice of the two resummation scales $Q_1 = m_H/2$, $Q_2 = m_{bot}$. The same $Q_1$ is used in the HQEFT computation by HRES as well. In order to appreciate the agreement between the two codes, in right plot of 55 we show the ratio of the POWHEG results over the HRES ones. We observe that, excluding the first bin, the POWHEG results evaluated with $h_b = 4.75$ GeV reproduce the HRES ones with an accuracy of better than 2%. One should also keep in mind that the first bin of the distribution is depleted by the Sudakov suppression and any small variation in the number of events of the whole distribution is reflected here in the a large percent variation with respect to the HQEFT results. To a very large extent, the size of the quark-mass effects is independent, for $m_H = 125$ GeV, of the specific value chosen for $h_t$.

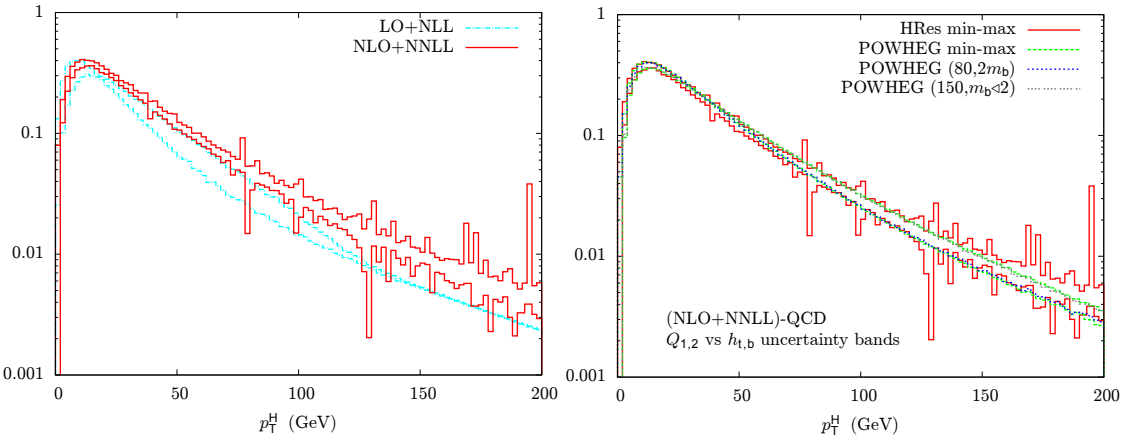


**Figure 57:** On the left uncertainty band obtained with HRES by varying the resummation scale. On the right comparison between the HRES and the POWHEG uncertainty band.

*Comparison of the one scale vs two-scale approach in* POWHEG

In the case of a light SM Higgs, it is interesting to check how well a single-scale computation of the $p_T^H$ distribution agrees with the two-scale one. In section 5.6.2 we have shown the results for the complete amplitude which comes from the sum of the top and the bottom part. We will now consider two single-scale cases with $h = 50$ GeV and $h = m_H/1.2$ GeV, the first value comes from figure 54 while the second one is again the one recommended by the LHC-HXSWG [40]. For the two scale case, we take $h_t$ equal to these two values and we combine it with $h_b = \{m_{bot}, 4m_{bot}\}$. The results are presented in figure 56. In the left plot we show the Higgs transverse momentum distribution in the single and in the two scale approach for these of values of $h$, $h_t$ and $h_b$. We can see that $h_t$ plays a major role in determining the shape of the distribution. This is a direct reflection of the dominant role of the top quark amplitude. In the right plot we show the percent relative deviation from the one-scale results, for different choice of $h_b$. We observe that the bottom-quark corrections are almost independent of $h_t$ and that the two approaches differ at most by 5% for $p_T^H > 10$ GeV.

*Uncertainty band for the $p_T^H$ distribution in* POWHEG *and in* HRES

The uncertainty bands obtained with HRES due to the resummation scales $Q_1, Q_2$ variation, at fixed renormalization and factorization scales, are presented in left plot of figure 57, at LO+NLL (light blue) and at NLO+NNLL (red). In the left plot we show the minimum and maximum prediction obtained by varying the scales in the intervals $m_H/4 \leqslant Q_1 \leqslant m_H$ and $m_b/2 \leqslant Q_2 \leqslant 2m_{bot}$. In the right plot we show the percent width of the band, computed with respect to its mid-point (symmetrized uncertainty). We want to identify, at NLO+NNLL QCD, a suitable range of the scales $h_t, h_b$ that yields a similar variation of the POWHEG prediction, which is rescaled by an appropriate $K_{NNLO}$ factor to account for the different normalization. We perform the scan over the entire range of combinations of the scales $h_t, h_b$ by varying $50 \leqslant h_t \leqslant 150$ GeV in steps of 5 GeV and $2.5 \leqslant h_b \leqslant 9.5$ GeV in steps of 1 GeV. We consider for each bin the minimum and the maximum value among the predictions. The resulting band is plotted in green in the right plot of figure 57 and is well approximated by the curves computed with $h_t = 80$, $h_b = 2m_{bot}$ (blue) and with $h_t = 150$, $h_b = m_{bot}/2$ (gray). A simple indicator of the

difference between the HRES and the POWHEG bands is given by the value of the integrated cross section of the lower (upper) bound of the two uncertainties bands. The POWHEG value is 6% larger than the HRES when considering the lower bounds and 2% smaller when comparing upper bounds.

### 5.6.4 Bottom effects in the 2HDM

We want now to understand the role of the scale $h_b$ when we compute a prediction for the Higgs transverse momentum distribution in a beyond SM models where the coupling of the Higgs to the bottom quark is possibly enhanced. Hence we choose the type-II 2HDM and set $\tan\beta = 40$. The CP-even neutral mixing angle is taken in the decoupling limit, $\alpha = \beta - \pi/2$. With such choices we have a light Higgs $h$ that is SM-like, that we assume with $m_h = 125$ GeV, and an exotic heavy Higgs boson, for which we set $m_H = 500$ GeV. This corresponds to an interesting phenomenological case, which could be compatible with the current observations from the LHC.

In figure 58 we show the results for the light Higgs for different choices of $h$. The $h = \infty$ choice as expected produces a $p_T^h$ distribution with a raised tail with the respect to the NLO curve. All the other choices have a compatible behavior for $p_T^h \geqslant 120$ GeV and tend to the NLO curve in this region. In the low- and middle-$p_T^h$ region, the three curves have different behavior, with a common crossing point at around 30 GeV. The blue curve, which corresponds to the choice $h = \infty$, is over the other two for $p_T \geqslant 30$ GeV and then, as $p_T^h \to 0$, it stays below the others. This is not completely unexpected, since due to the unitarity constraint and the fact that low values of $h$ tend to suppress the high-$p_T^h$ tail, the other two curves are bound to be higher in the low-$p_T^h$ region. We also check that, when taking the same combination of scales, the behavior, given by the red curve, is at it should, identical to the SM one, represented by the green curve.

In figure 59 we plot the results for a heavy Higgs H with mass $m_H = 500$ GeV in the same parameter space point. We notice that the standardly used scale choice of $m_H/2$ gives a substantially different result from the ones obtained by using the scales coming from the helicity amplitude study. We also observe that, since here the amplitude is completely dominated by the bottom quark, the black curve, where a single scale equals to $h = 60$ GeV, and the red curve, with $h_t = 125$ GeV and $h_b = 60$ GeV, are almost coincident. They also follow closely the NLO curve for $p_T^H \geqslant 100$ GeV.

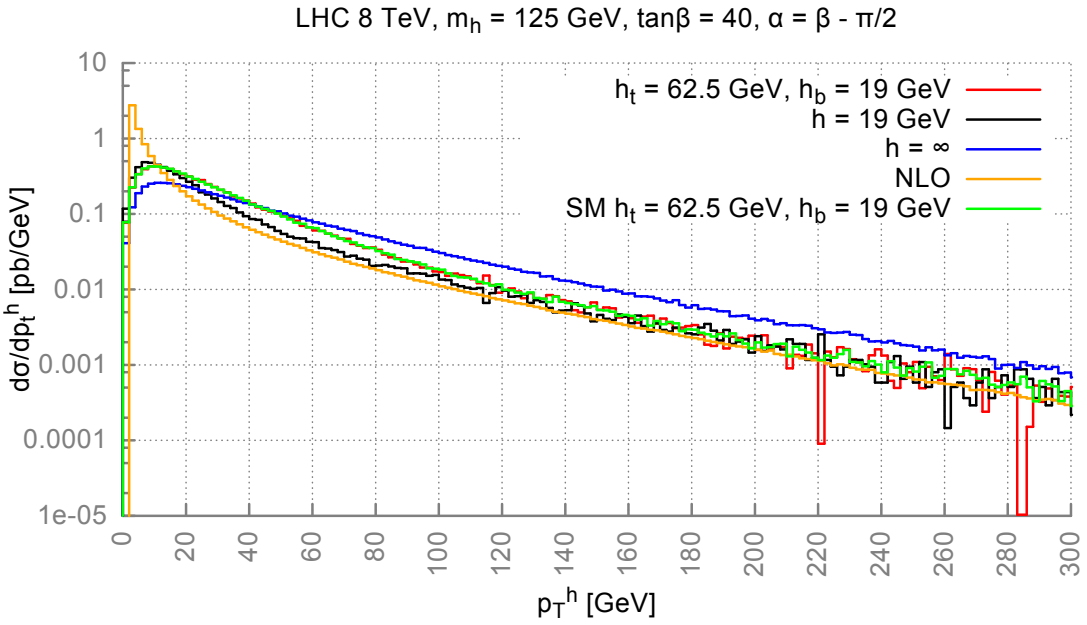


**Figure 58:** Transverse momentum distribution of the light Higgs boson h, with a mass of 125 GeV, in the 2HDM for $\tan\beta = 40$ and $\alpha = \beta - \pi/2$. In orange we show the fixed order result; in blue the result with $h = \infty$; in black $h = 19$ GeV; in red we plot the distribution with the composed result obtained with $h_t = 62.5$ GeV and $h_b = 19$ GeV. As a reference curve we also plot the SM curve for $h_t = 62.5$ GeV and $h_b = 19$ GeV.

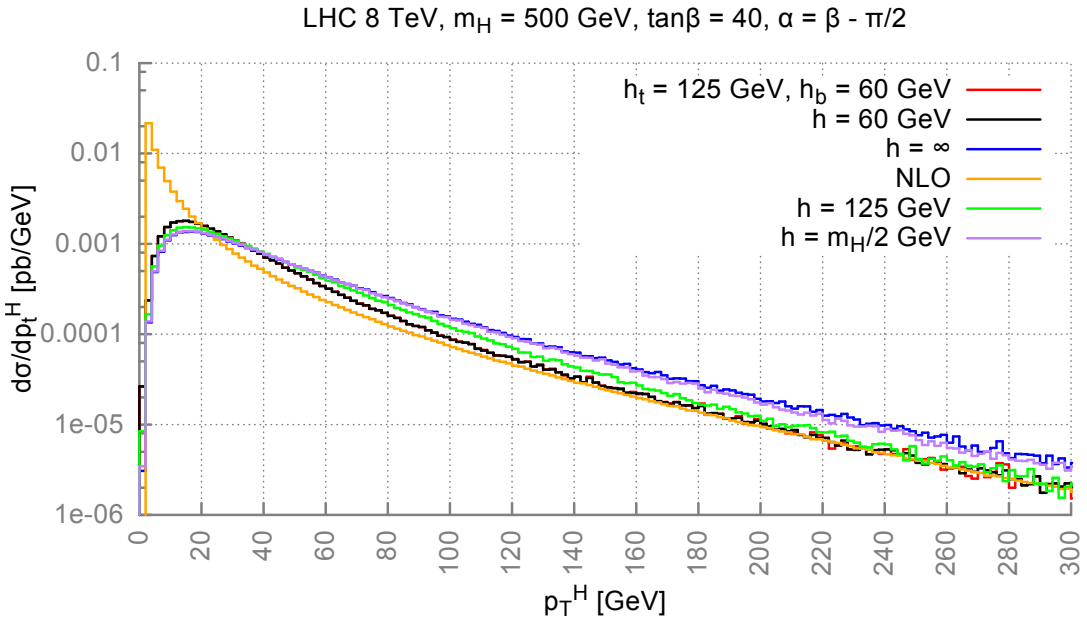


**Figure 59:** Transverse momentum distribution of the heavy Higgs boson H, with a mass of $m_H = 500$ GeV in the 2HDM for $\tan\beta = 40$ and $\alpha = \beta - \pi/2$. In orange we show the fixed order result; in blue the result with $h = \infty$; in black $h = 19$ GeV; finally in red we plot the distribution with the composed result obtained with $h_t = 62.5$ GeV and $h_b = 19$ GeV.

# 6 CONCLUSIONS

Now that a SM-like Higgs boson has been discovered at the LHC, it will be of primary importance to compare its measured properties with our theoretical expectations with the aim of understanding its nature. To achieve this goal, it is fundamental to have a complete control over theoretical predictions, by having very accurate computations and a thorough understanding of their uncertainties. Taking this necessity into consideration, we focused on the study of two different observables that are relevant for Higgs-related studies.

At first we discussed the total production rates for the production of the neutral Higgs bosons of the MSSM in a set of scenarios compatible with the LHC results. These observables are one of the most important, since their values are indispensable to set exclusion limits for supersymmetric Higgs production, or, in the case of discovered resonances, to understand if they are compatible with the MSSM.

We used the code `SusHi` [87], which implements state-of-the-art calculations for MSSM Higgs production in gluon fusion and in bottom annihilation, to compute the total inclusive cross sections. We observed that the latter can be substantially different from the SM prediction. Indeed in the MSSM the importance of the top and bottom contributions – and their relative weight in the complete result – can be substantially different from the SM and can lead to strikingly different results in some regions of the MSSM parameter space. We have also found that, for scenarios with relatively light squarks, the gluon-fusion cross section can be significantly suppressed due the presence of superparticles running in the loops.

Next we studied the various uncertainties that affect the prediction of the cross section. Some of these uncertainties, namely the ones associated to the choice of renormalization and factorization scales, to the PDF parameterization and to the input value for the strong coupling constant, are relevant also for the production of the SM Higgs, although their size may differ in the case of the production of non-standard Higgs bosons. In contrast, the uncertainties associated to the definition of the bottom mass and Yukawa coupling are practically negligible in the SM – where the bottom-quark contributions amount only to a few percent of the total cross section – but they can become dominant in regions of the MSSM parameter space where the couplings of the Higgs bosons to bottom quarks are enhanced. In the particular case of heavy-scalar and pseudoscalar production at large $\tan\beta$, we found that legitimate variations in the renormalization scheme and scale of the bottom Yukawa coupling can suppress the gluon-fusion cross section by more than 60%, due to the presence of large QCD corrections enhanced by logarithms of the ratio $m_\Phi^2/m_b^2$ . Luckily, in this case the total cross section is dominated by the contribution of bottom-quark annihilation, which is subject to a considerably smaller scale uncertainty. Finally, we studied the uncertainties associated to our implementation of the SUSY contributions to gluon fusion at the NLO and, partially, at the NNLO. With the exception of a gluophobic region in the *light-stop* scenario, these uncertainties are generally small, reflecting the sub-dominant nature of the SUSY contributions themselves for values of the squark masses compatible with the LHC bounds.

Then we turned our attention to another observable, the transverse momentum distribution of the Higgs boson in gluon fusion. It is important for two reasons: the prediction, in all models, is required by

experimenters to estimate the acceptance of their detectors to the process; moreover it represents another opportunity to check for compatibility with the SM.

We have seen that the computation of the transverse momentum distribution requires the resummation of terms of the form $\log(p_t/m_H)$. This is usually achieved either by performing the analytic resummation of these logarithms or by using a parton shower Monte Carlo. We followed the latter option and we used our implementations (in the SM, 2HDM and MSSM) of the gluon fusion Higgs production channel in the POWHEG-BOX framework.

At first we studied the differences between the complete SM prediction and the one obtained in the $m_t \to \infty$ limit. We observe that, for a 125 GeV Higgs, the inclusion of the top-mass effects and of the bottom contribution in POWHEG produces a characteristic distortion of the shape, with a suppression in the low- and in the high-$p_T$ region. The former is caused by the top-bottom interference term while the latter is a purely top amplitude effect. This behavior is already present at NLO and it is enhanced by the specific structure of the POWHEG Sudakov form factor. Indeed, other computations like the one in the MC@NLO framework or the analytic one show reduced effects. On the other hand, for a 500 GeV Higgs, only the top quark is relevant and we observe only the suppression in the high-$p_T$ tail of the distribution.

Next we turned to the type-II 2HDM. In this case the quark couplings can be reduced/enhanced with respect to the SM and we expect an effect due to this on the transverse momentum distribution. Indeed we observe that, when the coupling to the bottom is enhanced, we have a softer (harder) distribution for a light (heavy) Higgs. Here the effect, at variance with the SM, is due to squared bottom quark amplitude. On the other hand, if we increase the importance of the top quark, the shape of the distribution of a light Higgs is softer while the the one of a heavy Higgs is unchanged.

We have also analyzed the $p_T$ spectrum in the light stop scenario of the MSSM, for the light and heavy scalars and for the pseudoscalar. Our parameter space point is characterized by an enhanced bottom coupling. We have found that all the spectra show a distortion of the distribution, aside from a different normalization. For $h$ we have a non-trivial distortion of the shape, with suppression in both the low and high-$p_T$ region and a central enhancement. For $H$ and $A$ we observe a softer distribution with respect to the SM case.

Finally, spurred by the differences between our results, obtained with POWHEG , and the ones from MC@NLO and the analytic computations, we performed a detailed analysis to understand the origin of the discrepancies. We found that it lies in the different definition of the Sudakov form factor and in the way the mass scales of the gluon fusion process are accounted for, especially the bottom one. We implemented the correspondent of the recipe presented in [82], where separate resummation scales are used for the top and the bottom contribution, in POWHEG , using an independent analysis based on the study of the helicity amplitudes for the process $gg \to Hg$ to determine the values of the scales. We have found that with our prescription POWHEG produces results in a very good agreement with the one of ref. [82] for a SM Higgs with $m_H = 125$ GeV. We also extended this prescription to a heavy Higgs with $m_H = 500$ GeV and we have also briefly studied how the choice of the scales affects the distribution in the 2HDM, in the case when the coupling to the bottom is enhanced.

While in recent years the accuracy of theoretical predictions has constantly improved, many developments are still possible in the area of Higgs precision physics. With respect to the SM, N3LO approximate computations in the HQEFT are starting to appear and they seem to indicate a quite substantial increase over the NNLO result. Concerning the MSSM, the resummation of the QCD corrections enhanced by $\ln(m_\phi^2/m_b^2)$, analogous to the one performed in ref. [123] for the Higgs decay to photons, will be neces-

sary to reduce the large uncertainty in the production of non-standard Higgs bosons via gluon fusion (incidentally, such calculation would benefit all models with enhanced Higgs couplings to bottom quarks, whether they are supersymmetric or not). Implementing the existing results for the two-loop contributions to $\Delta_b$ [77], in both the Higgs mass and cross-section calculations, will also reduce the uncertainty in scenarios where the bottom contributions are relevant. Moreover, it could be worthwhile to improve the calculation of the gluon-fusion cross section by taking into account the full Higgs-mass dependence of the two-loop squark-gluon [1] contributions [50, 51, 60] – to cover scenarios in which the non-standard Higgs bosons are heavier than the third-generation squarks – and by including the genuine three-loop effects [73, 74].

1 As well as the two-loop quark-squark-gluino contributions [61, 62], when they become available.

# A OBSERVABLE TABLES

Table 11 - 12 summarize the data that is analyzed in the course of this project. Table 11 contains the higher order corrections for observables without initial state hadrons. Every non-hadronic observable is written in the following form

$$O_k(Q, \mu_r) = \sum_{n=1}^{k} \alpha_s(\mu_r) c_n(Q, \mu_r)\,, \tag{197}$$

where $\mu_r$ is the renormalization scale of the strong coupling. We recall that for this class of observables, the coefficients $c_0$ are not used in the analysis. Every observable with initial state hadrons is written as

$$O_k(Q, \mu_r, \mu_f) = \sum_{n=1}^{k} \alpha_s(\mu_r, \mu_f) c_n(Q, \mu_r, \mu_f)\,, \tag{198}$$

and we have always assumed $\mu \equiv \mu_r = \mu_f$. The convolution of the parton luminosity with the hard scattering coefficient function is implicit in the definition of $c_n$.

## Non-Hadronic observables

| | Parameters | | | Coefficients | | | | |
|---|---|---|---|---|---|---|---|---|
| Observable | Q(GeV) | $\alpha_s(Q)$ | $l$ | $c_l$ | $c_{l+1}$ | $c_{l+2}$ | $c_{l+3}$ | $c_{l+4}$ |
| $R = \frac{\sigma(e^+e^-\to\text{hadr})}{\sigma_0(e^+e^-\to\text{hadr})}$ | 91.19 | 0.118 | 0 | 1 | 0.318 | 0.143 | -0.413 | |
| Bjorken sum rule | 91.19 | 0.118 | 0 | 1 | -0.212 | -0.238 | -0.274 | |
| GLS sum rule | 91.19 | 0.118 | 0 | 6. | -1.910 | -1.773 | -1.117 | |
| $\frac{\Gamma(b\to ce\bar{\nu}_e)}{\Gamma_0(b\to ce\bar{\nu}_e)}$ | 4.6 | 0.22 | 0 | 1 | -0.566 | -1.408 | | |
| $\Gamma(Z\to\text{hadr})$[GeV] | 91.19 | 0.118 | 0 | 1.674 | 0.533 | 0.130 | -0.837 | -1.173 |
| $\frac{\Gamma(Z\to b\bar{b})}{\Gamma_0(Z\to b\bar{b})\vert_{m_b=0}}$ | 91.19 | 0.118 | 0 | 0.997 | 0.315 | -0.156 | -0.796 | |
| $\Gamma(H\to gg)$ [MeV] | 125 | 0.113 | 2 | 14.43 | 82.28 | 223.6 | 181.6 | |
| $\Gamma(H\to b\bar{b})\vert_{m_b=0}$[MeV] | 125 | 0.113 | 0 | 1.850 | 3.338 | 5.465 | 2.492 | -15.685 |
| $\Gamma(H\to\gamma\gamma)$ [KeV] | 125 | 0.113 | 0 | 9.379 | 1.494 | 0.627 | | |
| ⟨3-jets Thrust⟩ | 91.19 | 0.118 | 1 | 0.030 | 0.149 | 0.686 | | |
| ⟨3-jets Heavy jet mass⟩ | 91.19 | 0.118 | 1 | 0.030 | 0.069 | 0.141 | | |
| ⟨3-jets Wide jet broadening⟩ | 91.19 | 0.118 | 1 | 0.054 | 0.098 | 0.166 | | |
| ⟨3-jets Total jet broadening⟩ | 91.19 | 0.118 | 1 | 0.054 | 0.356 | 1.219 | | |
| ⟨3-jets C parameter⟩ | 91.19 | 0.118 | 1 | 0.387 | 1.933 | 8.731 | | |
| ⟨3-to-2 jet transition⟩ | 91.19 | 0.118 | 1 | 0.013 | 0.029 | 0.044 | | |
| $\gamma_{ns}^{(+)}(N=2)$ | 91.19 | 0.118 | 1 | 0.283 | 0.206 | 0.081 | | |
| $\gamma_{qq}(N=2)$ | 91.19 | 0.118 | 1 | 0.283 | 0.143 | -0.068 | | |
| $\gamma_{qg}(N=2)$ | 91.19 | 0.118 | 1 | -0.265 | -0.239 | 0.058 | | |

**Table 11:** QCD perturbative corrections for observables without initial-state hadrons. The coefficients $c_n$ are defined by $O_k = \sum_{n=l}^{k} \alpha_s^n c_n$, where $O_k$ is an observable computed at the $k^{th}$ order in perturbative QCD. Note that $l = 0$ coefficients are **not** used in the Bayesian non-hadronic analysis.

## Hadronic observables

| Parameters | | | | Coefficients | | |
|---|---|---|---|---|---|---|
| Observable (LHC, $\sqrt{s} = 8$ TeV) | Q | $\alpha_s(Q)$ | l | $c_l$ | $c_{l+1}$ | $c_{l+2}$ |
| $\sigma(pp \to H)$ [pb] | 125 | 0.115 | 2 | 424. | 5072. | 29097. |
| $\sigma(pp \to b\bar{b} \to H)$ 5FS [pb] | 125 | 0.113 | 0 | 0.402 | -0.854 | -4.951 |
| $\sigma(pp \to Z^* + X \to ZH + X)$ [pb] | 216.2 | 0.105 | 0 | 0.332 | 0.587 | 2.734 |
| $\sigma(pp \to W^* + X \to WH + X)$ [pb] | 205.6 | 0.105 | 0 | 0.626 | 1.108 | 1.834 |
| $\sigma(pp \to b\bar{b})$ [μb] | 20 | 0.155 | 2 | 5371. | 31190. | |
| $\sigma(pp \to t\bar{t})$ [pb] | 173.3 | 0.108 | 2 | 12449. | 55769. | 195299. |
| $\sigma(pp \to Z + X \to e^+e^-$ [nb] | 91.19 | 0.119 | 0 | 0.500 | 0.486 | -0.164 |
| $\sigma(pp \to Z + j)$ [nb] | 91.19 | 0.119 | 1 | 1.186 | 2.831 | |
| $\sigma(pp \to Z + 2j)$ [nb] | 91.19 | 0.119 | 2 | 3.659 | 5.138 | |
| $\sigma(pp \to ZZ)$ [fb] | 182.4 | 0.108 | 0 | 4.949 | 14.311 | |
| $\sigma(pp \to W^- + X \to e^- + \nu_e + X)$ [nb] | 80.4 | 0.121 | 0 | 2.241 | 2.108 | -2.074 |
| $\sigma(pp \to W^+ + X \to e^+ + \bar{\nu}_e + X)$ [nb] | 80.4 | 0.121 | 0 | 3.328 | 3.212 | -0.922 |
| $\sigma(pp \to W^+ + j)$ [nb] | 80.4 | 0.121 | 1 | 6.182 | 17.547 | |
| $\sigma(pp \to W^- + j)$ [nb] | 80.4 | 0.121 | 1 | 4.385 | 11.573 | |
| $\sigma(pp \to W^+ + 2j)$ [nb] | 80.4 | 0.121 | 2 | 19.450 | 28.868 | |
| $\sigma(pp \to W^- + 2j)$ [nb] | 80.4 | 0.121 | 2 | 12.993 | 20.632 | |
| $\sigma(pp \to W^+W^-)$ [pb] | 160.8 | 0.109 | 0 | 0.175 | 0.742 | |

**Table 12:** QCD perturbative corrections for observables with initial-state hadrons. The coefficients $c_n$ are defined by $O_k = \sum_{n=l}^{k} \alpha_s^n c_n \equiv \sum_{n=l}^{k} \alpha_s^n \mathcal{L} \otimes C_n$, where $O_k$ is an observable computed at $k^{th}$ order in perturbative QCD. All observables have been computed for the LHC (proton-proton collisions at $\sqrt{s} = 8$ TeV) with the cuts given in table 13.

## Hadronic analysis cuts

| Cut | Description |
|---|---|
| $0 \leqslant m_{34}^{min} \leqslant 14$ TeV | Invariant mass of particles 3 and 4 in the process |
| $0 \leqslant m_{34}^{min} \leqslant 14$ TeV | Invariant mass of particles 5 and 6 in the process |
| $m_{34}^{T} \geqslant 0$ GeV | Transverse mass of particles 3 and 4 in the process |
| Anti-$k_T$ [146], R = 0.4 | Jet algorithm |
| $p_T^{jet} \geqslant 15$ GeV | Jet transverse momentum $p_T$ |
| $0 \leqslant \lvert\eta^{jet}\rvert \leqslant 3.5$ | Jet pseudorapidity |
| $p_T^{lept} \geqslant 20$ GeV | Lepton transverse momentum |
| $0 \leqslant \lvert\eta^{lept}\rvert \leqslant 2.5$ | Lepton pseudorapidity |
| $p_T^{miss} \geqslant 25$ GeV | Missing (neutrinos) transverse momentum |
| $\Delta R_{jj} > 0.5$ | Jet-jet separation $\Delta R_{jj} = \sqrt{\Delta\eta_{jj}^2 + \Delta\phi_{jj}^2}$ |
| $\Delta R_{jl} > 0.4$ | Jet-lepton $\Delta R_{jl} = \sqrt{\Delta\eta_{jl}^2 + \Delta\phi_{jl}^2}$ |
| $\Delta R_{ll} > 0.4$ | Lepton-lepton $\Delta R_{ll} = \sqrt{\Delta\eta_{ll}^2 + \Delta\phi_{ll}^2}$ |
| $\Delta\eta_{jj} > 0$ | Jet-jet pseudorapidity separation |

**Table 13:** Cuts used in the hadronic analysis.

# B $\overline{\text{CH}}$ MODEL WITHOUT FACTORIAL

THE $\overline{\text{CH}}$ model can also be defined without the factorial. Then, the series expansion is given by

$$O = \sum_{n=1}^{\infty} \frac{\alpha_s^n}{\lambda^n} \lambda^n c_n \equiv \sum_{n=0}^{\infty} \left(\frac{\alpha_s}{\lambda}\right)^n a_n \tag{199}$$

with

$$a_n \equiv \lambda^n c_n \,. \tag{200}$$

If we submit the new coefficients $a_n$ to the same priors originally used for $b_n$ we obtain the credibility intervals

$$d_k^{(p)} = \begin{cases} \left(\frac{\alpha_s}{\lambda}\right)^{k+1} \bar{a}_{(k)} \frac{n_c+1}{n_c} p\% & \text{if} \quad p\% \leqslant \frac{n_c}{n_c+1} \\ \left(\frac{\alpha_s}{\lambda}\right)^{k+1} \bar{a}_{(k)} \left[(n_c+1)(1-p\%)\right]^{(-1/n_c)} & \text{if} \quad p\% > \frac{n_c}{n_c+1} \end{cases} \tag{201}$$

and the uncertainty density profile

$$f(\Delta_k | a_1, \ldots, a_k) \simeq \left(\frac{n_c}{n_c+1}\right) \frac{1}{2(\alpha_s/\lambda)^{k+1} \bar{a}_{(k)}} \begin{cases} 1 & \text{if } |\Delta_k| \leqslant \left(\frac{\alpha_s}{\lambda}\right)^{k+1} \bar{a}_k \\ \left(\frac{(\alpha_s/\lambda)^{k+1} \bar{a}_{(k)}}{|\Delta_k|}\right)^{n_c+1} & \text{if } |\Delta_k| > \left(\frac{\alpha_s}{\lambda}\right)^{k+1} \bar{a}_k \end{cases} . \tag{202}$$

We then perform the same analysis as in section 4 for the group of non-hadronic observables. The results of this survey are displayed in figure 60. We see that the performance of the modified $\overline{\text{CH}}$ are worse than the original model. Indeed the peaks of the two histograms are more separated and at NLO the model prefers the unnatural low value for non-hadronic observables of $\lambda = 0.5 - 0.6$.

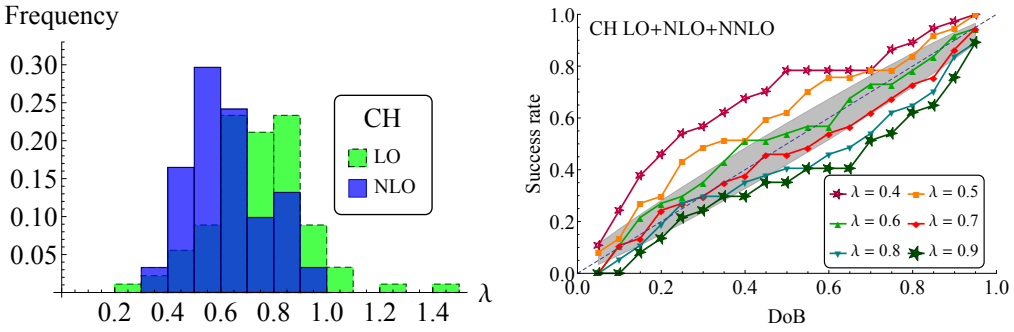


**Figure 60:** Comparisons between DoB and actual frequency, to determine the most appropriate value for $\lambda$ at LO and NLO for the $\overline{\text{CH}}$ model without the factorial.

# C STATISTICAL UNCERTAINTY IN THE λ DETERMINATION PROCEDURE

In this appendix we discuss the estimation of the statistical uncertainty that surrounds the frequentist determination of λ, following ref. [147]. We recall that we determine λ by measuring, for different requested DoBs, the success rate of the Bayesian model on a finite set of test observables. The success rate has statistical fluctuations that can be assumed following a binomial distribution, since it is equivalent to a product of Bernoulli process (the subsequent order is either inside the computed band or not, i.e. a stochastic binary system). We have then that

$$P(k, N, p) = \frac{N!}{k!\,(N-k)!} p^k (1-p)^{N-k}, \tag{203}$$

where $k$ is the number of subsequent orders contained in the DoB interval, $N$ the number of observables and $p$ is the true value of the success rate (which is, of course, unknown) . Since we are interested in determining a confidence interval, we shift to using the continuous version of the binomial distribution, the beta-distribution:

$$B(a, b) = \frac{(a+b-1)!}{(a-1)!\,(b-1)!} p^{a-1} (1-p)^{b-1}\,, \tag{204}$$

with $a = k+1$ and $b = N-k+1$. As the true success rate $p$ is unknown, we assume a uniform prior $\pi(p) = 1$ for $0 < p < 1$. We choose $k$ such that the fraction $k/N$ corresponds to the given DoB. As an alternative, $k$ can be chosen such that the fraction corresponds to the actual success rate. In this way, one could obtain error bars for the 'measured' success rate. For a 68% confidence level, 68% of the error bars of a given curve are expected to at least touch the ideal curve. The method has the disadvantage that the size of the error bars has to be determined separately for each success rate. As long as the actual success rate is close to the expected one, the credibility interval of the ideal curve (the one with a "success rate" equals to the "requested DoB") serves the same purpose. For a good choice of λ, roughly 68% of the measured points should lie within the 1-σ interval around the ideal curve. The size of the 1-σ interval can be calculated using Bayesian inference. For a nominal confidence level $CL = 1-\alpha$, we use

$$\int_0^{p_l} dp\, \pi(p) B(a, b) = \int_0^{p_l} dp\, B(a, b) = \frac{\alpha}{2} \quad \text{and} \quad \int_{p_u}^{1} dp\, B(a, b) = \frac{\alpha}{2} \tag{205}$$

to determine the lower boundary $p_l$ and the upper boundary $p_u$ of the credibility interval.

# D MELLIN MOMENT ANALYSIS

The preferred extension of the $\overline{\text{CH}}$ to hadronic observables is the one based on the integrated coefficients method, due to its ability to capture effectively the complexity of the behavior of a process with initial state hadrons. However it could be instructive to check and compare its results with the extension based on the Mellin moment method. In this section we review two processes: the gluon fusion Higgs production process, where, as we will see, the Mellin method and the coefficient-based one are substantially equivalent and the Drell-Yan process, where the Mellin method fails to capture the essence of the process.

## d.1 Higgs production in gluon fusion at the LHC

This process is characterized by the presence of a single strongly dominant channel, the gluon-gluon one. The other channels which enters at NLO and at NNLO order are much less relevant. This is the optimal application case for the application of the $\overline{\text{CH}}$ family of models, both the coefficient- and the Mellin-based kind. Following the analysis of ref. [15], we have extracted the dominant moment from the Higgs coefficient function in Mellin space taken from [148], where it is given in the limit $m_t \to \infty$.

We recall briefly that the estimation of the interval in Mellin space proceeds through the following steps: at first the error bars interval are determined on the coefficient function in Mellin space, evaluated at the dominant Mellin moment; then the relative width of the interval is used to determine the error bar in the physical space for the complete result, to have the correct normalization. We stress that we do not use the precise value of the cross section obtained with the saddle point approximation in the determination of the bars.

We see from table 14 that the behavior of the coefficient function at the dominant Mellin moment at the various order, is very similar to one of the coefficients extracted after the PDF convolution. Indeed the resulting intervals in the two approaches agree very well.

| $pp \to H$ (Mellin) | | | | | | |
|---|---|---|---|---|---|---|
| Order | $\sigma_k$[pb] | C(N* = 2) | $\overline{\text{CH}}$ Mellin, 68% | $\overline{\text{CH}}$ Mellin, 95% | $\overline{\text{CH}}$, 68% | $\overline{\text{CH}}$, 95% |
| k = 2 | 5.6 | 1 | ±3.35 | ±21.46 | ±3.35 | ±21.46 |
| k = 3 | 13.3 | 12.12 | ±4.54 | ±11.48 | ±4.51 | ±11.42 |
| k = 4 | 18.38 | 71.19 | ±3.70 | ±6.99 | ±3.52 | ±6.65 |

**Table 14:** Analysis results for $pp(gg) \to H$ with the Mellin moment method. We recall that the total cross section is the complete one and not the The meaning of the columns is the same as in section 5.

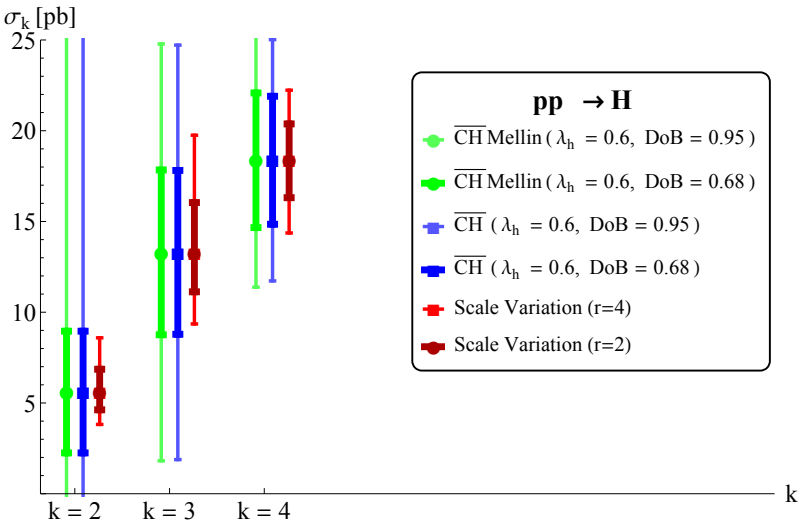


**Figure 61:** Error bars for Higgs production in gluon fusion, with the coefficient method and the Mellin moment method.

## d.2 The Drell-Yan process at the LHC

The analysis of [14] shows that a dominant Mellin moment exists also for the Drell-Yan process. In this section we focus on the production of a Z boson and we discuss why the Mellin method fails in this case.

We know that the Drell-Yan process is dominated by the $q\bar{q}$ channel both at LO (where it is the only channel) and at NLO. At NLO we have the appearance of the gluon-quark channel, whose contribution to the total cross section can be thought as negative, and at NNLO of the gluon-gluon initiated subprocess, which is positively contributing though smaller in magnitude. It is known that the resulting effect of the new channels on the total NNLO contribution is PDF dependent, due to the uncertainties that plague the gluon PDF, and it is therefore positive or negative according to the PDF set used. In our case, with NNLO NNPDF-2.3 set, we observe a NNLO negative contribution, due to the predominance of the quark-gluon channel at this order.

On the other hand the behavior of the coefficient function for the channel that is used for the Mellin analysis, the $q\bar{q}$ channel, is such that the value of the coefficient function always increases order by order[1]. Hence it is not able to capture the true pattern of the perturbative expansion for the process. Indeed we see that, starting from the NLO, the uncertainty interval obtained with the Mellin method is systematically bigger than the one obtained with the standard coefficient-based one.

It would be possible to work around this issue by performing a Mellin analysis for each separate channel. However, to recombine the different uncertainties to get a single band for the complete cross section requires the knowledge of the weight of the different channels in the complete result. This in turn requires the use of the PDFs, rendering the Mellin moment method dependent again on the long-range physics and therefore spoiling its main attractive feature.

1 Extracted again from [148]

| $pp \to Z$ (Mellin) | | | | | | |
|---|---|---|---|---|---|---|
| Order | $\sigma_k$ | C(N* = 2) | $\overline{\text{CH}}$ Mellin, 68% | $\overline{\text{CH}}$ Mellin, 95% | $\overline{\text{CH}}$, 68% | $\overline{\text{CH}}$, 95% |
| k = 0 | 0.499 | 1 | ±0.155 | ±0.991 | ±0.155 | ±0.991 |
| k = 1 | 0.557 | 2.92 | ±0.029 | ±0.074 | ±0.020 | ±0.051 |
| k = 2 | 0.555 | 7.53 | ±0.014 | ±0.027 | ±0.007 | ±0.013 |

**Table 15:** Analysis results for $pp \to Z$ with the Mellin moment method. The meaning of the columns is the same as in section 5.

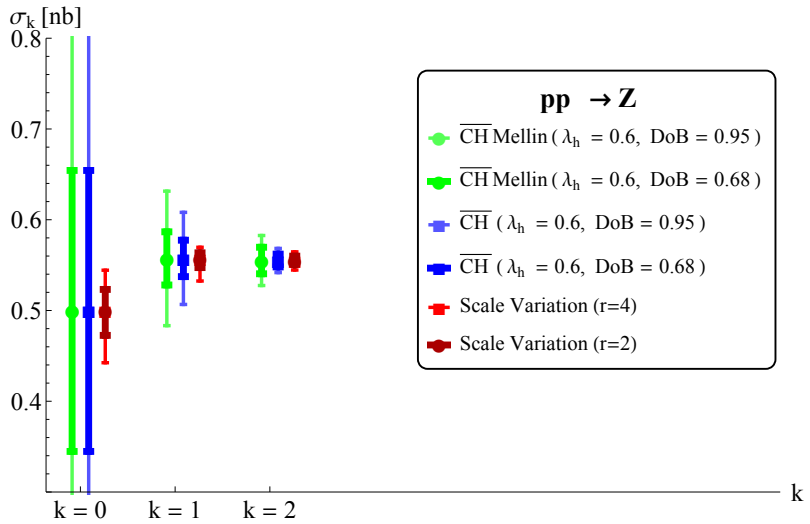


**Figure 62:** Error bars for Z production at the LHC, with the coefficient method and the Mellin moment method.

# E ALTERNATIVE PARAMETERIZATION OF THE INCLUSION OF THE FULL SM MATRIX ELEMENT IN THE POWHEG-BOX

It is possible to perform a different rearrangement of the real emission contribution following the natural hierarchy of the terms that are present in the matrix elements. For instance, for a light Higgs, the HQEFT limit provides a good approximation of the full NLO-QCD result in the SM. We can rewrite the squared real matrix element as

$$R_{\text{div}} = R_{\text{div}}^{\text{HQEFT}} + \left[ R_{\text{div}} - R_{\text{div}}^{\text{HQEFT}} \right] . \tag{206}$$

The squared brackets contain now the the correction due to the full dependence on the top quark mass and the bottom contribution to the leading term $R_{\text{div}}^{\text{HQEFT}}$. Following this remark, we can built an explicit expression for the term $R^s$ that enters the POWHEG Sudakov form factor and for the corresponding finite remainder $R^f$. We have

$$R^s = c R_{\text{div}}^{\text{HQEFT}} + b \left[ R_{\text{div}}^{\text{HQEFT}} - c R_{\text{div}}^{\text{HQEFT}} \right] , \tag{207}$$

$$R^f = R_{\text{div}} - R^s = (1 - b) \left[ R_{\text{div}} - c R_{\text{div}}^{\text{HQEFT}} \right] , \tag{208}$$

$$c = B / B^{\text{HQEFT}} , \tag{209}$$

where the parameter is defined in the region $b \in [0, 1]$. When we set $b = 0$, the Sudakov form factor contains only the HQEFT approximation of the real amplitude. The corrections due to the full dependence on the quark mass are taken into account as a finite remainder. On the other hand, when we take $b = 1$, we recover the default POWHEG implementation. Any other intermediate value of $b$ offers an interpolation between these two extrema. In figure 63 we can see the ratio between the $p_T^H$ distribution for various values of the parameter $b$ for $m_H = 120$ GeV. It is interesting to point out the correlated behavior of the low- and high-$p_T^H$ tails due to the unitarity constraint for different values of the parameter $b$. We know that with the default choice of $b = 1$ the effect of the inclusion of the full matrix element is to suppress the distribution for low $p_T^H$. Smaller values of $b$ tends to restore the HQEFT behavior, i.e. the ratio of the distributions tend to one for $p_T^H \to 0$. This in turn implies a raise of the high-$p_T^H$ tail, to satisfy the constraint that the integral of the curve should be the same NLO cross section. An analogous behavior can be seen in figure 64 for a heavy Higgs of $m_H = 500$ GeV. We remark that the use of $b = 0$ does not recover the exact NLO behavior in the large $p_T^H$ limit of the distribution, since we have that the $R^s$ contribution is still multiplied by the ratio $\bar{B}/B$. However, it could be probably recovered by using a combination of the parameter $b$ and the damping factor $D_h$.

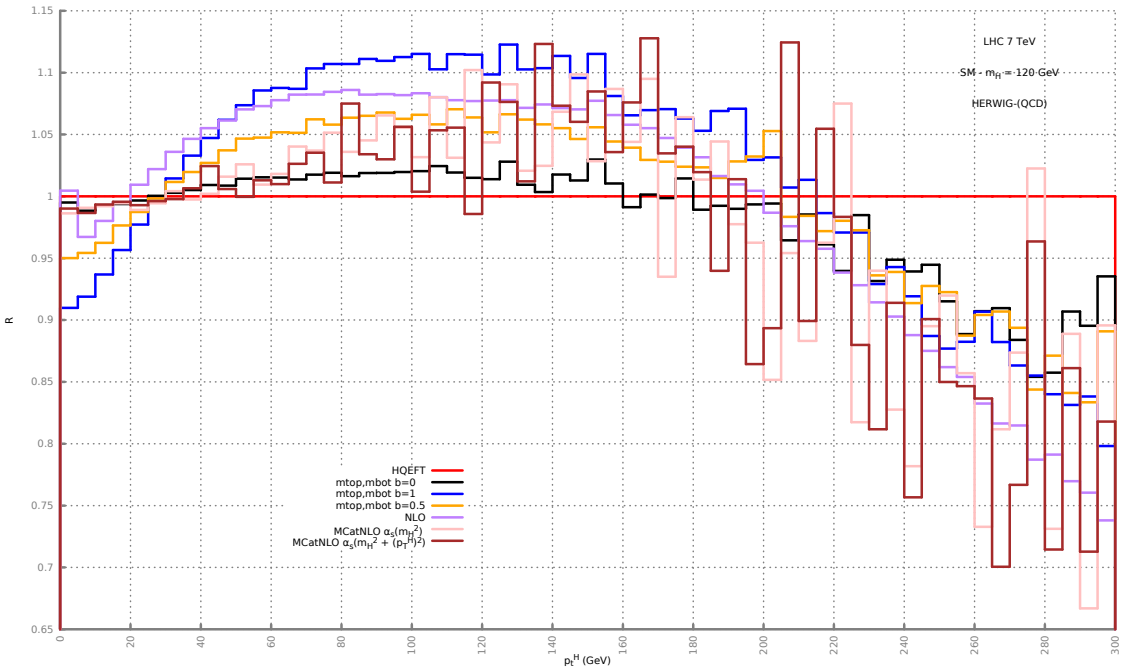


**Figure 63:** Ratio of the shapes for an Higgs of $m_h = 125$ GeV for various values of b.

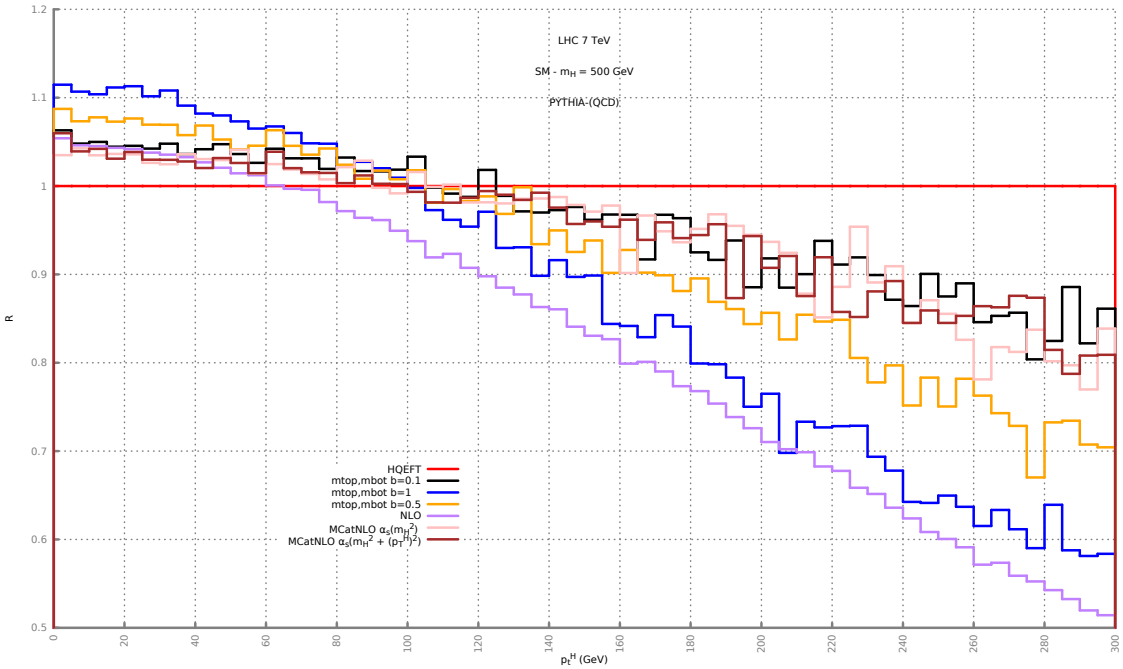


**Figure 64:** Ratio of the shapes for an Higgs of $m_h = 500$ GeV for various values of b.

# F CROSS SECTIONS AND UNCERTAINTIES

In this appendix we include three tables, listing the cross sections and uncertainties for the production at the LHC of the three neutral Higgs bosons in the light stop scenario. We use version `1.3.0` of `SusHi` , and provide separate results for gluon fusion and bottom-quark annihilation. Input files for the six scenarios can be found on the code's website [87]. We set $\sqrt{s} = 8$ TeV, $m_t = 173.2$ GeV and $m_b(m_b) = 4.16$ GeV, and we choose thirty combinations of the parameters $m_A$ and $\tan\beta$. The predictions for the scalar masses are obtained with version `2.10.0` of `FeynHiggs`. The uncertainties provided in the tables are computed as follows:

- The renormalization- and factorization-scale uncertainties are summarized in the quantities $\Delta^{\pm}_{\mu}$, defined as in section 4.2.1, eq. (150). For gluon fusion we consider the seven combinations obtained from $\mu_R = \{m_\phi/4,\ m_\phi/2,\ m_\phi\}$ and $\mu_F = \{m_\phi/4,\ m_\phi/2,\ m_\phi\}$, where we discard the two pairs with the largest variation of the ratio $\mu_R/\mu_F$ with respect to the central choice. For bottom-quark annihilation we proceed accordingly, using $\mu_R = \{m_\phi/2, m_\phi, 2\,m_\phi\}$ and $\mu_F = \{m_\phi/8, m_\phi/4, m_\phi/2\}$.

- The uncertainty $\delta Y_b$ of the gluon-fusion process, related to the definition of the bottom Yukawa coupling and discussed in section 4.2.2, is computed as the relative difference between the cross section calculated with $Y_b^\phi \propto m_b(m_\phi/2)$ and the cross section calculated with $Y_b^\phi \propto M_b$. In the case of bottom-quark annihilation, the scale dependence of $Y_b^\phi$ is included in the computation of $\Delta^{\pm}_{\mu}$.

- The uncertainty $\delta\Delta_b$, stemming from the resummation of $\tan\beta$-enhanced corrections to $Y_b^\phi$ and described in section 4.2.2, is computed by adding an uncertainty of $\pm 10\%$ to the value of $\Delta_b$ obtained from `FeynHiggs`.

The PDF uncertainties are not included in the tables, but they were extensively discussed in section 4.2.3. In section 4.2.3 we pointed out that the relative size of the PDF+$\alpha_s$ uncertainty depends mainly on the value of the Higgs mass, thus it can be taken over directly from the existing estimates for the production of the SM Higgs. Apart from the PDF+$\alpha_s$ uncertainty, in the case of bottom-quark annihilation an additional uncertainty of $\pm 6\%$ has to be added due to the dependence of the bottom-quark PDF on the pole bottom mass (see section 4.2.3). The uncertainties associated to our incomplete knowledge of the SUSY contributions to the gluon-fusion cross section can become sizable in the *light-stop* scenario, especially in the case of H production at large $m_A$ and moderate $\tan\beta$. However we do not include them in the tables, pointing the reader to the discussion in section 4.2.4.

| $m_A$ [GeV] | $\tan\beta$ | $m_h$ [GeV] | $\sigma_{ggh}$ [pb] | $\Delta_\mu^\pm$ [%] | $\delta Y_b$ [%] | $\delta\Delta_b$ [%] | $\sigma_{bbh}$ [pb] | $\Delta_\mu^\pm$ [%] | $\delta\Delta_b$ [%] |
|---|---|---|---|---|---|---|---|---|---|
| 100 | 5 | 88.1 | 18.27 | $^{+17.4}_{-14.6}$ | −37.3 | $^{+0.8}_{-0.8}$ | 12.88 | $^{+9.8}_{-18.8}$ | $^{+1.1}_{-1.1}$ |
| 100 | 10 | 94.3 | 41.55 | $^{+17.3}_{-14.4}$ | −52.2 | $^{+2.2}_{-2.1}$ | 39.99 | $^{+9.1}_{-17.1}$ | $^{+2.2}_{-2.1}$ |
| 100 | 15 | 95.8 | 81.16 | $^{+16.7}_{-14.1}$ | −53.6 | $^{+3.3}_{-3.1}$ | 79.26 | $^{+9.0}_{-16.7}$ | $^{+3.1}_{-3.0}$ |
| 100 | 20 | 96.4 | 130.2 | $^{+16.3}_{-13.9}$ | −53.7 | $^{+4.2}_{-4.0}$ | 126.6 | $^{+8.9}_{-16.6}$ | $^{+4.0}_{-3.8}$ |
| 100 | 30 | 96.8 | 243.2 | $^{+15.9}_{-13.7}$ | −53.5 | $^{+5.8}_{-5.4}$ | 235.0 | $^{+8.9}_{-16.4}$ | $^{+5.6}_{-5.2}$ |
| 100 | 50 | 97.0 | 484.8 | $^{+15.5}_{-13.5}$ | −53.4 | $^{+8.4}_{-7.5}$ | 468.1 | $^{+8.8}_{-16.4}$ | $^{+8.1}_{-7.2}$ |
| 120 | 5 | 101.2 | 12.97 | $^{+13.5}_{-12.4}$ | −13.9 | $^{+0.3}_{-0.3}$ | 6.357 | $^{+8.4}_{-15.4}$ | $^{+1.0}_{-1.0}$ |
| 120 | 10 | 110.5 | 16.39 | $^{+15.3}_{-13.3}$ | −35.5 | $^{+1.5}_{-1.4}$ | 17.64 | $^{+7.7}_{-13.6}$ | $^{+2.1}_{-2.0}$ |
| 120 | 15 | 113.6 | 26.08 | $^{+15.9}_{-13.6}$ | −47.5 | $^{+2.8}_{-2.7}$ | 34.69 | $^{+7.5}_{-13.1}$ | $^{+3.0}_{-2.9}$ |
| 120 | 20 | 115.0 | 40.03 | $^{+15.9}_{-13.6}$ | −52.3 | $^{+4.0}_{-3.7}$ | 56.34 | $^{+7.4}_{-12.9}$ | $^{+3.9}_{-3.7}$ |
| 120 | 30 | 116.3 | 76.24 | $^{+15.4}_{-13.3}$ | −54.9 | $^{+5.8}_{-5.4}$ | 108.8 | $^{+7.3}_{-12.7}$ | $^{+5.5}_{-5.1}$ |
| 120 | 50 | 117.1 | 161.4 | $^{+14.7}_{-13.0}$ | −55.3 | $^{+8.5}_{-7.6}$ | 227.6 | $^{+7.3}_{-12.5}$ | $^{+8.0}_{-7.1}$ |
| 150 | 5 | 111.2 | 15.00 | $^{+9.8}_{-10.3}$ | — | — | 2.282 | $^{+7.7}_{-13.5}$ | $^{+0.8}_{-0.8}$ |
| 150 | 10 | 119.6 | 14.84 | $^{+9.7}_{-10.1}$ | −0.3 | — | 3.057 | $^{+7.1}_{-12.2}$ | $^{+1.6}_{-1.6}$ |
| 150 | 15 | 121.7 | 15.04 | $^{+9.6}_{-10.0}$ | −0.4 | — | 3.313 | $^{+7.0}_{-11.9}$ | $^{+2.4}_{-2.3}$ |
| 150 | 20 | 122.6 | 15.13 | $^{+9.5}_{-9.9}$ | −0.4 | — | 3.345 | $^{+7.0}_{-11.8}$ | $^{+3.0}_{-2.9}$ |
| 150 | 30 | 123.2 | 15.16 | $^{+9.3}_{-9.9}$ | −0.5 | — | 3.210 | $^{+6.9}_{-11.7}$ | $^{+4.1}_{-3.8}$ |
| 150 | 50 | 123.7 | 15.11 | $^{+9.0}_{-9.7}$ | −0.7 | — | 2.843 | $^{+6.9}_{-11.6}$ | $^{+5.8}_{-5.2}$ |
| 200 | 5 | 115.9 | 16.78 | $^{+8.3}_{-9.5}$ | +1.8 | — | 0.837 | $^{+7.4}_{-12.7}$ | $^{+0.5}_{-0.5}$ |
| 200 | 10 | 121.5 | 15.99 | $^{+8.0}_{-9.3}$ | +1.8 | — | 0.805 | $^{+7.0}_{-11.9}$ | $^{+1.0}_{-1.0}$ |
| 200 | 15 | 122.7 | 15.83 | $^{+7.9}_{-9.3}$ | +1.7 | — | 0.781 | $^{+7.0}_{-11.7}$ | $^{+1.5}_{-1.4}$ |
| 200 | 20 | 123.1 | 15.76 | $^{+7.8}_{-9.2}$ | +1.6 | — | 0.759 | $^{+6.9}_{-11.7}$ | $^{+1.9}_{-1.8}$ |
| 200 | 30 | 123.5 | 15.70 | $^{+7.8}_{-9.2}$ | +1.3 | — | 0.720 | $^{+6.9}_{-11.6}$ | $^{+2.5}_{-2.3}$ |
| 200 | 50 | 123.8 | 15.63 | $^{+7.7}_{-9.1}$ | +0.5 | $^{+0.1}_{-0.1}$ | 0.663 | $^{+6.9}_{-11.6}$ | $^{+3.4}_{-3.1}$ |
| 300 | 5 | 117.8 | 17.32 | $^{+7.7}_{-9.3}$ | +1.7 | — | 0.421 | $^{+7.2}_{-12.4}$ | $^{+0.3}_{-0.3}$ |
| 300 | 10 | 122.1 | 16.36 | $^{+7.5}_{-9.1}$ | +1.6 | — | 0.383 | $^{+7.0}_{-11.8}$ | $^{+0.5}_{-0.5}$ |
| 300 | 15 | 123.0 | 16.14 | $^{+7.6}_{-9.1}$ | +1.6 | — | 0.371 | $^{+6.9}_{-11.7}$ | $^{+0.7}_{-0.7}$ |
| 300 | 20 | 123.3 | 16.08 | $^{+7.5}_{-9.1}$ | +1.4 | — | 0.364 | $^{+6.9}_{-11.7}$ | $^{+0.9}_{-0.8}$ |
| 300 | 30 | 123.6 | 16.00 | $^{+7.5}_{-9.1}$ | +1.0 | — | 0.354 | $^{+6.9}_{-11.6}$ | $^{+1.2}_{-1.1}$ |
| 300 | 50 | 123.8 | 15.92 | $^{+7.4}_{-9.0}$ | +0.2 | — | 0.340 | $^{+6.9}_{-11.6}$ | $^{+1.5}_{-1.4}$ |

**Table 16:** Cross sections and uncertainties for lightest-scalar production in the *light-stop* scenario for $\sqrt{s} = 8$ TeV. Uncertainties below 0.1% are not listed (—). For the PDF uncertainties see text.

| $m_A$ [GeV] | $\tan\beta$ | $m_H$ [GeV] | $\sigma_{ggH}$ [pb] | $\Delta_\mu^\pm$ [%] | $\delta Y_b$ [%] | $\delta\Delta_b$ [%] | $\sigma_{bbH}$ [pb] | $\Delta_\mu^\pm$ [%] | $\delta\Delta_b$ [%] |
|---|---|---|---|---|---|---|---|---|---|
| 100 | 5 | 130.9 | 13.85 | $^{+5.9}_{-8.4}$ | −5.0 | $^{+0.2}_{-0.2}$ | 0.650 | $^{+6.5}_{-10.7}$ | $^{+1.8}_{-1.7}$ |
| 100 | 10 | 125.9 | 17.64 | $^{+6.4}_{-8.7}$ | −6.5 | $^{+0.4}_{-0.4}$ | 1.163 | $^{+6.8}_{-11.3}$ | $^{+3.2}_{-3.0}$ |
| 100 | 15 | 124.7 | 19.01 | $^{+6.6}_{-8.8}$ | −6.7 | $^{+0.5}_{-0.5}$ | 1.287 | $^{+6.9}_{-11.5}$ | $^{+4.5}_{-4.3}$ |
| 100 | 20 | 124.3 | 19.53 | $^{+6.6}_{-8.8}$ | −6.7 | $^{+0.7}_{-0.6}$ | 1.283 | $^{+6.9}_{-11.5}$ | $^{+5.8}_{-5.4}$ |
| 100 | 30 | 124.0 | 19.79 | $^{+6.6}_{-8.8}$ | −6.7 | $^{+0.9}_{-0.8}$ | 1.184 | $^{+6.9}_{-11.6}$ | $^{+8.1}_{-7.4}$ |
| 100 | 50 | 123.9 | 19.64 | $^{+6.6}_{-8.8}$ | −6.8 | $^{+1.2}_{-1.1}$ | 0.982 | $^{+6.9}_{-11.6}$ | $^{+12.0}_{-10.5}$ |
| 200 | 5 | 203.7 | 0.919 | $^{+4.6}_{-7.3}$ | −23.8 | $^{+0.5}_{-0.5}$ | 0.715 | $^{+4.4}_{-5.7}$ | $^{+1.3}_{-1.3}$ |
| 200 | 10 | 199.9 | 1.266 | $^{+8.9}_{-9.7}$ | −48.9 | $^{+2.0}_{-1.9}$ | 2.943 | $^{+4.5}_{-5.9}$ | $^{+2.3}_{-2.2}$ |
| 200 | 15 | 199.1 | 2.178 | $^{+10.4}_{-10.7}$ | −54.6 | $^{+3.2}_{-3.0}$ | 6.144 | $^{+4.5}_{-5.9}$ | $^{+3.2}_{-3.1}$ |
| 200 | 20 | 198.9 | 3.341 | $^{+10.9}_{-11.0}$ | −56.2 | $^{+4.2}_{-3.9}$ | 9.987 | $^{+4.5}_{-5.9}$ | $^{+4.1}_{-3.9}$ |
| 200 | 30 | 198.7 | 6.051 | $^{+11.2}_{-11.2}$ | −57.1 | $^{+5.8}_{-5.4}$ | 18.77 | $^{+4.5}_{-5.9}$ | $^{+5.6}_{-5.2}$ |
| 200 | 50 | 198.5 | 11.88 | $^{+11.2}_{-11.1}$ | −57.5 | $^{+8.5}_{-7.6}$ | 37.63 | $^{+4.5}_{-5.9}$ | $^{+8.1}_{-7.2}$ |
| 300 | 5 | 301.7 | 0.161 | $^{+2.9}_{-6.7}$ | −20.3 | $^{+0.4}_{-0.4}$ | 0.150 | $^{+3.2}_{-3.2}$ | $^{+1.3}_{-1.2}$ |
| 300 | 10 | 299.6 | 0.137 | $^{+6.6}_{-9.3}$ | −50.1 | $^{+1.9}_{-1.9}$ | 0.567 | $^{+3.2}_{-3.2}$ | $^{+2.3}_{-2.2}$ |
| 300 | 15 | 299.2 | 0.211 | $^{+8.6}_{-10.6}$ | −57.7 | $^{+3.2}_{-3.1}$ | 1.159 | $^{+3.3}_{-3.2}$ | $^{+3.2}_{-3.1}$ |
| 300 | 20 | 299.1 | 0.315 | $^{+9.5}_{-11.0}$ | −59.6 | $^{+4.3}_{-4.0}$ | 1.869 | $^{+3.3}_{-3.2}$ | $^{+4.1}_{-3.9}$ |
| 300 | 30 | 299.0 | 0.564 | $^{+10.1}_{-11.3}$ | −60.5 | $^{+6.0}_{-5.5}$ | 3.493 | $^{+3.3}_{-3.2}$ | $^{+5.6}_{-5.2}$ |
| 300 | 50 | 298.9 | 1.107 | $^{+10.2}_{-11.4}$ | −60.9 | $^{+8.7}_{-7.7}$ | 6.979 | $^{+3.3}_{-3.2}$ | $^{+8.1}_{-7.2}$ |
| 400 | 5 | 401.0 | $80.4\times10^{-3}$ | $^{—}_{-4.2}$ | −6.6 | $^{+0.1}_{-0.1}$ | $41.8\times10^{-3}$ | $^{+2.6}_{-2.0}$ | $^{+1.2}_{-1.2}$ |
| 400 | 10 | 399.6 | $27.0\times10^{-3}$ | $^{+0.6}_{-5.1}$ | −39.5 | $^{+1.6}_{-1.5}$ | 0.154 | $^{+2.6}_{-2.0}$ | $^{+2.3}_{-2.2}$ |
| 400 | 15 | 399.3 | $31.4\times10^{-3}$ | $^{+2.5}_{-7.1}$ | −61.0 | $^{+3.4}_{-3.3}$ | 0.313 | $^{+2.6}_{-2.0}$ | $^{+3.2}_{-3.1}$ |
| 400 | 20 | 399.2 | $45.9\times10^{-3}$ | $^{+5.2}_{-9.1}$ | −65.4 | $^{+4.7}_{-4.4}$ | 0.504 | $^{+2.6}_{-2.0}$ | $^{+4.1}_{-3.9}$ |
| 400 | 30 | 399.1 | $84.9\times10^{-3}$ | $^{+7.5}_{-10.6}$ | −65.7 | $^{+6.5}_{-6.0}$ | 0.941 | $^{+2.6}_{-2.0}$ | $^{+5.6}_{-5.2}$ |
| 400 | 50 | 399.1 | 0.173 | $^{+8.8}_{-11.2}$ | −64.9 | $^{+9.2}_{-8.1}$ | 1.878 | $^{+2.6}_{-2.0}$ | $^{+8.1}_{-7.2}$ |
| 500 | 5 | 500.4 | $23.6\times10^{-3}$ | $^{+1.3}_{-9.1}$ | +4.4 | $^{—}_{—}$ | $14.2\times10^{-3}$ | $^{+2.3}_{-1.4}$ | $^{+1.2}_{-1.2}$ |
| 500 | 10 | 499.4 | $2.81\times10^{-3}$ | $^{+18.6}_{-46.2}$ | −1.3 | $^{+0.9}_{-0.9}$ | $51.6\times10^{-3}$ | $^{+2.3}_{-1.4}$ | $^{+2.3}_{-2.2}$ |
| 500 | 15 | 499.3 | $2.47\times10^{-3}$ | $^{+9.8}_{-32.2}$ | −69.4 | $^{+5.2}_{-4.9}$ | 0.105 | $^{+2.3}_{-1.4}$ | $^{+3.2}_{-3.1}$ |
| 500 | 20 | 499.2 | $5.12\times10^{-3}$ | $^{+1.2}_{-7.5}$ | −80.8 | $^{+6.6}_{-6.1}$ | 0.169 | $^{+2.3}_{-1.4}$ | $^{+4.1}_{-3.9}$ |
| 500 | 30 | 499.2 | $13.4\times10^{-3}$ | $^{+5.2}_{-9.3}$ | −75.8 | $^{+7.8}_{-7.1}$ | 0.315 | $^{+2.3}_{-1.4}$ | $^{+5.6}_{-5.2}$ |
| 500 | 50 | 499.1 | $33.2\times10^{-3}$ | $^{+8.3}_{-11.3}$ | −70.6 | $^{+10.1}_{-8.9}$ | 0.628 | $^{+2.3}_{-1.4}$ | $^{+8.1}_{-7.2}$ |

**Table 17:** Cross sections and uncertainties for heaviest-scalar production in the *light-stop* scenario for $\sqrt{s} = 8$ TeV. Uncertainties below 0.1% are not listed (—). For the PDF uncertainties see text.

| $m_A$ [GeV] | $\tan\beta$ | $\sigma_{ggA}$ [pb] | $\Delta_\mu^\pm$ [%] | $\delta Y_b$ [%] | $\delta\Delta_b$ [%] | $\sigma_{bbA}$ [pb] | $\Delta_\mu^\pm$ [%] | $\delta\Delta_b$ [%] |
|---|---|---|---|---|---|---|---|---|
| 100 | 5 | 9.685 | $^{+15.5}_{-13.5}$ | −47.8 | $^{+1.2}_{-1.2}$ | 9.841 | $^{+8.6}_{-15.7}$ | $^{+1.2}_{-1.2}$ |
| 100 | 10 | 36.48 | $^{+15.5}_{-13.5}$ | −54.1 | $^{+2.4}_{-2.3}$ | 35.29 | $^{+8.6}_{-15.7}$ | $^{+2.3}_{-2.2}$ |
| 100 | 15 | 76.79 | $^{+15.2}_{-13.3}$ | −53.4 | $^{+3.4}_{-3.2}$ | 71.44 | $^{+8.6}_{-15.7}$ | $^{+3.2}_{-3.1}$ |
| 100 | 20 | 125.2 | $^{+15.0}_{-13.2}$ | −53.1 | $^{+4.2}_{-4.0}$ | 114.8 | $^{+8.6}_{-15.7}$ | $^{+4.1}_{-3.9}$ |
| 100 | 30 | 235.2 | $^{+14.7}_{-13.1}$ | −52.9 | $^{+5.8}_{-5.4}$ | 214.0 | $^{+8.6}_{-15.7}$ | $^{+5.6}_{-5.2}$ |
| 100 | 50 | 467.6 | $^{+14.3}_{-12.9}$ | −52.9 | $^{+8.4}_{-7.5}$ | 426.8 | $^{+8.6}_{-15.7}$ | $^{+8.1}_{-7.2}$ |
| 200 | 5 | 0.534 | $^{+7.8}_{-9.1}$ | −4.0 | $^{+0.2}_{-0.2}$ | 0.845 | $^{+4.5}_{-5.9}$ | $^{+1.2}_{-1.2}$ |
| 200 | 10 | 0.808 | $^{+12.7}_{-11.9}$ | −57.8 | $^{+2.4}_{-2.4}$ | 3.030 | $^{+4.5}_{-5.9}$ | $^{+2.3}_{-2.2}$ |
| 200 | 15 | 1.831 | $^{+12.3}_{-11.7}$ | −59.5 | $^{+3.5}_{-3.3}$ | 6.135 | $^{+4.5}_{-5.9}$ | $^{+3.2}_{-3.1}$ |
| 200 | 20 | 3.125 | $^{+11.9}_{-11.5}$ | −58.6 | $^{+4.4}_{-4.1}$ | 9.859 | $^{+4.5}_{-5.9}$ | $^{+4.1}_{-3.9}$ |
| 200 | 30 | 6.097 | $^{+11.5}_{-11.3}$ | −57.6 | $^{+5.9}_{-5.4}$ | 18.38 | $^{+4.5}_{-5.9}$ | $^{+5.6}_{-5.2}$ |
| 200 | 50 | 12.39 | $^{+11.0}_{-11.0}$ | −57.0 | $^{+8.4}_{-7.5}$ | 36.65 | $^{+4.5}_{-5.9}$ | $^{+8.1}_{-7.2}$ |
| 300 | 5 | 0.310 | $^{+5.5}_{-8.0}$ | +8.0 | $^{+0.1}_{-0.1}$ | 0.159 | $^{+3.2}_{-3.2}$ | $^{+1.2}_{-1.2}$ |
| 300 | 10 | $87.7\times10^{-3}$ | $^{+8.5}_{-9.6}$ | −27.2 | $^{+1.3}_{-1.2}$ | 0.568 | $^{+3.2}_{-3.2}$ | $^{+2.3}_{-2.2}$ |
| 300 | 15 | 0.150 | $^{+11.9}_{-12.0}$ | −60.4 | $^{+3.6}_{-3.4}$ | 1.151 | $^{+3.2}_{-3.2}$ | $^{+3.2}_{-3.1}$ |
| 300 | 20 | 0.269 | $^{+12.0}_{-12.2}$ | −62.9 | $^{+4.6}_{-4.3}$ | 1.849 | $^{+3.2}_{-3.2}$ | $^{+4.1}_{-3.9}$ |
| 300 | 30 | 0.564 | $^{+11.5}_{-12.0}$ | −61.4 | $^{+6.1}_{-5.6}$ | 3.447 | $^{+3.2}_{-3.2}$ | $^{+5.6}_{-5.2}$ |
| 300 | 50 | 1.201 | $^{+10.7}_{-11.7}$ | −59.8 | $^{+8.5}_{-7.6}$ | 6.874 | $^{+3.2}_{-3.2}$ | $^{+8.1}_{-7.2}$ |
| 400 | 5 | 0.334 | $^{+4.8}_{-7.8}$ | −1.9 | — | $42.8\times10^{-3}$ | $^{+2.6}_{-2.0}$ | $^{+1.2}_{-1.2}$ |
| 400 | 10 | $98.9\times10^{-3}$ | $^{+9.0}_{-10.2}$ | −14.5 | $^{+0.5}_{-0.5}$ | 0.154 | $^{+2.6}_{-2.0}$ | $^{+2.3}_{-2.2}$ |
| 400 | 15 | $73.4\times10^{-3}$ | $^{+13.5}_{-12.8}$ | −35.0 | $^{+1.8}_{-1.7}$ | 0.311 | $^{+2.6}_{-2.0}$ | $^{+3.2}_{-3.1}$ |
| 400 | 20 | $81.1\times10^{-3}$ | $^{+14.7}_{-13.7}$ | −48.4 | $^{+3.2}_{-3.0}$ | 0.500 | $^{+2.6}_{-2.0}$ | $^{+4.1}_{-3.9}$ |
| 400 | 30 | 0.123 | $^{+13.7}_{-13.5}$ | −57.2 | $^{+5.4}_{-4.9}$ | 0.932 | $^{+2.6}_{-2.0}$ | $^{+5.6}_{-5.2}$ |
| 400 | 50 | 0.227 | $^{+11.7}_{-12.6}$ | −59.7 | $^{+8.2}_{-7.3}$ | 1.858 | $^{+2.6}_{-2.0}$ | $^{+8.1}_{-7.2}$ |
| 500 | 5 | $96.7\times10^{-3}$ | $^{+3.5}_{-7.0}$ | −4.0 | — | $14.3\times10^{-3}$ | $^{+2.3}_{-1.4}$ | $^{+1.2}_{-1.2}$ |
| 500 | 10 | $31.9\times10^{-3}$ | $^{+7.1}_{-9.5}$ | −17.7 | $^{+0.6}_{-0.5}$ | $51.4\times10^{-3}$ | $^{+2.3}_{-1.4}$ | $^{+2.3}_{-2.2}$ |
| 500 | 15 | $23.9\times10^{-3}$ | $^{+11.0}_{-11.9}$ | −34.4 | $^{+1.7}_{-1.6}$ | 0.104 | $^{+2.3}_{-1.4}$ | $^{+3.2}_{-3.1}$ |
| 500 | 20 | $24.9\times10^{-3}$ | $^{+12.4}_{-12.9}$ | −45.8 | $^{+2.9}_{-2.8}$ | 0.167 | $^{+2.3}_{-1.4}$ | $^{+4.1}_{-3.9}$ |
| 500 | 30 | $33.9\times10^{-3}$ | $^{+12.2}_{-13.1}$ | −55.2 | $^{+5.0}_{-4.6}$ | 0.312 | $^{+2.3}_{-1.4}$ | $^{+5.6}_{-5.2}$ |
| 500 | 50 | $58.0\times10^{-3}$ | $^{+10.8}_{-12.5}$ | −59.3 | $^{+8.0}_{-7.1}$ | 0.622 | $^{+2.3}_{-1.4}$ | $^{+8.1}_{-7.2}$ |

**Table 18:** Cross sections and uncertainties for pseudoscalar production in the *light-stop* scenario for $\sqrt{s} = 8$ TeV. Uncertainties below 0.1% are not listed (—). For the PDF uncertainties see text.

# BIBLIOGRAPHY


[1] Matteo Cacciari and Nicolas Houdeau. Meaningful characterisation of perturbative theoretical uncertainties. *JHEP*, 1109:039, 2011. doi: 10.1007/JHEP09(2011)039.

[2] E. T. Jaynes. *Probability Theory: The Logic of Science*. Cambridge University Press, April 2003. ISBN 0521592712. URL http://www.amazon.com/exec/obidos/redirect?tag=citeulike07-20&path=ASIN/0521592712.

[3] Giulio d'Agostini. *Bayesian Reasoning in data analysis - A critical introduction*. Cambridge University Press, 2003.

[4] Bruno de Finetti. La prévision : ses lois logiques, ses sources subjectives. *Annales de l'institut Henri Poincaré*, 7(1):1–68, 1937. URL http://eudml.org/doc/79004.

[5] Bradley Efron. Controversies in the foundations of statistics. *The American Mathematical Monthly*, 85(4):pp. 231–246, 1978. ISSN 00029890. URL http://www.jstor.org/stable/2321163.

[6] Charalampos Anastasiou, Kirill Melnikov, and Frank Petriello. Fully differential Higgs boson production and the di-photon signal through next-to-next-to-leading order. *Nucl.Phys.*, B724:197–246, 2005. doi: 10.1016/j.nuclphysb.2005.06.036.

[7] Charalampos Anastasiou and Kirill Melnikov. Higgs boson production at hadron colliders in NNLO QCD. *Nucl.Phys.*, B646:220–256, 2002. doi: 10.1016/S0550-3213(02)00837-4.

[8] A. I. Vainshtein and V. I. Zakharov. Ultraviolet-renormalon calculus. *Phys. Rev. Lett.*, 73:1207–1210, Aug 1994. doi: 10.1103/PhysRevLett.73.1207. URL http://link.aps.org/doi/10.1103/PhysRevLett.73.1207.

[9] Valentin I. Zakharov. QCD perturbative expansions in large orders. *Nucl.Phys.*, B385:452–480, 1992. doi: 10.1016/0550-3213(92)90054-F.

[10] Jan Fischer. On the role of power expansions in quantum field theory. *Int.J.Mod.Phys.*, A12:3625–3663, 1997. doi: 10.1142/S0217751X97001870.

[11] M. Beneke. Renormalons. *Phys.Rept.*, 317:1–142, 1999. doi: 10.1016/S0370-1573(98)00130-6.

[12] Stefano Forte, Andrea Isgrò, and Gherardo Vita. Do we need N$^3$LO Parton Distributions? *Phys.Lett.*, B731:136–140, 2014. doi: 10.1016/j.physletb.2014.02.027.

[13] Stefano Goria, Giampiero Passarino, and Dario Rosco. The Higgs Boson Lineshape. *Nucl.Phys.*, B864:530–579, 2012. doi: 10.1016/j.nuclphysb.2012.07.006.

[14] Marco Bonvini, Stefano Forte, and Giovanni Ridolfi. Soft gluon resummation of Drell-Yan rapidity distributions: Theory and phenomenology. *Nucl.Phys.*, B847:93–159, 2011. doi: 10.1016/j.nuclphysb.2011.01.023.

[15] Marco Bonvini, Stefano Forte, and Giovanni Ridolfi. The Threshold region for Higgs production in gluon fusion. *Phys.Rev.Lett.*, 109:102002, 2012. doi: 10.1103/PhysRevLett.109.102002.

[16] P.A. Baikov, K.G. Chetyrkin, and Johann H. Kuhn. Order alpha**4(s) QCD Corrections to Z and tau Decays. *Phys.Rev.Lett.*, 101:012002, 2008. doi: 10.1103/PhysRevLett.101.012002.

[17] S.A. Larin, F.V. Tkachov, and J.A.M. Vermaseren. The alpha(s**3) correction to the Bjorken sum rule. *Phys.Rev.Lett.*, 66:862–863, 1991. doi: 10.1103/PhysRevLett.66.862.

[18] S.A. Larin and J.A.M. Vermaseren. The alpha-s**3 corrections to the Bjorken sum rule for polarized electroproduction and to the Gross-Llewellyn Smith sum rule. *Phys.Lett.*, B259:345–352, 1991. doi: 10.1016/0370-2693(91)90839-I.

[19] Sandip Biswas and Kirill Melnikov. Second order QCD corrections to inclusive semileptonic b —> X(c) l anti-nu(l) decays with massless and massive lepton. *JHEP*, 1002:089, 2010. doi: 10.1007/JHEP02(2010)089.

[20] P.A. Baikov, K.G. Chetyrkin, J.H. Kuhn, and J. Rittinger. Complete $\mathcal{O}(\alpha_s^4)$ QCD Corrections to Hadronic Z-Decays. *Phys.Rev.Lett.*, 108:222003, 2012. doi: 10.1103/PhysRevLett.108.222003.

[21] K.G. Chetyrkin, Johann H. Kuhn, and A. Kwiatkowski. QCD corrections to the $e^+e^-$ cross-section and the Z boson decay rate. 1994.

[22] Stefan Weinzierl. Moments of event shapes in electron-positron annihilation at NNLO. *Phys.Rev.*, D80:094018, 2009. doi: 10.1103/PhysRevD.80.094018.

[23] S. A. Larin, P. Nogueira, T. van Ritbergen, and J. A. M. Vermaseren. The 3-loop QCD calculation of the moments of deep inelastic structure functions. *Nuclear Physics B*, 492:338–378, May 1997. doi: 10.1016/S0550-3213(97)80038-7.

[24] P.A. Baikov, K.G. Chetyrkin, and Johann H. Kuhn. Scalar correlator at O(alpha(s)**4), Higgs decay into b-quarks and bounds on the light quark masses. *Phys.Rev.Lett.*, 96:012003, 2006. doi: 10.1103/PhysRevLett.96.012003.

[25] P.A. Baikov and K.G. Chetyrkin. Higgs Decay into Hadrons to Order alpha**5(s). *Phys.Rev.Lett.*, 97:061803, 2006. doi: 10.1103/PhysRevLett.97.061803.

[26] P. Maierhöfer and P. Marquard. Complete three-loop QCD corrections to the decay $H \to \gamma\gamma$. *Phys.Lett.*, B721:131–135, 2013. doi: 10.1016/j.physletb.2013.02.040.

[27] M. Spira, A. Djouadi, D. Graudenz, and P.M. Zerwas. Higgs boson production at the LHC. *Nucl.Phys.*, B453:17–82, 1995. doi: 10.1016/0550-3213(95)00379-7.

[28] Michael Spira. HIGLU: A program for the calculation of the total Higgs production cross-section at hadron colliders via gluon fusion including QCD corrections. 1995.

[29] Robert V. Harlander and William B. Kilgore. Higgs boson production in bottom quark fusion at next-to-next-to leading order. *Phys.Rev.*, D68:013001, 2003. doi: 10.1103/PhysRevD.68.013001.

[30] Michal Czakon, Paul Fiedler, and Alexander Mitov. The total top quark pair production cross-section at hadron colliders through $O(\alpha_s^4)$. 2013.

[31] Stefano Catani, Leandro Cieri, Giancarlo Ferrera, Daniel de Florian, and Massimiliano Grazzini. Vector boson production at hadron colliders: A Fully exclusive QCD calculation at NNLO. *Phys.Rev.Lett.*, 103:082001, 2009. doi: 10.1103/PhysRevLett.103.082001.

[32] Oliver Brein, Abdelhak Djouadi, and Robert Harlander. NNLO QCD corrections to the Higgs-strahlung processes at hadron colliders. *Phys.Lett.*, B579:149–156, 2004. doi: 10.1016/j.physletb.2003.10.112.

[33] John M. Campbell and R. Keith Ellis. Next-to-leading order corrections to $W^+$ 2 jet and $Z^+$ 2 jet production at hadron colliders. *Phys.Rev.*, D65:113007, 2002. doi: 10.1103/PhysRevD.65.113007.

[34] John M. Campbell and R. Keith Ellis. An Update on vector boson pair production at hadron colliders. *Phys.Rev.*, D60:113006, 1999. doi: 10.1103/PhysRevD.60.113006.

[35] Julien Baglio and Abdelhak Djouadi. Predictions for Higgs production at the Tevatron and the associated uncertainties. *JHEP*, 1010:064, 2010. doi: 10.1007/JHEP10(2010)064.

[36] J. Baglio, A. Djouadi, and R.M. Godbole. The apparent excess in the Higgs to di-photon rate at the LHC: New Physics or QCD uncertainties? *Phys.Lett.*, B716:203–207, 2012. doi: 10.1016/j.physletb.2012.08.013.

[37] Georges Aad et al. Observation of a new particle in the search for the Standard Model Higgs boson with the ATLAS detector at the LHC. *Phys.Lett.*, B716:1–29, 2012. doi: 10.1016/j.physletb.2012.08.020.

[38] Serguei Chatrchyan et al. Observation of a new boson at a mass of 125 GeV with the CMS experiment at the LHC. *Phys.Lett.*, B716:30–61, 2012. doi: 10.1016/j.physletb.2012.08.021.

[39] S. Dittmaier et al. Handbook of LHC Higgs Cross Sections: 1. Inclusive Observables. 2011.

[40] S. Dittmaier, S. Dittmaier, C. Mariotti, G. Passarino, R. Tanaka, et al. Handbook of LHC Higgs Cross Sections: 2. Differential Distributions. 2012. doi: 10.5170/CERN-2012-002.

[41] S Heinemeyer et al. Handbook of LHC Higgs Cross Sections: 3. Higgs Properties. 2013. doi: 10.5170/CERN-2013-004.

[42] Abdelhak Djouadi. The Anatomy of electro-weak symmetry breaking. I: The Higgs boson in the standard model. *Phys.Rept.*, 457:1–216, 2008. doi: 10.1016/j.physrep.2007.10.004.

[43] Stephen P. Martin. A Supersymmetry primer. *Adv.Ser.Direct.High Energy Phys.*, 21:1–153, 2010. doi: 10.1142/9789814307505_0001.

[44] Abdelhak Djouadi. The Anatomy of electro-weak symmetry breaking. II. The Higgs bosons in the minimal supersymmetric model. *Phys.Rept.*, 459:1–241, 2008. doi: 10.1016/j.physrep.2007.10.005.

[45] G.C. Branco, P.M. Ferreira, L. Lavoura, M.N. Rebelo, Marc Sher, et al. Theory and phenomenology of two-Higgs-doublet models. *Phys.Rept.*, 516:1–102, 2012. doi: 10.1016/j.physrep.2012.02.002.

[46] Robert V. Harlander. Virtual corrections to g g → H to two loops in the heavy top limit. *Phys.Lett.*, B492:74–80, 2000. doi: 10.1016/S0370-2693(00)01042-X.
Stefano Catani, Daniel de Florian, and Massimiliano Grazzini. Higgs production in hadron collisions: Soft and virtual QCD corrections at NNLO. *JHEP*, 0105:025, 2001. doi: 10.1088/1126-6708/2001/05/025.
Robert V. Harlander and William B. Kilgore. Soft and virtual corrections to proton proton → H + x at NNLO. *Phys.Rev.*, D64:013015, 2001. doi: 10.1103/PhysRevD.64.013015.
Robert V. Harlander and William B. Kilgore. Next-to-next-to-leading order Higgs production at hadron colliders. *Phys.Rev.Lett.*, 88:201801, 2002. doi: 10.1103/PhysRevLett.88.201801.
V. Ravindran, J. Smith, and W. L. van Neerven. NNLO corrections to the total cross-section for Higgs boson production in hadron hadron collisions. *Nucl.Phys.*, B665:325–366, 2003. doi: 10.1016/S0550-3213(03)00457-7.

[47] S. Moch and A. Vogt. Higher-order soft corrections to lepton pair and Higgs boson production. *Phys.Lett.*, B631:48–57, 2005. doi: 10.1016/j.physletb.2005.09.061.
V. Ravindran. Higher-order threshold effects to inclusive processes in QCD. *Nucl.Phys.*, B752:173–196, 2006. doi: 10.1016/j.nuclphysb.2006.06.025.
Richard D. Ball, Marco Bonvini, Stefano Forte, Simone Marzani, and Giovanni Ridolfi. Higgs production in gluon fusion beyond NNLO. 2013.
Stephan Buehler and Achilleas Lazopoulos. Scale dependence and collinear subtraction terms for Higgs production in gluon fusion at N3LO. *JHEP*, 1310:096, 2013. doi: 10.1007/JHEP10(2013)096.
Charalampos Anastasiou, Claude Duhr, Falko Dulat, Elisabetta Furlan, Thomas Gehrmann, et al. Higgs boson gluon-fusion production at threshold in N3LO QCD. 2014.

[48] S. Dawson. Radiative corrections to Higgs boson production. *Nucl.Phys.*, B359:283–300, 1991. doi: 10.1016/0550-3213(91)90061-2.
A. Djouadi, M. Spira, and P.M. Zerwas. Production of Higgs bosons in proton colliders: QCD corrections. *Phys.Lett.*, B264:440–446, 1991. doi: 10.1016/0370-2693(91)90375-Z.

[49] Robert Harlander and Philipp Kant. Higgs production and decay: Analytic results at next-to-leading order QCD. *JHEP*, 0512:015, 2005. doi: 10.1088/1126-6708/2005/12/015.

[50] Charalampos Anastasiou, Stefan Beerli, Stefan Bucherer, Alejandro Daleo, and Zoltan Kunszt. Two-loop amplitudes and master integrals for the production of a Higgs boson via a massive quark and a scalar-quark loop. *JHEP*, 0701:082, 2007. doi: 10.1088/1126-6708/2007/01/082.

[51] U. Aglietti, R. Bonciani, G. Degrassi, and A. Vicini. Analytic Results for Virtual QCD Corrections to Higgs Production and Decay. *JHEP*, 0701:021, 2007. doi: 10.1088/1126-6708/2007/01/021.
R. Bonciani, Giuseppe Degrassi, and A. Vicini. Scalar particle contribution to Higgs production via gluon fusion at NLO. *JHEP*, 0711:095, 2007. doi: 10.1088/1126-6708/2007/11/095.

[52] Michael Kramer, Eric Laenen, and Michael Spira. Soft gluon radiation in Higgs boson production at the LHC. *Nucl.Phys.*, B511:523–549, 1998. doi: 10.1016/S0550-3213(97)00679-2.
Stefano Catani, Daniel de Florian, Massimiliano Grazzini, and Paolo Nason. Soft gluon resummation for Higgs boson production at hadron colliders. *JHEP*, 0307:028, 2003. doi: 10.1088/1126-6708/2003/07/028.
Ahmad Idilbi, Xiang-dong Ji, Jian-Ping Ma, and Feng Yuan. Threshold resummation for Higgs production in effective field theory. *Phys.Rev.*, D73:077501, 2006. doi: 10.1103/PhysRevD.73.077501.
Ahmad Idilbi, Xiang-dong Ji, and Feng Yuan. Resummation of threshold logarithms in effective field theory for DIS, Drell-Yan and Higgs production. *Nucl.Phys.*, B753:42–68, 2006. doi: 10.1016/j.nuclphysb.2006.07.002.
Valentin Ahrens, Thomas Becher, Matthias Neubert, and Li Lin Yang. Renormalization-Group Improved Prediction for Higgs Production at Hadron Colliders. *Eur.Phys.J.*, C62:333–353, 2009. doi: 10.1140/epjc/s10052-009-1030-2.

[53] A. Djouadi and P. Gambino. Leading electroweak correction to Higgs boson production at proton colliders. *Phys.Rev.Lett.*, 73:2528–2531, 1994. doi: 10.1103/PhysRevLett.73.2528.
A. Djouadi, P. Gambino, and Bernd A. Kniehl. Two loop electroweak heavy fermion corrections to Higgs boson production and decay. *Nucl.Phys.*, B523:17–39, 1998. doi: 10.1016/S0550-3213(98)00147-3.

[54] U. Aglietti, R. Bonciani, G. Degrassi, and A. Vicini. Two loop light fermion contribution to Higgs production and decays. *Phys.Lett.*, B595:432–441, 2004. doi: 10.1016/j.physletb.2004.06.063.
U. Aglietti, R. Bonciani, G. Degrassi, and A. Vicini. Master integrals for the two-loop light fermion contributions to gg $\to$ H and H $\to$ gamma gamma. *Phys.Lett.*, B600:57–64, 2004. doi: 10.1016/j.physletb.2004.09.001.

[55] Giuseppe Degrassi and Fabio Maltoni. Two-loop electroweak corrections to Higgs production at hadron colliders. *Phys.Lett.*, B600:255–260, 2004. doi: 10.1016/j.physletb.2004.09.008.

[56] Stefano Actis, Giampiero Passarino, Christian Sturm, and Sandro Uccirati. NLO Electroweak Corrections to Higgs Boson Production at Hadron Colliders. *Phys.Lett.*, B670:12–17, 2008. doi: 10.1016/j.physletb.2008.10.018.
Stefano Actis, Giampiero Passarino, Christian Sturm, and Sandro Uccirati. NNLO Computational Techniques: The Cases H $\to$ gamma gamma and H $\to$ g g. *Nucl.Phys.*, B811:182–273, 2009. doi: 10.1016/j.nuclphysb.2008.11.024.

[57] R. Bonciani, G. Degrassi, and A. Vicini. On the Generalized Harmonic Polylogarithms of One Complex Variable. *Comput.Phys.Commun.*, 182:1253–1264, 2011. doi: 10.1016/j.cpc.2011.02.011.

[58] Charalampos Anastasiou, Radja Boughezal, and Frank Petriello. Mixed QCD-electroweak corrections to Higgs boson production in gluon fusion. *JHEP*, 0904:003, 2009. doi: 10.1088/1126-6708/2009/04/003.

[59] S. Dawson, A. Djouadi, and M. Spira. QCD corrections to SUSY Higgs production: The Role of squark loops. *Phys.Rev.Lett.*, 77:16–19, 1996. doi: 10.1103/PhysRevLett.77.16.

[60] Margarete Muhlleitner and Michael Spira. Higgs Boson Production via Gluon Fusion: Squark Loops at NLO QCD. *Nucl.Phys.*, B790:1–27, 2008. doi: 10.1016/j.nuclphysb.2007.08.011.

[61] Charalampos Anastasiou, Stefan Beerli, and Alejandro Daleo. The Two-loop QCD amplitude gg $\rightarrow$ h,H in the Minimal Supersymmetric Standard Model. *Phys.Rev.Lett.*, 100:241806, 2008. doi: 10.1103/PhysRevLett.100.241806.

[62] M. Muhlleitner, H. Rzehak, and M. Spira. SUSY-QCD Corrections to MSSM Higgs Boson Production via Gluon fusion. *PoS*, RADCOR2009:043, 2010.

[63] Robert V. Harlander and Matthias Steinhauser. Hadronic Higgs production and decay in supersymmetry at next-to-leading order. *Phys.Lett.*, B574:258–268, 2003. doi: 10.1016/j.physletb.2003.09.013.

[64] Robert V. Harlander and Matthias Steinhauser. Supersymmetric Higgs production in gluon fusion at next-to-leading order. *JHEP*, 0409:066, 2004. doi: 10.1088/1126-6708/2004/09/066.

[65] G. Degrassi and P. Slavich. On the NLO QCD corrections to Higgs production and decay in the MSSM. *Nucl.Phys.*, B805:267–286, 2008. doi: 10.1016/j.nuclphysb.2008.07.022.

[66] Robert V. Harlander and Franziska Hofmann. Pseudo-scalar Higgs production at next-to-leading order SUSY-QCD. *JHEP*, 0603:050, 2006. doi: 10.1088/1126-6708/2006/03/050.

[67] G. Degrassi, S. Di Vita, and P. Slavich. NLO QCD corrections to pseudoscalar Higgs production in the MSSM. *JHEP*, 1108:128, 2011. doi: 10.1007/JHEP08(2011)128.

[68] G. Degrassi and P. Slavich. NLO QCD bottom corrections to Higgs boson production in the MSSM. *JHEP*, 1011:044, 2010. doi: 10.1007/JHEP11(2010)044.

[69] Robert V. Harlander, Franziska Hofmann, and Hendrik Mantler. Supersymmetric Higgs production in gluon fusion. *JHEP*, 1102:055, 2011. doi: 10.1007/JHEP02(2011)055.

[70] G. Degrassi, S. Di Vita, and P. Slavich. On the NLO QCD Corrections to the Production of the Heaviest Neutral Higgs Scalar in the MSSM. *Eur.Phys.J.*, C72:2032, 2012. doi: 10.1140/epjc/s10052-012-2032-z.

[71] K.G. Chetyrkin, Bernd A. Kniehl, M. Steinhauser, and William A. Bardeen. Effective QCD interactions of CP odd Higgs bosons at three loops. *Nucl.Phys.*, B535:3–18, 1998. doi: 10.1016/S0550-3213(98)00594-X.
Robert V. Harlander and William B. Kilgore. Production of a pseudoscalar Higgs boson at hadron colliders at next-to-next-to leading order. *JHEP*, 0210:017, 2002. doi: 10.1088/1126-6708/2002/10/017.
Charalampos Anastasiou and Kirill Melnikov. Pseudoscalar Higgs boson production at hadron colliders in NNLO QCD. *Phys.Rev.*, D67:037501, 2003. doi: 10.1103/PhysRevD.67.037501.
Fabrizio Caola and Simone Marzani. Finite fermion mass effects in pseudoscalar Higgs production via gluon-gluon fusion. *Phys.Lett.*, B698:275–283, 2011. doi: 10.1016/j.physletb.2011.03.019.
Alexey Pak, Mikhail Rogal, and Matthias Steinhauser. Production of scalar and pseudo-scalar Higgs bosons to next-to-next-to-leading order at hadron colliders. *JHEP*, 1109:088, 2011. doi: 10.1007/JHEP09(2011)088.

[72] Robert Harlander and Matthias Steinhauser. Effects of SUSY QCD in hadronic Higgs production at next-to-next-to-leading order. *Phys.Rev.*, D68:111701, 2003. doi: 10.1103/PhysRevD.68.111701.

[73] Alexey Pak, Matthias Steinhauser, and Nikolai Zerf. Towards Higgs boson production in gluon fusion to NNLO in the MSSM. *Eur.Phys.J.*, C71:1602, 2011. doi: 10.1140/epjc/s10052-012-2182-z, 10.1140/epjc/s10052-011-1602-9.

[74] Alexey Pak, Matthias Steinhauser, and Nikolai Zerf. Supersymmetric next-to-next-to-leading order corrections to Higgs boson production in gluon fusion. *JHEP*, 1209:118, 2012. doi: 10.1007/JHEP09(2012)118.

[75] Marcela S. Carena, David Garcia, Ulrich Nierste, and Carlos E.M. Wagner. Effective Lagrangian for the $\bar{t}bH^+$ interaction in the MSSM and charged Higgs phenomenology. *Nucl.Phys.*, B577: 88–120, 2000. doi: 10.1016/S0550-3213(00)00146-2.

[76] Jaume Guasch, Petra Hafliger, and Michael Spira. MSSM Higgs decays to bottom quark pairs revisited. *Phys.Rev.*, D68:115001, 2003. doi: 10.1103/PhysRevD.68.115001.

[77] David Noth and Michael Spira. Higgs Boson Couplings to Bottom Quarks: Two-Loop Supersymmetry-QCD Corrections. *Phys.Rev.Lett.*, 101:181801, 2008. doi: 10.1103/PhysRevLett.101.181801.
David Noth and Michael Spira. Supersymmetric Higgs Yukawa Couplings to Bottom Quarks at next-to-next-to-leading Order. *JHEP*, 1106:084, 2011. doi: 10.1007/JHEP06(2011)084.
L. Mihaila and C. Reisser. O(alpha_s^2) corrections to fermionic Higgs decays in the MSSM. *JHEP*, 1008:021, 2010. doi: 10.1007/JHEP08(2010)021.

[78] Stefan Dittmaier, 1 Kramer, Michael, and Michael Spira. Higgs radiation off bottom quarks at the Tevatron and the CERN LHC. *Phys.Rev.*, D70:074010, 2004. doi: 10.1103/PhysRevD.70.074010.
S. Dawson, C.B. Jackson, L. Reina, and D. Wackeroth. Exclusive Higgs boson production with bottom quarks at hadron colliders. *Phys.Rev.*, D69:074027, 2004. doi: 10.1103/PhysRevD.69.074027.

[79] D. Dicus, T. Stelzer, Z. Sullivan, and S. Willenbrock. Higgs boson production in association with bottom quarks at next-to-leading order. *Phys.Rev.*, D59:094016, 1999. doi: 10.1103/PhysRevD.59.094016.
F. Maltoni, Z. Sullivan, and S. Willenbrock. Higgs-boson production via bottom-quark fusion. *Phys.Rev.*, D67:093005, 2003. doi: 10.1103/PhysRevD.67.093005.

[80] Stefan Dittmaier, 1 Kramer, Michael, Alexander Muck, and Tobias Schluter. MSSM Higgs-boson production in bottom-quark fusion: Electroweak radiative corrections. *JHEP*, 0703:114, 2007. doi: 10.1088/1126-6708/2007/03/114.
S. Dawson, C.B. Jackson, and P. Jaiswal. SUSY QCD Corrections to Higgs-b Production : Is the $\Delta_b$ Approximation Accurate? *Phys.Rev.*, D83:115007, 2011. doi: 10.1103/PhysRevD.83.115007.

[81] R. Harlander et al. ggh@nnlo, . URL `http://particle.uni-wuppertal.de/harlander/software/ggh@nnlo/`.

[82] Stefano Catani and Massimiliano Grazzini. An NNLO subtraction formalism in hadron collisions and its application to Higgs boson production at the LHC. *Phys.Rev.Lett.*, 98:222002, 2007. doi: 10.1103/PhysRevLett.98.222002.
Massimiliano Grazzini. NNLO predictions for the Higgs boson signal in the H —> WW —> lnu lnu and H —> ZZ —> 4l decay channels. *JHEP*, 0802:043, 2008. doi: 10.1088/1126-6708/2008/02/043.
Massimiliano Grazzini and Hayk Sargsyan. Heavy-quark mass effects in Higgs boson production at the LHC. *JHEP*, 1309:129, 2013. doi: 10.1007/JHEP09(2013)129.

[83] Charalampos Anastasiou, Stephan Buehler, Franz Herzog, and Achilleas Lazopoulos. Total cross-section for Higgs boson hadroproduction with anomalous Standard Model interactions. *JHEP*, 1112:058, 2011. doi: 10.1007/JHEP12(2011)058.

[84] R. Harlander et al. bbh@nnlo, . URL `http://particle.uni-wuppertal.de/harlander/software/bbh@nnlo/`.

[85] E. Bagnaschi, G. Degrassi, P. Slavich, and A. Vicini. Higgs production via gluon fusion in the POWHEG approach in the SM and in the MSSM. *JHEP*, 1202:088, 2012. doi: 10.1007/JHEP02(2012)088.

[86] Stefano Frixione, Paolo Nason, and Carlo Oleari. Matching NLO QCD computations with Parton Shower simulations: the POWHEG method. *JHEP*, 0711:070, 2007. doi: 10.1088/1126-6708/2007/11/070.
Simone Alioli, Paolo Nason, Carlo Oleari, and Emanuele Re. A general framework for implementing NLO calculations in shower Monte Carlo programs: the POWHEG BOX. *JHEP*, 1006:043, 2010. doi: 10.1007/JHEP06(2010)043.

[87] Robert V. Harlander, Stefan Liebler, and Hendrik Mantler. SusHi: A program for the calculation of Higgs production in gluon fusion and bottom-quark annihilation in the Standard Model and the MSSM. *Computer Physics Communications*, 184:1605–1617, 2013. doi: 10.1016/j.cpc.2013.02.006.

[88] S. Heinemeyer, O. Stal, and G. Weiglein. Interpreting the LHC Higgs Search Results in the MSSM. *Phys.Lett.*, B710:201–206, 2012. doi: 10.1016/j.physletb.2012.02.084.

[89] A. Arbey, M. Battaglia, A. Djouadi, F. Mahmoudi, and J. Quevillon. Implications of a 125 GeV Higgs for supersymmetric models. *Phys.Lett.*, B708:162–169, 2012. doi: 10.1016/j.physletb.2012.01.053.

[90] M. Carena, S. Heinemeyer, O. Stål, C.E.M. Wagner, and G. Weiglein. MSSM Higgs Boson Searches at the LHC: Benchmark Scenarios after the Discovery of a Higgs-like Particle. *Eur.Phys.J.*, C73:2552, 2013. doi: 10.1140/epjc/s10052-013-2552-1.

[91] The sm inputs agreed upon by the "lhc higgs cross section working group" are listed here. URL `https://twiki.cern.ch/twiki/bin/view/LHCPhysics/SMInputParameter`.

[92] Mathew Muether and CDF. Combination of CDF and DO results on the mass of the top quark using up to 8.7 fb^-1 at the Tevatron. 2013.

[93] Johann H. Kuhn, Matthias Steinhauser, and Christian Sturm. Heavy Quark Masses from Sum Rules in Four-Loop Approximation. *Nucl.Phys.*, B778:192–215, 2007. doi: 10.1016/j.nuclphysb.2007.04.036.
K.G. Chetyrkin, J.H. Kuhn, A. Maier, P. Maierhofer, P. Marquard, et al. Charm and Bottom Quark Masses: An Update. *Phys.Rev.*, D80:074010, 2009. doi: 10.1103/PhysRevD.80.074010.

[94] S. Heinemeyer, W. Hollik, and G. Weiglein. FeynHiggs: A Program for the calculation of the masses of the neutral CP even Higgs bosons in the MSSM. *Comput.Phys.Commun.*, 124:76–89, 2000. doi: 10.1016/S0010-4655(99)00364-1.

[95] M. Frank, T. Hahn, S. Heinemeyer, W. Hollik, H. Rzehak, et al. The Higgs Boson Masses and Mixings of the Complex MSSM in the Feynman-Diagrammatic Approach. *JHEP*, 0702:047, 2007. doi: 10.1088/1126-6708/2007/02/047.

[96] S. Heinemeyer, W. Hollik, and G. Weiglein. The Masses of the neutral CP - even Higgs bosons in the MSSM: Accurate analysis at the two loop level. *Eur.Phys.J.*, C9:343–366, 1999. doi: 10.1007/s100529900006.

[97] Giuseppe Degrassi, Pietro Slavich, and Fabio Zwirner. On the neutral Higgs boson masses in the MSSM for arbitrary stop mixing. *Nucl.Phys.*, B611:403–422, 2001. doi: 10.1016/S0550-3213(01)00343-1.
Andrea Brignole, Giuseppe Degrassi, Pietro Slavich, and Fabio Zwirner. On the O(alpha(t)**2) two loop corrections to the neutral Higgs boson masses in the MSSM. *Nucl.Phys.*, B631:195–218, 2002. doi: 10.1016/S0550-3213(02)00184-0.

[98] A. Brignole, G. Degrassi, P. Slavich, and F. Zwirner. On the two loop sbottom corrections to the neutral Higgs boson masses in the MSSM. *Nucl.Phys.*, B643:79–92, 2002. doi: 10.1016/S0550-3213(02)00748-4.
Athanasios Dedes, Giuseppe Degrassi, and Pietro Slavich. On the two loop Yukawa corrections to the MSSM Higgs boson masses at large tan beta. *Nucl.Phys.*, B672:144–162, 2003. doi: 10.1016/j.nuclphysb.2003.08.033.

[99] S. Heinemeyer, W. Hollik, H. Rzehak, and G. Weiglein. High-precision predictions for the MSSM Higgs sector at O(alpha(b) alpha(s)). *Eur.Phys.J.*, C39:465–481, 2005. doi: 10.1140/epjc/s2005-02112-6.

[100] S. Heinemeyer, W. Hollik, H. Rzehak, and G. Weiglein. The Higgs sector of the complex MSSM at two-loop order: QCD contributions. *Phys.Lett.*, B652:300–309, 2007. doi: 10.1016/j.physletb.2007.07.030.

[101] G. Degrassi, S. Heinemeyer, W. Hollik, P. Slavich, and G. Weiglein. Towards high precision predictions for the MSSM Higgs sector. *Eur.Phys.J.*, C28:133–143, 2003. doi: 10.1140/epjc/s2003-01152-2.
B.C. Allanach, A. Djouadi, J.L. Kneur, W. Porod, and P. Slavich. Precise determination of the neutral Higgs boson masses in the MSSM. *JHEP*, 0409:044, 2004. doi: 10.1088/1126-6708/2004/09/044.

[102] Stephen P. Martin. Two loop effective potential for the minimal supersymmetric standard model. *Phys.Rev.*, D66:096001, 2002. doi: 10.1103/PhysRevD.66.096001.
Stephen P. Martin. Complete two loop effective potential approximation to the lightest Higgs scalar boson mass in supersymmetry. *Phys.Rev.*, D67:095012, 2003. doi: 10.1103/PhysRevD.67.095012.
Stephen P. Martin. Strong and Yukawa two-loop contributions to Higgs scalar boson self-energies and pole masses in supersymmetry. *Phys.Rev.*, D71:016012, 2005. doi: 10.1103/PhysRevD.71.016012.

[103] Stephen P. Martin. Three-loop corrections to the lightest Higgs scalar boson mass in supersymmetry. *Phys.Rev.*, D75:055005, 2007. doi: 10.1103/PhysRevD.75.055005.

[104] R.V. Harlander, P. Kant, L. Mihaila, and M. Steinhauser. Higgs boson mass in supersymmetry to three loops. *Phys.Rev.Lett.*, 100:191602, 2008. doi: 10.1103/PhysRevLett.101.039901,10.1103/PhysRevLett.100.191602.
P. Kant, R.V. Harlander, L. Mihaila, and M. Steinhauser. Light MSSM Higgs boson mass to three-loop accuracy. *JHEP*, 1008:104, 2010. doi: 10.1007/JHEP08(2010)104.

[105] 1229975. Search for strongly produced superpartners in final states with two same sign leptons with the ATLAS detector using 21 fb-1 of proton-proton collisions at sqrt(s)=8 TeV. 2013.

[106] Georges Aad et al. Search for new phenomena in final states with large jet multiplicities and missing transverse momentum at sqrt(s)=8 TeV proton-proton collisions using the ATLAS experiment. *JHEP*, 1310:130, 2013. doi: 10.1007/JHEP10(2013)130.
The ATLAS collaboration. Search for squarks and gluinos with the ATLAS detector in final states with jets and missing transverse momentum and 20.3 $\mathrm{fb}^{-1}$ of $\sqrt{s}$ = 8 TeV proton-proton collision data. 2013.
The ATLAS collaboration. Search for strong production of supersymmetric particles in final states with missing transverse momentum and at least three b-jets using 20.1 fb−1 of pp collisions at sqrt(s) = 8 TeV with the ATLAS Detector. 2013.
The ATLAS collaboration. Search for squarks and gluinos in events with isolated leptons, jets and missing transverse momentum at $\sqrt{s}$ = 8 TeV with the ATLAS detector. 2013.
The ATLAS collaboration. Search for strongly produced supersymmetric particles in decays with two leptons at $\sqrt{s}$ = 8 TeV. 2013.

[107] Serguei Chatrchyan et al. Search for supersymmetry in hadronic final states with missing transverse energy using the variables $\alpha_T$ and b-quark multiplicity in pp collisions at $\sqrt{s}$ = 8 TeV. *Eur.Phys.J.*, C73:2568, 2013. doi: 10.1140/epjc/s10052-013-2568-6.

[108] Serguei Chatrchyan et al. Search for new physics in events with same-sign dileptons and jets in pp collisions at $\sqrt{s}$ = 8 TeV. *JHEP*, 1401:163, 2014. doi: 10.1007/JHEP01(2014)163.
CMS Collaboration. A search for anomalous production of events with three or more leptons using 19.5/fb of sqrt(s)=8 TeV LHC data. 2013.
CMS Collaboration. Search for supersymmetry in pp collisions at sqrt(s) = 8 TeV in events with three leptons and at least one b-tagged jet. 2013.

[109] Serguei Chatrchyan et al. Search for supersymmetry in pp collisions at $\sqrt{s}$=8 TeV in events with a single lepton, large jet multiplicity, and multiple b jets. *Phys.Lett.*, B733:328–353, 2014. doi: 10.1016/j.physletb.2014.04.023.
Serguei Chatrchyan et al. Search for new physics in the multijet and missing transverse momentum final state in proton-proton collisions at $\sqrt{s}$ = 8 TeV. 2014. doi: 10.1007/JHEP06(2014)055.
CMS Collaboration. Search for supersymmetry using razor variables in events with b-jets in pp collisions at 8 TeV. 2013.

[110] Georges Aad et al. Search for direct top-squark pair production in final states with two leptons in pp collisions at sqrt(s)=8TeV with the ATLAS detector. 2014. doi: 10.1007/JHEP06(2014)124.

[111] Serguei Chatrchyan et al. Search for top-squark pair production in the single-lepton final state in pp collisions at $\sqrt{s}$ = 8 TeV. *Eur.Phys.J.*, C73:2677, 2013. doi: 10.1140/epjc/s10052-013-2677-2.
CMS Collaboration. Search for top squarks in multijet events with large missing momentum in proton-proton collisions at 8 TeV. 2013.

[112] The ATLAS collaboration. Search for pair-produced top squarks decaying into a charm quark and the lightest neutralinos with 20.3 $fb^{-1}$ of pp collisions at $\sqrt{s}$ = 8 TeV with the ATLAS detector at the LHC. 2013.

[113] CMS Collaboration. Search for top squarks decaying to a charm quark and a neutralino in events with a jet and missing transverse momentum. 2014.

[114] Georges Aad et al. Search for direct third-generation squark pair production in final states with missing transverse momentum and two b-jets in $\sqrt{s}$ = 8 TeV pp collisions with the ATLAS detector. *JHEP*, 1310:189, 2013. doi: 10.1007/JHEP10(2013)189.

[115] Michael Spira. QCD effects in Higgs physics. *Fortsch.Phys.*, 46:203–284, 1998. doi: 10.1002/(SICI)1521-3978(199804)46:3<203::AID-PROP203>3.0.CO;2-4.

[116] Robert Harlander. Supersymmetric Higgs production at the Large Hadron Collider. *Eur.Phys.J.*, C33:S454–S456, 2004. doi: 10.1140/epjcd/s2003-03-426-4.

[117] A.D. Martin, W.J. Stirling, R.S. Thorne, and G. Watt. Parton distributions for the LHC. *Eur.Phys.J.*, C63:189–285, 2009. doi: 10.1140/epjc/s10052-009-1072-5.

[118] Eduard Boos and Tilman Plehn. Higgs boson production induced by bottom quarks. *Phys.Rev.*, D69:094005, 2004. doi: 10.1103/PhysRevD.69.094005.

[119] K.G. Chetyrkin and M. Steinhauser. The Relation between the MS-bar and the on-shell quark mass at order alpha(s)**3. *Nucl.Phys.*, B573:617–651, 2000. doi: 10.1016/S0550-3213(99)00784-1.
Kirill Melnikov and Timo van Ritbergen. The Three loop relation between the MS-bar and the pole quark masses. *Phys.Lett.*, B482:99–108, 2000. doi: 10.1016/S0370-2693(00)00507-4.

[120] K.G. Chetyrkin. Quark mass anomalous dimension to O (alpha-s**4). *Phys.Lett.*, B404:161–165, 1997. doi: 10.1016/S0370-2693(97)00535-2.
J.A.M. Vermaseren, S.A. Larin, and T. van Ritbergen. The four loop quark mass anomalous dimension and the invariant quark mass. *Phys.Lett.*, B405:327–333, 1997. doi: 10.1016/S0370-2693(97)00660-6.

[121] Simone Marzani, Richard D. Ball, Vittorio Del Duca, Stefano Forte, and Alessandro Vicini. Higgs production via gluon-gluon fusion with finite top mass beyond next-to-leading order. *Nucl.Phys.*, B800:127–145, 2008. doi: 10.1016/j.nuclphysb.2008.03.016.
Robert V. Harlander and Kemal J. Ozeren. Top mass effects in Higgs production at next-to-next-to-leading order QCD: Virtual corrections. *Phys.Lett.*, B679:467–472, 2009. doi: 10.1016/j.physletb.2009.08.012.
Robert V. Harlander and Kemal J. Ozeren. Finite top mass effects for hadronic Higgs production at next-to-next-to-leading order. *JHEP*, 0911:088, 2009. doi: 10.1088/1126-6708/2009/11/088.
Alexey Pak, Mikhail Rogal, and Matthias Steinhauser. Virtual three-loop corrections to Higgs boson production in gluon fusion for finite top quark mass. *Phys.Lett.*, B679:473–477, 2009. doi: 10.1016/j.physletb.2009.08.016.
Alexey Pak, Mikhail Rogal, and Matthias Steinhauser. Finite top quark mass effects in NNLO Higgs boson production at LHC. *JHEP*, 1002:025, 2010. doi: 10.1007/JHEP02(2010)025.
Robert V. Harlander, Hendrik Mantler, Simone Marzani, and Kemal J. Ozeren. Higgs production in gluon fusion at next-to-next-to-leading order QCD for finite top mass. *Eur.Phys.J.*, C66:359–372, 2010. doi: 10.1140/epjc/s10052-010-1258-x.

[122] Julien Baglio and Abdelhak Djouadi. Higgs production at the lHC. *JHEP*, 1103:055, 2011. doi: 10.1007/JHEP03(2011)055.

[123] M.I. Kotsky and Oleg I. Yakovlev. On the resummation of double logarithms in the process Higgs → gamma gamma. *Phys.Lett.*, B418:335–344, 1998. doi: 10.1016/S0370-2693(97)01260-4.
R. Akhoury, H. Wang, and Oleg I. Yakovlev. On the Resummation of large QCD logarithms in Higgs → gamma gamma decay. *Phys.Rev.*, D64:113008, 2001. doi: 10.1103/PhysRevD.64.113008.

[124] Lawrence J. Hall, Riccardo Rattazzi, and Uri Sarid. The Top quark mass in supersymmetric SO(10) unification. *Phys.Rev.*, D50:7048–7065, 1994. doi: 10.1103/PhysRevD.50.7048.
Ralf Hempfling. Yukawa coupling unification with supersymmetric threshold corrections. *Phys.Rev.*, D49:6168–6172, 1994. doi: 10.1103/PhysRevD.49.6168.

[125] Hung-Liang Lai, Marco Guzzi, Joey Huston, Zhao Li, Pavel M. Nadolsky, et al. New parton distributions for collider physics. *Phys.Rev.*, D82:074024, 2010. doi: 10.1103/PhysRevD.82.074024.

[126] Richard D. Ball, Valerio Bertone, Stefano Carrazza, Christopher S. Deans, Luigi Del Debbio, et al. Parton distributions with LHC data. *Nucl.Phys.*, B867:244–289, 2013. doi: 10.1016/j.nuclphysb.2012.10.003.

[127] Federico Demartin, Stefano Forte, Elisa Mariani, Juan Rojo, and Alessandro Vicini. The impact of PDF and alphas uncertainties on Higgs Production in gluon fusion at hadron colliders. *Phys.Rev.*, D82:014002, 2010. doi: 10.1103/PhysRevD.82.014002.

[128] Sergey Alekhin, Simone Alioli, Richard D. Ball, Valerio Bertone, Johannes Blumlein, et al. The PDF4LHC Working Group Interim Report. 2011.
Michiel Botje, Jon Butterworth, Amanda Cooper-Sarkar, Albert de Roeck, Joel Feltesse, et al. The PDF4LHC Working Group Interim Recommendations. 2011.

[129] J. Beringer et al. Review of Particle Physics (RPP). *Phys.Rev.*, D86:010001, 2012. doi: 10.1103/PhysRevD.86.010001.

[130] A.D. Martin, W.J. Stirling, R.S. Thorne, and G. Watt. Heavy-quark mass dependence in global PDF analyses and 3- and 4-flavour parton distributions. *Eur.Phys.J.*, C70:51–72, 2010. doi: 10.1140/epjc/s10052-010-1462-8.

[131] Richard D. Ball, Valerio Bertone, Francesco Cerutti, Luigi Del Debbio, Stefano Forte, et al. Impact of Heavy Quark Masses on Parton Distributions and LHC Phenomenology. *Nucl.Phys.*, B849:296–363, 2011. doi: 10.1016/j.nuclphysb.2011.03.021.

[132] G. Bozzi, S. Catani, D. de Florian, and M. Grazzini. The q(T) spectrum of the Higgs boson at the LHC in QCD perturbation theory. *Phys.Lett.*, B564:65–72, 2003. doi: 10.1016/S0370-2693(03)00656-7.
Giuseppe Bozzi, Stefano Catani, Daniel de Florian, and Massimiliano Grazzini. Transverse-momentum resummation and the spectrum of the Higgs boson at the LHC. *Nucl.Phys.*, B737:73–120, 2006. doi: 10.1016/j.nuclphysb.2005.12.022.
Giuseppe Bozzi, Stefano Catani, Daniel de Florian, and Massimiliano Grazzini. Higgs boson production at the LHC: Transverse-momentum resummation and rapidity dependence. *Nucl.Phys.*, B791:1–19, 2008. doi: 10.1016/j.nuclphysb.2007.09.034.

[133] D. de Florian, G. Ferrera, M. Grazzini, and D. Tommasini. Higgs boson production at the LHC: transverse momentum resummation effects in the $H \to \gamma\gamma$, $H \to WW \to l\nu l\nu$ and $H \to ZZ \to 4l$ decay modes. *JHEP*, 1206:132, 2012. doi: 10.1007/JHEP06(2012)132.

[134] Hendrik Mantler and Marius Wiesemann. Top- and bottom-mass effects in hadronic Higgs production at small transverse momenta through LO+NLL. *Eur.Phys.J.*, C73:2467, 2013. doi: 10.1140/epjc/s10052-013-2467-x.

[135] Stefano Frixione and Bryan R. Webber. Matching NLO QCD computations and parton shower simulations. *JHEP*, 0206:029, 2002. doi: 10.1088/1126-6708/2002/06/029.

[136] Simone Alioli, Paolo Nason, Carlo Oleari, and Emanuele Re. NLO Higgs boson production via gluon fusion matched with shower in POWHEG. *JHEP*, 0904:002, 2009. doi: 10.1088/1126-6708/2009/04/002.

[137] Keith Hamilton, Peter Richardson, and Jon Tully. A Positive-Weight Next-to-Leading Order Monte Carlo Simulation for Higgs Boson Production. *JHEP*, 0904:116, 2009. doi: 10.1088/1126-6708/2009/04/116.

[138] S. Frixione, Z. Kunszt, and A. Signer. Three jet cross-sections to next-to-leading order. *Nucl.Phys.*, B467:399–442, 1996. doi: 10.1016/0550-3213(96)00110-1.

[139] S. Frixione. A General approach to jet cross-sections in QCD. *Nucl.Phys.*, B507:295–314, 1997. doi: 10.1016/S0550-3213(97)00574-9.

[140] Wai-Yee Keung and Frank J. Petriello. Electroweak and finite quark-mass effects on the Higgs boson transverse momentum distribution. *Phys.Rev.*, D80:013007, 2009. doi: 10.1103/PhysRevD.80.013007.
Charalampos Anastasiou, Stefan Bucherer, and Zoltan Kunszt. HPro: A NLO Monte-Carlo for Higgs production via gluon fusion with finite heavy quark masses. *JHEP*, 0910:068, 2009. doi: 10.1088/1126-6708/2009/10/068.
Oliver Brein. Electroweak and Bottom Quark Contributions to Higgs Boson plus Jet Production. *Phys.Rev.*, D81:093006, 2010. doi: 10.1103/PhysRevD.81.093006.

[141] U. Langenegger, M. Spira, A. Starodumov, and P. Trueb. SM and MSSM Higgs Boson Production: Spectra at large transverse Momentum. *JHEP*, 0606:035, 2006. doi: 10.1088/1126-6708/2006/06/035.

[142] Oliver Brein and Wolfgang Hollik. MSSM Higgs bosons associated with high p(T) jets at hadron colliders. *Phys.Rev.*, D68:095006, 2003. doi: 10.1103/PhysRevD.68.095006.

[143] Oliver Brein and Wolfgang Hollik. Distributions for MSSM Higgs boson + jet production at hadron colliders. *Phys.Rev.*, D76:035002, 2007. doi: 10.1103/PhysRevD.76.035002.

[144] Torbjorn Sjostrand, Stephen Mrenna, and Peter Z. Skands. PYTHIA 6.4 Physics and Manual. *JHEP*, 0605:026, 2006. doi: 10.1088/1126-6708/2006/05/026.

[145] U. Baur and E.W. Nigel Glover. Higgs Boson Production at Large Transverse Momentum in Hadronic Collisions. *Nucl.Phys.*, B339:38–66, 1990. doi: 10.1016/0550-3213(90)90532-I.

[146] Matteo Cacciari, Gavin P. Salam, and Gregory Soyez. The Anti-k(t) jet clustering algorithm. *JHEP*, 0804:063, 2008. doi: 10.1088/1126-6708/2008/04/063.

[147] Ewan Cameron. On the Estimation of Confidence Intervals for Binomial Population Proportions in Astronomy: The Simplicity and Superiority of the Bayesian Approach. 2010.

[148] Petra Kovacikova. A Mellin Space Program for $W^{+/-}$ and $Z^0$ Production at NNLO. *Fortsch.Phys.*, 59:1070–1074, 2011. doi: 10.1002/prop.201100053.

Troisième partie

# RÉSUMÉ EN FRANÇAIS

## PLAN DE LA THÈSE

Le Modèle Standard (MS) des interactions électrofaibles et fortes a été très efficace dans la description des plusieurs processus de collision des particules à échelles d'énergie différentes mais beaucoup de problèmes restent ouverts. Par exemple, si on considère les relations entre la physique des particules et la cosmologie, il est immédiatement clair que l'asymétrie entre la matière et l'antimatière dans l'Univers ne peut pas être expliquée seulement en termes des interactions présentes dans le MS mais requiert d'une extension avec un spectre des particules plus grand. Cette modification est aussi nécessaire pour expliquer la présence de la matière noire observée dans l'univers. En plus, le MS ne comprend pas les masses des neutrinos et, de côte plus théorique, présente le problème "de la hiérarchie" (i.e. la dépendance quadratique de la masse du boson de Higgs du cutoff UV utilisé dans la computation des corrections radiatives) et, en plus, les structures de jauge et de Yukawa sont assumées et pas expliquées.

Au delà de ces problèmes, maintenant que le boson de Higgs a été découvert, le premier but est de comprendre si ses propriétés sont compatibles avec les prédictions du MS. Le Large Hadron Collider (LHC) a été conçu pour répondre à toutes ces questions différentes, en produisant les instruments nécessaires pour découvrir et comprendre le boson du Higgs et permettre la production de nouvelles particules de masse dans la région du TeV, si elles existent. Le premier démarrage de l'accélérateur a fourni déjà beaucoup de données de haute qualité. L'analyse des ces données à montré que, apparemment, il n'y a pas de déviations concernant les prédictions du MS. La conséquence est que la prochaine étape logique est l'usage de cette grande quantité de données pour faire des analyses de précision. Cette classe d'études a besoin d'un fort contrôle pas seulement sur les incertitudes expérimentales mais aussi sur les incertitudes théoriques.

Par conséquent, pendant mes études doctorales, j'ai participé à une série des projet qui avaient comme but l'amélioration ou de la justesse des prédictions, en ajoutant des nouveaux effets, ou du contrôle sur les incertitudes des calcules théoriques.

Entre tous les incertitudes théoriques, un rôle prédominant est occupé par le problème de l'estimation des contributions des corrections perturbatives qui ne sont pas calculées, qui usuellement sont appelées "Missing Higher Order Uncertainty" (MHOU). Traditionnellement, ces incertitudes ont été estimées par la variation des échelles non-physiques, qui sont présentes dans le résultat, autour de leurs valeurs centrales. En fait, il y a plusieurs prescriptions pour cette procédure, mais toutes sont basées sur des conventions arbitraires et ne donnent pas une interprétation statistique aux intervalles qu'elles produisent. Avec M.Cacciari (LPTHE), A.Guffanti et L.Jenniches (Institut N.Bohr à Copenhagen), nous avons étudié l'extension du modèle Bayésien de Cacciari-Houdeau (CH) aux observables hadroniques, avec le but de fournir des prédictions pour les incertitudes des observables du LHC en général et en particulier pour celles du boson de Higgs. Le modèle CH cherche à fixer les défauts de la procédure standard d'évaluation de MHOU, la variation d'échelle. Ce modèle est basé sur une approche totalement différente, avec la quelle le comportement de la série perturbative est compris dans le contexte de la probabilité Bayésien. L'avantage de ce système est la cohérence de la formulation théorique et le fait qu'il produise un intervalle d'incertitude qui a une interprétation statistique en termes de Degré de Confiance (DdC) et qui peut être directement inséré dans la machine que les physiciens expérimentaux utilisent pour analyser les données

du LHC. Comme corollaire, on a aussi retravaillé l'application de ce modèle à les observables sans hadrons dans l'état initial, qui ont le champ de définition originaire.

À cause de l'importance de la physique du boson de Higgs au LHC, il est de première importance d'avoir des prédictions précises et le contrôle sur les incertitudes pour les observables du Higgs qui sont mesurées au LHC. J'ai suivi deux lignes de recherche. La premier a été l'étude des incertitudes théoriques de la section efficace totale pour la production du Higgs en fusion de gluons et en annihilation de bottom quarks dans le "Minimal Supersymmetric Standard Model" (MSSM). Il s'agit non seulement des MHOUs mais aussi des incertitudes PDF+$\alpha_s$ , choix de l'échelle de renormalisation pour le Yukawa du bottom et le domaine de validité des approximations utilisées dans le calcul des corrections supersymétriques. Ce travail a été réalisé en collaboration avec R. Harlander (U. Wuppertal), S. Liebler (U. Hamburg), H. Mantler (CERN), P. Slavich (LPTHE) et A. Vicini (U. Milano) et il a récemment mené à une publication dans le Journal de Physique des Hautes Énergies [1].

Depuis quelques années, avec G. Degrassi (U. Roma 3), P. Slavich et A. Vicini, j'ai étudié la production du boson de Higgs dans le processus de fusion de gluons, dans le cadre du `POWHEG-BOX` , avec une attention particulière au problème de l'inclusion des amplitudes complètes pour le top et le bottom quark, et d'étudier leurs effets sur le calcul de l'impulsion transverse du Higgs. La méthode `POWHEG` fournit une recette systématique pour obtenir la mise en correspondance d'un calcul NLO avec un Parton Shower (PS). Ces calculs unifiés sont extrêmement importants pour simuler correctement et de façon réaliste les processus physiques dans un collisionneur, avec la possibilité d'imposer de manière flexible les réductions d'acceptation expérimental et d'avoir, à la fin, une comparaison raisonnable entre les données et les prédictions théoriques. Notre contribution a été très appréciée par les collaborations expérimentales de ATLAS et CMS, qui utilisent maintenant notre logiciel dans la cadre des leurs analyses. En outre, il a créé un riche débat dans la communauté et a conduit à plusieurs réunions entre théoriciens et expérimentateurs sur la question. Le travail a été fait originairement pour le MS et pour le Higgs léger des MSSM et a été publié dans [2]. Il a ensuite été étendu au Higgs lourd et au pseudoscalaire du MSSM [3, 4] et du "Two Higgs Doublet Model" (2HDM). La totalité du code est librement disponible dans le répertoire SVN du `POWHEG-BOX` . Plus récemment, j'ai étudié avec Alessandro Vicini la question des incertitudes liées à la procédure de correspondance NLO+PS dans le calcul de cette observable [5].

Au cours de mes études doctorales j'ai également participé au calcul des corrections de seuil dans les modèles de "split-SUSY" et "high-scale SUSY", mais ces travaux n'apparaissent pas dans cette thèse. L'idée à la base de split-SUSY est que l'échelle de masse $\tilde{m}$ des superpartenaires scalaires des MS est beaucoup plus élevée que l'échelle électrofaible. Les superpartenaires qui restent à l'échelle électrofaible sont les higgsinos et les gauginos. En "high-scale SUSY", ces derniers sont aussi censés être à la grande échelle $\tilde{m}$. Pour bien étudier ces théories et leurs prédictions à l'échelle EW, il est nécessaire de définir une théorie efficace dans laquelle les particules lourdes ont été intégrées. Ceci et l'utilisation des méthodes du groupe de renormalisation, permettent de resommer correctement les grands logarithmes du rapport de $\tilde{m}$ sur l'échelle électrofaible, qu'autrement gâcheraient la précision de la prédiction. Ce calcul technique fait partie d'une étude de la prédiction de la masse du Higgs dans ces modèles. La masse du Higgs peut en effet être utilisé comme un proxy pour obtenir une estimation de l'échelle de masse $\tilde{m}$ et donc effectuer une étude phénoménologique de ces deux modèles. Le travail a été effectué en collaboration avec G. Giudice (CERN), P. Slavich (LPTHE) et A. Strumia (U. Pisa) [6]. Comme préparation complémentaire j'ai aussi fait un stage de trois mois chez Wolfram Research, à Champaign (Illinois, États-Unis), au cours du lequel j'ai écrit une implémentation de haut niveau des fonctions de Mathieu dans Mathematica.

Tout mon travail a été soutenu par l'Agence exécutive pour la recherche (REA) de la Commission européenne dans le cadre des accords de subvention PITN-GA-2010-264564 (LHCPhenoNet).

# BIBLIOGRAPHIE


[1] E. Bagnaschi, R.V. Harlander, S. Liebler, H. Mantler, P. Slavich, et al. Towards precise predictions for Higgs-boson production in the MSSM. *JHEP*, 06 :167, 2014. doi : 10.1007/JHEP06(2014)167.

[2] E. Bagnaschi, G. Degrassi, P. Slavich, and A. Vicini. Higgs production via gluon fusion in the POWHEG approach in the SM and in the MSSM. *JHEP*, 1202 :088, 2012. doi : 10.1007/JHEP02(2012)088.

[3] S. Dittmaier, S. Dittmaier, C. Mariotti, G. Passarino, R. Tanaka, et al. Handbook of LHC Higgs Cross Sections : 2. Differential Distributions. 2012. doi : 10.5170/CERN-2012-002.

[4] S Heinemeyer et al. Handbook of LHC Higgs Cross Sections : 3. Higgs Properties. 2013. doi : 10.5170/CERN-2013-004.

[5] E. Bagnaschi and A. Vicini. "Matching uncertainties in the computation of the resummed transverse momentum distribution of the Higgs boson in gluon fusion in the POWHEG framework". *In preparation*.

[6] Emanuele Bagnaschi, Gian F. Giudice, Pietro Slavich, and Alessandro Strumia. Higgs Mass and Unnatural Supersymmetry. *arXiv :1407.4081*, 2014.

# 1 LE MODÈLE CH ET L'APPROCHE BAYÉSIEN À L'ESTIMATION DES MHOUS

La phénoménologie de précision visée par le programme de physique du LHC nécessite de la précision pas seulement dans les mesures expérimentales mais aussi dans les prédictions théoriques. Une fois que la précision devient élevée, et les incertitudes expérimentales et théoriques sont similaires, il devient important d'être en mesure d'évaluer quantitativement l'importance des termes perturbatifs d'ordre supérieur qui ne sont pas disponibles dans les calculs.

Dans les calculs de QCD, que nous prenons comme modèle ici compte tenu de leur importance dans la physique au LHC, l'incertitude théorique en raison des ordres supérieurs manquants est généralement estimée en faisant varier les échelles non-physiques, celle de renormalisation et celle de factorisation, qui apparaissent dans le calcul. Cette approche a bien servi la communauté de QCD pendant plus de trente ans, et doit toujours être considérée comme le moyen le plus efficace pour estimer rapidement cette incertitude. Elle souffre toutefois de quelques inconvénients. Parmi ceux-ci, par exemple, le fait que les intervalles d'incertitudes que cette approche produit ne peuvent pas être caractérisés statistiquement et ne peuvent donc pas être combinés de façon significative avec, par exemple, les profils de vraisemblance d'autres incertitudes, par exemple d'origine expérimentale.

M. Cacciari et N. Houdeau essayèrent dans [1], pour surmonter cette limitation, d'estimer les MHOUs dans un cadre bayésien, de manière à obtenir un profil de densité de probabilité statistiquement significative de l'intervalle d'incertitude. L'approche Cacciari-Houdeau conduit à un modèle (dénoté CH) qui repose sur des lois a priori simples qui, à leur base, essaient d'imiter des hypothèses qui sont tout de même implicitement fait quand on utilise la méthode de variation des échelles.

Le but de cette étude est double. D'une part, nous voulons revoir le modèle de CH, et proposer une version légèrement modifiée (que nous noterons $\overline{\text{CH}}$) qui change une partie de la simplicité du modèle CH original pour une meilleure adaptabilité à une large classe d'observables, notamment ceux relatifs aux processus avec des hadrons dans l'état initial. Aussi nous voulons étudier les résultats de la variation d'échelle et de CH sur un grand nombre d'observables perturbatifs, afin d'être en mesure d'évaluer leur performance dans une manière (fréquentiste) statistiquement significative. Pour l'approche de la variation de l'échelle, cela signifie que on peut tenter de caractériser ses intervalles d'incertitude *a posteriori*, en termes d'un certain niveau de confiance. Pour l'approche bayésienne avec le modèle $\overline{\text{CH}}$ cette étude permettra de tester si le Degré de Confiance (DdC) que $\overline{\text{CH}}$ renvoie pour les intervalles d'incertitude est correct ou, le cas échéant, d'estimer le paramètre d'expansion approprié qui assure que ce sera le cas.

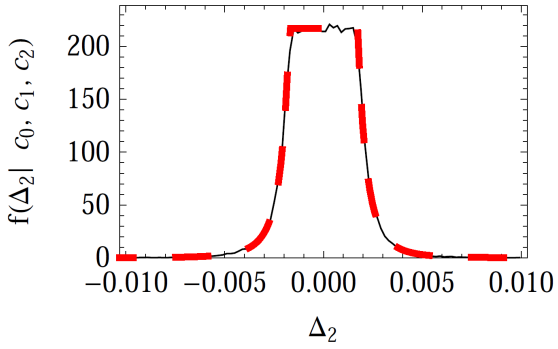


**Figure 65 –** Graphique de la distribution a posteriori pour le $\Delta_2$ dans le modèle CH, pour un jouet observable avec $\bar{c}_k = 1$ et $\alpha_s = 0,1$ comme indiqué dans [1]. La courbe rouge est le rapprochement analytique de l'eq. (211) tandis que la courbe noire représente le résultat exact.

## 1.1 Le modèle CH et ses développements

L'approche de Cacciari et Houdeau [1] est un modèle de probabilité bayésienne récemment introduit pour calculer les MHOUs. Il est basé sur diverses hypothèses sur le comportement des coefficients d'une série de la forme

$$O_k(Q,Q) = \sum_{n=l}^{k} \alpha_s^n(Q) c_n(Q,Q) \equiv \sum_{n=l}^{k} \alpha_s^n c_n \,, \tag{210}$$

pour une observable perturbative qui commence à l'ordre $l$ de $\alpha_s$ et il est connu jusqu'à l'ordre $k$. Les échelles non physiques ont été mis à la valeur centrale $Q$, et nous avons également défini implicitement $\alpha_s \equiv \alpha_s(Q)$ et $c_n \equiv c_n(Q,Q)$.

Le modèle postule comme hypothèse de base que tous les coefficients perturbatifs ont des magnitudes similaires. Cela peut être quantitativement traduit dans la déclaration que tous les coefficients perturbatifs $c_n$ partagent une limite supérieure à leur valeur absolue que nous noterons $\bar{c}$. Ceci et d'autres hypothèses sont codés dans les distributions a priori spécifiques du modèle, et dans le choix du paramètre d'expansion, pris soit $\alpha_s$, et permettent de déterminer un profil de densité d'incertitude (le distribution a posteriori du modèle) en fonction de la taille du reste inconnu de la série $\Delta_k \equiv \sum_{n=k+1}^{\infty} \alpha_s^n c_n$.

Si le paramètre de développement de la série est suffisamment faible, on peut supposer que le reste est dominée par le premier ordre inconnu, c'est à dire $\Delta_k \simeq \alpha_s^{k+1} c_{k+1}$. Ensuite, la distribution a posteriori du modèle pour $\Delta_k$ peut être calculé analytiquement et exprimé sous une forme simple

$$f(\Delta_k|c_1,\ldots,c_k) \simeq \left(\frac{n_c}{n_c+1}\right) \frac{1}{2\alpha_s^{k+1}\bar{c}_{(k)}} \begin{cases} 1 & \text{if } |\Delta_k| \leqslant \alpha_s^{k+1}\bar{c}_{(k)} \\ \left(\frac{\alpha_s^{k+1}\bar{c}_{(k)}}{|\Delta_k|}\right)^{n_c+1} & \text{if } |\Delta_k| > \alpha_s^{k+1}\bar{c}_{(k)} \end{cases}, \tag{211}$$

où $\bar{c}_{(k)} \equiv \max(|c_1|,\cdots,|c_k|)$ et $n_c = k - l + 1$ est le nombre de coefficients perturbatifs connus. De eq. (211) et de la figure 65il est possible d'apprécier les caractéristiques de la distribution a posteriori pour ce modèle : un plateau central avec des queues supprimées avec une loi à puissance. L'existence d'une telle distribution de densité de probabilité pour l'intervalle d'incertitude représente la principale différence avec la procédure de variation d'échelle, qui donne seulement un intervalle sans un profil de crédibilité.

Dans la même approximation, $\Delta_k \simeq \alpha_s^{k+1} c_{k+1}$, on peut aussi calculer le plus petit intervalle de crédibilité pour $\Delta_k$ avec un DdC égal à $p\%$ (où $p\% \equiv p/100$ et $p \in [0, 100]$), c'est à dire tel que $\Delta_k$ devrait être contenue à l'intérieur de l'intervalle $[-d_k^{(p)}, d_k^{(p)}]$ avec $p\%$ crédibilité :

$$d_k^{(p)} = \begin{cases} \alpha_s^{k+1} \bar{c}_{(k)} \frac{n_c+1}{n_c} p\% & \text{if} \quad p\% \leqslant \frac{n_c}{n_c+1} \\ \alpha_s^{k+1} \bar{c}_{(k)} \left[(n_c+1)(1-p\%)\right]^{(-1/n_c)} & \text{if} \quad p\% > \frac{n_c}{n_c+1} \end{cases} . \tag{212}$$

### 1.1.1 Le modèle de Cacciari-Houdeau modifiée ($\overline{\text{CH}}$)

Le modèle de CH décrit ci-dessus repose sur une forme spécifique de la développement perturbatif, voire eq. (210). En conséquence, son estimation de l'incertitude n'est pas invariant par changement du paramètre d'expansion, $\alpha_s \to \alpha_s/\lambda$.

Une autre question connexe est que, comme on a vu dans la section précédente, le modèle suppose que le paramètre d'expansion est tel que tous les coefficients perturbatifs $c_n$ sont du même ordre $\mathcal{O}(c_1) \simeq \mathcal{O}(c_{l+1}) \simeq \cdots$. A priori cela ne pouvait être le cas pour la simple expansion de $\alpha_s$.

Des tentatives ont été faites pour reformuler le modèle afin de résoudre ces deux problèmes. Enfin, aucune d'entre elle était satisfaisante, dans la mesure où elles nécessitaient nécessaire la formulation des hypothèses trop restrictives.

Nous avons finalement utilisé à la place une version légèrement modifiée du modèle de CH. Dans le modèle modifié, désormais notée $\overline{\text{CH}}$, on récrit le développement perturbatif sous la forme

$$O_k = \sum_{n=l}^{k} \frac{\alpha_s^n}{\lambda^n} (n-1)! \, \frac{\lambda^n c_n}{(n-1)!} \equiv \sum_{n=l}^{k} \left(\frac{\alpha_s}{\lambda}\right)^n (n-1)! \; b_n \,, \tag{213}$$

avec

$$b_n \equiv \frac{\lambda^n c_n}{(n-1)!} \,, \tag{214}$$

et on utilise les nouveaux coefficients $b_n$ pour les mêmes distributions a priori utilisées à l'origine pour le $c_n$ . Cela conduit à un profil de densité de probabilité pour l'incertitude

$$f(\Delta_k | b_l, \ldots, b_k) \simeq \left(\frac{n_c}{n_c+1}\right) \frac{1}{2k! \, (\alpha_s/\lambda)^{k+1} \bar{b}_k} \begin{cases} 1 & \text{if} \, |\Delta_k| \leqslant k! \left(\frac{\alpha_s}{\lambda}\right)^{k+1} \bar{b}_k \\ \left(\frac{k!(\alpha_s/\lambda)^{k+1} \bar{b}_k}{|\Delta_k|}\right)^{n_c+1} & \text{if} \, |\Delta_k| > k! \left(\frac{\alpha_s}{\lambda}\right)^{k+1} \bar{b}_k \end{cases} , \tag{215}$$

et à l'intervalle de crédibilité

$$d_k^{(p)} = \begin{cases} k! \left(\frac{\alpha_s}{\lambda}\right)^{k+1} \bar{b}_k \frac{n_c+1}{n_c} p\% & \text{if} \quad p\% \leqslant \frac{n_c}{n_c+1} \\ k! \left(\frac{\alpha_s}{\lambda}\right)^{k+1} \bar{b}_k \left[(n_c+1)(1-p\%)\right]^{(-1/n_c)} & \text{if} \quad p\% > \frac{n_c}{n_c+1} \end{cases} . \tag{216}$$

Le facteur $(n-1)!$ , qui représente la principale modification par rapport au modèle CH original , peut être justifié par le fait qu'il devrait apparaître dans les ordres supérieurs des calculs perturbatifs, par

exemple ceux dans le limite de gros-$\beta_0$ et dans le cadre de renormalons [2–5].

Le facteur $\lambda$ est libre et doit être déterminé a posteriori. Le meilleur choix pour déterminer $\lambda$ peut être de le faire empiriquement, en observant la façon dont le modèle s'accomplit en décrivant les incertitudes des observables qui sont connus à un ordre perturbatif au-delà où nous utilisons le modèle. Nous allons voir que la valeur optimale s'avère $\lambda \simeq 1$ pour observables qui n'impliquent pas hadrons dans l'état initial, tandis qu'une valeur de $\lambda \simeq 0,6$ est favorisée dans les processus avec des hadrons initiaux. Cette méthode de détermination $\lambda$ (plus détaillé ci-dessous) apporte évidemment une certaine contamination fréquentiste dans l'approche bayésienne. Nous considérons cet inconvénient acceptable au stade actuel, mais nous notons que l'on pourrait améliorer le modèle par l'introduction d'une distribution a priori pour la valeur de $\lambda$ et d'éviter ainsi la contamination fréquentiste. L'étude fréquentiste de $\lambda$ effectuée dans ce travail peut alors éventuellement être utilisée comme un guide pour la formulation d'une telle distribution a priori.

### 1.1.2 Extension du modèle $\overline{\text{CH}}$ à observables avec des hadrons dans l'état initial

Le modèle de CH original a été formulé pour les observables non-hadroniques [1]. Ce n'est pas une tâche facile de l'étendre à des observables avec hadrons dans l'état initial (observables hadroniques).

Une observable hadronique générique (par exemple une section efficace totale) peut être écrit comme une intégrale de convolution

$$O_k(\tau, Q) = \int_\tau^1 \frac{dz}{z} \mathcal{L}\left(\frac{\tau}{z}, Q\right) \sum_{n=l}^{k} \alpha_s^n C_n(z, Q) \equiv \mathcal{L}(Q) \otimes \sum_{n=l}^{k} \alpha_s^n C_n(Q)\,, \tag{217}$$

où $\mathcal{L}$ est la luminosité parton-parton, $c_n(Q)$ est la fonction du coefficient de diffusion dure, $\tau$ est une variable d'échelle hadronique appropriée et $Q$ est l'échelle d'énergie caractéristique du processus. Toutes les échelles de renormalisation et factorisation non physiques sont choisies être égal à $Q$, comme dans le cas de non-hadronique, et elles ne sont pas explicitement indiquées. Dans eq. (217) les fonctions des coefficients perturbatifs $c_n$ sont des distributions, et non de simples nombres, comme les coefficients $c_n$ des observables non hadronique. Cela signifie qu'il n'est pas possible d'appliquer directement la méthode $\overline{\text{CH}}$ décrit dans la section 1.1.1 pour les observables hadroniques de la forme (217).

On peut surmonter ce problème de deux manières :

*i)* Une première approche consiste à exprimer la section hadronique comme une série dont les coefficients incluent la convolution avec la luminosité partonique, c'est à dire que l'on peut réécrire l'équation (217) sous la forme

$$O_k(\tau, Q) = \mathcal{L}(Q) \otimes \sum_{n=l}^{k} \alpha_s^n C_n(Q) \equiv \sum_{n=l}^{k} \left(\frac{\alpha_s}{\lambda_h}\right)^n (n-1)!\; H_n(\tau, Q)\,, \tag{218}$$

où on a définit

$$H_n(\tau, Q) \equiv \frac{\lambda_h^n}{(n-1)!} \mathcal{L}(Q) \otimes C_n(Q)\,. \tag{219}$$

1 Par "observables non-hadroniques", nous entendons observables sans hadrons dans l'état initial et donc dépourvus de la dépendance sur l'échelle de factorisation.

On procède ensuite comme dans le cas des observables non-hadronique, à l'application des distribution a priori bayésiens aux les coefficients $H_n$. Dans la pratique, on est en supposant que la physique non-perturbative contenue dans la luminosité partonique met de l'ordre par ordre à peu près la même contribution, ou, plus généralement, que sa présence ne gâte pas les hypothèses du modèle. Ceci est censé également vrai de les contributions perturbatives qui viennent de évolution DGLAP. Dans nos études, à tenir compte de ces hypothèses, nous utilisons toujours les mêmes PDF à toutes les ordres. Cette approche a également été adoptée dans un certain nombre des articles qui ont fait usage du modèle de CH d'origine, par exemple, [6, 7].

Notez que dans l'équation (218), nous avons introduit un paramètre $\lambda_h$ qui est potentiellement différent de $\lambda$ employé dans l'expansion des observables non-hadronique.

*ii)* Une deuxième approche consiste à traduire l'observable à l'espace de Mellin, et écrire

$$O_k(N, Q) = \mathcal{L}(N+1) \sum_{n=l}^{k} \left(\frac{\alpha_s}{\lambda_h}\right)^n (n-1)!\; B_n(N, Q)\,, \tag{220}$$

où

$$B_n(N, Q) \equiv \frac{\lambda_h^n}{(n-1)!} \int_0^1 dx\, x^{N-1}\, C_n(x, Q)\,, \tag{221}$$

est la transformation de Mellin de la fonction de coefficient courte distance $C_N$, avec les mêmes facteurs habituels adoptés dans le modèle $\overline{\text{CH}}$ , et $\mathcal{L}(N+1)$ est la transformation de Mellin du flux partonique On observe alors que, s'il peut être démontrer que l'inversion de la transformation de Mellin est dominée par un seul moment de Mellin $N^*$, on peut simplement appliquer les mêmes distributions à priori de l'approche $\overline{\text{CH}}$ aux *numéros* $B_n(N^*, Q)$ et trouver l'incertitude pertinente, qui peut ensuite être transportée vers le résultat complet avec un facteur multiplicatif de manière appropriée.

Cette approche est viable, car on peut montrer que, au moins dans certains cas (voir par exemple [8, 9]) un tel moment Mellin dominante existe et donne une bonne approximation du résultat complet ou au moins des k-factors.

La principale limitation de cette procédure, qui a priori serait préférable à la première car elle ne contamine pas les coefficients qui sont utilisés par le modèle bayésien avec la physique non-perturbative, est qu'elle repose fortement pas seulement sur la prédominance d'un seul moment de Mellin, mais aussi sur l'existence d'un canal de production dominant à toutes les ordres (par exemple la fusion de gluons et de gluons dans la production de Higgs au LHC). Si ce n'est pas le cas, la nécessité de faire la moyenne pondérée entre les différents moments de Mellin dominantes, dans les différents canaux, va réintroduire la contamination de la physique non-perturbative.

Une seconde limitation pratique est que les résultats perturbatifs sont rarement disponibles dans l'espace de Mellin dans les codes publics.

## 1.2 Résultats

Dans cette section, nous essayons d'évaluer la qualité de la procédure de variations de l'échelle et du modèle $\overline{\text{CH}}$ par l'étude de leurs performances comme estimateurs de la MHOUs lorsqu'il sont appliqués à un ensemble d'observables. Pour chaque observable dans l'ensemble, nous considérons deux quantités :

*i)* la taille de l'incertitude prédite à un ordre perturbatif donné $n$ par l'approche à l'étude ;

*ii)* le résultat perturbatif connu pour la même observable à l'ordre $n + 1$.

Pour chacun des observables nous calculons les taux de réussite global de la méthode en question, c'est à dire la fraction d'observables, pour lesquels le résultat à l'ordre perturbatif $n + 1$ tombe effectivement dans l'intervalle d'incertitude prédit par le modèle à l'ordre $n$.

Dans le cas du modèle bayésien nous répétons l'analyse décrite ci-dessus pour différentes valeurs de $\lambda$ et DdC. Cela nous permet de dériver la valeur optimale de $\lambda$ à utiliser dans le modèle $\overline{\text{CH}}$ , qui est défini comme la valeur de $\lambda$ pour laquelle le modèle a un taux de réussite global qui est le plus proche du DdC demandé, pour chaque DdC possible.

Dans le cas de la méthode de variation de l'échelle, on fait varier le facteur d'échelle $r$. Puisque cette méthode ne donne pas des intervalles d'incertitude statistiquement significatifs, nous ne pouvons pas déterminer une valeur optimale de $r$ à partir de cette analyse, comme c'est le cas de $\lambda$ dans l'approche bayésienne. Plutôt, nous pouvons attribuer un niveau de confiance heuristique (dénotée par l'anglais CL), *a posteriori*, aux intervalles d'incertitude pour chaque $r$.

### 1.2.1 Analyse globale

On a fait l'analyse des performances de la procédure de variation d'échelles et du modèle $\overline{\text{CH}}$ sur la liste d'observables définis en appendis A à page 141. Les résultats sont reportés en figures 66 et 67 pour la variation d'échelles non-hadronique et hadronique respectivement. Dans le graphique de gauche de la figure 66 on a fait varier l'échelle de renormalisation dans l'intervalle $[Q/r, rQ]$ et on a pris la valeur maximale et minimale. Dans le graphique de droite on a pris simplement la valeur maximale ou minimale de l'observable évaluée a $\mu_r = \{Q, Q/r, rQ\}$. L'analyse à été faite au LO e au NLO. On peux voir qu'au LO le valeur de $r$ qui correspond à 68% CL est plutôt proche de 4 que la valeur usuel de 2. À NLO cette valeur se réduit à la tranche de $2.5 - 3$. On peux aussi dénoter que faire la scan dans l'intervalle donne des CLs plus hauts pour de valeur de $r > 3.5$ que prendre simplement les valeurs extrêmes.

L'analyse hadronique a été faite en prenant seulement les valeur extrêmes. On a fait l'analyse en utilisant la même NNLO PDF à tous les ordres ou en prenant la PDF correspondante pour chaque ordre. Les PDFs utilisées sont produites par la collaboration NNPDF. On a utilisé les version 2.3 pour la PDF NNLO et NLO, et la 2.1 pour la PDF LO (il n'y a pas de version 2.3 pour la PDF LO disponible). Aussi dans le cas hadronique, on peux voir que la variation d'échelles à LO est pas du tout fiable, comme attendu. On peux aussi voir que le 68% CL est obtenu pour des valeurs de $r$ plus hautes que le valeur usuel de 2. En fait, on a besoin de $r$ entre $3 - 4$ si on utilise la PDF NNLO à tous les ordre, ou de $r$ entre $4 - 5$ si on change la PDF à chaque ordre.

Dans les figures 68 et 69 on présente les résultats de l'analyse du modèle $\overline{\text{CH}}$ . On utilise deux types de graphiques. Le premier est un histogramme qui est construit dans la façon suivant : on prendre un

intervalle des valeurs de DdC, entre 0.05 et 0.95, et pour chaque DdC on détermine le meilleur valeur de $\lambda$, c'est à dire la valeur pour laquelle le DdC est égal au taux de succès. Le deuxième est un graphique qui montre le taux de succès en fonction du DdC demandé, pour des valeurs différentes de $\lambda$. On a fait l'analyse pour le cas non-hadronique et le cas hadronique. On voit que la meilleure estimation pour $\lambda$ est $\lambda \simeq 1$ dans le premier cas et $\lambda_h \simeq 0.6$ pour le deuxième.

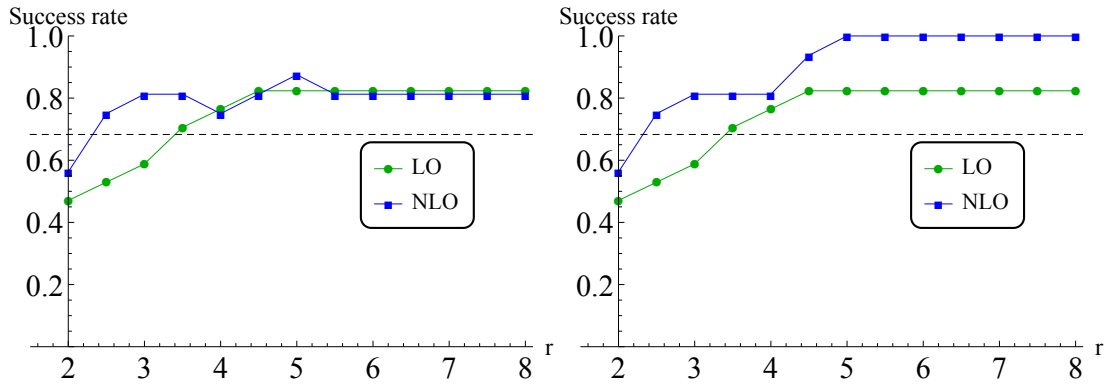


**Figure 66 –** Fraction des observables contenus dans la bande d'erreur pour la variation d'échelle entre $\mu_R = Q/r$ et $\mu_R = rQ$ ; en prenant les valeurs aux extrêmes de l'intervalle de variation (gauche), en prenant le maximum ou le minimum obtenu par le scan de l'intervalle de variation (droite).

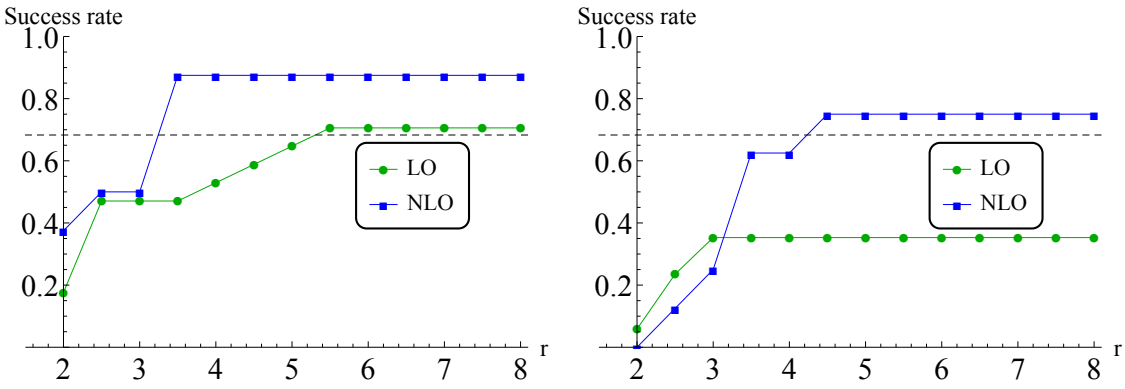


**Figure 67 –** Variation d'échelles pour les processus avec hadrons dans l'état initial : NNLO PDF à tous les ordres (gauche), ordre-synchronisé PDF (droite). Les combinaisons comme $\mu_R = rQ$, $\mu_F = Q/r$ ne sont pas inclus.

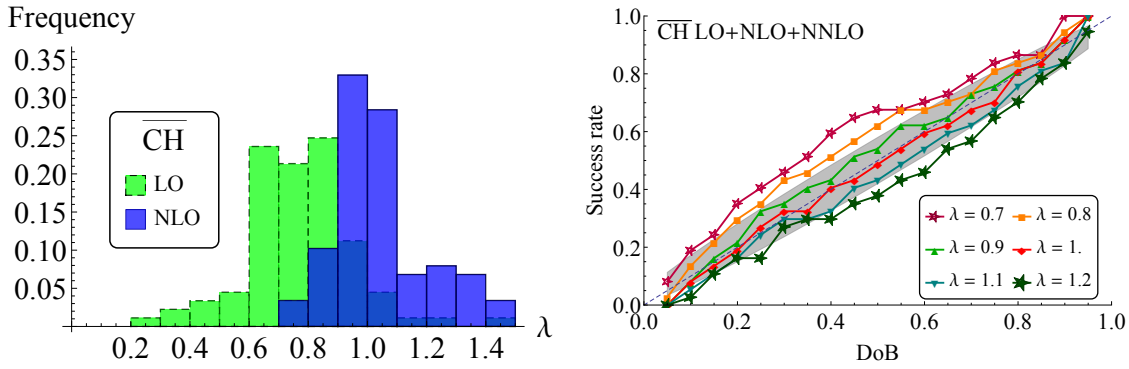


**Figure 68 –** Étude non-hadronique : comparaison entre le DdC et le taux de succès pour déterminer la meilleure estimation de λ. À gauche, histogramme de λ obtenu avec un scan de DdC. À droite, graphique du taux de succès vs le DdC pour six valeurs de λ.

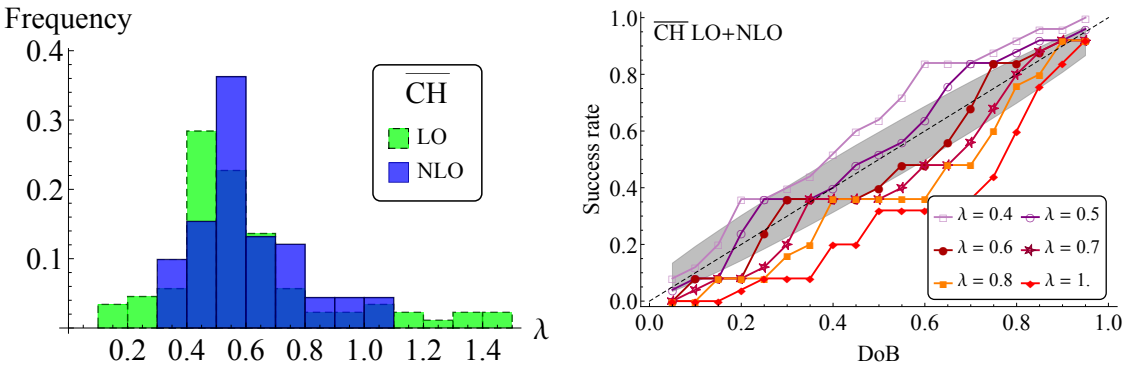


**Figure 69 –** Étude hadronique : comparaison entre le DdC et le taux de succès pour déterminer la meilleure estimation de λ. À gauche, histogramme de λ obtenu avec un scan de DdC. À droite, graphique du taux de succès vs le DdC pour six valeurs de λ.

### 1.2.2 Exemples des processus

Dans cette section on présente comment le modèle $\overline{\text{CH}}$ fonctionne dans le cas de deux observables qui sont particulièrement importantes.

Le première est la production de hadrons dans des collisions de $e^+$ et $e^-$, une des observables plus bien connues des collisionneurs leptoniques. Dans figure 70 on montre les barres d'erreur calculées par le modèle $\overline{\text{CH}}$ et par la procédure de variation de l'échelle. On peut voir que l'intervalle bayésien correspondant au 68% DdC est plutôt comparable à l'intervalle $r = 4$ qu'à l'intervalle standard correspondant au $r = 2$. Ce-ci n'est pas surprenant, en fait l'analyse globale a montrée que, pour la procédure de la variation de l'échelle, le 68% CL correspond à des valeurs de $r$ dans la tranche $2.5 - 3$ à NLO. En figure 71, on montre la distribution a posteriori du modèle $\overline{\text{CH}}$ . On peux voir que l'intervalle correspondant à la variation d'échelle $r = 2$ est toujours contenu dans le plateau de la distribution.

On montre les mêmes donnés pour un observable hadronique. On a choisi la production de Higgs en fusion des gluons pour sa importance au LHC. Dans les figure 72 et figure 73 sont montrées les barre d'erreur et la distribution a posteriori pour $\Delta_k$ du modèle à chaque ordre. On peut voir que dans ce cas, en raison de la mauvaise convergence de la série perturbative, la dimension des barres d'erreur ne rétrécit pas tandis que les ordres augmentent.

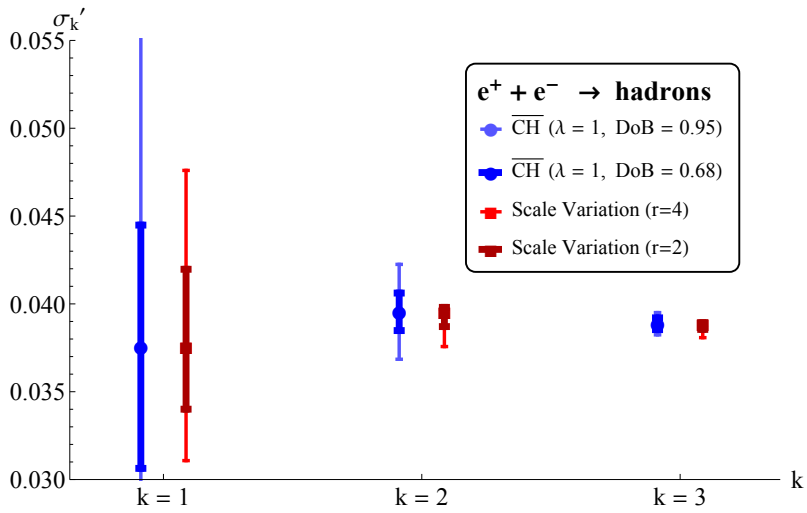


**Figure 70 –** Barres d'erreur à LO, NLO et NNLO pour $\overline{CH}$ avec $\lambda = 1$, comparées avec la prédiction obtenue avec la procédure de variation d'échelle, pour la production des hadrons dans les collisions de $e^+$ et $e^-$.

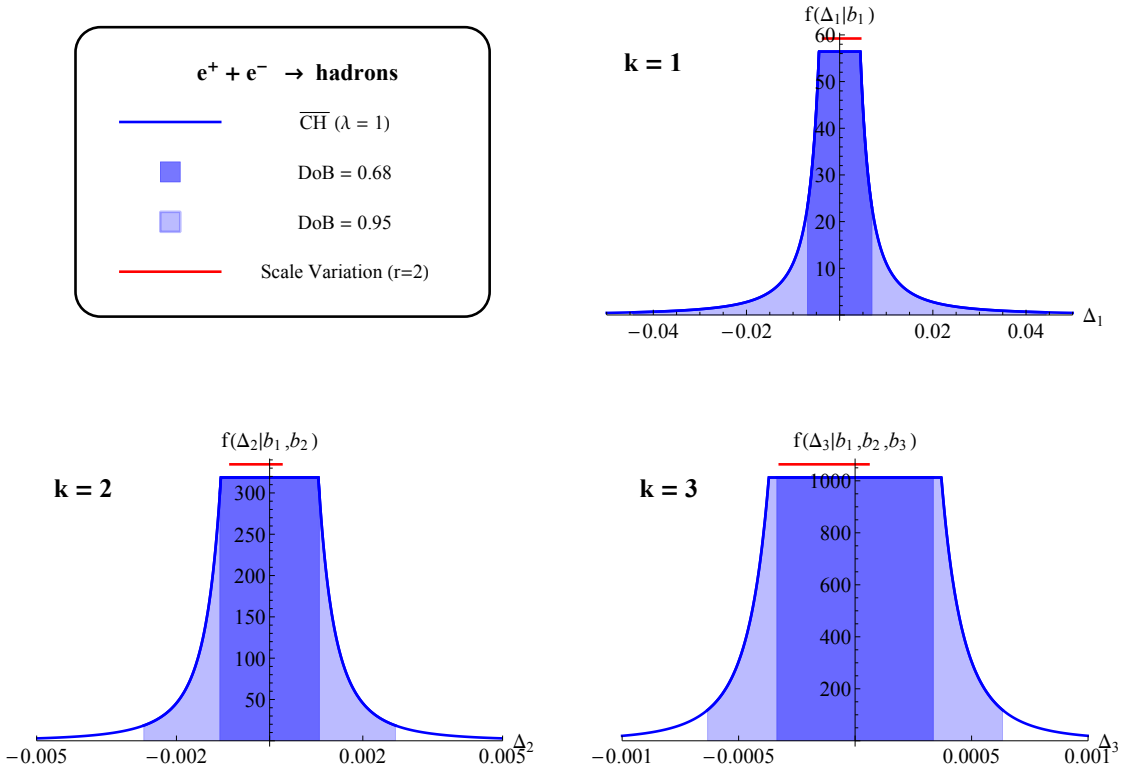


**Figure 71 –** Distribution a posteriori calculée par le modèle Bayésien pour $\Delta_k = \sum_{n=k+1}^{\infty} \alpha_s^n c_n$ (ligne bleu), intervalle 68% DdC (zone bleu), intervalle 95% DdC (zone bleu clair), intervalle de la variation d'échelle (rouge solide), pour la production des hadrons dans les collisions de $e^+$ et $e^-$.

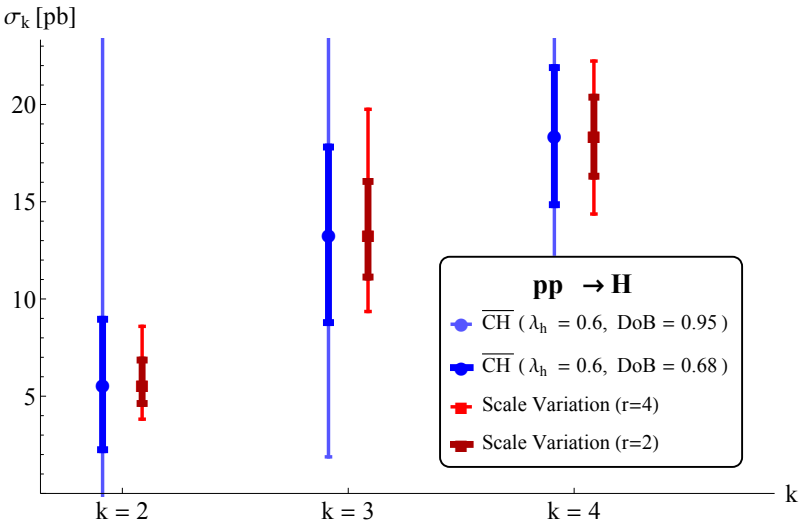


**Figure 72 –** Barres d'erreur à LO, NLO et NNLO pour $\overline{\text{CH}}$ avec $\lambda_h = 0.6$, comparées avec la prédiction obtenue avec la procédure de variation d'échelle, pour la production du Higgs en fusion des gluons.

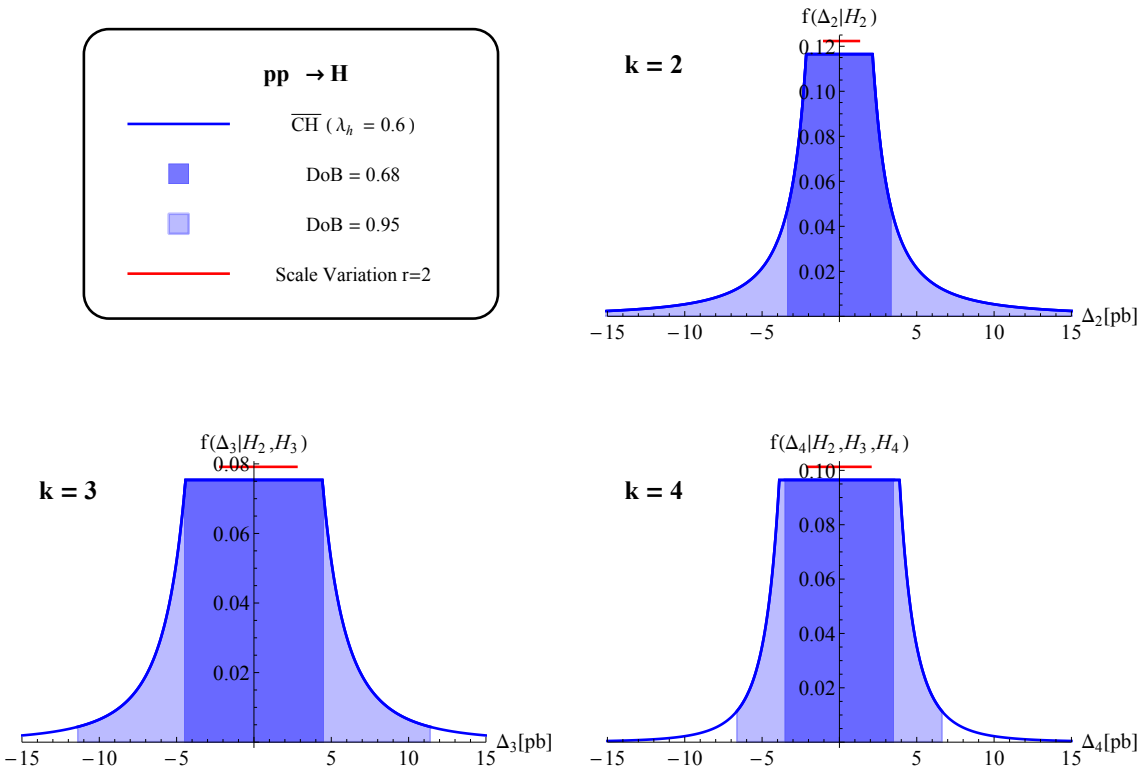


**Figure 73 –** Distribution a posteriori calculée par le modèle Bayésien pour $\Delta_k = \sum_{n=k+1}^{\infty} \alpha_s^n c_n$ (ligne bleu), intervalle 68% DdC (zone bleu), intervalle 95% DdC (zone bleu clair), intervalle de la variation d'échelle (rouge solide), pour la production du Higgs en fusion des gluons.

## 1.3 Conclusions

Maintenant que nous rentrons dans l'ère de la physique de précision au LHC, il sera extrêmement important de n'avoir pas seulement un contrôle qualitatif mais aussi un contrôle quantitatif sur les incertitudes, expérimentales et théoriques. En ce qui concerne le premier point, la communauté des expérimentateurs porte la responsabilité de les évaluer. Concernant le seconde et mettant l'accent sur les incertitudes provenant des corrections d'ordre supérieur qui ne sont pas calculées (et qui sont l'objet de notre étude), la communauté théorique a compté pour les 20 dernières années sur une recette heuristique, à savoir la méthode échelle de variation. Toutefois, cette procédure n'est pas construite sur des fondements théoriques solides et elle ne parvient pas à donner une définition statistique approfondie en terme de niveau de confiance (CL) des intervalles qu'il fournit. Celui-ci est nécessaire pour interpréter correctement les marges d'erreur et de combiner incertitudes d'origine différente. En outre, jusqu'à ce moment, il n'y avait pas d'études spécialisées pour comprendre son comportement sur un large ensemble d'observables.

La portée de ce travail était d'améliorer notre connaissance du problème en effectuant une enquête complète de la prescription couramment utilisé (la variation d'échelle) et également par l'évaluation de la performance d'une méthode beaucoup plus moderne, celle introduite récemment par Cacciari et Houdeau [1]. Comme sous-produit nous avons également créé une version modifiée de celui-ci, que nous avons nommé $\overline{\text{CH}}$ . Nous avons également étendu les applications de la méthode $\overline{\text{CH}}$ aux observables avec hadrons état initial, qui n'était pas dans le domaine de définition original.

Par conséquent, nous avons produit la première enquête sur le comportement statistique de ces deux méthodes. Tout d'abord, nous avons réalisé une étude sur un large ensemble d'observables, classés par leur état initial étant avec ou sans hadrons. Ensuite, nous avons examiné en détail les résultats d'un ensemble spécifique d'observables que nous avons jugé important du point de vue phénoménologique.

En ce qui concerne la procédure de variation de l'échelle, nous avons trouvé que le facteur de $r = 2$ habituellement utilisée pour déterminer l'incertitude, n'est pas associé avec un CL-heuristique de 68% , mais avec une valeur inférieure. Cela est vrai pour les observables non-hadronique et, de façon plus marquée, pour les observables hadroniques. Un facteur $r$ de l'ordre de $3 - 4$ est probablement un choix plus conservateur dans les deux cas.

Relativement au modèle bayésienne $\overline{\text{CH}}$ , nous avons montré qu'il est capable de capturer le comportement fondamental des observables non-hadroniques et hadroniques. Alors que la tendance générale de la performance est bonne, il est probablement possible d'améliorer le modèle en limitant sa définition (et le réglage) à des plus petites (et plus homogènes) classes d'observables. De plus, notre modification introduit dans le modèle un nouvel paramètre libre, $\lambda$, qui doit être déterminé à l'aide d'une procédure externe. En effet, nous avons utilisé une analyse fréquentiste de la performance du modèle pour le définir. Cependant, cela introduit une contamination fréquentiste dans le cadre bayésien qui devrait probablement être évitée par souci de cohérence. Bien entendu, un potentiel de développement est le remplacement de la détermination de $\lambda$ a posteriori avec une distribution a priori ad-hoc, inclus directement dans le modèle, dans le but de faire une marginalisation ultérieure sur elle lors du calcul de la distribution a posteriori de l'intervalle d'incertitude. D'autres développements futurs incluent également l'extension aux observables différentiels, ce qui est absolument nécessaire pour exploiter pleinement le potentiel phénoménologique du modèle.

Notre conclusion est que, pour la variation de l'échelle, le coefficient couramment utilisé de $r = 2$ peut souvent conduire à une sous-estimation de la vraie MHOU. En outre, le cadre bayésien nouvellement in-

troduit par Cacciari et Houdeau, dans sa réalisation sous la forme du modèle de $\overline{\mathrm{CH}}$, offre une alternative intéressante, que est capable de produire ce qui semble être une estimation réaliste des intervalles d'incertitude et, en même temps, une interprétation statistique précise en termes de crédibilité bayésien. À la lumière des résultats, il peut être utilisé pour fournir l'estimation des incertitudes théoriques au côté de la variation d'échelle.

# 2 CARACTÉRISATION DU BOSON DE HIGGS ET SES INCERTITUDES

La découverte d'une résonance scalaire de masse autour de 125.5 GeV par les expériences ATLAS et CMS au Large Hadrons Collider (LHC) [10, 11] met un nouvel accent sur la nécessité de prédictions théoriques précises pour les processus de production et pour les taux de désintégration du boson de Higgs, à la fois dans le Modèle Standard (MS) et dans ses extensions plausibles comme le "Minimal Supersymmetric Standard Model" (MSSM). Le rôle de ces résultats théoriques très précis est d'être à la base des études en cours pour déterminer les propriétés de la résonance nouvellement découverte et de tester sa compatibilité avec le boson de Higgs du MS. Dans le détail, la comparaison entre les mesures expérimentales et les prédictions théoriques de la section efficace totale de production et des branchements dans les différents canaux de désintégration serviront à apprécier si et avec quelle force le nouveau état se couple aux fermions et aux bosons de jauge du MS. D'autres études visent la cinématique des produits de désintégration pour essayer de distinguer entre les différents combinaisons de spin-parité. Enfin, d'autres travaux seront nécessaires pour préciser la nature du potentiel scalaire en mesurant les couplages des bosons de Higgs avec lui-même. L'état actuel de ces calculs est résumée dans les rapports de "Higgs Cross Section Working Group" [12–14].

Comme nous l'avons déjà souligné dans la première partie de la thèse, un degré élevé de contrôle sur les incertitudes théoriques est aussi important que le contrôle sur les résultats expérimentaux. Notre objectif est donc de fournir un nouvel éclairage sur les incertitudes théoriques qui entrent dans les observables qui sont actuellement à la base des analyses expérimentales du boson de Higgs. Nous utilisons les résultats et les outils informatiques les plus récentes pour atteindre cet objectif.

Spécifiquement, nous allons à analyser deux observables qui sont relevant pour la caractérisation du boson de Higgs au LHC. La première est la section efficace total pour la production des boson de Higgs neutres à LHC. Les résultats sont présentés dans la section 2.1.

Un autre observable particulièrement important est l'impulsion transverse du boson de Higgs. Une description correcte de cet observable a besoin d'utiliser une procédure de resommation des logarithmes colineaires. Pour ce faire on utilise les générateurs d'événements Monte Carlo que nous avons développées dans la cadre du POWHEG-BOX. La méthode POWHEG est une construction théorique-informatique qui permet des faire la resommation des logarithmes colinéaires pour des calculs NLO en permettant leur association au avec un logiciel Parton Shower (PS) Monte Carlo.

## 2.1 Production de bosons de Higgs dans de scénarios viables du MSSM

La découverte d'un scalaire léger avec une masse atour de 125.5 GeV met les études MSSM dans une nouvelle perspective. Les scénarios MSSM ne doivent maintenant pas seulement éviter les limites sur la production directe des particules supersymétriques mais aussi avoir une prédiction pour la masse du

| Scenario | $M_S$ [GeV] | $X_t$ [GeV] | $\mu$ [GeV] | $M_2$ [GeV] |
|---|---|---|---|---|
| $m_h^{max}$ | 1000 | 2000 | 200 | 200 |
| $m_h^{mod+}$ | 1000 | 1500 | 200 | 200 |
| $m_h^{mod-}$ | 1000 | −1900 | 200 | 200 |
| *light stop* | 500 | 1000 | 400 | 400 |
| *light stau* | 1000 | 1600 | 500 | 200 |
| *tau-phobic* | 1500 | 3675 | 2000 | 200 |

**Table 19 –** Choix des paramétrés du MSSM pour les scénarios proposés en ref. [15].

Higgs correcte. Pour notre étude nous avons pris les scénarios publiés dans [15] et reportés en table 19. Nous avons modifié le scénario "light stop" pour éviter l'exclusion expérimentale en raison des études de recherche de production directe de stops et sbottoms en fixant $M_2 = \mu = 400$ GeV et $M_1 = 340$ GeV.

Les processus de production que nous avons pris en considération sont la fusion de gluons et la production en annihilation de bottom quarks. Nous avons étudié la section efficace total en utilisant le code `SusHi` (qui comprend toutes les correction plus avancées disponibles) à LHC avec 8 TeV comme énergie de centre de masse.

Les résultats de la section efficace totale pour le scénario light stop sont présentés dans la figure 74 pour le scalaire léger et le scalaire lourd et dans la figure 75 pour le pseudoscalaire.

Le comportement qualitatif des sections dans les figures 74 et 75 peut être facilement à interprété compte tenu des relations entre les masses de scalaires et la masse du pseudoscalaire dans le secteur de Higgs du MSSM, et de la façon dont chacun des Higgs bosons se couplent aux quarks top et bottom (les contributions de squark sont généralement sous-dominantes).

Par exemple, pour le scalaire léger, dans la limite de découplage, $m_A \gg m_Z$, le scalaire plus léger ,h, a des couplage aux quarks qui sont presque comme dans le MS, tandis que sa masse est essentiellement indépendante de $m_A$ et, pour $\tan\beta \gtrsim 10$, ne dépend que faiblement de $\tan\beta$. La section efficace totale de production pour $h$ varie très peu dans cette région, et diffère du résultat du MS pour un boson de Higgs de masse égale en raison des contributions des squarks au processus gluon-fusion. Pour $m_A \lesssim 130$ GeV, d'autre part, le couplage de $h$ au quark top (bottom) n'est pas standard, puisque qu'il est est supprimées (amélioré) par $\tan\beta$. Dans cette région étroite de la section totale de $h$ la production est dominée par les contributions des diagrammes qui impliquent le couplage Higgs-bottom quark, et il se développe de manière significative avec $\tan\beta$.

On peux expliquer le comportement pour $H$ et $A$ de la même façon.

Même si ce n'est pas présenté dans ce résumé, nous avons aussi étudie l'importance du canal d'annihilation de bottom en relation à la fusion de gluons et l'impact de particules supersymétriques sur la section efficace.

### 2.1.1 Incertitudes théoriques de la section efficace

Pendant notre travaux nous avons étudié différentes sources d'incertitude :

- L'incertitude mesurées par la variation d'échelle, en fusion de gluon et annihilation des bottom quarks. On a vu que la variation d'échelle de la fusion des gluon a un comportement non banal,

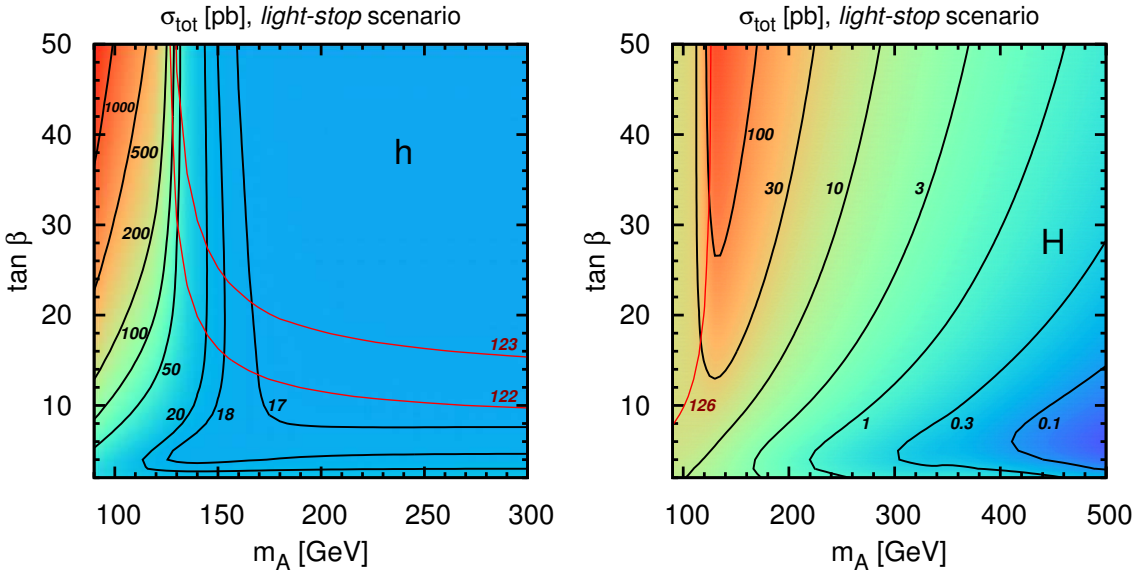


**Figure 74 –** Section efficace totale en pb pour la production de h (gauche) et H (droite), comme fonction de $m_A$ et tan β dans le scénario light stop. Les courbes en rouge sont les contours de masse égale pour chaque scalaire.

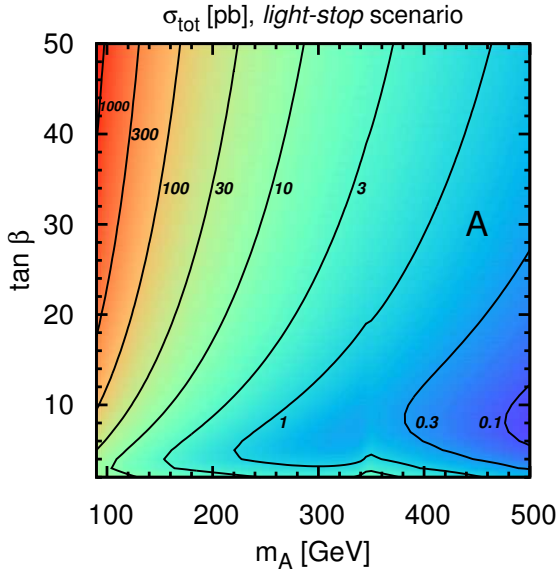


**Figure 75 –** Section efficace totale en pb pour la production de pseudoscalaire A.

qui dépend du la valeur précise des paramètres supersymétriques choisis (voir figure 76). Cela s'explique par le fait que la section efficace totale est la somme des contributions séparées qui sont calculées à des ordres différentes (le top est à NNLO dans le limite $m_t \to \infty$ et exact à NLO, le bottom est exact à NLO, les contributions supersymétriques sont exactes à LO, approximés à NLO). Donc, selon la prédominance d'une contribution sur l'autre dans le plan $m_A - \tan\beta$, la variation d'échelle est différente. Dans le cas de l'annihilation des bottom quarks, le comportement est plus simple et est dépendant plus de la masse du Higgs que des paramètres supersymétriques.

- L'incertitude due à la définition du couplage de Yukawa du bottom quark dans le processus de fusion des gluons. Nous avons montré qu'il y a un très grand différence si fait le calcul de la section efficace total en utilisant la masse "on-shell" ou la masse $\overline{\text{MS}}$. En fait il peut atteindre 60% dans les régions où la section efficace est dominée par la contribution du bottom quark, même si on doit rappeler que dans ces régions la contribution de la fusion des gluons est dominée par celle qui vient de l'annihilation des bottom quarks.

- L'incertitude dans l'inclusion des corrections améliorées par $\tan\beta$. Nous avons étudié ces ambiguïtés en appliquant un facteur de test de 10% à la valeur utilisée par défaut.

- Les incertitudes qui dérivent des PDF et de $\alpha_s$. Ces incertitudes a été computées avec la procédure standard de groupe PDF4LHC . Nous avons montré que elles sont plus grand lorsque la masse du Higgs devient plus lourde. En plus, elle est la même que dans le MS.

- L'incertitude qui dérive de la dépendance de masse du bottom dans la PDF. Nous avons fait l'étude en utilisant les PDF extraites avec différentes valeurs de la masse du bottom.

- L'incertitude qui vient de l'utilisation des approximations dans le calcul des corrections supersymétrique. Cette incertitude a été évaluée en utilisant un facteur de test. Nous avons vu qu'elle est particulièrement importante pour le scalaire lourde dans la région gluophobique de l'espace des paramètres MSSM, dans le scénario light stop.

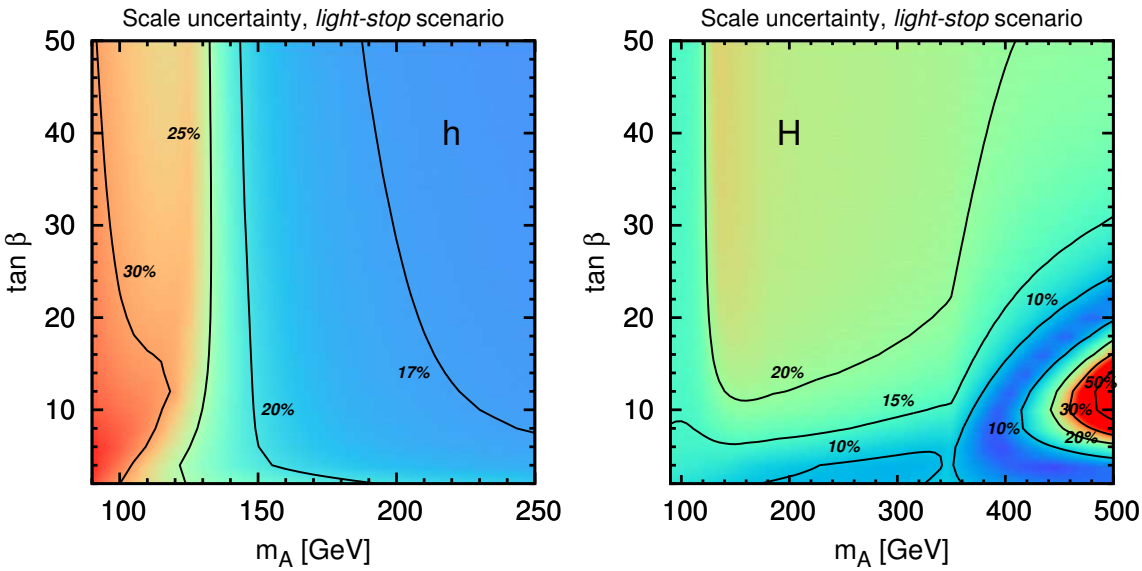


**Figure 76 –** Importance relative (en pourcentage) de la variation d'échelle pour la production de h (gauche) et H (droite) dans le processus de fusion des gluons.

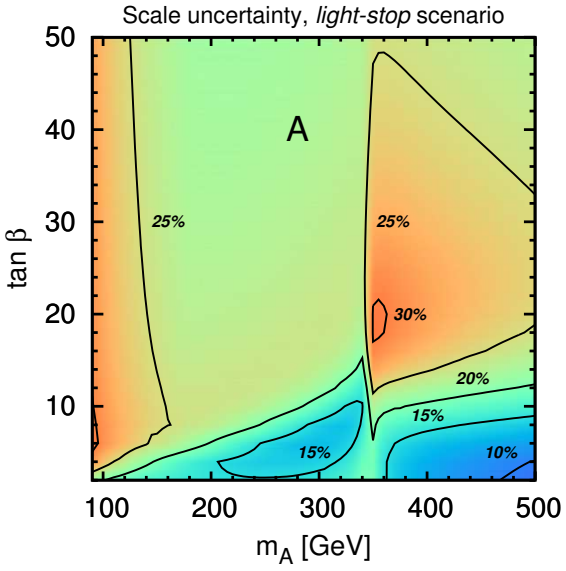


**Figure 77 –** Comme en figure 76 mais pour la production du pseudoscalaire A.

## 2.2 L'impulsion transverse du boson de Higgs en fusion de gluons

Le boson de Higgs acquiert une dynamique transversale $p_T$ en raison de son recul contre le rayonnement de la QCD. Dans la théorie des perturbations d'ordre fixe l'émission des bosons de jauge sans masse de l'état initial donnent, dans la limite de colinéaires, une divergence logarithmique de la distribution en impulsion transversale Higgs, signalant un défaut de l'approche perturbative, avec un paramètre de développement efficace $\alpha_s(p_T)\log(p_T/m_H) \sim 1$ dans la région de l'espace des phases de disparition $p_T$. La resommation analytique à tous les ordres des termes $\alpha_s(p_T)\log\left(p_T/m_H\right))^n$ est réalisée en exploitant les propriétés universelles du rayonnement de QCD dans la limite de colinéaires et rétablit un comportement physique acceptable (la suppression Sudakov) de la distribution d'impulsion transverse Higgs dans la limite $p_T \to 0$.

On a étudié le calcul numérique de l'impulsion transverse dans la cadre du méthode POWHEG , avec les générateurs des éventés que on a écrit dans le POWHEG-BOX . Nous avons prêté une attention spécifique au problème de l'inclusion des masses du quarks, par rapport aux résultat dans le limite $m_t \to \infty$, dans la cadre de la "Heavy Quark Effective Field Theory" (HQEFT). Nous avons déterminé les paramètres optimaux pour calculer l'impulsion en respectant les propriétés de colinéarité de la QCD dans le SM, le MSSM et le 2HDM.

### 2.2.1 Résultats

Nous avons utilisé le POWHEG-BOX pour étudier l'inclusion des amplitudes avec la dépendance complète de masse du quark dans la fusion des gluons. Les résultat pour le MS avec la configuration de défaut de POWHEG sont présentés dans les figures 46. On peut voir que l'inclusion du top quark modifie la distribution avec une suppression pour large $p_T^H$, tandis que l'inclusion du bottom quark a des effets aussi dans la région de petit $p_T^H$. Dans la figure 47 on montre la différence entre POWHEG et MC@NLO . On peux voir que les effets de masse du quark bottom sont plus marqués dans POWHEG . On peut montrer que la raison est la structure particulière du facteur de forme de Sudakov en POWHEG et que si on utilise des échelles de resommation égale la différence entre le deux se réduit très fortement.

Nous avons fait un étude similaire pour l'impulsion transverse dans le MSSM et dans le 2HDM. Le choix des échelles dans ces deux modèles est encore plus important parce que le bottom quark joue un rôle prédominant dans certaines régions de l'espace des paramètres.

## 2.3 Conclusions

Maintenant qu'un boson de Higgs avec des propriétés compatibles avec le MS a été découvert au LHC, il sera très important de comparer ses propriétés mesurées avec nos attentes théoriques dans le but de comprendre sa nature. Pour atteindre cet objectif, il est fondamental d'avoir un contrôle complet sur les prédictions théoriques, en ayant des calculs très précis et une compréhension approfondie de leurs incertitudes. Prenant en considération cette nécessité, nous nous sommes concentrés sur l'étude de deux observables différents qui sont pertinents pour les études liées au boson de Higgs.

Au début, nous avons discuté les sections efficaces totales pour la production des bosons de Higgs neutres des MSSM dans un ensemble de scénarios compatibles avec les résultats du LHC. Ces observables

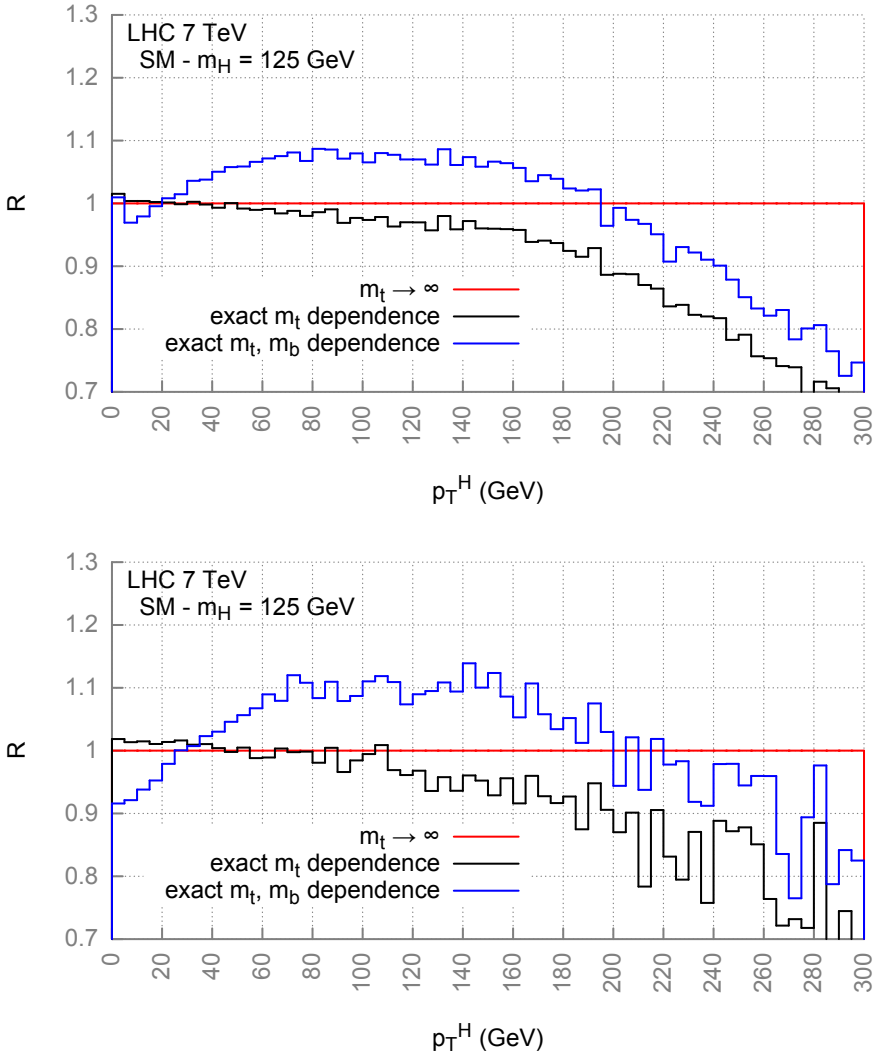


**Figure 78 –** Rapport des distributions de $p_T^H$ normalisées dans le MS, avec le top et le bottom quark (bleu), seulement le top (noir) sur la même distribution obtenue dans la limite $m_t \to \infty$ à NLO (au-sus) et après le showering (au-sous).

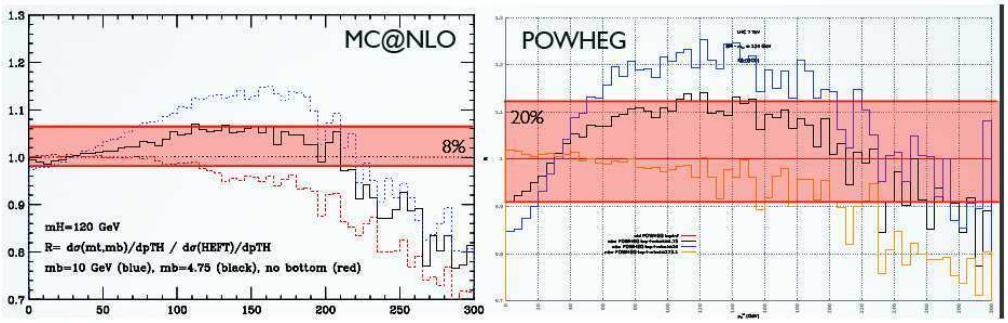


**Figure 79 –** Rapport des distributions de $p_T^H$ normalisées dans le MS (top et bottom quarks) sur la même distribution dans l'HQEFT, calculé par MC@NLO (gauche) et POWHEG (droite), pour des valeurs différentes de la masse du bottom quark (séminaire de S.Frixione).

sont entre les plus importants, car leurs valeurs sont indispensables pour afficher les limites d'exclusion pour la production de Higgs supersymétrique, ou, dans le cas des résonances découvertes, de comprendre si elles sont compatibles avec le MSSM.

Nous avons utilisé le code `SusHi` [16], qui met en œuvre les calculs les plus à jour pour la production MSSM Higgs dans gluon fusion et à l'annihilation des quarks bottom, pour calculer les sections efficaces totales. Nous avons observé que celles-ci peuvent être sensiblement différentes des prédictions du SM. En effet, dans le MSSM l'importance de la contribution du top et de la contribution du bottom - et leur poids relatif dans le résultat complet - peut être sensiblement différente du MS et peut conduire à des résultats extrêmement différents dans certaines régions de l'espace des paramètres du MSSM. Nous avons également constaté que, pour les scénarios avec des squarks relativement légers, la section efficace en fusion de gluons peut être supprimée de manière significative en raison de la présence de superparticules dans les boucles.

Ensuite, nous avons étudié les diverses incertitudes qui affectent la prédiction de la section efficace totale. Certaines de ces incertitudes, notamment celles associées au choix des échelles de renormalisation et factorisation, à la paramétrisation de PDF et à la valeur d'entrée pour la constante de couplage fort, sont pertinentes également pour la production de la SM Higgs, bien que leur taille peut différer dans le cas de la production de bosons de Higgs non standards. Au contraire, les incertitudes associées à la définition de la masse et du couplage de Yukawa de quark bottom sont pratiquement négligeable dans le SM - où la contribution du bottom quark ne s'élève qu'à quelques pour cents de la la section efficace totale - mais il devient dominant dans les régions du espace des paramètres du MSSM où les couplages des bosons de Higgs au bottom quark sont améliorés. Dans le cas particulier du scalaire lourd et de la production du pseudoscalaire à grand tan $\beta$, nous avons constaté que la variation du schéma de renormalisation et de l'échelle de Yukawa du bottom peut supprimer la section gluon-fusion de plus de 60%, en raison de la présence de grandes corrections QCD renforcée par les logarithmes du rapport $m_\phi^2/m_b^2$ . Heureusement, dans ce cas, la section totale est dominée par la contribution qui vient de l'annihilation des bottom quarks, qui est soumise à une incertitude d'échelle beaucoup plus petite. Enfin, nous avons étudié les incertitudes liées à notre mise en œuvre des contributions supersymétriques dans le processus de fusion des gluons à NLO et, partiellement, à NNLO. A l'exception d'une région gluophobique dans le cas du scénario light stop, ces incertitudes sont généralement petites taille, ce qui reflète la nature sous-dominante des contributions SUSY elles-mêmes pour des valeurs des masses compatibles avec les limites du LHC pour

les squarks.

Puis nous avons tourné notre attention à l'autre observable désigné, la distribution d'impulsion transverse du boson de Higgs dans la fusion de gluons. Il est important pour deux raisons : la prévision, dans tous les modèles, est exigé par les expérimentateurs pour estimer l'acceptation de leurs détecteurs au processus ; en outre, il représente une autre occasion de vérifier la compatibilité avec le SM.

Nous avons vu que le calcul de la distribution en impulsion transversale nécessite la resommation de termes de la forme $\log(p_t/m_H)$. Ceci est généralement réalisé soit en effectuant une resommation analytique de ces logarithmes ou en utilisant de Parton Shower Monte Carlo. Nous avons suivi cette dernière option et nous avons utilisé nos implémentations (dans le SM, 2HDM et MSSM) du processus de fusion des gluons dans le cadre de POWHEG-BOX .

Dans un premier temps, nous avons étudié les différences entre la prédiction complète SM et celle obtenue dans la limite de $m_t \to \infty$. Nous observons que, pour un boson de Higgs avec une masse de 125 GeV , l'inclusion des effets des quarks top et bottom dans POWHEG produit des distorsions caractéristiques de la forme, avec une suppression dans la région de petit- et grand-$p_T^H$. La première distorsion est due ou le terme d'interférence top-bottom tandis que la seconde est un effet purement du au top quark. Cette distorsion est déjà présent à NLO et elle est renforcée par la structure spécifique du facteur de forme de Sudakov utilisé en POWHEG . En effet, d'autres calculs comme celui dans le cadre de MC@NLO ou celui analytique, montrent des effets réduits. D'autre part, pour un boson de Higgs de 500 GeV , seul le quark top est pertinent et nous observons une suppression dans la queue à haut-$p_T$ de la distribution.

Ensuite, nous tournons à 2HDM de type II. Dans ce cas, les couplages des quarks peuvent être réduits/améliorés par rapport au SM et nous nous attendons à un effet sur la distribution en impulsion transverse. En effet on observe que, lorsque le couplage au bottom quark est renforcée, nous avons une distribution plus douce (plus dure) pour un Higgs plus léger (lourd). Cette l'effet, en contradiction avec le SM, est en raison de l'amplitude carré du bottom quark. D'autre part, si nous augmentons l'importance du quark top, la forme de la distribution d'un Higgs léger est plus douce alors que le celui d'un Higgs lourd est inchangée.

Nous avons également analysé le spectre du $p_T$ dans le scénario light stop du MSSM, pour le scalaire léger, celui lourd et pour le pseudoscalaire. Notre point de l'espace des paramètres est caractérisé par un couplage renforcé au bottom quark . Nous avons découvert que tous les spectres montrent une distorsion de la distribution, en dehors de la normalisation. Pour $h$, nous avons une distorsion non négligeable de la forme, avec la suppression à la fois la haute et basse-$p_T$ région et une amélioration central. Pour $H$ et $A$ on observe une distribution plus souple par rapport au SM.

Enfin, stimulée par les différences entre nos résultats, obtenus avec POWHEG , et ceux de MC@NLO et des calculs analytiques, nous avons effectué une analyse détaillée de comprendre l'origine de ces divergences. Nous avons trouvé qu'elle se trouve dans la définition différente du facteur de forme Sudakov et de la manière dont les échelles de masse du processus de fusion de gluons sont comptabilisés, en particulier celle du bottom quark. Nous avons mis le correspondant de la recette présentée dans [16], où les échelles de resommation distincts sont utilisés pour la contribution du top et la contribution du bottom, dans POWHEG , en utilisant une analyse indépendante basée sur l'étude des amplitudes d'hélicité pour le processus $gg \to Hg$ afin de déterminer les valeurs des échelles. Nous avons constaté que notre prescription POWHEG produit des résultats en très bon accord avec l'une des ref. [16], pour un Higgs du MS avec $m_H = 125$ GeV. Nous avons également étendu cette prescription à une Higgs lourd avec $m_H = 500$ GeV et nous avons également étudié brièvement comment le choix des échelles affecte la distribution

dans le 2HDM, dans le cas où le couplage au bottom quark est renforcée.

Bien que ces dernières années la précision des prédictions théoriques se soit constamment améliorée, de nombreux développements sont encore possibles dans le domaine de la physique du précision du boson de Higgs. En ce qui concerne le SM, des calculs approximatifs à N3LO dans le HQEFT commencent à apparaître et ils semblent indiquer une augmentation très importante par rapport au résultat NNLO. En ce qui concerne le MSSM, la resommation des corrections QCD renforcée par $\ln(m_\phi^2/m_b^2)$, analogue à celle effectuée dans la référence [17] pour la désintégration du boson de Higgs en deux photons, il sera nécessaire de réduire la grande incertitude dans la production de bosons de Higgs non standard via gluon fusion (d'ailleurs, ce calcul serait bénéfique pour tous les modèles avec un couplage améliorée, qu'ils soient supersymétrique ou non). La mise en œuvre des résultats existants pour les contributions à deux boucles à $\Delta_b$ [18], à la fois dans la masse du Higgs et de la section efficace, permettra également de réduire l'incertitude dans les scénarios où les contributions de bottom sont pertinentes. En outre, il pourrait être utile d' améliorer le calcul de la section efficace gluon-fusion en prenant en compte de la dépendance complète de la masse du Higgs dans les diagrammes squark-gluon à deux boucles [1] contributions [21–23] - pour couvrir les scénarios dans lesquels les bosons de Higgs non standards sont plus lourds que la troisième génération squarks - et en incluant les effets à trois-boucles [24, 25].

1 Et les contributions à deux boucles de quark-squark-gluino [19, 20], dès qu'ils seront disponibles

# BIBLIOGRAPHIE


[1] Matteo Cacciari and Nicolas Houdeau. Meaningful characterisation of perturbative theoretical uncertainties. *JHEP*, 1109 :039, 2011. doi : 10.1007/JHEP09(2011)039.

[2] A. I. Vainshtein and V. I. Zakharov. Ultraviolet-renormalon calculus. *Phys. Rev. Lett.*, 73 :1207–1210, Aug 1994. doi : 10.1103/PhysRevLett.73.1207. URL `http://link.aps.org/doi/10.1103/PhysRevLett.73.1207`.

[3] Valentin I. Zakharov. QCD perturbative expansions in large orders. *Nucl.Phys.*, B385 :452–480, 1992. doi : 10.1016/0550-3213(92)90054-F.

[4] Jan Fischer. On the role of power expansions in quantum field theory. *Int.J.Mod.Phys.*, A12 : 3625–3663, 1997. doi : 10.1142/S0217751X97001870.

[5] M. Beneke. Renormalons. *Phys.Rept.*, 317 :1–142, 1999. doi : 10.1016/S0370-1573(98)00130-6.

[6] Stefano Forte, Andrea Isgrò, and Gherardo Vita. Do we need N$^3$LO Parton Distributions ? *Phys.Lett.*, B731 :136–140, 2014. doi : 10.1016/j.physletb.2014.02.027.

[7] Stefano Goria, Giampiero Passarino, and Dario Rosco. The Higgs Boson Lineshape. *Nucl.Phys.*, B864 :530–579, 2012. doi : 10.1016/j.nuclphysb.2012.07.006.

[8] Marco Bonvini, Stefano Forte, and Giovanni Ridolfi. Soft gluon resummation of Drell-Yan rapidity distributions : Theory and phenomenology. *Nucl.Phys.*, B847 :93–159, 2011. doi : 10.1016/j.nuclphysb.2011.01.023.

[9] Marco Bonvini, Stefano Forte, and Giovanni Ridolfi. The Threshold region for Higgs production in gluon fusion. *Phys.Rev.Lett.*, 109 :102002, 2012. doi : 10.1103/PhysRevLett.109.102002.

[10] Georges Aad et al. Observation of a new particle in the search for the Standard Model Higgs boson with the ATLAS detector at the LHC. *Phys.Lett.*, B716 :1–29, 2012. doi : 10.1016/j.physletb.2012.08.020.

[11] Serguei Chatrchyan et al. Observation of a new boson at a mass of 125 GeV with the CMS experiment at the LHC. *Phys.Lett.*, B716 :30–61, 2012. doi : 10.1016/j.physletb.2012.08.021.

[12] S. Dittmaier et al. Handbook of LHC Higgs Cross Sections : 1. Inclusive Observables. 2011.

[13] S. Dittmaier, S. Dittmaier, C. Mariotti, G. Passarino, R. Tanaka, et al. Handbook of LHC Higgs Cross Sections : 2. Differential Distributions. 2012. doi : 10.5170/CERN-2012-002.

[14] S Heinemeyer et al. Handbook of LHC Higgs Cross Sections : 3. Higgs Properties. 2013. doi : 10.5170/CERN-2013-004.

[15] M. Carena, S. Heinemeyer, O. Stål, C.E.M. Wagner, and G. Weiglein. MSSM Higgs Boson Searches at the LHC : Benchmark Scenarios after the Discovery of a Higgs-like Particle. *Eur.Phys.J.*, C73 : 2552, 2013. doi : 10.1140/epjc/s10052-013-2552-1.

[16] Robert V. Harlander, Stefan Liebler, and Hendrik Mantler. SusHi : A program for the calculation of Higgs production in gluon fusion and bottom-quark annihilation in the Standard Model and the MSSM. *Computer Physics Communications*, 184 :1605–1617, 2013. doi : 10.1016/j.cpc.2013.02.006.
Massimiliano Grazzini and Hayk Sargsyan. Heavy-quark mass effects in Higgs boson production at the LHC. *JHEP*, 1309 :129, 2013. doi : 10.1007/JHEP09(2013)129.

[17] M.I. Kotsky and Oleg I. Yakovlev. On the resummation of double logarithms in the process Higgs → gamma gamma. *Phys.Lett.*, B418 :335–344, 1998. doi : 10.1016/S0370-2693(97)01260-4.
R. Akhoury, H. Wang, and Oleg I. Yakovlev. On the Resummation of large QCD logarithms in Higgs → gamma gamma decay. *Phys.Rev.*, D64 :113008, 2001. doi : 10.1103/PhysRevD.64.113008.

[18] David Noth and Michael Spira. Higgs Boson Couplings to Bottom Quarks : Two-Loop Supersymmetry-QCD Corrections. *Phys.Rev.Lett.*, 101 :181801, 2008. doi : 10.1103/PhysRevLett.101.181801.
David Noth and Michael Spira. Supersymmetric Higgs Yukawa Couplings to Bottom Quarks at next-to-next-to-leading Order. *JHEP*, 1106 :084, 2011. doi : 10.1007/JHEP06(2011)084.
L. Mihaila and C. Reisser. O(alpha_s^2) corrections to fermionic Higgs decays in the MSSM. *JHEP*, 1008 :021, 2010. doi : 10.1007/JHEP08(2010)021.

[19] Charalampos Anastasiou, Stefan Beerli, and Alejandro Daleo. The Two-loop QCD amplitude gg → h,H in the Minimal Supersymmetric Standard Model. *Phys.Rev.Lett.*, 100 :241806, 2008. doi : 10.1103/PhysRevLett.100.241806.

[20] M. Muhlleitner, H. Rzehak, and M. Spira. SUSY-QCD Corrections to MSSM Higgs Boson Production via Gluon fusion. *PoS*, RADCOR2009 :043, 2010.

[21] Charalampos Anastasiou, Stefan Beerli, Stefan Bucherer, Alejandro Daleo, and Zoltan Kunszt. Two-loop amplitudes and master integrals for the production of a Higgs boson via a massive quark and a scalar-quark loop. *JHEP*, 0701 :082, 2007. doi : 10.1088/1126-6708/2007/01/082.

[22] U. Aglietti, R. Bonciani, G. Degrassi, and A. Vicini. Analytic Results for Virtual QCD Corrections to Higgs Production and Decay. *JHEP*, 0701 :021, 2007. doi : 10.1088/1126-6708/2007/01/021.
R. Bonciani, Giuseppe Degrassi, and A. Vicini. Scalar particle contribution to Higgs production via gluon fusion at NLO. *JHEP*, 0711 :095, 2007. doi : 10.1088/1126-6708/2007/11/095.

[23] Margarete Muhlleitner and Michael Spira. Higgs Boson Production via Gluon Fusion : Squark Loops at NLO QCD. *Nucl.Phys.*, B790 :1–27, 2008. doi : 10.1016/j.nuclphysb.2007.08.011.

[24] Alexey Pak, Matthias Steinhauser, and Nikolai Zerf. Towards Higgs boson production in gluon fusion to NNLO in the MSSM. *Eur.Phys.J.*, C71 :1602, 2011. doi : 10.1140/epjc/s10052-012-2182-z, 10.1140/epjc/s10052-011-1602-9.

[25] Alexey Pak, Matthias Steinhauser, and Nikolai Zerf. Supersymmetric next-to-next-to-leading order corrections to Higgs boson production in gluon fusion. *JHEP*, 1209 :118, 2012. doi : 10.1007/JHEP09(2012)118.